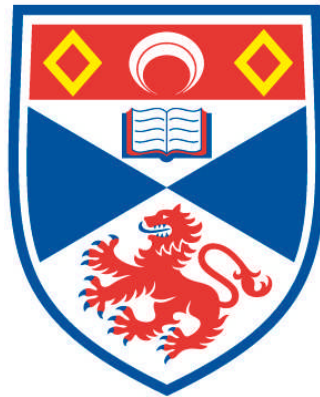


**ON THE PROPERTIES OF SINGLE-SEPARATOR MHS
EQUILIBRIA AND THE NATURE OF SEPARATOR
RECONNECTION**

Julie Elizabeth Helen Stevenson

**A Thesis Submitted for the Degree of PhD
at the
University of St Andrews**



2015

**Full metadata for this item is available in
Research@StAndrews:FullText
at:**

<http://research-repository.st-andrews.ac.uk/>

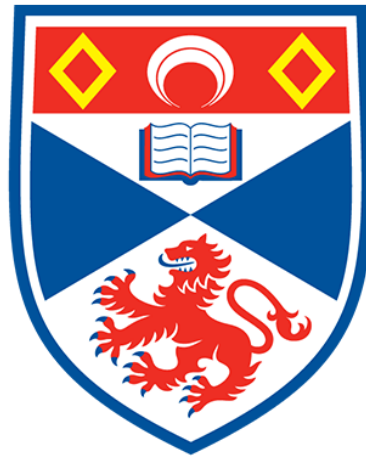
Please use this identifier to cite or link to this item:

<http://hdl.handle.net/10023/6678>

This item is protected by original copyright

**On the properties of single-separator
MHS equilibria and the nature of
separator reconnection**

Julie Elizabeth Helen Stevenson



**University of
St Andrews**

This thesis is submitted in partial fulfilment for the degree of
PhD
at the
University of St Andrews

30th April 2015

Abstract

This thesis considers the properties of MHS equilibria formed through non-resistive MHD relaxation of analytical non-potential magnetic field models, which contain two null points connected by a generic separator. Four types of analytical magnetic fields are formulated, with different forms of current. The magnetic field model which has a uniform current directed along the separator, is used through the rest of this thesis to form MHS equilibria and to study reconnection.

This magnetic field, which is not force-free, embedded in a high-beta plasma, relaxes non-resistively using a 3D MHD code. The relaxation causes the field about the separator to collapse leading to a twisted current layer forming along the separator. The MHS equilibrium current layer slowly becomes stronger, longer, wider and thinner with time. Its properties, and the properties of the plasma, are found to depend on the initial parameters of the magnetic field, which control the geometry of the magnetic configuration.

Such a MHS equilibria is used in a high plasma-beta reconnection experiment. An anomalous resistivity ensures that only the central strong current in the separator current layer is dissipated. The reconnection occurs in two phases characterised by fast and slow reconnection, respectively. Waves, launched from the diffusion site, communicate the loss of force balance at the current layer and set up flows in the system. The energy transport in this system is dominated by Ohmic dissipation.

Several methods are presented which allow a low plasma-beta value to be approached in the single-separator model. One method is chosen and this model is relaxed non-resistively to form a MHS equilibrium. A twisted current layer grows along the separator, containing stronger current than in the high plasma-beta experiments, and has a local enhancement in pressure inside it. The growth rate of this current layer is similar to that found in the high plasma-beta experiments, however, the current layer becomes thinner and narrower over time.

Declarations

I, Julie Elizabeth Helen Stevenson, hereby certify that this thesis, which is approximately 53000 words in length, has been written by me, and that it is the record of work carried out by me, or principally by myself in collaboration with others as acknowledged, and that it has not been submitted in any previous application for a higher degree.

I was admitted as a research student in September 2011 and as a candidate for the degree of PhD in September 2011; the higher study for which this is a record was carried out in the University of St Andrews between 2011 and 2015.

Date..... signature of candidate.....

I hereby certify that the candidate has fulfilled the conditions of the Resolution and Regulations appropriate for the degree of PhD in the University of St Andrews and that the candidate is qualified to submit this thesis in application for that degree.

Date..... signature of supervisor.....

In submitting this thesis to the University of St Andrews I understand that I am giving permission for it to be made available for use in accordance with the regulations of the University Library for the time being in force, subject to any copyright vested in the work not being affected thereby. I also understand that the title and the abstract will be published, and that a copy of the work may be made and supplied to any bona fide library or research worker, that my thesis will be electronically accessible for personal or research use unless exempt by award of an embargo as requested below, and that the library has the right to migrate my thesis into new electronic forms as required to ensure continued access to the thesis. I have obtained any third-party copyright permissions that may be required in order to allow such access and migration, or have requested the appropriate embargo below.

The following is an agreed request by candidate and supervisor regarding the publication of this thesis:

No embargo on print or electronic copies.

Date..... signature of candidate.....

signature of supervisor.....

Acknowledgements

I am very grateful to my supervisor Clare. She has guided me through my PhD and I appreciate all her advice. You have helped me to develop academically and gain confidence in my work and in myself. I also would like to thank Alan, Thomas and Eric for many useful discussions and input.

I am thankful to my wonderful Mum and Dad, without whose unceasing kindness and support I would not be who I am or where I am. I would also like to thank my Mum for her much appreciated food deliveries and long phone calls and my Dad for always making me smile and for being willing to read my thesis. Both of you have always made things in life easier for me.

I would like to thank my brother for being who he is and for challenging me as we grew up together. You have given me perseverance and determination!

I thank all my lovely friends who have filled these PhD years with laughter, especially Sarah, Solmaz, Gordon, Karen and Greg and to my friends Jenny, for many cake filled sessions, and Colleen, for many chatty brunches.

I thank my dear husband James, whose calmness and rational has helped me to get through these three and a half years. I don't think I would have got through it without your constant support. Thank you for always listening to me, for letting me talk things through with you and for sitting through my practice talks. Your patience astounds me and I adore you. You are my rock.

The piece of music printed on the page after the next one is the Prelude from Prelude and Fugue IX in E major by Johann Sebastian Bach. This is my favourite piece of music to play and is in memory of Rina, with whom I shared many merry evenings.

Publications

The following published paper includes material from Chapter 3 of this thesis:

- J. E. H. Stevenson, C. E. Parnell, E. R. Priest and A. L. Haynes. “The nature of separator current layers in MHS equilibria. I. Current parallel to the separator”, *Astronomy & Astrophysics*, Volume 573, 2015

Preludio IX.

Allegretto. ($\text{♩} = 84$)

p sempre legato.

cresc.

f

dimin.

p

cresc.

f

4 2 5 4 1 2 4
dimin. *p*
1 2 1 5

p *p*
7

cresc. *f*
4 2 1 2 1 5

sf *dimin.*
3 5 5 5 4 3

p *rallent.*
4 5 7 1 2 4 4 1 2 4 5

Contents

1	Introduction	1
1.1	Our Sun	1
1.2	MHD equations	7
1.2.1	Maxwell's equations	7
1.2.2	Fluid equations	9
1.2.3	Ohm's law	9
1.2.4	Summary of the MHD equations	10
1.2.5	Ideal and non-ideal regions	10
1.3	Magnetic null points	12
1.3.1	2D null points	12
1.3.2	3D null points	13
1.4	Magnetic reconnection in 2D and 3D	15
1.5	3D magnetic separators	19
1.6	Current layers	20
1.7	Numerical codes	21
1.7.1	MHD code: Lare3d	21
1.7.2	Finding the magnetic skeleton	23
1.7.3	Finding the skeleton of a 3D null point	25
1.8	Aims	26
2	Analytical forms for single-separator magnetic fields	28
2.1	Importance of separators	28
2.2	Potential separator magnetic structures	28
2.2.1	Condition 2: There are only two nulls in the model	29
2.2.2	Condition 3: Nature of the lower null ($x = y = z = 0$)	29
2.2.3	Condition 4: Nature of the upper null ($x = y = 0, z = L$)	30
2.2.4	Special case $b = 0$	31
2.2.5	Upper and lower nulls	32
2.2.6	General potential magnetic field local to the separator	35
2.2.7	Neglecting a fourth parameter	37
2.3	Effects of current parallel to the separator	40
2.3.1	Nature of the lower null ($x = y = z = 0$)	40
2.3.2	Nature of the upper null ($x = y = 0, z = L$)	41
2.3.3	Constraint to ensure there are only two nulls in the model	42
2.3.4	Non-potential single-separator magnetic field	42

2.3.5	Magnetic field local to the separator	43
2.3.6	Lorentz force	46
2.4	Effects of current perpendicular to the separator	46
2.4.1	Nature of the lower null ($x = y = z = 0$)	48
2.4.2	Nature of the upper null ($x = y = 0, z = L$)	48
2.4.3	Non-potential single-separator magnetic field with current perpendicular to separator	49
2.4.4	Magnetic field local to the separator	49
2.4.5	Lorentz force	49
2.5	Effects of current parallel and perpendicular to the separator	50
2.5.1	Nature of the lower null $x = y = z = 0$	51
2.5.2	Nature of the upper null $x = y = 0, z = L$	51
2.5.3	Non-potential single-separator magnetic field with current parallel and perpendicular to the separator	52
2.5.4	Magnetic field local to the separator	53
2.5.5	Lorentz force	53
2.6	Summary	54
3	Non-resistive MHD relaxation to form a separator current layer: high plasma-beta experiments	56
3.1	Initial setup	57
3.1.1	Magnetic field	57
3.1.2	Plasma	57
3.1.3	Initial field properties	58
3.2	Results	60
3.2.1	Comparison of the initial and final total forces	60
3.2.2	Equilibrium skeleton	64
3.2.3	Energetics	67
3.2.4	Pressure	68
3.2.5	Current	70
3.3	The effects of varying j_{sep}	71
3.3.1	Current layer dimensions	73
3.3.2	Current layer twist	76
3.3.3	Pressure along the length, through the depth and across the width of the current layer	77
3.3.4	Total force along the length, through the depth and across the width of the current layer	79
3.3.5	Growth rate of the current layer	80
3.4	Summary	81
4	The effects of varying the initial separator magnetic field on the MHS equilibrium and its current layer	82
4.1	Evolution of each experiment	83
4.2	Initial Lorentz force	85
4.3	MHS equilibria A: The effects of varying parameter a	86
4.3.1	Initial and equilibrium magnetic skeleton	86

4.3.2	Properties of the current layer	89
4.3.3	Current layer twist	92
4.3.4	Pressure along the length, through the depth and across the width of the current layer	92
4.3.5	Total force along the length, through the depth and across the width of the current layer	96
4.4	MHS equilibria B: The effects of varying parameter b	99
4.4.1	Initial and equilibrium magnetic skeleton	100
4.4.2	Properties of the current layer	102
4.4.3	Current layer twist	105
4.4.4	Pressure along the length, through the depth and across the width of the current layer	106
4.4.5	Total force along the length, through the depth and across the width of the current layer	109
4.5	MHS equilibria C: The effects of varying parameter c	111
4.5.1	Initial and equilibrium magnetic skeleton	112
4.5.2	Properties of the current layer	114
4.5.3	Current layer twist	116
4.5.4	Pressure along the length, through the depth and across the width of the current layer	117
4.5.5	Total force along the length, through the depth and across the width of the current layer	121
4.6	Growth rate of the current layer	121
4.7	Summary	125
5	Spontaneous reconnection at a high plasma-beta separator current layer	131
5.1	Properties of the equilibrium field and the plasma	132
5.2	Energetics	135
5.3	Evolution of the magnetic field	137
5.4	Effects of residual forces during the reconnection experiment	143
5.5	Analysis of waves in the system	148
5.5.1	Perturbed current $ \mathbf{j} - \mathbf{j}_{MHS} $	148
5.5.2	Perturbed pressure $p - p_{MHS}$	152
5.6	Vorticity and velocity	156
5.7	Transport of energy	162
5.7.1	Transport of magnetic energy	164
5.7.2	Transport of internal energy	164
5.7.3	Transport of kinetic energy	165
5.7.4	Main terms involved in the transport of energy	165
5.8	Parameter analysis: η_d , j_{crit} and ν	166
5.8.1	Effects of η_d , j_{crit} and ν on the reconnection rate	166
5.8.2	Effects of varying the resistivity, η_d	167
5.8.3	Effects of varying j_{crit}	168
5.8.4	Effects of varying the background viscosity, ν	169
5.9	Summary	170

6	Non-resistive MHD relaxation to form a separator current layer: achieving low plasma-beta	172
6.1	Approaching a low plasma beta	172
6.1.1	Lowering the value of the plasma beta	173
6.2	Low plasma-beta magnetic field and plasma properties	174
6.2.1	Initial forces on the magnetic field	176
6.3	Energetics	178
6.4	Evolution of the magnetic field and plasma	180
6.5	Current layer formation	182
6.6	Pressure along the length, through the depth and across the width of the current layer	187
6.7	Total force along the length, through the depth and across the width of the current layer	190
6.8	Growth rate	191
6.9	Achieving a low plasma beta	192
6.10	Summary	195
7	Summary and future work	197
7.1	Analytical forms for single-separator magnetic fields	197
7.2	Non-resistive MHD relaxation to form a separator current layer: high plasma-beta experiments	198
7.3	The effects of varying the initial separator magnetic field on the MHS equilibrium and its current layer	199
7.4	Spontaneous reconnection at a high plasma-beta separator current layer	201
7.5	Non-resistive MHD relaxation to form a separator current layer: achieving a low plasma-beta	202
7.6	Future work	203
A	Values of y for the potential magnetic field	204
B	Values of y for the magnetic field with current parallel to the separator	205

Chapter 1

Introduction

1.1 Our Sun

The Sun is the most luminous object in our solar system and without it, life as we know it would not exist. The Sun is of vast importance to (most) life on Earth and, due to this fact itself, deserves to be studied and has been studied in varying degrees since at least 2000B.C.

The Sun is a large ball of plasma (defined below), of radius $r_{\odot} = 6.96 \times 10^8 \text{m}$ ($= 1R_{\odot}$). This value can be measured by firstly working out the distance between the Earth and the Sun, which can be calculated by using the distance between the Earth and Venus, Fig. 1.1. One can measure the angle (x) between Venus and the Sun when Venus is at its greatest extension and the distance between the Earth and Venus can be calculated using radar (a timed pulse is sent from Earth to Venus at a known speed). This then allows the distance between the Earth and the Sun to be measured as roughly $d = 1.5 \times 10^8 \text{km}$ ($= 1\text{AU}$). The radius of the Sun can now be calculated from knowing d and that the Sun subtends an angle of $\theta = 0.5^\circ$. Thus, the radius of the Sun is $r_{\odot} = d \tan(\theta)/2$.

The mass of the Sun can now be calculated using Newton's universal law of gravitation. If we allow the force of gravitational attraction to be equal to the centripetal force we find

$$M_{\odot} = \frac{v^2 d}{G}, \quad (1.1)$$

where $v = 2\pi d/T$, $T = 1\text{yr}$ and $G = 6.67 \times 10^{-11} \text{Nm}^2 \text{kg}^{-2}$. This yields the mass of the Sun as $M_{\odot} = 2 \times 10^{30} \text{kg}$ and so the Sun is considered to be a typical star for the Milky Way galaxy. Finally, the age of the Sun can be determined from the radioactive dating of meteorites and is estimated to be 4.6×10^9 years old.

The Sun is held together by its own gravitational attraction and, as mentioned previously, is a large, almost perfect sphere of plasma. Plasma, which is also known as the fourth state of matter, was first identified in 1879 by Sir William Crookes [Cro, 1880]. Initially used as a term in medical science, Nobel Laureate Irving Langmuir called this state of matter "plasma" in 1928 to describe ionised regions in gas discharges [Langmuir, 1928]. A plasma is formed when high temperatures cause the electrons of an atom to be stripped away from the protons. This results in a sea of positive ions (made up of positive protons and neutral neutrons) and negative electrons, both of which can be accelerated and moved by the force produced by electric and magnetic fields. In turn, the movement

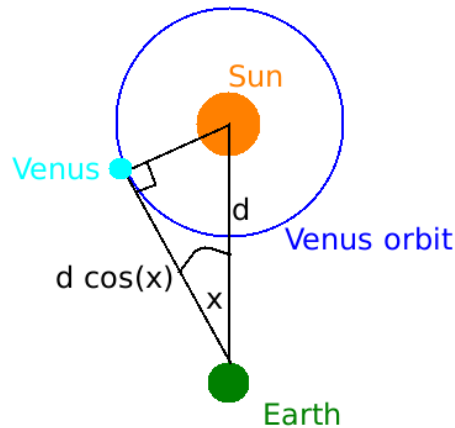


Figure 1.1: Measuring the distance between the Earth and the Sun using Venus.

of particles within a plasma creates electric and magnetic fields. 99% of the universe is made up of plasmas which originate in the thermonuclear burn in the core of stars. The Sun consists of plasma from its core, through all its layers, to its outer atmosphere, known as the corona, which stretches out beyond all the planets to the edge of the solar system, called the heliopause. Fig. 1.2 shows the different layers within the interior of the Sun which are discussed below.

Nuclear reactions occur in the very dense core of the Sun, where fast moving hydrogen (H) is fused together to produce helium (He). Helium was discovered on the Sun before it was on Earth through the study of emission lines and hence was named after the Greek word for the Sun, helios, by Sir Norman Lockyer in 1868 [Loc, 1871].

Sir Arthur Eddington was the first person to note that the core of the Sun acts as a nuclear reactor in 1920 [Eddington, 1920]. This reaction is able to occur due to the high temperature (which ranges from $1.5 \times 10^7\text{K}$ to $7 \times 10^6\text{K}$) and density (which ranges from $1.5 \times 10^5\text{kg/m}^3$ to $1 \times 10^4\text{kg/m}^3$) here in the core, a region which is thought to extend to $0.25R_{\odot}$. The gamma rays (high energy photons) which are produced in this process travel away from the centre of the Sun via the radiative zone where the temperature is cooler than the core. The photons here bounce from particle to particle, being absorbed and re-emitted, and hence take about a million years to leave this layer which extends from outside the core to $0.7R_{\odot}$. The temperature is $2 \times 10^6\text{K}$ just outside the radiative zone at the base of the next layer, the convective zone, where the density is less than 10kg/m^3 .

Within the convective zone, the hot plasma from the top of the radiative zone rises up through the cooler convective region and then sinks as it cools. As the cool plasma sinks it is again heated by the higher temperatures beneath and hence rises through this zone again transporting heat via convection. This process of energy transport occurs much quicker than radiation (on a time scale of about a week) and produces a boiling effect on the Sun's surface, the photosphere (which means ball of light), found at $1R_{\odot}$.

With the invention of the telescope in around 1608 came a realisation that the perfect

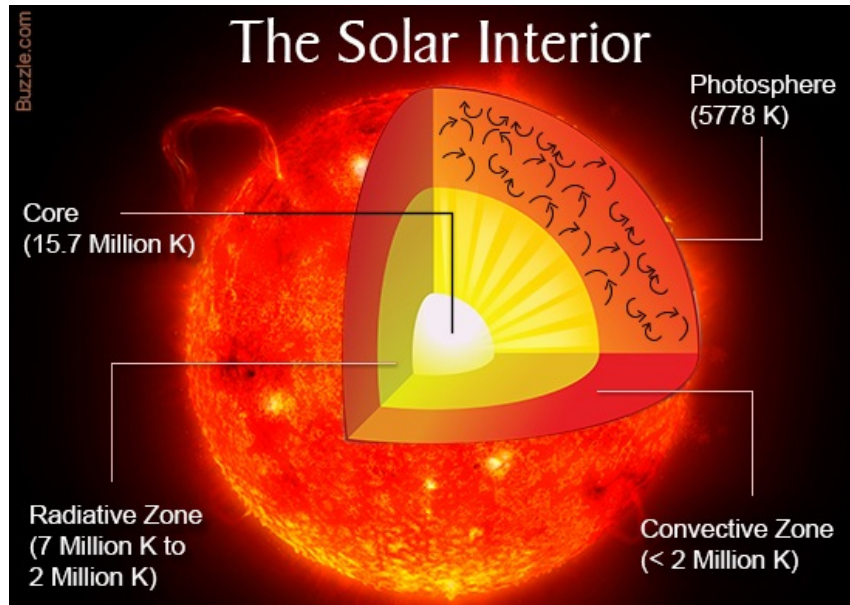


Figure 1.2: The interior of the Sun.

celestial object known as the Sun was, in fact, imperfect with blemishes. Although the inventor of the telescope is still debated today (the earliest patent for the telescope is in the name of Hans Lippershey dated the 25th of September 1608), the first piece of work which used the telescope to study sunspots, which appear on the photosphere, was published in 1611 by Johannes Fabricius (“De Maculis in Sole Observatis”).

The photosphere is at a temperature of around 5800K which drops to around 4300K within the photosphere and then starts to increase into the layer called the chromosphere. Photons from the Sun’s interior finally escape at the photosphere which is much less dense than the interior of the Sun and which emits light at all wavelengths; a continuous spectrum. Absorption lines are seen when analysing light from the photosphere due to particles lying in the photosphere and in the regions above the photosphere. The first known photograph of the Sun, which was taken in 1845 by Fizeau and Foucault, shows some small dark regions which are called sunspots (Fig. 1.3). These features, and others, are described in more detail below.

The photosphere appears to be constantly changing as the cool plasma from below rises up and appears like bubbling caramel on the Sun’s surface. This effect is known as granulation and can be observed well in continuum images (in which parts of the visible spectrum are filtered), Fig. 1.4a, and more clearly also in a close up image Fig. 1.4b which shows the TiO line. In Fig. 1.4a, a few dark orange marks, sunspots, are visible on the solar surface.

Sunspots, which consist of a dark umbra and lighter penumbra (Fig. 1.4b), appear on the photosphere due to the inhibition of convection by strong vertical magnetic fields from the solar interior. They have the strongest magnetic fields of any feature on the Sun. An example of such sunspots can be seen in Fig. 1.4c which shows a magnetogram of the Sun where the white areas represent the magnetic field which is pointing out of the Sun and the black areas represent the magnetic field which is pointing into the Sun. All images in

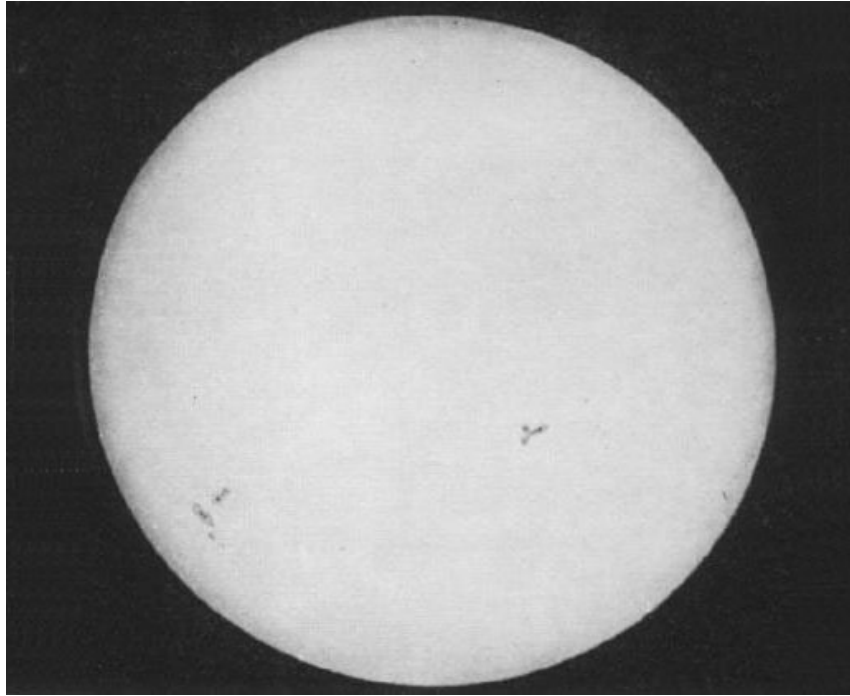


Figure 1.3: The first known picture taken of the Sun in 1845.

Fig. 1.4 were taken at a similar time (except Fig. 1.4b). Indications of these features were visible in the continuum image shown in Fig. 1.4a.

Magnetic fields thread in and out of the photosphere across the entire Sun. These fields are generated in the interior of the Sun, caused by the rotation of the plasma. The number of sunspots on the Sun follows an eleven year solar cycle. Throughout the cycle an increase in the number of regions of magnetic activity is observed and about half way through the cycle the polarity at the poles reverses. This reversal is brought about as sunspots with opposite polarity to that of the hemisphere's polar flux, drift towards the poles and cause flux cancellation [Babcock, 1961]. The magnetic field at the poles of the Sun is open which means that the magnetic field lines here extend out into space away from the Sun. Other features which appear on the photosphere of the Sun include,

- Faculae - bright areas produced by the clumping of magnetic field lines which are most visible near the limb of the Sun due to limb darkening. This effect occurs since the light from the photosphere travels through regions where it is absorbed. This in turn means that we can see deeper into the Sun at its centre than we can at the limb where only the top of the photosphere is visible. Faculae are visible in Fig. 1.4b as small white blobs.
- Granules - these are short-lived (~ 20 mins) regions which are on average 1.0×10^6 m across, split apart by dark bands (Fig. 1.4b). These areas are the tops of the convection cells within which hot plasma is brought to the surface where it cools and expands before sinking down through the dark bands. The granulation cells continually evolve. The image in Fig. 1.4b shows an area of the Sun covering

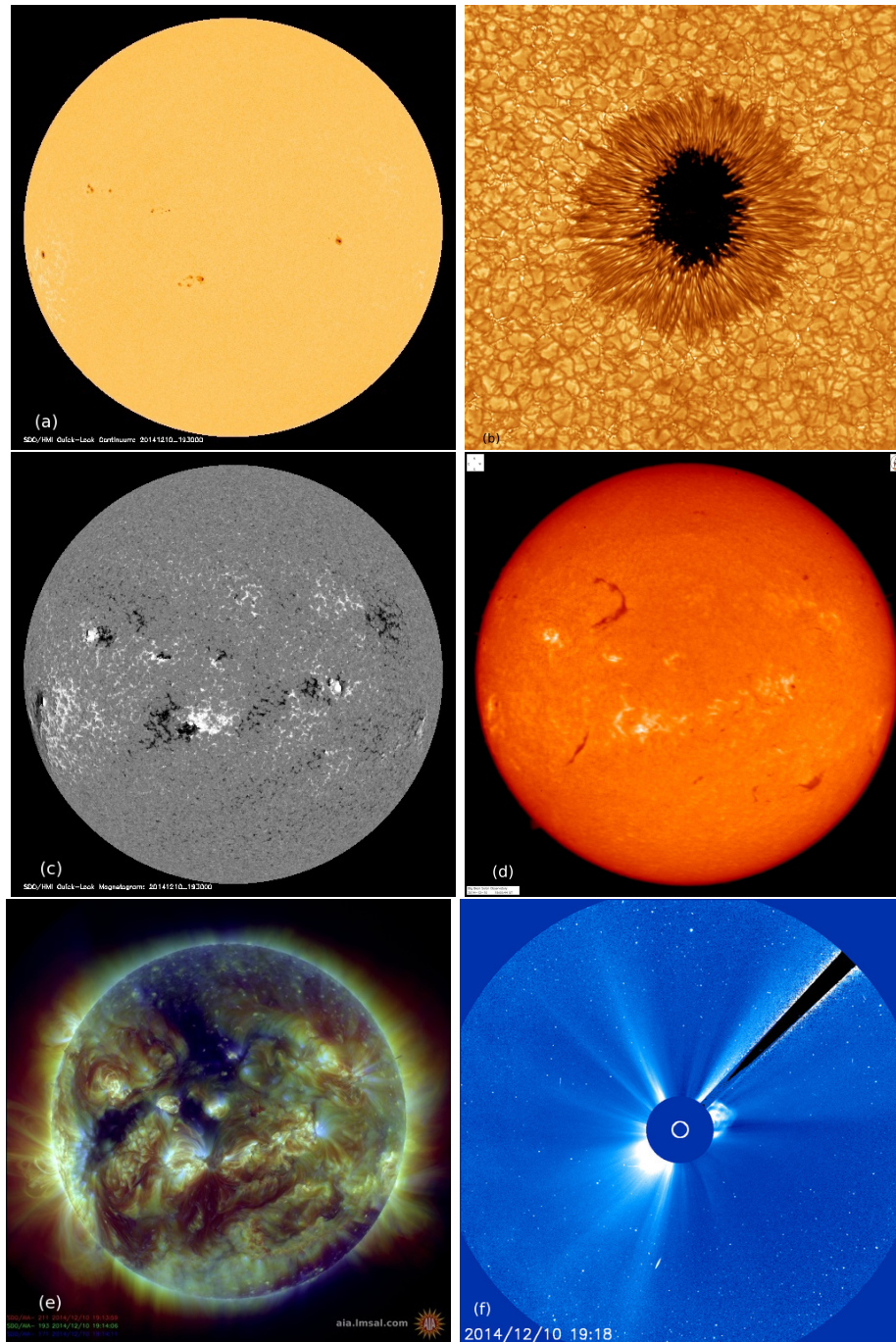


Figure 1.4: (a) Continuum image of the Sun taken by HMI on the 10th of December 2014 at 19:30. (b) Close up of the Sun showing granulation and a sunspot taken by the Big Bear Solar Observatory in July 2010. (c) Magnetogram image of the Sun taken by HMI on the 10th of December 2014 at 19:30. (d) H-alpha image of the Sun taken by the Big Bear Solar Observatory on the 10th of December 2014 at 19:16. (e) Composite image of the lines 17.1nm (blue), 19.3nm (green) and 21.1nm (red) taken by AIA on the 10th of December 2014 at 19:14 and a (f) coronagraph of the Sun taken by LASCO C3 (which has a 16 degree field of view) on the 10th of December 2014 at 19:18.

roughly 23300km by 23300km.

- Supergranules - these features consist of large groups of granules (about 2 to 3.5×10^7 m across) which appear to move together and carry the magnetic field bundles with them. These features exist for about 1-2 days and are observed to continually evolve. Supergranules are most easily identified using measurements of Doppler shift.

The chromosphere (which means ball of colour) is 2×10^6 m thick and reaches temperatures of around 20×10^3 K. Fig. 1.4d highlights the strong magnetic field which was visible at the sunspots as white areas here, but dark features are also seen elsewhere on the disk. These features are called filaments and they are dense ribbons of plasma which are cooler, $\sim 8 \times 10^3$ K, than the surrounding plasma. Most of the energy which is absorbed by atoms in the chromosphere is emitted as red light. Above the chromosphere lies the thin transition region (about 1×10^5 m thick) within which the temperature exponentially increases to more than a million degrees.

Finally, beyond the transition region lies the most outer part of the Sun's atmosphere, the corona. Fig. 1.4e was taken by the AIA instrument on board SDO and shows a composite of the 17.1nm, 19.3nm and 21.1 nm lines. This image highlights coronal loops, which are associated with closed field lines. The footpoints of these loops lie within magnetic regions of opposite polarity (bright areas). Also, dark spots, called coronal holes, are visible in this image. These are regions where the magnetic field is open. Finally, Fig. 1.4f shows a coronagraph image of the Sun which essentially simulates an eclipse by holding a disk over the surface of the Sun. In this way, details of the coronal magnetic field may be seen. In Fig. 1.4f the bright white area to the right of the disk of the Sun is a coronal mass ejection. These violent events see great quantities of solar material erupting out into interplanetary space. The other white areas around the Sun, in this image, represent hot emission outflowing from the Sun.

The corona, named after the Latin word for crown due to its halo like appearance, was first photographed in 1851 by Berkowski [Schielicke and Wittmann, 2005]. This outer region of the Sun's atmosphere, has temperatures of the same order as that of the core of the Sun but has a much lower density of 10^{11} to 10^{12} particles per m^3 . The temperature of the corona (and indeed the chromosphere) is surprising because one would imagine that moving away from a hot body the temperature should fall off. However, the temperature of the atmosphere, above the photosphere, increases in the chromosphere and then sharply increases through the transition region reaching a maximum in the corona to 2×10^6 K or more, with a background temperature of about 1×10^6 K in the low corona. The temperature of the corona then decreases gradually as the corona extends out, as the solar wind, through the heliosphere to its edge, the heliopause, where it meets the interstellar medium.

The origin of the extremely high temperatures, which were first discovered by Grotrian and Edlén [Grotrian, 1939, Edlén, 1942], is still debated today. The high temperature of the solar corona was noticed through the examination of emission lines from which it was inferred that highly ionised elements (e.g., iron, calcium and nickel) existed there. It is possible that the energy release produced during the reconnection of magnetic fields in the corona allows for these gross temperatures. Field lines, which thread the photosphere of the Sun, are jostled continuously by sub-surface convective motions. The time scales of the field line motions lead to two outcomes. Firstly, magnetic structures which are

stressed by slow motions of the field ($\mathbf{v} < \mathbf{v}_A$) will form equilibria with current layers associated with them. These current layers are dissipated by a process known as magnetic reconnection. Secondly, if the field lines are jostled by fast motions ($\mathbf{v} \geq \mathbf{v}_A$), waves are generated. It seems highly plausible that, due to the complex nature of the solar corona, both mechanisms are at work but, in this thesis I study the former, magnetic reconnection.

In the introductory sections that follow, the magnetohydrodynamic (MHD) equations are introduced (Sect. 1.2) before a discussion of the properties of ideal and non-ideal regions which can exist in a magnetised plasma (Sect. 1.2.5). After this, the theory of two dimensional (2D) and three dimensional (3D) magnetic nulls is detailed (Sect. 1.3) before an overview of 2D and 3D magnetic reconnection (Sect. 1.4). Next, 3D magnetic separators, which are the focus of this thesis, are introduced and a discussion of current layer build up at these and other topological features is given (Sects. 1.5 and 1.6). The numerical scheme used to carry out the experiments in this thesis and the codes used for finding the magnetic skeleton of our models are discussed (Sect. 1.7). Finally, the aims of this thesis are outline in Sect. 1.8.

1.2 MHD equations

The MHD equations are a combination of Maxwell's equations of electromagnetism and the four fluid equations [Priest, 2014]. Various assumptions about the plasma are made in formulating the MHD equations and these are;

- the plasma is assumed to be quasi-neutral (overall the plasma acts as if it has equal numbers of positive and negative charges, but on smaller scales charged regions may be observed),
- the speeds involved are much smaller than the speed of light, c ,
- the pressure is assumed to be a scalar,
- the length scales of interest are much greater than the kinetic length scales,
- the time scales of interest are much longer than the kinetic time scales.

The MHD equations describe the movement of magnetic fields which are, in the case of this work, embedded in a plasma.

1.2.1 Maxwell's equations

Maxwell's equations define the fundamentals of electricity and magnetism. These four equations are listed below in mks units (meters, kilograms, seconds) for the solar plasma (where the magnetic permeability, μ , and the permittivity of free space, ϵ , take on their vacuum values denoted by subscript 0)

- Ampere's Law

$$\nabla \times \mathbf{B} = \mu_0 \mathbf{j} + \frac{1}{c^2} \frac{\partial \mathbf{E}}{\partial t}, \quad (1.2)$$

- Faraday's Law

$$\nabla \times \mathbf{E} = -\frac{\partial \mathbf{B}}{\partial t}, \quad (1.3)$$

- Solenoidal Constraint

$$\nabla \cdot \mathbf{B} = 0, \quad (1.4)$$

- Gauss' Law

$$\nabla \cdot \mathbf{E} = \frac{\rho^*}{\epsilon_0}. \quad (1.5)$$

Here $\mathbf{B} = (B_x, B_y, B_z)$ is the magnetic field (T) and $\mathbf{E} = (E_x, E_y, E_z)$ is the electric field (Vm^{-1}). The terms in Maxwell's equations are as follows; $\mu_0 = 4\pi \times 10^{-7} \text{Hm}^{-1}$, \mathbf{j} is the current density (Am^{-2}), c is the speed of light ($3 \times 10^8 \text{ms}^{-1}$), t is time (s), $\rho^* (= e(z^+n^+ - n^-))$ is the charge density (Cm^{-3}) where e is the electron charge ($1.6 \times 10^{-19} \text{C}$), z^+ is the ion number and n^+ and n^- are the positive and negative ion number densities per unit volume respectively and finally ϵ_0 , the permittivity of free space, is equal to $8.9 \times 10^{-12} \text{Fm}^{-1}$.

Eq. 1.2, known as Ampere's law, indicates that gradients in a magnetic field create electric currents. Here, if we use the MHD approximation, which says that characteristic plasma velocities (v_0) are much smaller than the speed of light (c) and hence the system is non-relativistic, then Ampere's law may be written as $\nabla \times \mathbf{B} = \mu_0 \mathbf{j}$ as follows. Firstly, it can be shown by using Faraday's law (Eq. 1.3) that

$$E = \frac{l_0}{t_0} B,$$

where E has the units of an electric field, l_0 and t_0 are typical length and time scales, respectively, and B has the units of a magnetic field. Therefore, the left hand side of Ampere's Law (Eq. 1.2) can be written as B/l_0 and the second term on the right hand side of Eq. 1.2 can be written as $v_0^2 B/c^2 l_0$, where $v_0 = l_0/t_0$ is a typical plasma velocity. Hence, if $v_0^2 \ll c^2$, then the displacement current satisfies the relationship

$$|\nabla \times \mathbf{B}| \gg \frac{1}{c^2} \frac{\partial |\mathbf{E}|}{\partial t},$$

which implies Ampere's Law may be written as $\nabla \times \mathbf{B} = \mu_0 \mathbf{j}$ and so the current is divergence free.

Faraday's law (Eq. 1.3) states that a spatially varying electric field can induce a magnetic field.

The solenoidal constraint (Eq. 1.4) states that there can be no magnetic monopoles. $\nabla \cdot \mathbf{B} = 0$ is an initial condition and it can be shown by taking the divergence of Faraday's equation, that if the solenoidal constraint is true initially then it will always be true

$$\begin{aligned} \frac{\partial(\nabla \cdot \mathbf{B})}{\partial t} &= -\nabla \cdot (\nabla \times \mathbf{E}) \\ &= 0. \end{aligned} \quad (1.6)$$

Finally, Eq. 1.5 is Gauss' Law. In the solar atmosphere the plasma is approximately neutral (equal numbers of negative and positive ions) and so $\rho^* \approx 0$. Therefore, $\nabla \cdot \mathbf{E} \approx 0$. In MHD, the electric field is induced by a changing magnetic field.

1.2.2 Fluid equations

There are four fluids equations,

- Continuity equation

$$\frac{\partial \rho}{\partial t} + \nabla \cdot (\rho \mathbf{v}) = 0, \quad (1.7)$$

- Equation of motion

$$\rho \frac{\partial \mathbf{v}}{\partial t} + \rho (\mathbf{v} \cdot \nabla) \mathbf{v} = -\nabla p + \mathbf{j} \times \mathbf{B} + \mathbf{F}, \quad (1.8)$$

- Energy equation

$$\frac{\rho^\gamma}{\gamma - 1} \frac{D}{Dt} \left(\frac{p}{\rho^\gamma} \right) = -\mathcal{L}, \quad (1.9)$$

- Equation of state

$$p = \frac{k_B}{m} \rho T. \quad (1.10)$$

Here ρ is the plasma density (kgm^{-3}), $\mathbf{v} = (v_x, v_y, v_z)$ is the velocity (ms^{-1}), p is the plasma pressure (Pa), \mathbf{F} represents the sum of the gravitational (\mathbf{F}_g) and viscous (\mathbf{F}_ν) forces (N), γ is the ratio of specific heats (equal to 5/3 for an ideal monatomic gas), \mathcal{L} is the energy loss function, k_B is Boltzmann's constant ($1.38 \times 10^{-23} \text{ m}^2 \text{ kgs}^{-2} \text{ K}^{-1}$), m is the mean particle mass (kg) and T is the plasma temperature (K).

The continuity equation (Eq. 1.7) tells us that matter can not be created or destroyed or, in other words, the rate of mass entering a system is equal to the amount of mass leaving a system.

Eq. 1.8, the equation of motion, is essentially Newton's second law which states that the acceleration of an object multiplied by its mass is equivalent to the sum of the forces on the object.

The energy equation (Eq. 1.9) states that the rate of increase of heat per unit volume as it moves in space is due to the net effect of energy sinks and sources. If the energy loss function $\mathcal{L} = 0$, then there are no thermal exchanges between the plasma and its surroundings (hence the plasma is adiabatic) and so entropy is conserved. The energy loss function, \mathcal{L} , can be written as $\mathcal{L} = \nabla \cdot \mathbf{q} + L_r - j^2/\sigma - H$ where \mathbf{q} is the heat flux due to particle conduction, L_r is the net radiation, the term j^2/σ represents Ohmic dissipation, where σ is the electrical conductivity (Sm^{-1}) and the term H represents all other sources of heating such as viscous heating or wave heating.

Finally the equation of state, which is the closure equation, is the perfect gas law. Eq. 1.10 states there are no interactions between particles in a perfect gas.

1.2.3 Ohm's law

Ohm's law couples the electromagnetic equations to the plasma fluid equations and states that the current density of a system is proportional to the electric field, which is made up of the electric field which would act on a stationary plasma plus the electric field produced by the moving magnetic field. The classical form of Ohm's law may be written as

$$\mathbf{j} = \sigma(\mathbf{E} + \mathbf{v} \times \mathbf{B}). \quad (1.11)$$

1.2.4 Summary of the MHD equations

The MHD equations which we will use throughout this work are as follows (neglecting the effects of gravity)

- Ampere's Law

$$\nabla \times \mathbf{B} = \mu_0 \mathbf{j}, \quad (1.12)$$

- Faraday's Law

$$\nabla \times \mathbf{E} = -\frac{\partial \mathbf{B}}{\partial t}, \quad (1.13)$$

- Ohm's Law

$$\mathbf{j} = \sigma(\mathbf{E} + \mathbf{v} \times \mathbf{B}), \quad (1.14)$$

- Continuity equation

$$\frac{\partial \rho}{\partial t} + \nabla \cdot (\rho \mathbf{v}) = 0, \quad (1.15)$$

- Equation of motion

$$\rho \frac{\partial \mathbf{v}}{\partial t} + \rho(\mathbf{v} \cdot \nabla) \mathbf{v} = -\nabla p + \mathbf{j} \times \mathbf{B} + \mathbf{F}_\nu, \quad (1.16)$$

- Energy equation

$$\frac{\partial p}{\partial t} + \frac{1}{\gamma - 1}(\mathbf{v} \cdot \nabla)p = -\frac{\gamma}{\gamma - 1}p \nabla \cdot \mathbf{v} - \mathcal{L}, \quad (1.17)$$

- Equation of state

$$p = \frac{k_B}{m} \rho T, \quad (1.18)$$

- Solenoidal Constraint

$$\nabla \cdot \mathbf{B} = 0. \quad (1.19)$$

1.2.5 Ideal and non-ideal regions

Combining Ohm's law (Eq. 1.14) with Faraday's law (Eq. 1.13) and Ampere's law (Eq. 1.12) we arrive at the induction equation

$$\frac{\partial \mathbf{B}}{\partial t} = \underbrace{\nabla \times (\mathbf{v} \times \mathbf{B})}_{\text{advection term}} - \underbrace{\nabla \times (\eta \nabla \times \mathbf{B})}_{\text{diffusion term}}, \quad (1.20)$$

which states that the magnetic field can either evolve by moving with the plasma flow or by diffusing through the plasma. Here, η is the magnetic diffusivity (m^2s^{-1}) equal to $1/(\mu_0\sigma)$. If η is constant then Eq. 1.20 can be written as

$$\frac{\partial \mathbf{B}}{\partial t} = \underbrace{\nabla \times (\mathbf{v} \times \mathbf{B})}_{\text{advection term}} + \underbrace{\eta \nabla^2 \mathbf{B}}_{\text{diffusion term}}. \quad (1.21)$$

This equation is made up of two terms, the advection and diffusion terms, and whether one or the other is dominant depends on a dimensionless parameter called the magnetic

Reynolds number (R_m). This number is the ratio of the advection and diffusion terms shown in Eq. 1.20

$$\begin{aligned} R_m &= \frac{|\nabla \times (\mathbf{v} \times \mathbf{B})|}{|\eta \nabla^2 \mathbf{B}|} \\ &= \frac{v_0 B L^2}{L \eta B} \\ &= \frac{v_0 L}{\eta}, \end{aligned} \tag{1.22}$$

where v_0 is a typical plasma velocity, B has units of the magnetic field and L has units of length. If $R_m \gg 1$ then the advection term is dominant. This is the case found throughout most of the Universe and, for example, in the global corona $R_m \sim 10^{10}$. If $R_m \ll 1$ then the diffusion term is dominant, and it is in these regions that magnetic reconnection can occur. There are differences between the properties of ideal ($R_m \gg 1$) and non-ideal ($R_m \ll 1$) regions in a plasma, and this is very important for much of the work in this thesis so we discuss these differences here.

Ideal regions

In an ideal region, Ohm's Law (Eq. 1.14) is reduced to

$$\mathbf{E} + \mathbf{v} \times \mathbf{B} = \mathbf{0}. \tag{1.23}$$

Alfvén's frozen-flux theorem, which states that the magnetic field is frozen into the plasma, holds in ideal regions. This means that the plasma can move freely along the field lines but motion perpendicular to the field lines will move the field lines with the plasma. In an ideal region, the flux (\mathbf{w}) and plasma (\mathbf{v}) velocities are equivalent. The flux velocity can be defined by the equation

$$\frac{\partial \mathbf{B}}{\partial t} = \nabla \times (\mathbf{w} \times \mathbf{B}). \tag{1.24}$$

It can be shown that the perpendicular components of the flux (\mathbf{w}) and plasma (\mathbf{v}) velocities are equivalent by taking the cross product of Eq. 1.23 with \mathbf{B} , and substituting $(\mathbf{v} \times \mathbf{B}) \times \mathbf{B}$ for $(\mathbf{B} \cdot \mathbf{v})\mathbf{B} - (\mathbf{B} \cdot \mathbf{B})\mathbf{v}$, [Priest et al., 2003]

$$\frac{\mathbf{E} \times \mathbf{B}}{B^2} = \mathbf{v}_\perp = \mathbf{w}_\perp. \tag{1.25}$$

Non-ideal regions

In a non-ideal region, Ohm's Law is written as

$$\mathbf{E} + \mathbf{v} \times \mathbf{B} = \mathbf{N}, \tag{1.26}$$

where \mathbf{N} is any general non-ideal term. This can be a resistive term, for example, due to collisions, fluctuations or particle inertia, here though in our equation \mathbf{N} is simply \mathbf{j}/σ . In these regions the flux (\mathbf{w}) and plasma (\mathbf{v}) velocities are no longer equivalent but a flux velocity \mathbf{w} can be defined in a non-ideal region if \mathbf{w} has the same flux-preserving property

as the ideal case (Eq. 1.24). We can find the relationship in a non-ideal region between the plasma and flux velocities by firstly taking the curl of Eq. 1.26 and substituting in Eq. 1.13

$$-\frac{\partial \mathbf{B}}{\partial t} + \nabla \times (\mathbf{v} \times \mathbf{B}) = \nabla \times \mathbf{N}. \quad (1.27)$$

We can define a slippage velocity $\mathbf{u} = \mathbf{v} - \mathbf{w}$ and so we can write the non-ideal term, \mathbf{N} , as

$$\mathbf{N} = \mathbf{u} \times \mathbf{B} + \nabla \phi, \quad (1.28)$$

where ϕ is a scalar potential. From Eqs. 1.26 and 1.28 we can write

$$\mathbf{E} + \mathbf{w} \times \mathbf{B} = \nabla \phi. \quad (1.29)$$

If we take the cross product of Eq. 1.26 with \mathbf{B} and subtract the cross product of Eq. 1.29 with \mathbf{B} we arrive at the general expression for the flux velocity in a non-ideal region [Priest et al., 2003]

$$\mathbf{w} = \mathbf{v} + \frac{(\mathbf{N} - \nabla \phi) \times \mathbf{B}}{B^2}. \quad (1.30)$$

1.3 Magnetic null points

All of the magnetic configurations studied in this thesis involve magnetic null points, which are points where all components of the magnetic field equal zero. Therefore, here, we give a brief introduction to them.

1.3.1 2D null points

To understand the structure of a 2D null we consider a simple 2D magnetic field

$$B_x = \frac{B_0 y}{r_0}, B_y = \frac{B_0 \alpha x}{r_0}, \quad (1.31)$$

where B_0 has units of magnetic field, r_0 has units of length and α is a constant. At the origin, $(x, y) = (0, 0)$, the magnetic field equals $\mathbf{B} = (0, 0)$. If we vary α , we gain different field line structures about this null point at the origin. If $\alpha < 0$ then the field lines are elliptic and this is called an O-type neutral point (Fig. 1.5a). If $\alpha > 0$ then the field lines are hyperbolic and this is a X-type neutral point (Fig. 1.5b). The green lines drawn at $y = \pm\sqrt{\alpha}x$ are called separatrices and split the field up into four topologically distinct flux domains. If $\alpha = 1$ then the current vanishes, the separatrices are at right angles to each other and the magnetic field can be described as being in equilibrium. If α is increased above 1, the separatrices will tend to close up on themselves towards the y -axis and the X-point will collapse. This occurs due to the Lorentz force which can be written in terms of a magnetic tension and magnetic pressure force

$$\mathbf{j} \times \mathbf{B} = \underbrace{\frac{1}{\mu_0}(\mathbf{B} \cdot \nabla)\mathbf{B}}_{\substack{\text{magnetic} \\ \text{tension} \\ \text{force}}} - \underbrace{\nabla\left(\frac{B^2}{2\mu_0}\right)}_{\substack{\text{magnetic} \\ \text{pressure} \\ \text{force}}}. \quad (1.32)$$

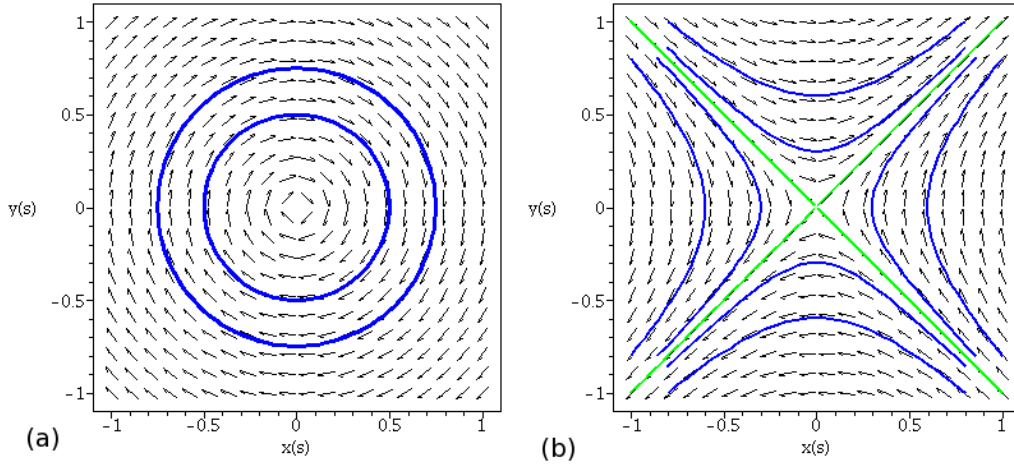


Figure 1.5: The structure of the magnetic field about an (a) O-type neutral point and a (b) X-type neutral point with separatrices drawn in green.

Since the Lorentz force is directed across the field lines, the components of magnetic tension and pressure parallel to the magnetic field must balance. The magnetic tension force is non-zero if \mathbf{B} varies along the direction of \mathbf{B} . It is produced by the effect of a tension along \mathbf{B} with magnitude B^2/μ_0 per unit area. The magnetic pressure force is due to a scalar magnetic pressure of magnitude $B^2/2\mu_0$ per unit area. It acts to compress the plasma through the magnetic pressure force and occurs where the magnetic field strength varies with position [Priest, 2014].

For the magnetic field shown in Eq. 1.31 the Lorentz force, $\mathbf{j} \times \mathbf{B} = B_0^2(1-\alpha)(\alpha x, -y)/r_0^2$, is such that the magnetic pressure force acts in towards the origin along the x -axis and the magnetic tension force acts outwards from the origin along the y -axis and hence the Lorentz force continues the perturbation [Dungey, 1953].

1.3.2 3D null points

Instead of having a pair of separatrix lines extending into the null and a pair extending out, as seen in 2D, in 3D one of these pairs of field lines is replaced by an infinite plane of field lines that emanate from the 3D null forming a surface known as the fan surface (or the separatrix surface) [Priest and Titov, 1996]. The spine consists of two field lines directed either into or out from the null and the separatrix surface is a surface of field lines pointing away from or into the null. It is possible to distinguish between a positive and negative null by the direction of the spine and separatrix-surface field lines. If the spine field lines point into the null and the separatrix-surface field lines point away from the null then it is a positive null and vice versa for a negative null. See Fig. 1.6 for an example of a positive null. It is shown in Parnell et al. [1996] that the linearised (local) field around a 3D null can be written as $\mathbf{B} = \mathbf{M} \cdot \mathbf{r}$ where $\mathbf{r} = (x, y, z)^T$ and

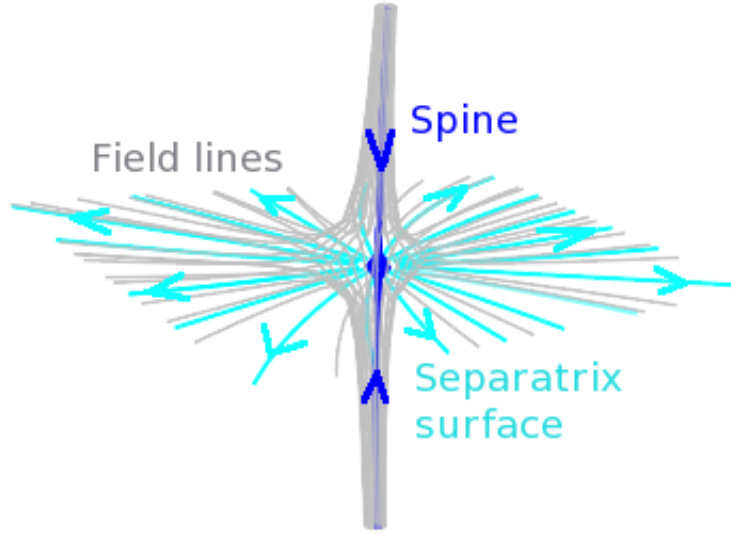


Figure 1.6: A positive 3D null with blue spine and pale-blue separatrix-surface field lines. The path of field lines in the vicinity of the null is represented by the grey lines which follow the direction of the spine or separatrix-surface field lines.

$$\mathbf{M} = \begin{pmatrix} a_{11} & a_{12} & a_{13} \\ a_{21} & a_{22} & a_{23} \\ a_{31} & a_{32} & a_{33} \end{pmatrix}, \quad (1.33)$$

such that

$$\begin{aligned} B_x &= a_{11}x + a_{12}y + a_{13}z, \\ B_y &= a_{21}x + a_{22}y + a_{23}z, \\ B_z &= a_{31}x + a_{32}y + a_{33}z. \end{aligned} \quad (1.34)$$

Since $\nabla \cdot \mathbf{B} = 0$ this implies the trace of \mathbf{M} must equal zero i.e., $a_{11} + a_{22} + a_{33} = 0$, and in turn this means that the sum of the eigenvalues of \mathbf{M} is equal to zero. We shall denote the eigenvalues by λ_s, λ_{f_1} and λ_{f_2} where s relates to the spine and f_1, f_2 relate to the separatrix surface (fan). It is also shown in Parnell et al. [1996] that if the matrix \mathbf{M} is diagonalisable then each field line can be represented in terms of the eigenvalues and eigenvectors associated with the matrix \mathbf{M}

$$\mathbf{r}(k) = Ae^{\lambda_{f_1}k}\mathbf{x}_{f_1} + Be^{\lambda_{f_2}k}\mathbf{x}_{f_2} + Ce^{\lambda_s k}\mathbf{x}_s. \quad (1.35)$$

In Eq. 1.35, \mathbf{r} represents the position vector of a point on a field line, k is an arbitrary parameter (denoting the distance along the field line), $\lambda_s, \lambda_{f_1}, \lambda_{f_2}, \mathbf{x}_s, \mathbf{x}_{f_1}$ and \mathbf{x}_{f_2} are the eigenvalues and eigenvectors associated with matrix \mathbf{M} and A, B and C are constants.

Since the sum of the eigenvalues must be zero at least one of the eigenvalues must be negative. Let us assume that $\lambda_{f_1} > \lambda_{f_2} > 0, \lambda_s < 0$ (as would be the case for a positive null). If we trace the field lines backwards away from the null ($k \rightarrow -\infty$) then the third term on the right hand side of Eq. 1.35 will be dominant and so $\mathbf{r}(k) \rightarrow Ce^{\lambda_s k}\mathbf{x}_s$. This

implies that the field lines heading into the null are parallel to the eigenvector \mathbf{x}_s and this defines the path of the spine, for a positive null.

Now if we trace field lines forwards away from the null ($k \rightarrow +\infty$) then the first two terms on the right hand side of Eq. 1.35 become dominant, but since we have $\lambda_{f_1} > \lambda_{f_2}$ then $\mathbf{r}(k) \rightarrow Ae^{\lambda_{f_1}k}\mathbf{x}_{f_1}$. This implies field lines heading away from the null lie parallel to the eigenvector \mathbf{x}_{f_1} and this defines the path of the field lines in the separatrix-surface plane. In this way it is possible to distinguish between a major and minor axis of the separatrix-surface plane. The major/minor axis of the separatrix surface is aligned along the vector associated with the eigenvalue of largest/smallest part.

So, for all 3D nulls, the two eigenvalues of the same sign have vectors associated with them defining the separatrix-surface plane. The spine lies along the vector associated with the single eigenvalue of opposite sign and if the separatrix-surface eigenvalues are positive/negative the null will be positive/negative [Parnell et al., 1996].

If the magnetic field local to a 3D null is such that the current is zero then the null is called a potential null. In this case the spine and separatrix surface of a null will be at right angles to each other.

1.4 Magnetic reconnection in 2D and 3D

Magnetic reconnection is a fundamental process of energy release in plasma physics. It permits the restructuring of the magnetic field both locally and globally enabling changes in the magnetic topology to occur and causes the field to release energy therefore achieving a lower energy state. When magnetic reconnection occurs magnetic energy is converted into thermal energy, kinetic energy (bulk plasma motions) and fast particle energy. The partitioning of magnetic energy into these three forms depends on the nature of the reconnection itself and the properties of the surrounding plasma. Magnetic reconnection plays a key role in many plasma processes on the Sun and other stars (e.g., coronal mass ejections, coronal heating, solar and stellar flares) and in the magnetosphere (e.g., powering flux transfer events, substorms). Magnetic reconnection can allow for the restructuring of the magnetic field and so it can change the topology.

Magnetic reconnection, which involves the breaking and joining of field lines, as first noted by Dungey [1953], can only occur in non-ideal regions ($R_m \ll 1$) where the length scales are small. As discussed previously, most of the plasma in the Universe is ideal and hence it is only in special localised regions, such as magnetic null points, magnetic separators (introduced below) and quasi-separatrix layers [Priest and Titov, 1996, Demoulin et al., 1996] where magnetic reconnection can occur.

Reconnection in 2D was first proposed as a mechanism for flares in the 1940's [Giovanelli, 1946, Hoyle, 1949] and has been studied in detail since the late 1950's, [e.g., Parker, 1957, Sweet, 1958, Biskamp, 1982, Priest and Forbes, 1986, Biskamp, 2000, Priest and Forbes, 2000], with various models produced describing different types of reconnection. In 2D there are two classical reconnection regimes: one is slow (Sweet-Parker) and the other is fast (Petschek) reconnection. Since both of these models are 2D, the reconnection takes place at a X-type neutral (or null) point since this is the only place in 2D where reconnection can occur.

The Sweet(1958)-Parker(1957) model is an order-of-magnitude estimate of the be-

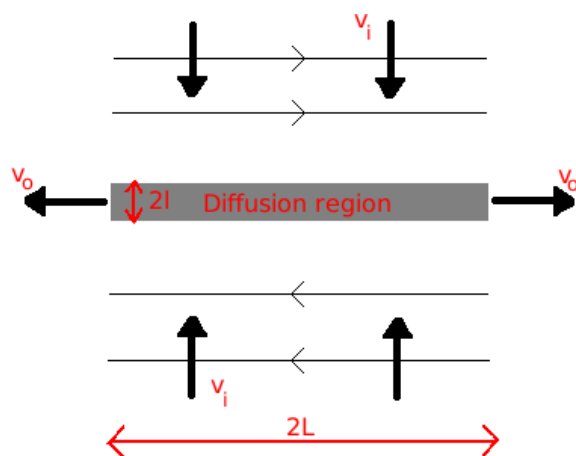


Figure 1.7: Sweet-Parker model: anti-parallel magnetic field lines (thin black lines) move into the diffusion region (grey rectangle) of length $2L$ and width $2l$ at the plasma inflow speed, v_i . The reconnected field lines leave the diffusion region at v_o . Thick black arrows represent the direction of the flow of the plasma.

haviour of the magnetic plasma within the current sheet. The reconnection occurs by bringing anti-parallel magnetic fields together at a current sheet (Fig. 1.7). This model aimed to explain the energy release observed in solar flares, however, the flux reconnection rate was found to be much too slow to account for this. This was due to the fact that the length of the diffusion region (which is large compared to the width of the diffusion region, l) was the same as the length of the system, $2L$, which leads to the reconnection rate of the magnetic field being equivalent to the inflow speed of the plasma. For a reconnection outflow, which is accelerated by the Lorentz force only, the dimensionless reconnection rate is equal to $R_m^{-\frac{1}{2}}$. The magnetic Reynolds number is high in the corona (of the order of 10^{10}) and hence this value is too small to account for the rate of change of energy during a flare.

Petschek's model (1964), considers not only the diffusion region, but also an extended region around (Fig. 1.8). Thus, in Petschek's model the length of the diffusion region is smaller than the length scale of the system and the length of the Sweet-Parker diffusion region. The length is not determined by the local length of the current sheet, as in the Sweet-Parker model, but by the external length. This model shows how magnetic energy can be converted into heat, by direct Ohmic dissipation in the diffusion region, and into kinetic energy, by acceleration of the newly reconnected field lines which have a large Lorentz force, as seen in the Sweet-Parker model, but also through the slow-mode shock waves which protrude from the ends of the diffusion region. It was found that most of the energy conversion occurs within the shocks. The reconnection rate here is faster than that seen in the Sweet-Parker model since the anti-parallel magnetic field lines meet over a diffusion region with a shorter length which can allow the diffusion region to be thinner hence leading to a faster reconnection rate.

There have been many other 2D reconnection models produced which develop these classical models further [e.g., Priest and Forbes, 1986, Biskamp, 1986]. New fast regime models generalise (in two ways) the fact that in Petschek's model the boundary conditions

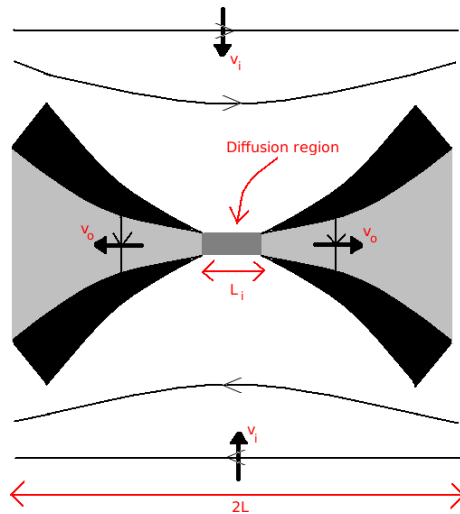


Figure 1.8: Petschek model: anti-parallel magnetic field lines (thin black lines) move towards the diffusion region (grey rectangle) of length L_i at the plasma inflow speed, v_i . There are two slow-mode shock waves (thick black curves) generated by the diffusion region. The reconnected field lines leave the diffusion region at v_o . Thick black lines represent the flow of plasma.

at large distances are implicit. This has been done by adopting different boundary conditions which produce regimes of (potential) almost-uniform reconnection and non-uniform reconnection [Priest and Forbes, 1986].

As stated previously, reconnection in 2D can only occur at X-points. A stagnation type flow is required and the existence of a current sheet is also essential. Imagine a pair of field lines with different connectivities ($A \rightarrow B$, $C \rightarrow D$), shown in Fig. 1.9. The in-coming field lines from opposite domains break and reconnect at the X-point forming a pair of field lines with different connectivities ($A \rightarrow D$, $C \rightarrow B$). In this way there is a discontinuity in the mapping of field lines and flux is transferred from one pair of flux domains into another [Dungey, 1953].

In more recent years, reconnection in 3D has been studied. 3D reconnection has proven to be much more complex than 2D reconnection due to the additional spatial dimension involved in the process, as well as the multitude of possible reconnection sites and the increased intricacy of the 3D magnetic skeleton.

There are significant differences between reconnection in 2D and 3D. Before these are discussed we note that there is one necessary and sufficient plasma condition that needs to be satisfied in order to allow 3D reconnection. This condition states that in a region of non-idealness

$$\int_l E_{\parallel} dl \neq 0, \quad (1.36)$$

must be satisfied, where E_{\parallel} is the electric field parallel to the magnetic field and the integral is along a field line [Schindler et al., 1988, Hesse and Schindler, 1988].

In 3D, unlike in 2D, the reconnection does not only happen at a single point, but occurs continually and continuously throughout the diffusion region volume. In this way the magnetic field lines are continually changing their connections throughout the diffusion

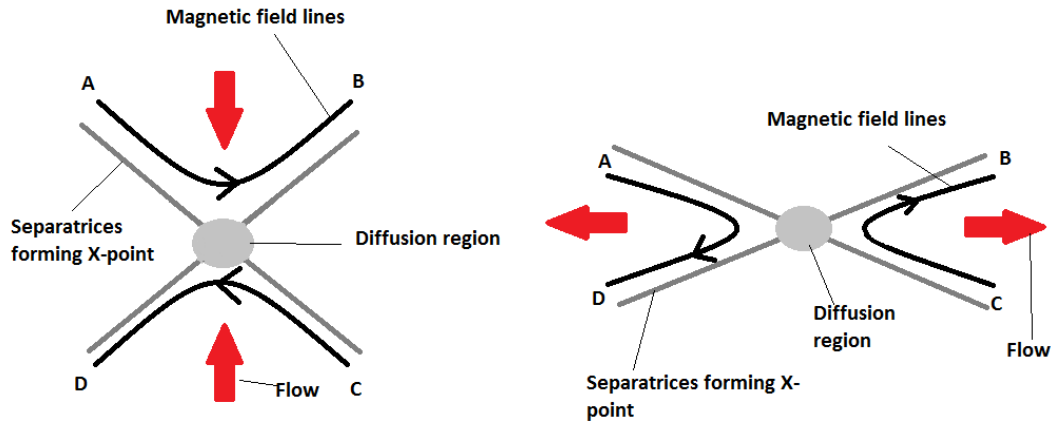


Figure 1.9: Pairs of field lines with different connectivities ($A \rightarrow B$, $C \rightarrow D$) come together and reconnect to form a new pair ($A \rightarrow D$, $C \rightarrow B$). The red arrows show direction of the inflow and then outflow of the field lines.

region. 3D reconnection does not require the presence of a null to occur. 3D reconnection can occur at 3D null points [e.g., Craig et al., 1995, Pontin et al., 2004, 2005b, Pontin and Galsgaard, 2007, Priest and Pontin, 2009, Pontin et al., 2011] or in the absence of 3D null points [Schindler et al., 1988, Hesse and Schindler, 1988]. For example, 3D reconnection can occur at separators [e.g., Priest and Titov, 1996, Longcope and Cowley, 1996, Longcope, 2001, Haynes et al., 2007, Parnell et al., 2010a,b, Wilmot-Smith and Hornig, 2011], at quasi-separatrix layers [e.g., Priest and Démoulin, 1995, Démoulin et al., 1996, 1997, Aulanier et al., 2005, Aulanier et al., 2006] and in twisted flux tubes [e.g., De Moortel and Galsgaard, 2006a,b, Browning et al., 2008, Hood et al., 2009, Bareford et al., 2013].

As long as the right plasma conditions are held (Eq. 1.36) in a region of non-idealness then 3D magnetic reconnection can occur. This implies that the field line mapping is not necessarily discontinuous. Magnetic field lines in 3D are not reconnected in a one-to-one fashion as in 2D. However, short length scales are required in 3D exactly as they are in 2D, e.g., current layers. Furthermore in general a flux velocity, \mathbf{w} , does not exist [Priest and Forbes, 2000, Priest et al., 2003, Pontin, 2012].

In this work, we focus on the properties of the current layer formed, and the reconnection which occurs, at magnetic separators, which are special topological features that have been recognised as important locations of 3D reconnection for many years, as current builds up easily along them [e.g. Sonnerup, 1979, Lau and Finn, 1990, Priest and Titov, 1996, Haynes et al., 2007, Parnell et al., 2011]. Despite this fact, very little is known about the detailed nature of separator reconnection and thus this thesis is aimed at addressing this anomaly. Separators are likely locations at which current will accumulate. We now introduce magnetic separators (Sect. 1.5) and begin a discussion of current layers, features at which magnetic reconnection may occur (Sect. 1.6).

1.5 3D magnetic separators

The aim of this work is to explore the properties of current accumulations that form after the non-resistive relaxation of a single non-potential separator and then to study the resulting reconnection that occurs in these current layers. A separator is a special field line which joins two 3D nulls (Fig. 1.10).

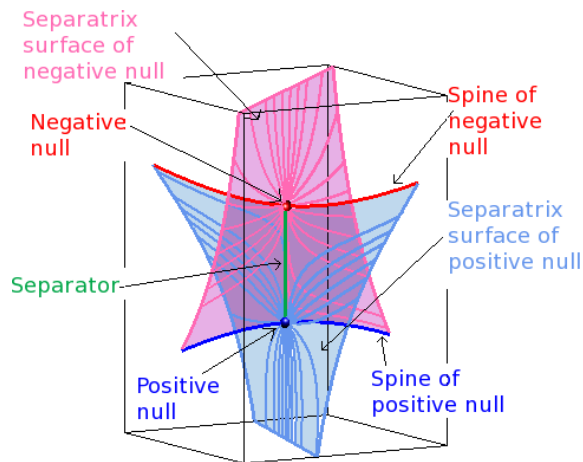


Figure 1.10: Schematic of a magnetic separator. Here, a green separator joins a positive 3D null point (blue with blue spine) to a negative 3D null point (red with red spine). This separator is formed by the intersection of the positive null’s separatrix surface (pale-blue) with the negative null’s separatrix surface (pink)

Separators may be formed by the co-alignment of specific field lines associated with 3D nulls. A separator can be formed by the co-alignment of the field lines of two separatrix surfaces from two oppositely signed nulls, a separatrix surface and a spine from two nulls of the same sign or two spines from oppositely signed nulls. The first type, formed by the intersection of the separatrix surface of a positive null with the separatrix surface of a negative null, is the only type which is both general and generic. Thus, this is the only type that will be discussed here. The other two types of co-alignments are non generic as they are topologically unstable (a slight perturbation could result in a loss of co-alignment).

Separators are the equivalent 3D topological features to 2D null points since they are lines that bound four topologically distinct flux domains, [Priest and Titov, 1996, Longcope and Silva, 1998, Haynes et al., 2007]. When separator reconnection occurs, flux from two oppositely situated flux domains is transformed into flux lying in the remaining two domains, which is akin to what is observed at 2D null point reconnection. In addition to this, the magnetic field lines in a cut perpendicular to a separator can be hyperbolic or elliptic which is locally analogous to the magnetic field structure about a 2D X-point or O-point, respectively, [Parnell et al., 2010a].

In 3D, magnetic reconnection at separators causes whole surfaces, or volumes to counter rotate about the separator as an infinite number of field lines are reconnected, unlike in 2D where only one pair of field lines is reconnected at a time. The amount of flux being reconnected, however, remains finite.

Although a separator joins two 3D nulls together, the reconnection which occurs at

a separator is distinct from that seen at 3D nulls. This has been noted through both numerical experiments [Haynes et al., 2007, Parnell et al., 2010a, 2011] and analytical work [Wilmot-Smith and Hornig, 2011]. In this way separator reconnection occurs along the separator where the component of the electric field which is parallel to the magnetic field, E_{\parallel} , is enhanced away from the 3D nulls.

Despite magnetic separators clearly being important locations for 3D magnetic reconnection to occur, the nature of current accumulations in the vicinity of separators has not yet been investigated nor has the associated reconnection.

1.6 Current layers

When magnetic reconnection occurs, a magnetic field is allowed to collapse to a lower energy state, the lowest of which, in a closed volume with the normal component imposed on the boundary, is called its potential state where $\mathbf{j} = \mathbf{0}$. Therefore, any state which is not in its lowest energy state must have a current density, \mathbf{j} , associated with it. For reconnection to occur we must have $R_m = vL/\eta \ll 1$ and hence we require short length scales over which the magnetic field can diffuse.

A current layer is a thin current-carrying region, either side of which the direction and/or magnitude of the magnetic field changes. A current layer can form for example due to the collapse of a 2D X-point, at the boundary between topologically distinct parts of a magnetic field which are brought together, or on features associated with 3D nulls which have collapsed (e.g., spines, fans or separators). The length scales associated with current layers are very small and so in these regions $R_m \lesssim 1$ which implies that the magnetic field in this vicinity is governed by diffusion. Therefore, current layers are regions at which magnetic reconnection can occur.

Current layers have been studied in 2D, where they form following the collapse of 2D null points, both in systems with the zero beta approximation [e.g., Green, 1965, Syrovatskii, 1971, Somov and Syrovatskii, 1976, Craig, 1994, Bungey and Priest, 1995] and in systems with the non-zero beta approximation [e.g., Rastätter et al., 1994, Craig and Litvinenko, 2005, Pontin and Craig, 2005, Fuentes-Fernández et al., 2011]. The particular features which are associated with these types of current layers are that the separatrices of the 2D nulls collapse and form cusps about the ends of the current layers and that the current collects in the vicinity of the null point and also along the separatrices extending beyond the ends of the main current layer. Also the plasma which lies within the cusp regions has a higher density than that lying outwith it. It has been shown analytically by Klapper [1998] that in 2D, in the absence of a plasma pressure, a current layer which lies at a null point can never truly be in equilibrium. This is due to the collapse time of the null being infinite. This finding holds in the presence of a plasma [Craig and Litvinenko, 2005, Pontin and Craig, 2005, Fuentes-Fernández et al., 2011]. Despite this, a state may be reached where the magnetic field is in equilibrium everywhere except at the current layer. This was shown by Fuentes-Fernández et al. [2011] who studied the MHD collapse of 2D nulls in the absence of resistivity.

Current layers in 3D have also been studied in various situations. Longbottom et al. [1998] and Bowness et al. [2013] have studied 3D current layers which are formed by the shearing of uniform magnetic fields while Wilmot-Smith et al. [2009a,b] considered

current layers generated by the tangling of multiple flux tubes. As mentioned previously, the collapse of a 3D null point can lead to current accumulations forming along the spine, separatrix surface or separator associated with the null [Pontin and Craig, 2005, Fuentes-Fernández and Parnell, 2012, 2013]. Current layers may also form due to ideal MHD instabilities [Browning et al., 2008] and at quasi-separatrix layers [Galsgaard et al., 2003, Titov et al., 2003, Aulanier et al., 2005, Wilmot-Smith et al., 2009c]. Therefore, as is mentioned previously, 3D reconnection can occur at 3D null points, as in 2D reconnection, but also in their absence.

1.7 Numerical codes

The main aspect of this thesis is to study the equilibrium fields formed by the non-resistive MHD relaxation of a single magnetic separator system, involving the intersection of the separatrix surfaces from two oppositely signed 3D nulls. The evolution of this MHS equilibrium is then studied in a resistive MHD reconnection experiment. Therefore, we are required to use numerical techniques to determine the MHD behaviour of our separator model system and then additional techniques are required to identify the magnetic skeleton of our model during its MHD evolution. Here, we discuss the three codes which we have employed to firstly perform the relaxation and subsequent reconnection of our field and then to locate and characterise the 3D null points, separatrix surfaces and separators throughout the experiments.

1.7.1 MHD code: Lare3d

We use the 3D MHD code, Lare3d, [Arber et al., 2001] to perform our numerical experiments. Lare3d is a staggered Lagrangian re-map code, in which the scalar quantities (ρ - density, ϵ - internal energy per unit mass and p - pressure) are defined at the cell centres and the magnetic field components, \mathbf{B} , are defined on the cell faces to help maintain $\nabla \cdot \mathbf{B} = 0$. This is done using the Evan's and Hawley constrained transport method for the magnetic flux [Evans and Hawley, 1988]. Also, the velocity components, \mathbf{v} , are staggered with respect to the pressure and magnetic field to prevent the checkerboard instability and so are placed at the cell vertices [Arber et al., 2001]. This layout is displayed in Fig. 1.11.

The code works in two steps with the first part being the Lagrangian step in which the code solves the MHD equations in a frame that moves with the fluid. The second step is a purely geometrical mapping of the Lagrangian grid back onto the original Eulerian grid. For a Lagrangian grid the code's mesh moves with the fluid and is deformed at each step so no mass crosses the cell boundaries. An Eulerian grid is fixed and the mass flows between the boundaries. Using a Lagrangian grid allows all the physics to be dealt with in one step and allows more physics to be easily added in.

The Lare3d code solves the normalised MHD equations and employs the following normalised quantities (using subscript n to denote the normalising factors and hats to

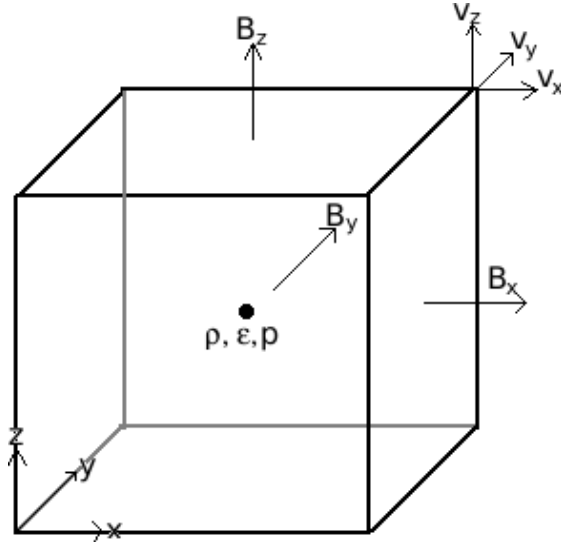


Figure 1.11: Cube displaying the positions of the scalar quantities and magnetic and velocity vector field components used by Lare3d.

represent dimensionless variables which the code uses)

$$\begin{aligned} \mathbf{x} &= L_n \hat{\mathbf{x}}, \\ \mathbf{B} &= B_n \hat{\mathbf{B}}, \\ \rho &= \rho_n \hat{\rho}, \end{aligned} \tag{1.37}$$

where $\mathbf{x} = (x, y, z)$ is the length. These factors then define the following normalising constants for the velocity, pressure, current and internal energy per unit mass, respectively,

$$\begin{aligned} v_n &= \frac{B_n}{\sqrt{\mu_0 \rho_n}}, \\ p_n &= \frac{B_n^2}{\mu_0}, \\ j_n &= \frac{B_n}{\mu_0 L_n}, \\ \epsilon_n &= v_n^2 = \frac{B_n^2}{\mu_0 \rho_n}, \end{aligned} \tag{1.38}$$

where $\mu_0 (= 1)$ is the dimensionless magnetic permeability. From these equations the plasma beta can be written as

$$\beta = \frac{2\hat{p}}{\hat{B}^2}. \tag{1.39}$$

Therefore, the standard MHD equations used in Lare3d, in the absence of gravity, are (note that the hats are dropped here)

$$\frac{D\rho}{Dt} = -\rho \nabla \cdot \mathbf{v}, \tag{1.40}$$

$$\frac{D\mathbf{v}}{Dt} = \frac{1}{\rho}(\nabla \times \mathbf{B}) \times \mathbf{B} - \frac{1}{\rho}\nabla p + \frac{1}{\rho}\mathbf{F}_\nu, \quad (1.41)$$

$$\frac{D\mathbf{B}}{Dt} = (\mathbf{B} \cdot \nabla)\mathbf{v} - \mathbf{B}(\nabla \cdot \mathbf{v}) - \nabla \times (\eta \nabla \times \mathbf{B}), \quad (1.42)$$

$$\frac{D\epsilon}{Dt} = -\frac{p}{\rho}\nabla \cdot \mathbf{v} + \frac{1}{\rho}H_\nu + \frac{\eta j^2}{\rho}. \quad (1.43)$$

Here $\mathbf{F}_\nu = \rho\nu(\nabla^2\mathbf{v} + \frac{1}{3}\nabla(\nabla \cdot \mathbf{v}))$ is the viscous force, where ν is the coefficient of kinematic viscosity, and $H_\nu = \rho\nu(\frac{1}{2}e_{ij}e_{ij} - \frac{2}{3}(\nabla \cdot \mathbf{v})^2)$ is the viscous heating term (an added contribution to the internal energy density), where $e_{ij} = (\partial v_i/\partial x_j) + (\partial v_j/\partial x_i)$ is the rate of strain tensor.

In the chapters where we are performing a non-resistive relaxation of our model, the resistivity, η , is set to zero.

1.7.2 Finding the magnetic skeleton

All of the work involved in this thesis involves magnetic separators and, hence, having run our numerical experiments we then need to determine the location and nature of the magnetic skeleton in every frame of our experiment.

3D nulls

In order to find the position within the numerical domain and type (positive or negative) of the 3D magnetic null points in the experiments discussed throughout this thesis, I have used the trilinear null finding method described in Haynes and Parnell [2007]. This null finding method assumes that the field within the cell varies in a trilinear manner, that is it is assumed to vary linearly in x , linearly in y and linearly in z . This assumption has the advantage that the null points found will agree with the field lines drawn, since to interpolate along a field line the same assumption is made.

This null finding method works in three steps:

- (i) Reduction - the first step scans each cell in the domain and removes those cells which can not possibly contain a 3D magnetic null point. In order to test whether a cell can contain a null or not, the signs of B_x , B_y and B_z on the eight vertices are considered (Fig. 1.12). If all three components of the magnetic field have the same sign at all eight vertices of a cell then the cell is removed from further consideration since the magnetic field can not be found to be zero at any point in the cell.
- (ii) Analysis - the remaining cells are now analysed to check if a null does actually exist inside them. For a null to exist within a cell, the three lines $B_x = B_y = 0$, $B_x = B_z = 0$ and $B_y = B_z = 0$ individually will either intersect the cell faces or form a loop within the cell. If the lines form a circuit within a cell then two 3D nulls points would lie within that cell indicating that the field within the cell is not properly resolved. Therefore, the null finding code considers the latter option.

Figs. 1.13a, 1.13b and 1.13c display three cells, containing surfaces of $B_x = 0$, $B_y = 0$ and $B_z = 0$, respectively. Using the bilinear nature of the field on the cell faces, all intersections of the pairs of curves $B_x = 0$, $B_y = 0$ and $B_z = 0$ are found on the

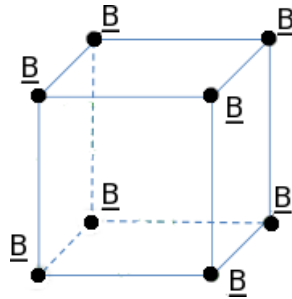


Figure 1.12: A cell with a value of $\mathbf{B} = (B_x, B_y, B_z)$ at each vertex.

cell faces (solid lines in Figs. 1.13a, 1.13b and 1.13c). For a null to exist each of these pairs of curves ($B_x = B_y = 0$, $B_x = B_z = 0$ and $B_y = B_z = 0$) must have a minimum of two intersections on the surfaces. Consider the pair of curves $B_x = 0$ and $B_y = 0$. Having found two intersections of these curves on the cell faces (asterisks in Fig. 1.13d), a null can only be found to exist within the cell if the sign of B_z at one of these intersections is the opposite of the sign of B_z at the other intersection, i.e., the surface $B_z = 0$ intersects the line of $B_x = B_y = 0$ which goes through the cell joining the asterisks in Fig. 1.13d.

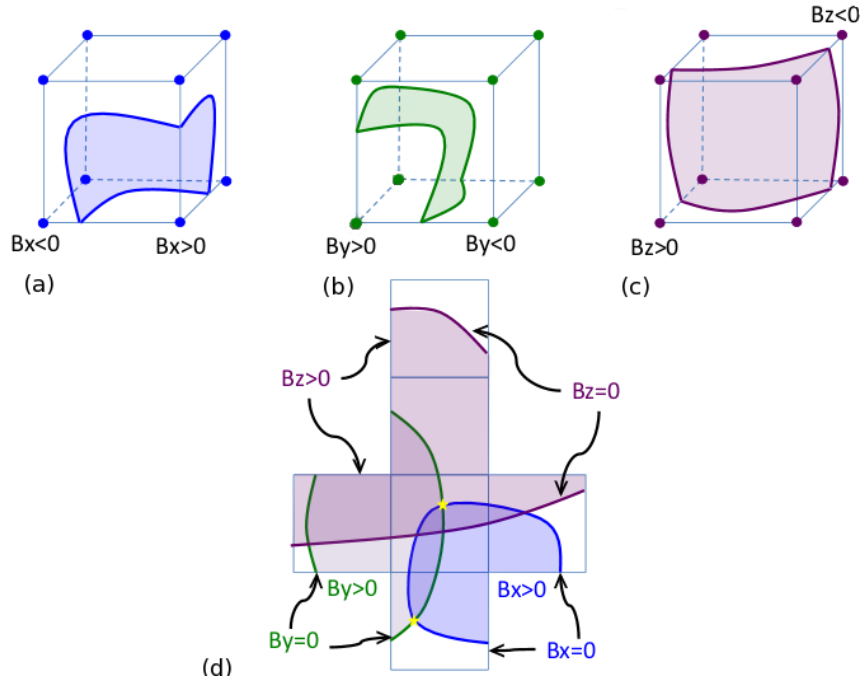


Figure 1.13: An example cell with surfaces of (a) $B_x = 0$ (blue), (b) $B_y = 0$ (green) and (c) $B_z = 0$ (maroon). The thick blue/green/maroon lines represent where these surfaces intersect the cell faces. (d) A cell containing these three surfaces, with all sides opened up, is displayed below the three individual cells.

- (iii) Position - if a cell has been identified as one which contains a null point, the location of the null is found to subgrid resolution by iterating from a set of initial points inside the cell in question using Newton-Raphson.

1.7.3 Finding the skeleton of a 3D null point

The spine's of the nulls which we discuss throughout this thesis are found using the eigenvector method as discussed in Haynes and Parnell [2010]. Using the eigenvector of the spine, \mathbf{x}_s , (which is associated with the eigenvalue λ_s of opposite sign to the other two eigenvalues) two initial points are placed a small radius away from the null on either side of it. These two points are in the directions $\pm\mathbf{x}_s$. A field line tracing method is then used to draw the spine out from either side of the null. For an analytical field, the eigenvalues and eigenvectors of a null can be easily found, but even for a numerical field where these values may not be known exactly, the eigenvector method still works. This is because field lines, which are traced from starting points sufficiently close to the null point such that the magnetic field is linear, will tend towards the spine according to Eq. 1.35

The method we employ for finding and tracing the separatrix surfaces of the nulls is also discussed in Haynes and Parnell [2010]. This method stores the data for the separatrix surfaces in rings which, depending on the nature of the null and its separatrix surface, may be a complete ring or a series of arcs separated by discontinuities. This method works in four distinct steps:

- (i) Initialisation - The first step draws a pair of rings, one is a single point at the null, and the other is a ring centred on the null, and on the plane spanned by \mathbf{x}_{f1} and \mathbf{x}_{f2} , with a radius small enough such that the magnetic field here is close to linear.
- (ii) Expansion - This step involves the creation of additional rings tracing out the separatrix surface. Field lines are traced out from the points on the initial ring and a new ring is formed a short distance along these lines such that the new ring is not too far from the previous ring. Now checks are implemented which ensure the points on the new ring are not too far apart from each other (within a given tolerance) and are not too close together. If points are found to be further apart than the tolerance then (linear) interpolation will be carried out between these points and additional points will be added to fill the gap. If the points are too close together then some points will be removed.
- (iii) Null-breaking - This stage sees null points being identified in the new ring. If the distance from a null point to any point on the $(n + 1)^{th}$ ring is smaller than a set distance, then the position of the point on the n^{th} ring closest to the null is moved to the location of the null. Two new points are placed onto the ring a small distance along the spine of the new null point (one on either side). This implies that rings drawn from this point onwards will have a discontinuity which lies between these two points. This step is repeated until either the separatrix surface reaches the boundary of the box or the whole surface is bounded by spines from oppositely signed null points.
- (iv) Trace-back - Finally the separators may be traced between the null points. As discussed previously, the separatrix surface has a break in it at each null of opposite

polarity. We have already mentioned that new rings are formed by tracing field lines from the points on the previous ring and so the position of the separator may be found by tracing backwards through these points from each of the null breaks that were found. This trace-back is done until we are back at the position of the original null.

1.8 Aims

The aims of this thesis are to study the equilibrium fields formed through the non-resistive MHD relaxation of a magnetic configuration which contains a magnetic separator and current layers and to investigate the subsequent magnetic reconnection which occurs at these current features. As such, we begin in Chapt. 2 by formulating an analytical expression for a magnetic configuration which contains two 3D null points whose separatrix surfaces intersect to form a separator. We look at four cases; one where there is no component of current, one where the current is directed along the separator, one where the current is directed perpendicular to the separator and finally a case where the current has a component directed perpendicular to the separator and along the separator. The second of these fields is used in the remaining chapters of this thesis.

In Chapt. 3 the analytical magnetic field, with current parallel to the separator, is used in a high plasma-beta, non-resistive MHD relaxation experiment using the Lare3d code. By using the term relaxation here, we refer to experiments in which magnetic energy is converted into internal energy and kinetic energy and which by the end have negligible velocities. A MHS equilibrium is formed through this relaxation which contains a current layer that lies along the separator. We analyse the effects that varying the initial magnitude of the current has on the properties of the MHS equilibrium and the current layer.

We vary the magnetic field parameters which control the initial magnetic configuration of the analytical magnetic field, with current parallel to the separator, in Chapt. 4. We examine the results of twelve experiments and compare the properties of the MHS equilibria formed, which contain separator current layers, in each case.

Next, in Chapt. 5 we use a MHS equilibrium, which contains a current layer, similar to those formed through the non-resistive relaxation experiments in Chapt. 3 as the initial condition for a high plasma-beta reconnection experiment using the Lare3d code with non-zero resistivity. We analyse the properties of the reconnection and study the waves that are launched into the system by the dissipation of the current layer and detail properties of the flows which are set up as a consequence of the waves. We also detail the effects that varying the strength of the reconnection, the size of the diffusion region and the value of the background viscosity has on the energetics and reconnection rate.

In Chapt. 6 we explore the different ways of lowering the plasma beta in our analytical single-separator magnetic field which has current parallel to the separator. We explain the best method we have found to approach a low plasma-beta value and then perform a non-resistive MHD relaxation on the model and discuss the properties of the MHS equilibrium formed which contains a strong current layer. We then explain how a low mean plasma-beta value can be achieved by using the MHS equilibrium which has already been discussed.

Finally, we summarise our findings and discuss future work which would be of interest to be done as an extension of the work detailed in this thesis in Chapt. 7.

Chapter 2

Analytical forms for single-separator magnetic fields

2.1 Importance of separators

One of the main places where magnetic reconnection can occur in three dimensions is at a separator. This is because, as previously explained, separators lie along the intersection of four topologically distinct flux domains, hence, current builds readily along them [Sonnerup, 1979]. In this chapter, we determine an analytical form for a 3D magnetic field containing a pair of oppositely-signed nulls connected by a separator. Firstly, a potential magnetic field model is derived and then we add in a uniform current which is parallel to the z -axis (and hence the separator) throughout the domain.

2.2 Potential separator magnetic structures

The lowest order magnetic field which can describe two nulls joined by a separator is quadratic. In general, such a magnetic field contains 27 unknown parameters, since for each component of \mathbf{B} (B_x, B_y, B_z) there are nine terms ($x, y, z, xy, xz, yz, x^2, y^2, z^2$). Without loss of generality most of these terms can be removed by satisfying a series of conditions. The conditions that we impose on our field are:

1. $\nabla \cdot \mathbf{B} = 0$ so we have a magnetic field.
2. $\mathbf{B} = \mathbf{0}$ at $x = y = z = 0$ and at $x = y = 0, z = L$ only so we have two nulls a distance L apart.
3. The lower null is positive with a vertical separatrix surface and spine lying in the $z = 0$ plane.
4. The upper null is negative with a vertical separatrix surface and spine lying in the $z = L$ plane.
5. There is only one separator and it lies along the z -axis.

In this chapter we firstly let $\mathbf{j} = \mathbf{0}$ which implies the magnetic field is potential. This is a big loss of generality and so this assumption is dropped later.

Satisfying these conditions allows the general expression to be reduced to a potential magnetic field of the form

$$\begin{aligned} B_x &= \frac{B_0}{L_0}(x + cxz + byz), \\ B_y &= \frac{B_0}{L_0}((2a - c)yz - (1 + aL)y + bxz), \\ B_z &= \frac{B_0}{L_0}(-a(z^2 - Lz) + \frac{1}{2}cx^2 + (a - \frac{1}{2}c)y^2 + bxy). \end{aligned} \quad (2.1)$$

There are six unknown parameters in Eq. 2.1 (B_0 , L_0 , L , a , b and c), which have constraints put on them by the conditions listed above. The parameters B_0 and L_0 are the magnetic field and length scaling factors respectively, while L determines the length of the separator. The parameters a , b and c alter the geometry of the field lines in the analytical model. These are discussed in more detail below. If we neglected condition number 5 then a seventh parameter d could be added in to allow the separator to bend; this is discussed in Sect. 2.2.7. Before that, though, we consider the conditions listed above and determine the constraints that they impose on the six unknowns.

2.2.1 Condition 2: There are only two nulls in the model

To ensure that there are null points only at $x = y = z = 0$ and $x = y = 0, z = L$ we must have $b^2 > a^2(cL + 2)^2/4(1 + aL)$. We arrive at this constraint by looking at one of the solutions to the magnetic field in Eq. 2.1 equalling 0. We gain this solution by solving $B_x = 0$ for z , substituting this into B_y and solving for x and finally substituting this into B_z to solve for y . From this we find

$$\begin{aligned} x &= -a(2 + cL)y \pm y\sqrt{a^2(2 + cL)^2 - 4b^2(1 + a)}, \\ z &= \frac{-2c \pm a(cL - 2) \pm \sqrt{a^2(2 + cL)^2 - 4b^2(1 + a)}}{2b^2 + 2c(c - 2a)}. \end{aligned} \quad (2.2)$$

The analytical expressions for y are large and can be found in Appendix A. The same square root which appears in x and z occurs often in the solution for y . For x , y and z to be real the value under the square root must be positive and hence we must ensure $b^2 > a^2(cL + 2)^2/4(1 + aL)$ so the only nulls that exist, other than the two at $(0, 0, 0)$ and $(0, 0, L)$, are located in the complex plane and so can be ignored.

2.2.2 Condition 3: Nature of the lower null ($x = y = z = 0$)

The linearised field around the lower null is

$$\begin{aligned} B_x &= \frac{B_0}{L_0}x, \\ B_y &= \frac{B_0}{L_0}(-(1 + aL)y), \\ B_z &= \frac{B_0}{L_0}aLz. \end{aligned} \quad (2.3)$$

This can be written in terms of $\mathbf{B} = \mathbf{M} \cdot \mathbf{r}$, where \mathbf{r} is the position vector $(x, y, z)^T$ and

$$\mathbf{M} = \frac{B_0}{L_0} \begin{pmatrix} 1 & 0 & 0 \\ 0 & -(1+aL) & 0 \\ 0 & 0 & aL \end{pmatrix}. \quad (2.4)$$

The matrix \mathbf{M} is analysed to find its eigenvalues and eigenvectors and to satisfy the requirements of condition 3 which will put constraints on a . We choose this null to be positive with its spine along the y -axis and so the eigenvalues of \mathbf{M} are chosen, with corresponding eigenvectors, as

$$\begin{aligned} \lambda_s &= -(1+aL), & \mathbf{e}_s &= \begin{pmatrix} 0 \\ 1 \\ 0 \end{pmatrix}, \\ \lambda_{f_1} &= 1, & \mathbf{e}_{f_1} &= \begin{pmatrix} 1 \\ 0 \\ 0 \end{pmatrix}, \\ \lambda_{f_2} &= aL, & \mathbf{e}_{f_2} &= \begin{pmatrix} 0 \\ 0 \\ 1 \end{pmatrix}. \end{aligned} \quad (2.5)$$

Here again “ s ” is related to the spine and “ f_1 ” and “ f_2 ” are related to the separatrix surfaces. Since this is a positive null, the spine eigenvalue must be negative and the separatrix-surface eigenvalues positive. This gives the constraint that $aL > 0$. Since the separator’s length, L , must be greater than zero, we find $a > 0$. It is clear from the eigenvectors that the spine and separatrix surfaces of this null are perpendicular, as they should be for a potential null.

Varying a changes the geometry of the field lines in the separatrix surface of the null and can change which fan eigenvalue is the major or minor one.

2.2.3 Condition 4: Nature of the upper null ($x = y = 0, z = L$)

Similar analysis is performed for the upper null. The linearised field around this null and matrix \mathbf{M} are

$$\begin{aligned} B_x &= (1+cL)x + bLy, \\ B_y &= bLx + (aL - cL - 1)y, \\ B_z &= -aLz, \end{aligned} \quad (2.6)$$

$$\mathbf{M} = \frac{B_0}{L_0} \begin{pmatrix} 1+cL & bL & 0 \\ bL & aL - cL - 1 & 0 \\ 0 & 0 & -aL \end{pmatrix}. \quad (2.7)$$

This is required to be a negative null with spine in the $z = L$ plane and separatrix-surface field lines in the vertical plane. The eigenvalues and corresponding eigenvectors chosen for this null to satisfy our conditions are

$$\begin{aligned}
\lambda_s &= \frac{aL}{2} + \frac{\sqrt{(aL-2-2cL)^2 + 4b^2L^2}}{2}, & \mathbf{e}_s &= \begin{pmatrix} \frac{aL-2-2cL+\sqrt{(aL-2-2cL)^2+4b^2L^2}}{2bL} \\ 1 \\ 0 \end{pmatrix}, \\
\lambda_{f_1} &= \frac{aL}{2} - \frac{\sqrt{(aL-2-2cL)^2 + 4b^2L^2}}{2}, & \mathbf{e}_{f_1} &= \begin{pmatrix} \frac{aL-2-2cL-\sqrt{(aL-2-2cL)^2+4b^2L^2}}{2bL} \\ 1 \\ 0 \end{pmatrix}, \\
\lambda_{f_2} &= -aL, & \mathbf{e}_{f_2} &= \begin{pmatrix} 0 \\ 0 \\ 1 \end{pmatrix}.
\end{aligned} \tag{2.8}$$

Since this is a negative null the separatrix-surface eigenvalues must be negative and from this we gain the constraint on b that $b^2L^2 > (aL - cL - 1)(cL + 1)$.

For the upper null, a and c are related to the major/minor axis of the separatrix surface and the spine and the geometry of the field lines. The parameter b allows the upper null's separatrix-surface plane to rotate in the xy -plane. Since this is a potential null, if the separatrix-surface plane rotates then the spine must also rotate to remain perpendicular to the separatrix surface. A point to note from Eq. 2.8 is that the square roots of the eigenvalues are clearly real, hence, the eigenvalues are real for all values of a, b and c .

Thus, the three constraints we have to satisfy, to ensure that our potential magnetic separator model with parameters a, b, c and L fulfils all the conditions we impose, are

- $a > 0$,
- $b^2 > \frac{(aL-cL-1)(cL+1)}{L^2}$,
- $b^2 > \frac{a^2(cL+2)^2}{4(1+aL)}$.

2.2.4 Special case $b = 0$

If $b = 0$ in Eq. 2.6 then the following eigenvalues and eigenvectors are found for the upper null

$$\begin{aligned}
\lambda_s &= 1 + cL, & \begin{pmatrix} 1 \\ 0 \\ 0 \end{pmatrix}, \\
\lambda_{f_1} &= aL - cL - 1, & \mathbf{e}_{f_1} = \begin{pmatrix} 0 \\ 1 \\ 0 \end{pmatrix},
\end{aligned} \tag{2.9}$$

$$\lambda_{f_2} = -aL, \quad \mathbf{e}_{f_2} = \begin{pmatrix} 0 \\ 0 \\ 1 \end{pmatrix}. \quad (2.10)$$

The eigenvalues and eigenvectors for the lower null are the same as those in Eq. 2.5. This puts new constraints on a and c such that $c > -1/L$ and (using $a > 0$ from the lower null) $0 < a < c + 1$. In order to maintain only two nulls in the model, we would be required to satisfy the constraint $1 + cL < 0$. However, for the upper null to be negative we require λ_s to be positive which implies $1 + cL > 0$. Hence, with $b = 0$, one always gains more than two nulls in the potential case.

2.2.5 Upper and lower nulls

Figs. 2.1, 2.2 and 2.3 show the nature of the magnetic field with $B_0 = L_0 = L = 1$ and various values of a , b and c as detailed in the figure captions. Only features of the magnetic skeleton are plotted in order to highlight the topologically distinct flux domains.

In these figures, the location of the positive (lower) and negative (upper) nulls are identified by blue and red spheres respectively. The spines are denoted by thick lines with the same colour as their null spheres. The field lines in the separatrix-surface plane of the lower null are pale-blue and pink for the upper null.

The separatrix-surface plane equation for the lower null is simply $y = 0$ and the separatrix-surface plane equation for the upper null is

$$y = \frac{2bL}{aL - 2 - 2cL + \sqrt{(aL - 2 - 2cL)^2 + 4b^2L^2}}x. \quad (2.11)$$

Fig. 2.1 shows how the geometry of the field lines of the lower and upper nulls are changed when a is increased. In this figure $b = 2.0$, $c = 0.5$ and a is varied from 0.5 to 1.3 to 2.1.

For the lower null it is evident that the major axis of the separatrix surface is affected by a as can be seen from Eq. 2.5. When $a = 0.5$ the eigenvector associated with λ_{f_1} is the major axis of the separatrix-surface plane since $\lambda_{f_1} > \lambda_{f_2}$ (Fig. 2.1a). However, when $a > 1$, as seen in Fig. 2.1b where $a = 1.3$, $\lambda_{f_2} > \lambda_{f_1}$ and the separatrix-surface field lines start to align with the z -axis. This is more pronounced in Fig. 2.1c where $a = 2.1$. For the lower null, the value of a has no effect on the plane of the separatrix surface, just the geometry of the field lines in this surface. Changing a has an effect on both the geometry of the field lines in the separatrix surface and the plane of the separatrix surface in the xy -plane of the upper null.

Fig. 2.2 shows how the magnetic field configuration changes when b is varied. In this figure $a = 1.0$, $c = 2.0$ and b is varied from -6.5 to 1.5 to 8.5. From these images it is evident that b rotates the separatrix surface of the upper null in the xy -plane and also changes the geometry of the field lines in the separatrix-surface. The geometry of the lower null's field lines is also changing as it is affected by the upper null although very close to the null these field lines are unaffected by b .

Finally Fig. 2.3 shows how the magnetic field behaves when c is varied. In this figure $a = 1.0$, $b = 1.5$ and c is varied from 0.1 to 1.1 to 2.1. As for the cases of varying a and b , changing c affects the geometry of the field lines in the separatrix-surface plane of both

nulls and also rotates the separatrix surface of the upper null in the xy -plane. Since these nulls are potential when the separatrix surface of the upper null rotates the spine must also rotate to stay perpendicular to the separatrix surface.

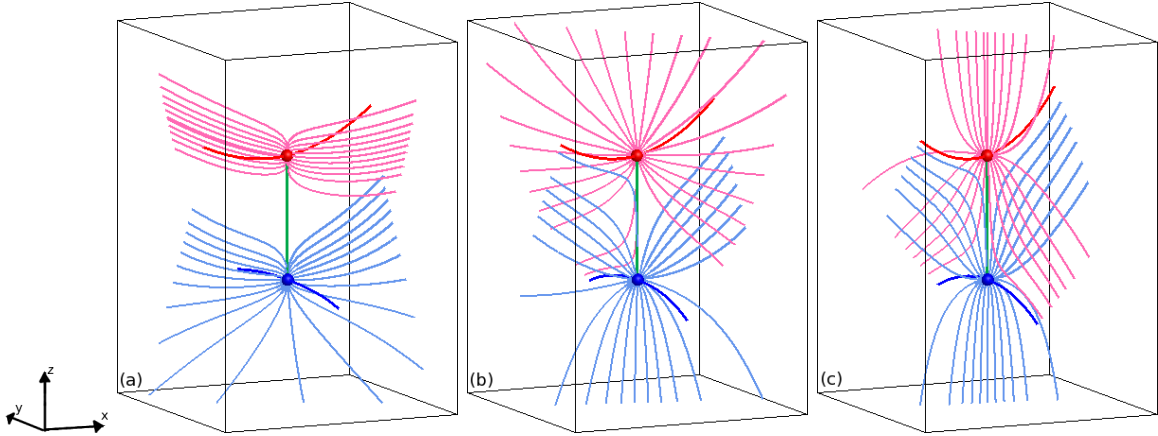


Figure 2.1: Images of the magnetic skeleton for our analytical magnetic field which includes two nulls joined by a separator. The nulls are identified by blue/red spheres for the positive/negative nulls, the separatrix-surface field lines by pale-blue/pink lines and the spines as blue/red thick lines for the positive/negative nulls. The separator is drawn here as a green line. The parameters of the magnetic field are $b = 2.0$, $c = 0.5$ and (a) $a = 0.5$, (b) $a = 1.3$ and (c) $a = 2.1$.

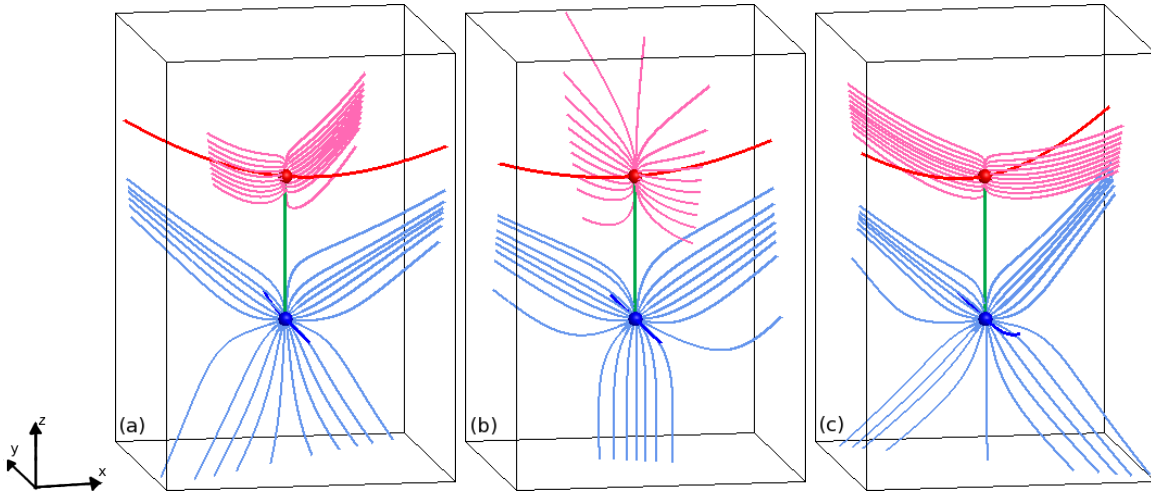


Figure 2.2: Images of the magnetic skeleton for our analytical magnetic field which includes two nulls joined by a separator. The nulls are identified by blue/red spheres for the positive/negative nulls, the separatrix-surface field lines by pale-blue/pink lines and the spines as blue/red thick lines for the positive/negative nulls. The separator is drawn here as a green line. The parameters of the magnetic field are $a = 1.0$, $c = 2.0$ and (a) $b = -6.5$, (b) $b = 1.5$ and (c) $b = 8.5$.

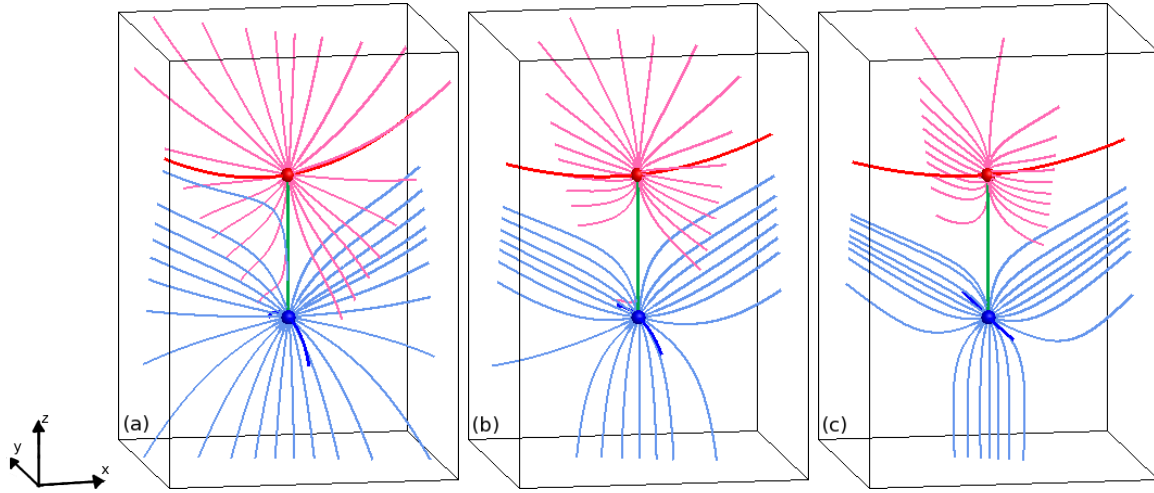


Figure 2.3: Images of the magnetic skeleton for our analytical magnetic field which includes two nulls joined by a separator. The nulls are identified by blue/red spheres for the positive/negative nulls, the separatrix-surface field lines by pale-blue/pink lines and the spines as blue/red thick lines for the positive/negative nulls. The separator is drawn here as a green line. The parameters of the magnetic field are $a = 1.0$, $b = 1.5$ and (a) $c = 0.1$, (b) $c = 1.1$ and (c) $c = 2.1$.

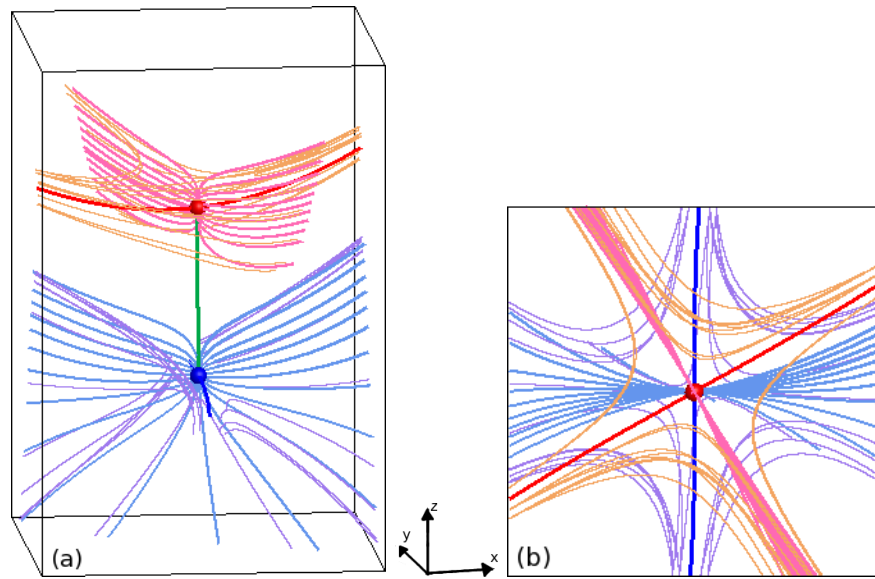


Figure 2.4: Images of both nulls joined by a separator (green line) with field lines drawn in the separatrix-surface plane in pale-blue for the lower null and pink for the upper null. Extra field lines are also drawn here out along the spines in green for the lower null and yellow for the upper. The spine of the lower null is blue and the upper null's spine is red. (a) Angled view. (b) Image shown in the xy -plane. Here $a = 0.5$, $b = 2.0$, $c = 0.5$, $B_0 = 1.0$, $L_0 = 1.0$ and $L = 1.0$.

Fig. 2.4 shows the field lines drawn in the separatrix-surface plane and also field lines drawn out along the spines of the nulls. The extra field lines drawn out along the spines are shown in mauve for the lower null and orange for the upper null. These figures highlight the behaviour of field lines in the vicinity of the magnetic skeleton: field lines close to the spines or separatrix surfaces of the nulls follow the same paths.

2.2.6 General potential magnetic field local to the separator

The results shown so far consider the potential magnetic field from the point of view of the nulls, separatrix surfaces and spines. Here we investigate the field local to the separator. Cuts in planes perpendicular to the separator can be studied in order to ascertain the geometry of the field lines and the magnetic skeleton in the local vicinity of the separator. Little is known about separator local magnetic field structures but it has been shown numerically that the geometry of the field lines in cuts perpendicular to the separator (not lying in the plane of the null) do not necessarily match the magnetic skeleton [Parnell et al., 2010a].

It can be shown in this model that at any cut perpendicular to the separator, at a height $z = z_0$, the eigenvalues of the linearised field are real. This result comes from finding the eigenvalues of the 2D magnetic field

$$\begin{aligned} B_x(x, y, z_0) &= \frac{B_0}{L_0}(x(1 + cz_0) + bz_0y), \\ B_y(x, y, z_0) &= \frac{B_0}{L_0}((2az_0 - cz_0 - 1 - aL)y + bz_0x), \end{aligned} \quad (2.12)$$

which produces the matrix

$$\mathbf{M} = \frac{B_0}{L_0} \begin{pmatrix} 1 + cz_0 & bz_0 \\ bz_0 & 2az_0 - cz_0 - 1 - aL \end{pmatrix}, \quad (2.13)$$

with eigenvalues

$$\lambda = \frac{a(2z_0 - L)}{2} \pm \frac{\sqrt{(2 + a(L - 2z_0) + 2cz_0)^2 + 4b^2z_0^2}}{2}. \quad (2.14)$$

Since the value under the square root is the sum of two squared quantities, the eigenvalues are real for all values of a, b, c, L and z_0 .

Fig. 2.5 shows cuts across the separator at heights $z_0 = 0.0, 0.2, 0.4, 0.6, 0.8$ and 1.0 . In these images $a = 2.0, b = 2.0, c = 0.5, B_0 = L_0 = L = 1.0$. The black lines show the location of the field lines superimposed onto the perpendicular plane. In all cases these lines are hyperbolic as expected since the eigenvalues of matrix Eq. 2.13 are always real. The eigenvalues at each of these cuts are unstable saddle points. The pale-blue line shows where the separatrix surface of the lower null intersects the cut of each plane and the pink line shows where the separatrix surface of the upper null intersects the cut of each plane. The geometry of the field lines does not match the magnetic skeleton in these images other than locally around each null, this is expected since the eigenvectors of Eq. 2.14 match the eigenvectors for the lower and upper nulls at $z_0 = 0.0$ and $z_0 = L (= 1.0)$ respectively (but not at any other value of z_0). In other words, the pale-blue and pink lines do not sit on top of the black lines. In the last image (at $z_0 = L (= 1.0)$) the blue line (separatrix-surface

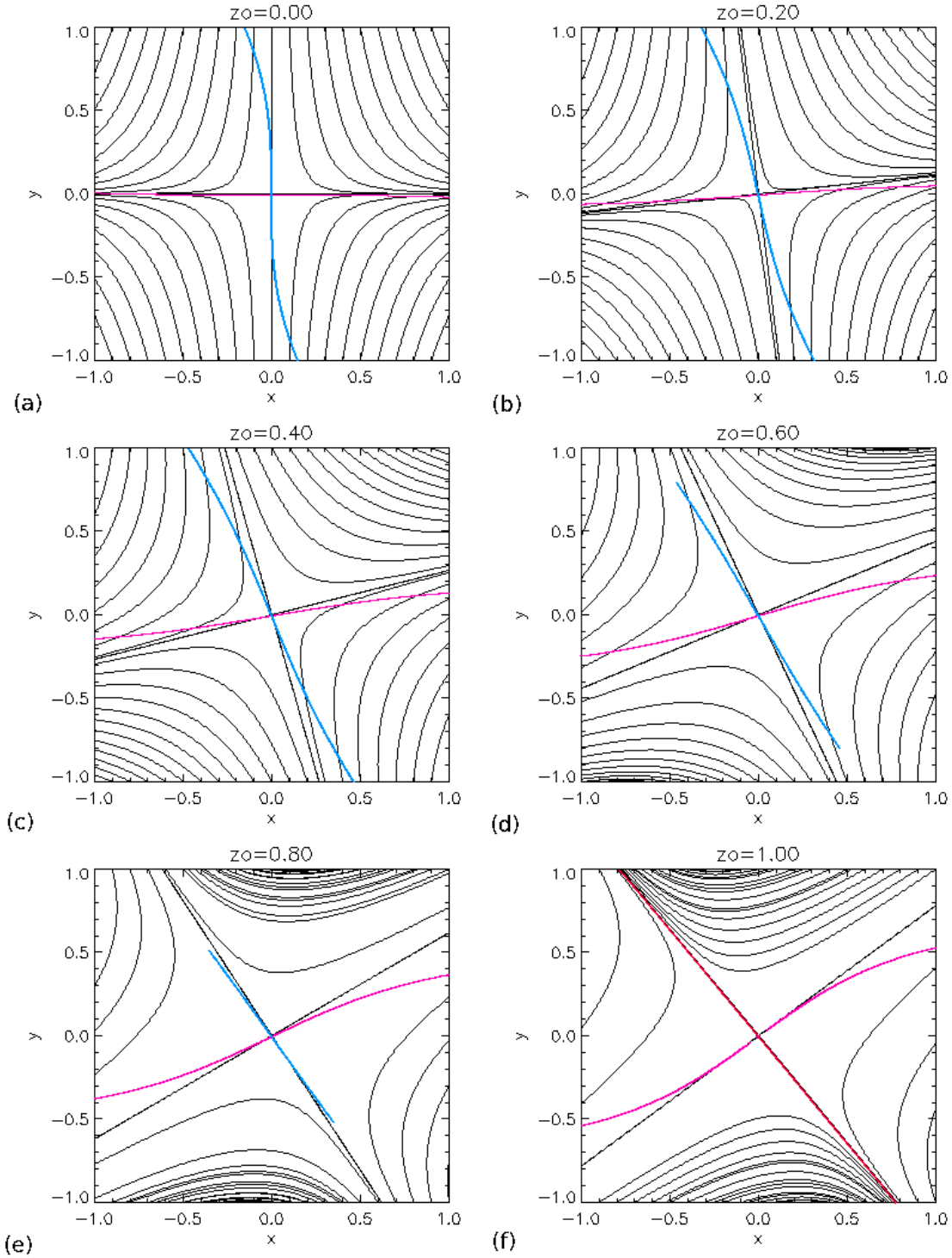


Figure 2.5: Images of the field lines (black) at cuts across the separator with the intersection of the separatrix-surface field lines with the plane shown in pale-blue for the lower null and pink for the upper null. Here $a = 2.0$, $b = 2.0$ and $c = 0.5$. The cuts are shown at heights of $z_0 =$ (a) 0.0, (b) 0.2, (c) 0.4, (d) 0.6, (e) 0.8 and (f) 1.0. The final image shows the spine of the upper null plotted in red.

of the lower null) is very small. This is due to the the fact that the separatrix-surface field lines are actually curving away from the upper null as they approach it and so not many intersect at this cut. So the spine of the upper null is plotted in the last cut in red instead.

2.2.7 Neglecting a fourth parameter

Eq. 2.1 can have a seventh parameter, d , added to it in the form shown below in order to allow for the separator to bend (i.e. it is no longer along the z -axis) with the nulls still located at $(0,0,0)$ and $(0,0,L)$

$$\begin{aligned} B_x &= \frac{B_0}{L_0}(x + cxz + byz + dz - dz^2 + dx^2), \\ B_y &= \frac{B_0}{L_0}((2a - c)yz - (1 + aL)y + bxz), \\ B_z &= \frac{B_0}{L_0}(-a(z^2 - Lz) + \frac{1}{2}cx^2 + (a - \frac{1}{2}c)y^2 + bxy + dx - 2dxz). \end{aligned} \quad (2.15)$$

In order for the separator to remain along the z -axis for all values of a, b, c and L we must have $B_x = B_y = 0$ when $x = y = 0$ and $0 < z < L$. This implies d must be 0 as shown below. Setting $x = y = 0$ in Eq. 2.15 we find

$$\begin{aligned} B_x(0, 0, z) &= \frac{B_0}{L_0}(dz - dz^2), \\ B_y(0, 0, z) &= 0, \\ B_z(0, 0, z) &= -\frac{B_0}{L_0}(a(z^2 - zL)). \end{aligned} \quad (2.16)$$

Analysis has been done on the effects of keeping d in the magnetic field equation and we find that d will often cause extra nulls to be added into the model. To carry out this analysis we allowed b to equal zero $B_0 = L_0 = L = 1$ which simplified the system of equations. We proceeded to try to show with a, c and d as parameters in the magnetic field that more often than not there will be more than two real nulls in our setup. If we can show this with $b = 0$ and $L = 1.0$ then adding in the parameter b or allowing L to vary will surely also lead to further complexity of the magnetic field. First, we write Eq. 2.15 with $b = 0$ and $B_0 = L_0 = L = 1.0$.

$$\begin{aligned} B_x &= x + cxz + dz - dz^2 + dx^2, \\ B_y &= (2a - c)yz - (1 + a)y, \\ B_z &= -a(z^2 - z) + \frac{1}{2}cx^2 + (a - \frac{1}{2}c)y^2 + dx - 2dxz, \end{aligned} \quad (2.17)$$

and apply the conditions as described before. For the lower null, which must be positive, the eigenvalues found from the magnetic field are,

$$\begin{aligned} \lambda_s &= -(1 + a), \\ \lambda_{f_1} &= \frac{1 + a + \sqrt{(a - 1)^2 + 4d^2}}{2}, \\ \lambda_{f_2} &= \frac{1 + a - \sqrt{(a - 1)^2 + 4d^2}}{2}, \end{aligned} \quad (2.18)$$

giving the constraints $a > -1$ and $a > d^2$. The second constraint implies that in fact $a > 0$ since d is real.

For the upper null, which is negative, the eigenvalues are

$$\begin{aligned}\lambda_s &= \frac{1+c-a}{2} + \frac{\sqrt{(a+c+1)^2 + 4d^2}}{2}, \\ \lambda_{f_1} &= a-c-1, \\ \lambda_{f_2} &= \frac{1+c-a}{2} - \frac{\sqrt{(a+c+1)^2 + 4d^2}}{2}.\end{aligned}\tag{2.19}$$

These eigenvalues give the constraints $c > a-1$ and $c > (-d^2/a) - 1$ and so we can proceed by considering the first only since $a-1$ will always be greater than $(-d^2/a) - 1$. Therefore the three constraints that are used for the analysis, when $b = 0$ and $L = 1$, are

- $a > 0$,
- $a > d^2$,
- $c > a - 1$.

One solution of Eq. 2.17 is

$$\begin{aligned}x &= \frac{-\frac{d}{2}(8a^2 - 12ac + 4a^2c - 6ac^2 - 16d^2 - 8cd^2) \pm \frac{d}{2}\sqrt{\alpha_1}}{-2ac^3 + 4a^2d^2 - 12acd^2 - 3c^2d^2 - 16d^4}, \\ y &= 0, \\ z &= \frac{-(cx+d) \pm \sqrt{(cx+d)^2 + 4d(x+dx^2)}}{-2d},\end{aligned}\tag{2.20}$$

where α_1 is

$$\begin{aligned}\alpha_1 &= d^2(8a^2 - 12ac + 4a^2c - 6ac^2 - 16d^2 - 8cd^2)^2 \\ &\quad - 4(-2ac^3 + 4a^2d^2 - 12acd^2 - 3c^2d^2 - 16d^4)(4a^2 + 4a^2c - 4acd^2 - 4d^4).\end{aligned}\tag{2.21}$$

Analysing the term α_1 it is possible to show that it is almost always positive, meaning that nulls, other than the two we want, will be found in most cases.

Using the constraints listed above, we can write c and d in terms of different parameters in order to help analyse the solution. We find

- $c + 1 = a/\delta_1$ where $0 < \delta_1 < 1$,
- $d^2 = a\epsilon_1$ where $0 < \epsilon_1 < 1$.

Using these, Eq. 2.21 can be written as

$$\begin{aligned}\alpha_1 &= \frac{4a^3}{\delta_1^4} \left[(a + 2\delta_1\epsilon_1 - \delta_1)^2(\delta_1^2\epsilon_1 + 8a^2 + a^2\epsilon_1 \right. \\ &\quad \left. + 4a^2\delta_1^2\epsilon_1 - 12a^2\delta_1\epsilon_1 + 14a\delta_1\epsilon_1 - 8a\delta_1 + 12a\delta_1^2\epsilon_1 - 16a\delta_1^2\epsilon_1^2) \right].\end{aligned}\tag{2.22}$$

If $\alpha_1 < 0$ then the nulls found are imaginary. Let $\alpha_1 = 0$ and solve for δ_1 . This gives

$$\begin{aligned}\delta_{11} &= \frac{a}{1 - 2\epsilon_1}, \\ \delta_{12,13} &= \frac{7a\epsilon_1 - 4a - 6a^2\epsilon_1 \pm 4a\sqrt{(a^2\epsilon_1 - a^2)(3a\epsilon_1 + 2a^2\epsilon_1 + a\epsilon_1^2 + 3\epsilon_1 - 1)}}{16a^2\epsilon_1 - 4a^2\epsilon_1 - 12a\epsilon_1 - \epsilon_1}.\end{aligned}\quad (2.23)$$

Under the square root the term in the first bracket is always negative and so we must have (from the second bracket)

$$\epsilon_1(3a + 2a^2 + a\epsilon_1 + 3) < 1. \quad (2.24)$$

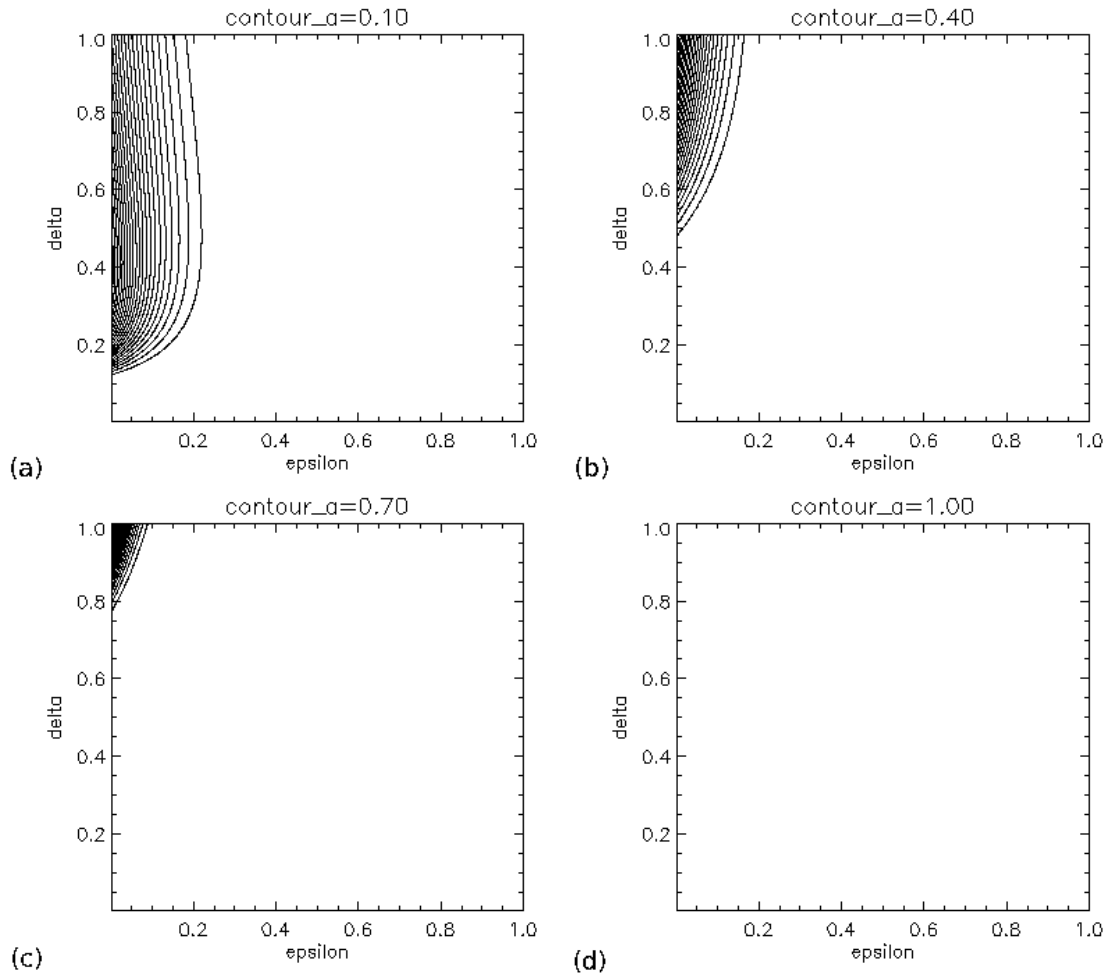


Figure 2.6: Contour plots of α_1 showing a equal to (a) 0.1,(b) 0.4, (c) 0.7 and (d) 1.0. The black areas show where α_1 is negative and hence the square root is imaginary. It is clear that mostly α_1 will be real and certainly, when $a \geq 1$, α_1 is positive for any δ_1 and ϵ_1 .

Contour plots (Fig. 2.6) were made for different values of a ranging from 0.1 to 1 with δ_1 and ϵ_1 varying between $1/500$ and 1 in Eq. 2.22. This shows that for values of $0 < a < 1$

there are limited values of δ_1 and ϵ_1 that will give an imaginary root but mostly a real root is found (Fig. 2.6). This means that for most values of δ_1 and ϵ_1 , x in Eq. 2.20 is real, y is real and, putting x into z , it is found that z is always real. Therefore, extra real nulls are invariably found. This tells us that when using the parameters a , c and d more often than not there will be more nulls than the two we want (at the origin and at $x = y = 0, z = L$). Therefore it seems logical that if we have all five parameters in our magnetic field, a, b, c, d and L , there will certainly be more than the two nulls we want present.

2.3 Effects of current parallel to the separator

To take steps towards creating a MHS field from which we may investigate separator reconnection, we now add a component of current parallel to the separator. The addition of this form of current will allow the field lines to curl around the separator. We still have many of the same conditions listed above, in Sect. 2.2, which allowed us to formulate our magnetic field except now $\mathbf{j} \neq \mathbf{0}$. The lower (positive) and upper (negative) null's spines are in the $z = 0$ and $z = L$ planes respectively and their separatrix surfaces are vertical. The magnetic field can now be written as

$$\begin{aligned} B_x &= \frac{B_0}{L_0}(x + cxz + byz - \frac{1}{2}j_{sep}y), \\ B_y &= \frac{B_0}{L_0}((2a - c)yz - (1 + aL)y + bxz + \frac{1}{2}j_{sep}x), \\ B_z &= \frac{B_0}{L_0}(-a(z^2 - zL) + \frac{1}{2}cx^2 + (a - \frac{1}{2}c)y^2 + bxy), \end{aligned} \quad (2.25)$$

where j_{sep} is a constant. This gives a current of the form

$$\mathbf{j} = \frac{B_0}{\mu_0 L_0}(0, 0, j_{sep}). \quad (2.26)$$

Once again we need to check through the conditions to see how the addition of this extra term (and extra parameter j_{sep}) affect the constraints.

2.3.1 Nature of the lower null ($x = y = z = 0$)

The magnetic field is linearised about the lower null as before and so

$$\mathbf{M} = \frac{B_0}{L_0} \begin{pmatrix} 1 & -\frac{1}{2}j_{sep} & 0 \\ \frac{1}{2}j_{sep} & -(1 + aL) & 0 \\ 0 & 0 & aL \end{pmatrix}. \quad (2.27)$$

The eigenvalues and eigenvectors are as follows

$$\lambda_s = \frac{-aL - \sqrt{(aL + 2)^2 - j_{sep}^2}}{2}, \quad \mathbf{e}_s = \begin{pmatrix} \frac{j_{sep}}{aL + 2 + \sqrt{(aL + 2)^2 - j_{sep}^2}} \\ 1 \\ 0 \end{pmatrix}, \quad (2.28)$$

$$\lambda_{f_1} = a, \quad \mathbf{e}_{f_1} = \begin{pmatrix} 0 \\ 0 \\ 1 \end{pmatrix},$$

$$\lambda_{f_2} = \frac{-aL + \sqrt{(aL+2)^2 - j_{sep}^2}}{2}, \quad \mathbf{e}_{f_2} = \begin{pmatrix} \frac{j_{sep}}{aL+2 - \sqrt{(aL+2)^2 - j_{sep}^2}} \\ 1 \\ 0 \end{pmatrix}.$$
(2.29)

Since this is a positive null we have the constraints $a > 0$ (since $L > 0$) as before, and also $j_{sep}^2 < 4(1+aL)$ and $j_{sep} < (aL+2)$. The stronger of the two latter constraints is $j_{sep}^2 < 4(1+aL)$ and so we drop the constraint $j_{sep} < (aL+2)$.

The separatrix-surface plane equation for the lower null is

$$y = -\frac{aL+2 + \sqrt{(aL+2)^2 - j_{sep}^2}}{j_{sep}}x,$$
(2.30)

and the spine is no longer lying along the x -axis, since the current has caused the spine and fan planes to close up in the same way that the separatrices of a 2D null close up with the addition of some current.

2.3.2 Nature of the upper null ($x = y = 0, z = L$)

Linearising around the upper null, the magnetic field can be written in terms of a matrix \mathbf{M} as follows

$$\mathbf{M} = \frac{B_0}{L_0} \begin{pmatrix} 1+cL & bL - \frac{1}{2}j_{sep} & 0 \\ bL + \frac{1}{2}j_{sep} & aL - cL - 1 & 0 \\ 0 & 0 & -aL \end{pmatrix}.$$
(2.31)

The eigenvalues and eigenvectors are as follows

$$\lambda_s = \frac{aL + \sqrt{(aL-2-2cL)^2 + 4b^2L^2 - j_{sep}^2}}{2}, \quad \mathbf{e}_s = \begin{pmatrix} \frac{2bL - j_{sep}}{aL-2-2cL + \sqrt{(aL-2-2cL)^2 + 4b^2L^2 - j_{sep}^2}} \\ 1 \\ 0 \end{pmatrix},$$

$$\lambda_{f_1} = -a, \quad \mathbf{e}_{f_1} = \begin{pmatrix} 0 \\ 0 \\ 1 \end{pmatrix},$$

$$\lambda_{f_2} = \frac{aL - \sqrt{(aL-2-2cL)^2 + 4b^2L^2 - j_{sep}^2}}{2}, \quad \begin{pmatrix} \frac{2bL - j_{sep}}{aL-2-2cL - \sqrt{(aL-2-2cL)^2 + 4b^2L^2 - j_{sep}^2}} \\ 1 \\ 0 \end{pmatrix}.$$
(2.32)

This is a negative null and so we find the constraint $b^2 > (1+c)(a-c-1)/L^2 + j_{sep}^2/(4L^2)$. To ensure the eigenvalues are real we must have $(aL-2-2cL)^2 + 4b^2L^2 > j_{sep}^2$. The separatrix-surface plane equation for the upper null is

$$y = \frac{aL - 2 - 2cL + \sqrt{(aL - 2 - 2cL)^2 + 4b^2L^2 - j_{sep}^2}}{2bL - j_{sep}}x, \quad (2.33)$$

and the spine lies along the line $\mathbf{r} = \mathbf{a} + k\mathbf{e}_s$ where $\mathbf{r} = (x, y, z)$, $\mathbf{a} = (0, 0, L)$ is the position of the upper null, k is a step along a field line and \mathbf{e}_s is the upper null's spine eigenvector.

2.3.3 Constraint to ensure there are only two nulls in the model

To ensure we have only two nulls (one at $x = y = z = 0$ and one at $x = y = 0, z = L$) we let each component of \mathbf{B} equal 0 and solve for x, y and z . The solution below was found by solving B_x for x , substituting this into B_y to solve for z and finally putting z into B_z to solve for y

$$\begin{aligned} x &= \frac{\pm(2a + cL - bj_{sep}y) + \frac{1}{2}\sqrt{4b^2(j_{sep}^2 - 4 - 4aL) + 4cj_{sep}^2(c - 2a) + 4a^2(2 + cL)^2}y}{\pm(2b - cj_{sep})}, \\ z &= \frac{\pm 2a \mp \frac{1}{2}cj_{sep}^2 \pm acL - \frac{1}{2}\sqrt{4b^2(j_{sep}^2 - 4 - 4aL) + 4cj_{sep}^2(c - 2a) + 4a^2(2 + cL)^2}}{\pm 2b^2 \mp 2ac \mp ac^2L + \frac{1}{2}c\sqrt{4b^2(j_{sep}^2 - 4 - 4aL) + 4cj_{sep}^2(c - 2a) + 4a^2(2 + cL)^2}}. \end{aligned} \quad (2.34)$$

The analytical solutions for y are very large and can be found in Appendix B. The same square root that appears in x and z occurs more than once in the solutions for y . Therefore, if the contents of this square root are positive another real null exists. As such we put a further constraint on our parameters to ensure any other nulls found will be imaginary

$$b^2 > c(2a - c) - \frac{(2a - acL - 2c)^2}{(j_{sep}^2 - 4 - 4aL)}. \quad (2.35)$$

Therefore, the five constraints we find for this magnetic field, under our conditions, are

1. $a > 0$,
2. $j_{sep}^2 < 4(1 + aL)$,
3. $4b^2L^2 - j_{sep}^2 > 4(1 + c)(a - c - 1)$,
4. $4b^2L^2 - j_{sep}^2 > -(aL - 2 - 2cL)^2$,
5. $b^2 > c(2a - c) - \frac{(2a - acL - 2c)^2}{(j_{sep}^2 - 4 - 4aL)}$.

2.3.4 Non-potential single-separator magnetic field

We now plot the magnetic field showing the geometry of the lower and upper nulls and their magnetic skeletons. Here, the separator length $L = 1.0$, $B_0 = L_0 = 1.0$ and we vary the four parameters a, b, c and j_{sep} to analyse their effect on the field lines. Fig. 2.7 displays the magnetic skeleton of the field with $b = 5.2, c = 4.0, j_{sep} = 1.1$ and a taking

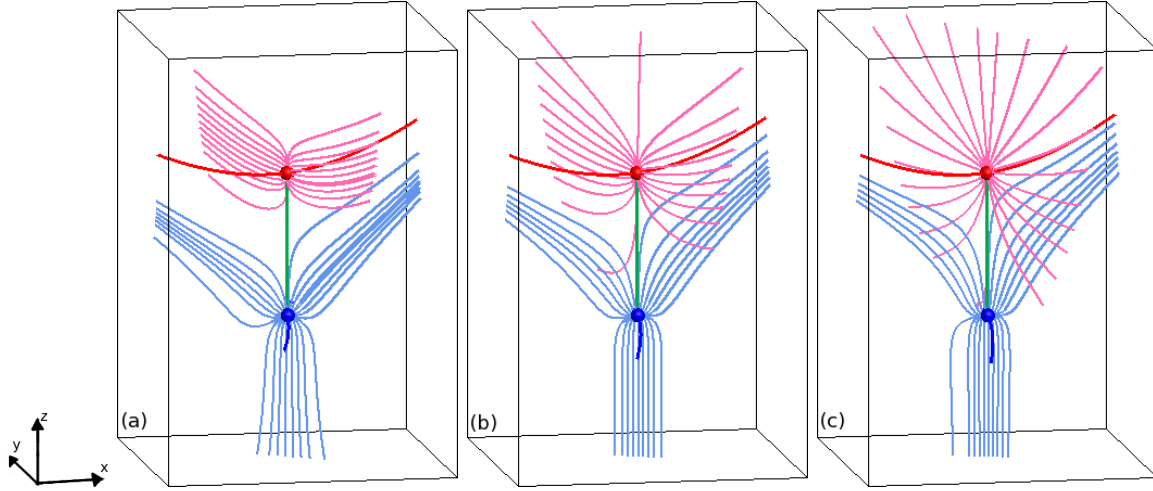


Figure 2.7: Images of the magnetic skeleton with current parallel to the separator which includes two nulls joined by a separator. The nulls are identified by blue/red spheres for the positive/negative nulls, the separatrix-surface field lines by pale-blue/pink lines and the spines as blue/red thick lines for the positive/negative nulls. The separator is drawn here as a green line. The parameters of the magnetic field are $b = 5.2$, $c = 4.0$, $j_{sep} = 1.1$ and for (a) $a = 1.5$, (b) $a = 2.5$ and (c) $a = 3.5$.

the values 1.5, 2.5 and 3.5. The geometry of the field lines in the separatrix surfaces of both nulls are altered and both nulls are rotated slightly in the xy -plane.

Fig. 2.8 shows that varying b from 5.1 to 6.1 to 7.1 alters the field lines in the separatrix surfaces of both nulls and rotates the separatrix surfaces and the spines of each null in the xy -plane. In this figure $a = 1.0$, $c = 3.0$ and $j_{sep} = 2.5$.

Fig. 2.9 shows c being varied from -1.0 to 1.0 to 2.0 while $a = 1.0$, $b = 5.1$ and $j_{sep} = 2.5$. Again here, varying the parameter c changes the geometry of the field lines in the separatrix surfaces, which also rotate in the xy -plane.

Finally in Fig. 2.10 the skeleton is drawn for the magnetic fields with $a = 2.0$, $b = 2.7$, $c = 2.0$ and j_{sep} taking the value 0.5, 1.5 and 2.5. Increasing j_{sep} causes the separatrix-surface field lines to curl more around the separator.

2.3.5 Magnetic field local to the separator

Now we consider the magnetic field in cuts perpendicular to the separator. Again we want to analyse the geometry of the field lines and the magnetic skeleton at these cuts. The 2D linearised magnetic field perpendicular to the separator about a point $z = z_0$ along the separator is

$$\begin{aligned} B_x(x, y, z_0) &= \frac{B_0}{L_0} (x + cxz_0 + byz_0 - \frac{1}{2}j_{sep}y), \\ B_y(x, y, z_0) &= \frac{B_0}{L_0} ((2a - c)y z_0 - (1 + aL)y + bxz_0 + \frac{1}{2}j_{sep}x), \end{aligned} \quad (2.36)$$

which corresponds to an \mathbf{M} matrix

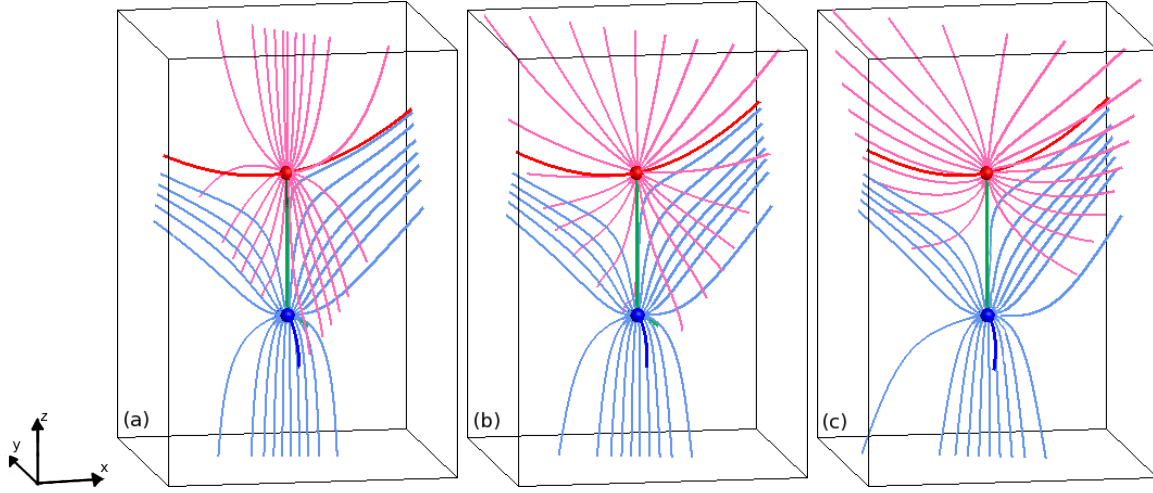


Figure 2.8: Images of the magnetic skeleton with current parallel to the separator which includes two nulls joined by a separator. The nulls are identified by blue/red spheres for the positive/negative nulls, the separatrix-surface field lines by pale-blue/pink lines and the spines as blue/red thick lines for the positive/negative nulls. The separator is drawn here as a green line. The parameters of the magnetic field are $a = 2.0$, $c = 1.0$, $j_{sep} = 0.5$ and for (a) $b = 2.0$, (b) $b = 3.0$ and (c) $b = 4.0$.

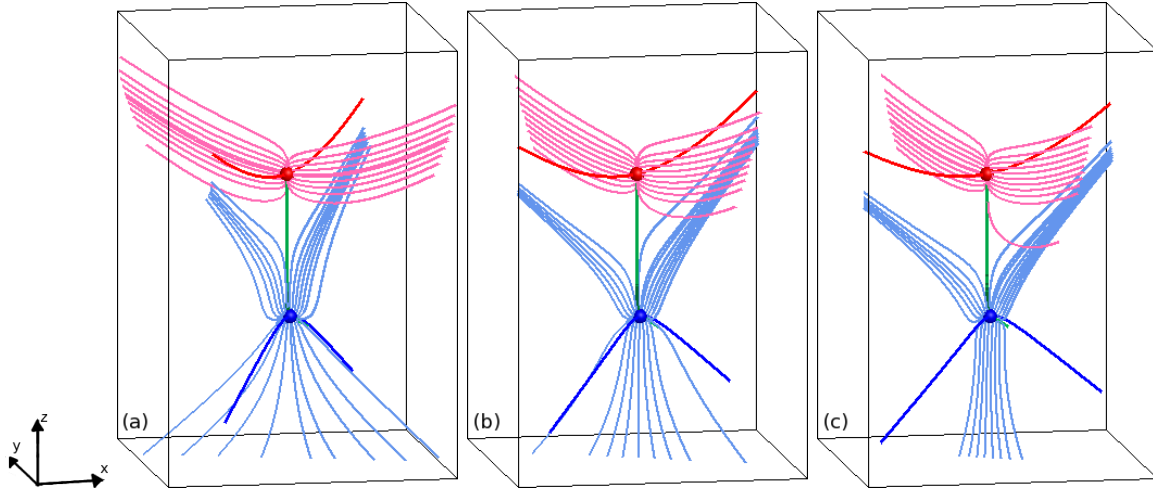


Figure 2.9: Images of the magnetic skeleton with current parallel to the separator which includes two nulls joined by a separator. The nulls are identified by blue/red spheres for the positive/negative nulls, the separatrix-surface field lines by pale-blue/pink lines and the spines as blue/red thick lines for the positive/negative nulls. The separator is drawn here as a green line. The parameters of the magnetic field are $a = 1.0$, $b = 5.1$, $j_{sep} = 2.5$ and for (a) $c = -1.0$, (b) $c = 1.0$ and (c) $c = 2.0$.

$$\mathbf{M} = \frac{B_0}{L_0} \begin{pmatrix} 1 + cz_0 & bz_0 - \frac{1}{2}j_{sep} \\ bz_0 + \frac{1}{2}j_{sep} & (2a - c)z_0 - (1 + aL) \end{pmatrix}. \quad (2.37)$$

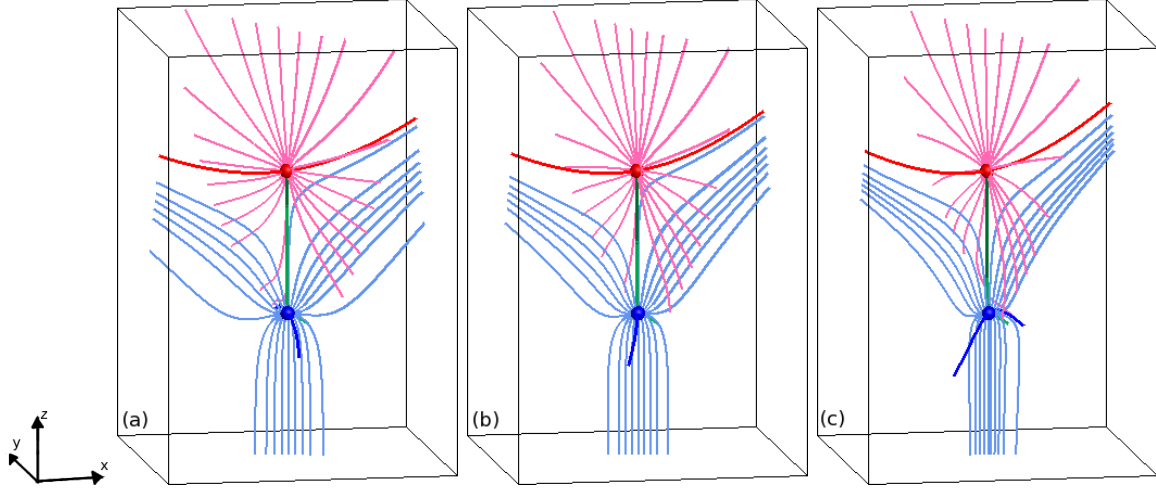


Figure 2.10: Images of the magnetic skeleton with current parallel to the separator which includes two nulls joined by a separator. The nulls are identified by blue/red spheres for the positive/negative nulls, the separatrix-surface field lines by pale-blue/pink lines and the spines as blue/red thick lines for the positive/negative nulls. The separator is drawn here as a green line. The parameters of the magnetic field are $a = 2.0$, $b = 2.7$, $c = 2.0$ and for (a) $j_{sep} = 0.5$, (b) $j_{sep} = 1.5$ and (c) $j_{sep} = 2.5$.

The eigenvalues of the matrix \mathbf{M} are

$$\lambda = \frac{a(2z_0 - L)}{2} \pm \frac{\sqrt{(2z_0(a - c) - aL - 2)^2 + 4b^2z_0^2 - j_{sep}^2}}{2}. \quad (2.38)$$

Therefore, unlike the potential case, the eigenvalues will be complex if

$$4b^2z_0^2 + (2az_0 - aL - 2 - 2cz_0)^2 < j_{sep}^2. \quad (2.39)$$

Complex eigenvalues would imply that the field lines in the vicinity of the separator become elliptic, as opposed to hyperbolic.

We check to see if it is possible to gain complex eigenvalues in our model bearing in mind the other constraints on the parameters of the model. To do this we compare the constraint to ensure there are only two nulls in the model with the constraint which would allow for complex eigenvalues. Putting these constraints together we can write

$$\frac{j_{sep}^2 - (2az_0 - 2cz_0 - aL - 2)^2}{4z_0^2} > b^2 > c(2a - c) - \frac{(2a - acL - 2c)^2}{j_{sep}^2 - 4 - 4aL}. \quad (2.40)$$

We multiply everything by $4z_0^2(j_{sep}^2 - 4 - 4aL)$ which flips the sign of the inequality since $j_{sep}^2 - 4 - 4aL < 0$ (constraint 2). In doing so we can write the inequality in terms of

$$z_0 = \frac{-4(a - c)(aL + 2)(j_{sep}^2 - 4 - 4aL) \pm \sqrt{-16a^2(4 + 4aL - j_{sep}^2)(-(aL + 2)(cL + 2) + j_{sep}^2)^2}}{2(-4(a - c)^2(j_{sep}^2 - 4 - 4aL) + 4(2a - acL - 2c)^2 - 4c(2a - c)(j_{sep}^2 - 4 - 4aL))}. \quad (2.41)$$

The terms of interest here are those under the square root. We see that

- $-16a^2$ is always negative,
- $(4 + 4aL - j_{sep}^2)$ is always positive since we have the constraint $j_{sep}^2 - 4 - 4a < 0$,
- $-(aL + 2)(cL + 2) + j_{sep}^2)^2$ is always positive since it is squared.

This means that our square root is the square root of a negative number. Therefore, z_0 is always imaginary and this shows us that it is not possible to gain complex eigenvalues with a magnetic field of this form. However, elliptic field lines about separators have been found by Parnell et al. [2010a].

2.3.6 Lorentz force

The introduction of a current to our magnetic field means that the configuration is no longer in force balance. Thus we look at the resulting Lorentz force ($\mathbf{j} \times \mathbf{B}$) which is calculated from the magnetic field shown in Eq. 2.25,

$$\begin{aligned} (\mathbf{j} \times \mathbf{B})_x &= -\frac{B_0^2}{\mu_0 L_0^2} j_{sep} \left((2a - c)z_0 y - (1 + aL)y + bz_0 x + \frac{1}{2} j_{sep} x \right), \\ (\mathbf{j} \times \mathbf{B})_y &= \frac{B_0^2}{\mu_0 L_0^2} j_{sep} \left(x + cz_0 x + bz_0 y - \frac{1}{2} j_{sep} y \right), \\ (\mathbf{j} \times \mathbf{B})_z &= 0. \end{aligned} \tag{2.42}$$

From the equations it is clear that the Lorentz force is going to act to fold the two separatrix surfaces from the oppositely signed nulls together, but the force does not act along the separator and is zero at the nulls. However, the particular direction and strength of the Lorentz force varies in z . In order to show this we consider cuts perpendicular to the separator and plot the geometry of the field lines, the intersection of the lower and upper null's separatrix-surface planes with the cut and the direction of the Lorentz force (Fig. 2.11). From these plots we see that the Lorentz force acts perpendicular to the field lines. Mathematically we know that magnetic pressure force is acting to move the field lines from regions where the magnitude of \mathbf{B} is great to where it is weaker and that the tension force is acting to try and straighten the field lines where they are curved.

2.4 Effects of current perpendicular to the separator

We now investigate the properties of our analytical model when a component of current is added to Eq. 2.1 which is directed along the y -axis (i.e., the current is directed perpendicular to the separator). Other than the form of current, our conditions are the same as those detailed in Sect. 2.3. The magnetic field can be written as

$$\begin{aligned} B_x &= \frac{B_0}{L_0} (x + cxz + byz), \\ B_y &= \frac{B_0}{L_0} ((2a - c)yz - (1 + aL)y + bxz), \\ B_z &= \frac{B_0}{L_0} (-a(z^2 - zL) + \frac{1}{2}cx^2 + (a - \frac{1}{2}c)y^2 + bxy - j_{\perp}x), \end{aligned} \tag{2.43}$$

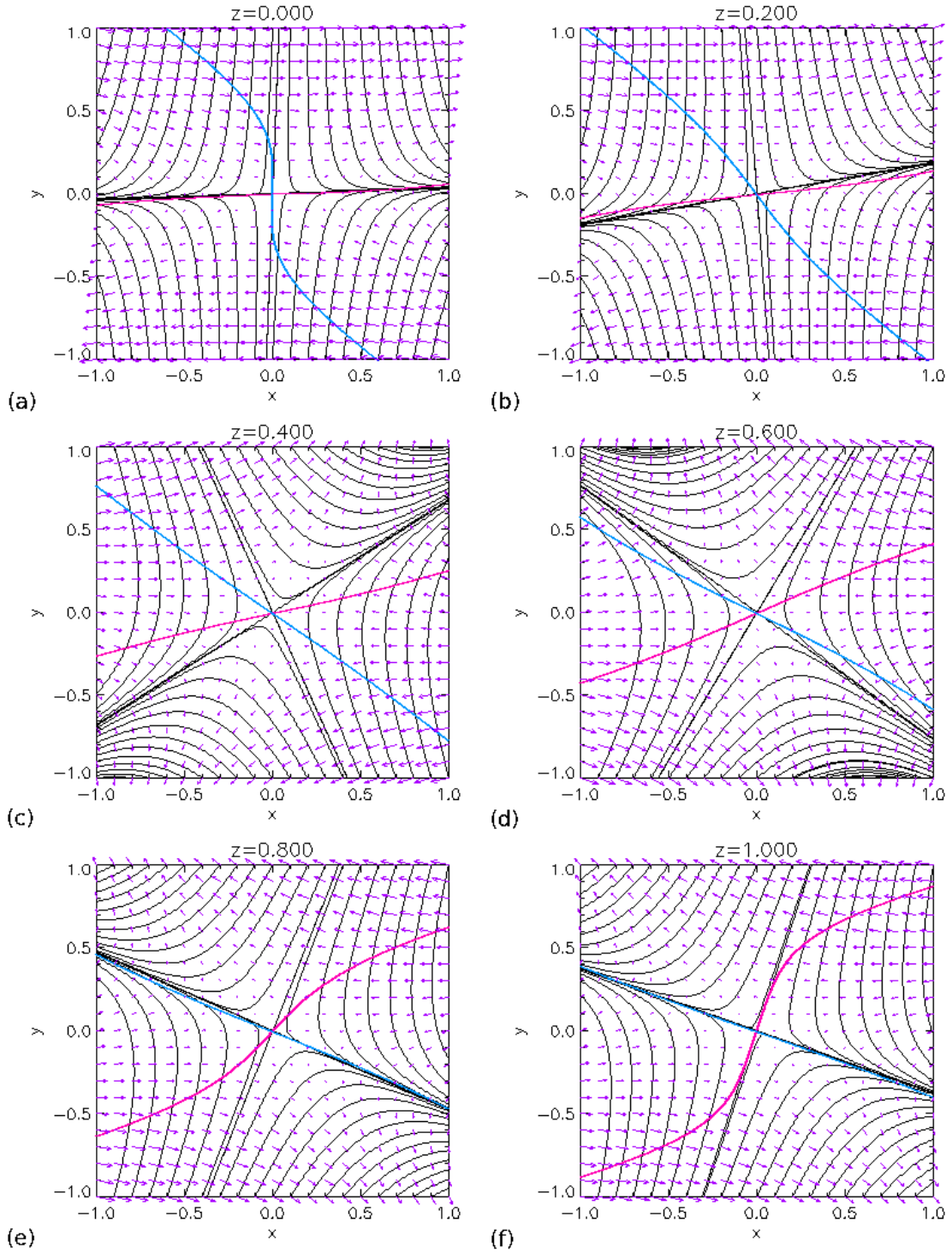


Figure 2.11: Plots showing cuts perpendicular to the separator. Here $a = 5.0, b = 2.7, c = -2.0$ and $j_{sep} = 0.5$. Where the separatrix surface of the lower/upper null intersects the cut is shown in pale-blue/pink. The field lines are shown in black and the direction of the Lorentz force is represented by the purple arrows.

where j_{\perp} is a constant. Hence, the current takes the form

$$\mathbf{j} = \frac{B_0}{\mu_0 L_0} (0, j_{\perp}, 0). \quad (2.44)$$

To ensure there are only two nulls in the model, we must have $b^2 > a^2(cL + 2)^2/4(1 + aL)$ which is identical to the constraint found for having only two nulls in the potential case. Therefore, the addition of a component of current perpendicular to the separator, and directed along the y -axis, does not affect the number of nulls found in the field.

2.4.1 Nature of the lower null ($x = y = z = 0$)

Following the same steps detailed in Sects. 2.2 and 2.3, the eigenvalues and eigenvectors of the lower null are found to be

$$\begin{aligned} \lambda_s &= -(1 + aL), & \mathbf{e}_s &= \begin{pmatrix} 0 \\ 1 \\ 0 \end{pmatrix}, \\ \lambda_{f_1} &= 1, & \mathbf{e}_{f_1} &= \begin{pmatrix} \frac{aL-1}{j_{\perp}} \\ 0 \\ 1 \end{pmatrix}, \\ \lambda_{f_2} &= aL, & \mathbf{e}_{f_2} &= \begin{pmatrix} 0 \\ 0 \\ 1 \end{pmatrix}. \end{aligned} \quad (2.45)$$

This null is positive and so we must have $a > 0$. As with the potential magnetic field (Sect. 2.2), the spine of the lower null lies along the y -axis here and the fan lies in a vertical plane.

2.4.2 Nature of the upper null ($x = y = 0, z = L$)

In a similar manner the eigenvalues and eigenvectors of the upper null are found as

$$\begin{aligned} \lambda_s &= \frac{aL}{2} + \frac{\sqrt{(aL - 2cL - 2)^2 + 4b^2L^2}}{2}, & \mathbf{e}_s &= \begin{pmatrix} \frac{-(3aL + \sqrt{(aL - 2cL - 2)^2 + 4b^2L^2})}{2j_{\perp}} \\ \frac{-(3aL - \sqrt{(aL - 2cL - 2)^2 + 4b^2L^2})}{2j_{\perp}} \\ 0 \end{pmatrix}, \\ \lambda_{f_1} &= \frac{aL}{2} - \frac{\sqrt{(aL - 2cL - 2)^2 + 4b^2L^2}}{2}, & \mathbf{e}_{f_1} &= \begin{pmatrix} \frac{(3aL + \sqrt{(aL - 2cL - 2)^2 + 4b^2L^2})bL}{j_{\perp}(aL - 2cL - \sqrt{(aL - 2cL - 2)^2 + 4b^2L^2} - 2)} \\ \frac{(3aL - \sqrt{(aL - 2cL - 2)^2 + 4b^2L^2})bL}{j_{\perp}(aL - 2cL - \sqrt{(aL - 2cL - 2)^2 + 4b^2L^2} - 2)} \\ 0 \end{pmatrix}, \\ \lambda_{f_2} &= -aL, & \mathbf{e}_{f_2} &= \begin{pmatrix} 0 \\ 0 \\ 1 \end{pmatrix}. \end{aligned} \quad (2.46)$$

The upper null is negative so $b^2L^2 > (aL - cL - 1)(cL + 1)$ as was found in the potential case. The spine lies in the xy -plane and the separatrix surface plane equation is

$$y = \frac{3aL - \sqrt{(aL - 2cL - 2)^2 + 4b^2L^2}}{3aL + \sqrt{(aL - 2cL - 2)^2 + 4b^2L^2}}x. \quad (2.47)$$

There are only three constraints which must be satisfied to satisfy the conditions for this model and these are identical to those found for the potential case,

1. $a > 0$,
2. $b^2 > \frac{(aL - cL - 1)(cL + 1)}{L^2}$,
3. $b^2 > \frac{a^2(cL + 2)^2}{4(1 + aL)}$.

2.4.3 Non-potential single-separator magnetic field with current perpendicular to separator

Fig. 2.12 displays the skeleton of the our model with the parameter j_\perp being increased from $j_\perp = 0.5$, $j_\perp = 1.5$ to $j_\perp = 2.5$. It is clear from these figures that varying j_\perp has no effect on the lower null's spine direction or plane of the separatrix surface since j_\perp lies along the y -axis parallel to the lower null's spine. However, the upper null's spine bends towards the separator as j_\perp is increased because current along the y -axis contributes components of current both parallel and perpendicular to the spine of the upper null.

The field lines in the separatrix surface of the lower null curl more tightly around the spine as j_\perp is increased however the plane is not affected. The plane of the upper null's separatrix surface is not affected by the value of j_\perp . The geometry of the field lines in the lower null's separatrix surface is twisted to a greater extent than the separatrix-surface field lines of the upper null. We note also that the separatrix surface field lines in both fan planes appear to spiral as j_\perp is increased.

2.4.4 Magnetic field local to the separator

The magnetic field in cuts perpendicular to the separator is found to be identical to the corresponding potential field (Eq. 2.12) since no component of current acts in the z -direction. This means that the eigenvalues of the linearised field are real for all values of B_0, L_0, L, a, b, c and j_\perp and hence the magnetic field will always be hyperbolic in cuts perpendicular to the separator.

2.4.5 Lorentz force

Due to the component of current perpendicular to the separator the Lorentz force acts as

$$\begin{aligned} (\mathbf{j} \times \mathbf{B})_x &= \frac{B_0^2}{\mu_0 L_0^2} j_\perp \left(-a(z^2 - Lz) + \frac{1}{2}cx^2 + (a - \frac{c}{2})y^2 + bxy - j_\perp x \right), \\ (\mathbf{j} \times \mathbf{B})_y &= 0, \\ (\mathbf{j} \times \mathbf{B})_z &= -\frac{B_0^2}{\mu_0 L_0^2} j_\perp (x + cxz + byz), \end{aligned} \quad (2.48)$$

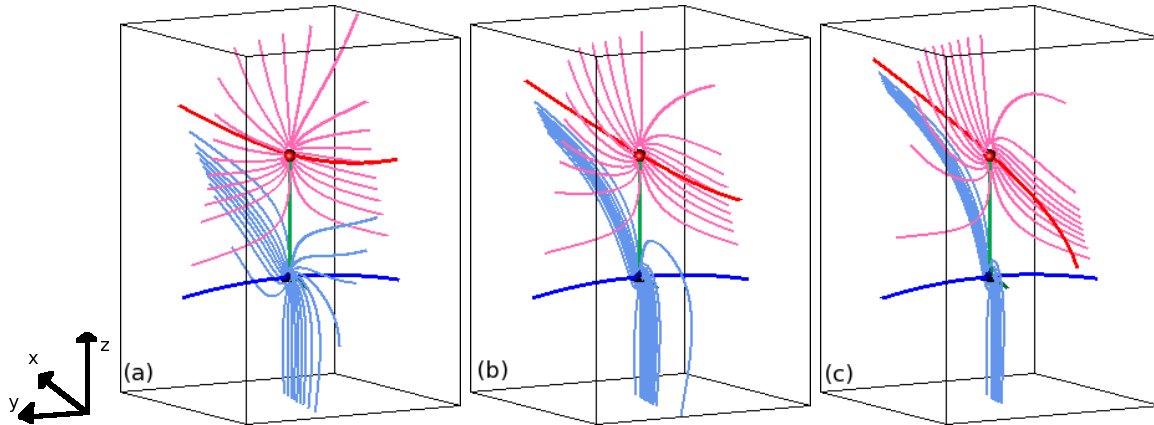


Figure 2.12: Images of the magnetic skeleton which includes two nulls joined by a separator with current directed along the y -axis. The nulls are identified by blue/red spheres for the positive/negative nulls, the separatrix-surface field lines by pale-blue/pink lines and the spines as blue/red thick lines for the positive/negative nulls. The separator is drawn here as a green line. The parameters of the magnetic field are $a = 1.0$, $b = 1.5$, $c = 1.0$ and (a) $j_{\perp} = 0.5$, (b) $j_{\perp} = 1.5$ and (c) $j_{\perp} = 2.5$.

and so there is a component of the Lorentz force directed along the separator as well as along the x -axis. This result is different to that seen in Sect. 2.3 where the Lorentz force acted to collapse the separatrix surfaces towards each other in the xy -plane. Here we see the Lorentz force is acting to bend the separator away from being fixed along the z -axis and may also be acting to collapse the spines (which lie in xy -planes) towards the separator. At both nulls the Lorentz force vanishes.

2.5 Effects of current parallel and perpendicular to the separator

Finally, we investigate the effects of having a component of current directed parallel to the separator, j_{sep} , and a component of current directed perpendicular to the separator along the y -axis, j_{\perp} . In other words, we are combining the forms of the magnetic field discussed in Sects. 2.3 and 2.4. Apart from the form of current we use here, the conditions we wish to satisfy are the same as those found in Sect. 2.2. The magnetic field can be written as

$$\begin{aligned} B_x &= \frac{B_0}{L_0}(x + cxz + byz - \frac{1}{2}j_{sep}y), \\ B_y &= \frac{B_0}{L_0}((2a - c)yz - (1 + aL)y + bxz + \frac{1}{2}j_{sep}x), \\ B_z &= \frac{B_0}{L_0}(-a(z^2 - zL) + \frac{1}{2}cx^2 + (a - \frac{1}{2}c)y^2 + bxy - j_{\perp}x), \end{aligned} \quad (2.49)$$

and the current has the form

$$\mathbf{j} = \frac{B_0}{\mu_0 L_0}(0, j_{\perp}, j_{sep}), \quad (2.50)$$

where j_{\perp} and j_{sep} are constants. In order to maintain the condition that there are only two nulls in the model at $(0, 0, 0)$ and $(0, 0, L)$, we must satisfy the constraint

$$b^2 > c(2a - c) - \frac{(2a - acL - 2c)^2}{j_{sep}^2 - 4 - 4aL}, \quad (2.51)$$

which is identical to the constraint found in Sect. 2.3 for ensuring only two nulls exist.

2.5.1 Nature of the lower null $x = y = z = 0$

The lower null is found to have the following eigenvalues and eigenvectors by using the linearised field around $(0, 0, 0)$

$$\begin{aligned} \lambda_s &= -\frac{aL}{2} - \frac{\sqrt{(aL+2)^2 - j_{sep}^2}}{2}, & \mathbf{e}_s &= \begin{pmatrix} \frac{3aL + \sqrt{(aL+2)^2 - j_{sep}^2}}{2j_{\perp}} \\ \frac{j_{sep}}{2j_{\perp}} \frac{3aL + \sqrt{(aL+2)^2 - j_{sep}^2}}{2+aL + \sqrt{(aL+2)^2 - j_{sep}^2}} \\ 1 \end{pmatrix}, \\ \lambda_{f_1} &= aL, & \mathbf{e}_{f_1} &= \begin{pmatrix} 0 \\ 0 \\ 1 \end{pmatrix}, \\ \lambda_{f_2} &= -\frac{aL}{2} + \frac{\sqrt{(aL+2)^2 - j_{sep}^2}}{2}, & \mathbf{e}_{f_2} &= \begin{pmatrix} \frac{3aL - \sqrt{(aL+2)^2 - j_{sep}^2}}{2j_{\perp}} \\ \frac{j_{sep}}{2j_{\perp}} \frac{3aL - \sqrt{(aL+2)^2 - j_{sep}^2}}{2+aL + \sqrt{(aL+2)^2 - j_{sep}^2}} \\ 1 \end{pmatrix}. \end{aligned} \quad (2.52)$$

Since this null is positive we must have $a > 0$ and $j_{sep}^2 < 4(1 + aL)$ as was found in Sect. 2.3. The spine of this null lies in a mix of the x, y, z lines and the separatrix surface lies in the plane

$$y = \frac{j_{sep}}{2 + aL - \sqrt{(aL+2)^2 - j_{sep}^2}} x. \quad (2.53)$$

2.5.2 Nature of the upper null $x = y = 0, z = L$

Similarly, the eigenvalues and eigenvectors of the upper null are found as

$$\begin{aligned} \lambda_s &= \frac{aL}{2} + \frac{\sqrt{(aL - 2cL - 2)^2 + 4b^2L^2 - j_{sep}^2}}{2}, \\ \mathbf{e}_s &= \begin{pmatrix} \frac{-3aL - \sqrt{(aL - 2cL - 2)^2 + 4b^2L^2 - j_{sep}^2}}{2j_{\perp}} \\ \frac{-3aL - \sqrt{(aL - 2cL - 2)^2 + 4b^2L^2 - j_{sep}^2}}{2j_{\perp}} \frac{2j_{\perp}}{(3aL + \sqrt{(aL - 2cL - 2)^2 + 4b^2L^2 - j_{sep}^2})} \\ \frac{2j_{\perp}(j_{sep} - 2bL)}{1} \end{pmatrix}, \end{aligned}$$

$$\begin{aligned}
 \lambda_{f_1} &= -aL, & \mathbf{e}_{f_1} &= \begin{pmatrix} 0 \\ 0 \\ 1 \end{pmatrix}, \\
 \lambda_{f_2} &= \frac{aL}{2} - \frac{\sqrt{(aL - 2cL - 2)^2 + 4b^2L^2 - j_{sep}^2}}{2}, \\
 \mathbf{e}_{f_2} &= \begin{pmatrix} \frac{-3aL + \sqrt{(aL - 2cL - 2)^2 + 4b^2L^2 - j_{sep}^2}}{2j_{\perp}} \\ \frac{(2 + 2cL - 2aL + \sqrt{(aL - 2cL - 2)^2 + 4b^2L^2 - j_{sep}^2})(\sqrt{(aL - 2cL - 2)^2 + 4b^2L^2 - j_{sep}^2} - 3aL)}{2j_{\perp}(j_{sep} - 2bL)} \\ 1 \end{pmatrix}.
 \end{aligned} \tag{2.54}$$

Since this is a negative null $b^2L^2 > (1+c)(a-c-1) + j_{sep}^2/4$ and to ensure the null is real $j_{sep}^2 < (aL - 2 - 2cL)^2 + 4b^2L^2$. These constraints are identical to those found in Sect. 2.3. The spine of this null lies in a mix of the x, y, z lines and the separatrix surface is in the plane

$$y = \frac{2 + 2cL - 2aL + \sqrt{(aL - 2cL - 2)^2 + 4b^2L^2 - j_{sep}^2}}{2bL - j_{sep}}x. \tag{2.55}$$

Therefore, when there is a component of current directed parallel to the separator as well as a component of current directed perpendicular to the separator (along the y -axis) we find the following constraints must be met to satisfy our conditions on the magnetic field

1. $a > 0$,
2. $4b^2L^2 - j_{sep}^2 > 4(1+c)(a-c-1)$,
3. $4b^2L^2 - j_{sep}^2 > -(aL - 2 - 2cL)^2$,
4. $j_{sep}^2 < 4(1+aL)$,
5. $b^2 > (2a-c) - \frac{(2a-acL-2c)^2}{(j_{sep}^2-4-4aL)}$.

These conditions are identical to those found in Sect. 2.3 where the current was directed only parallel to the separator. This indicates, as did the results of Sect. 2.4, that having a component of current perpendicular to the separator introduces no extra constraints to those found in the potential case (Sect. 2.2). We have seen, however, that both j_{sep} and j_{\perp} are involved in the eigenvectors of each null and so will affect the magnetic configuration.

2.5.3 Non-potential single-separator magnetic field with current parallel and perpendicular to the separator

The skeleton of our model with varying values of j_{\perp} and j_{sep} is shown in Fig. 2.13. A combination of the effects of increasing these two parameters is visible in this figure. Between Figs. 2.13a and 2.13b, j_{sep} remains constant but j_{\perp} is increased leading to an increased spiralling of the field lines of the lower null's fan plane around the spine but the plane of this fan is unaffected. Varying this value does not affect the upper null's fan plane. The spine of both nulls tends towards the z -axis as j_{\perp} is increased.

Between Figs. 2.13b and 2.13c, j_{\perp} remains constant but j_{sep} is increased. The separatrix surface field lines, of both nulls, curl more around the separator as j_{sep} is increased and the plane's of the fans are altered.

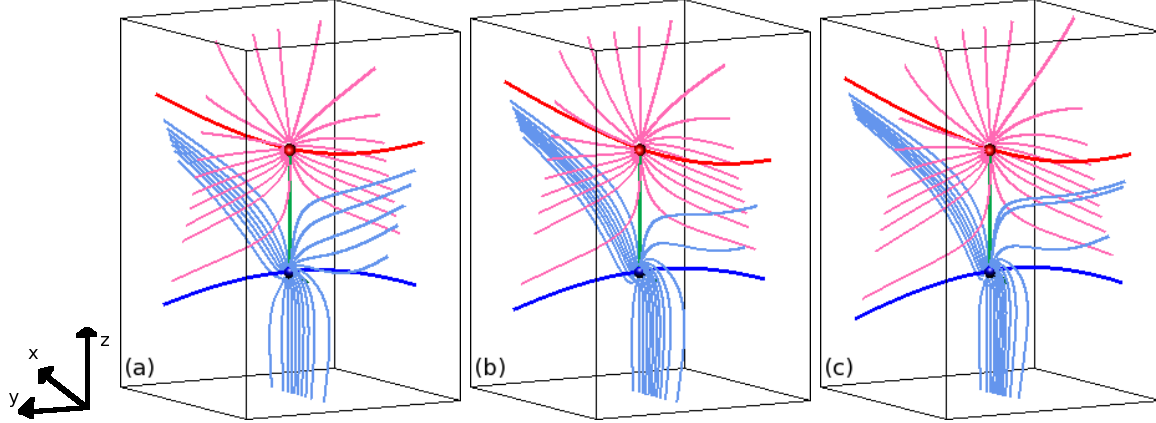


Figure 2.13: Images of the magnetic skeleton which includes two nulls joined by a separator with current directed along the y -axis. The nulls are identified by blue/red spheres for the positive/negative nulls, the separatrix-surface field lines by pale-blue/pink lines and the spines as blue/red thick lines for the positive/negative nulls. The separator is drawn here as a green line. The parameters of the magnetic field are $a = 1.0$, $b = 1.5$, $c = 1.0$ and (a) $j_{\perp} = 0.5$ and $j_{sep} = 1.5$, (b) $j_{\perp} = 1.0$ and $j_{sep} = 1.5$ and (c) $j_{\perp} = 1.0$ and $j_{sep} = 2.0$.

2.5.4 Magnetic field local to the separator

The magnetic field local to the separator is identical here to the local field found in Sect. 2.3. Hence, when the current has components directed parallel and perpendicular to the separator we find that the eigenvalues are always real for all values of B_0 , L_0 , L , a , b , c , j_{\perp} and j_{sep} . This implies the magnetic field lines will always be hyperbolic in cuts perpendicular to the separator.

2.5.5 Lorentz force

The Lorentz force associated with the magnetic field given in Eq. 2.49 can be written as

$$\begin{aligned}
 (\mathbf{j} \times \mathbf{B})_x &= \frac{B_0^2}{\mu_0 L_0^2} \left(\left(-a(z^2 - zL) + \frac{1}{2}cx^2 + (a - \frac{1}{2}c)y^2 + bxy - j_{\perp}x \right) j_{\perp} - \right. \\
 &\quad \left. \left((2a - c)yz - (1 + aL)y + bxz + \frac{1}{2}j_{sep}x \right) j_{sep} \right), \\
 (\mathbf{j} \times \mathbf{B})_y &= \frac{B_0^2}{\mu_0 L_0^2} (x + cxz + byz - \frac{1}{2}j_{sep}y) j_{sep}, \\
 (\mathbf{j} \times \mathbf{B})_z &= -\frac{B_0^2}{\mu_0 L_0^2} (x + cxz + byz - \frac{1}{2}j_{sep}y) j_{\perp}.
 \end{aligned} \tag{2.56}$$

As expected, the Lorentz force is acting to both close the separatrix surfaces of the lower and upper null's towards each other as was seen in Sect. 2.3 (x and y components of the Lorentz force) and to bend the separator away from being straight along the z -axis (z component of the Lorentz force). The latter effect may also act to bend the spines of the null's towards the separator as was observed in Sect. 2.4. The Lorentz force is again found to be zero at both nulls.

2.6 Summary

In this chapter we have found and analysed four analytical magnetic fields which represent magnetic configurations which contain two 3D null points whose separatrix surfaces are intersecting to form a magnetic separator linking the null points. The first of these fields, discussed in Sect. 2.2, was potential ($\mathbf{j} = \mathbf{0}$), the second field, discussed in Sect. 2.3, had a component of current which was directed along the separator ($\mathbf{j} = \frac{B_0}{\mu_0 L_0}(0, 0, j_{sep})$), the third field, discussed in Sect. 2.4, had a component of current directed perpendicular to the separator along the y -axis ($\mathbf{j} = \frac{B_0}{\mu_0 L_0}(0, j_{\perp}, 0)$) and finally the last field combined the previous two magnetic fields and so had both a component of current directed perpendicular to and parallel to the separator ($\mathbf{j} = \frac{B_0}{\mu_0 L_0}(0, j_{\perp}, j_{sep})$) in Sect. 2.5. The second field discussed here is used throughout this thesis.

The addition of j_{sep} to the potential field allows the magnetic fields to curl around the separator. This field, which can be written as

$$\begin{aligned} B_x &= \frac{B_0}{L_0}(x + cxz + byz - \frac{1}{2}j_{sep}y), \\ B_y &= \frac{B_0}{L_0}((2a - c)yz - (1 + aL)y + bxz + \frac{1}{2}j_{sep}x), \\ B_z &= \frac{B_0}{L_0}(-a(z^2 - zL) + \frac{1}{2}cx^2 + (a - \frac{1}{2}c)y^2 + bxy), \end{aligned} \quad (2.57)$$

has seven parameters, five of which, if varied, alter the initial magnetic field configuration. The scale factors B_0 and L_0 are both positive and have no effect on the field configuration. The values which these parameters can take are restricted by a series of conditions which we impose on the field. These conditions are:

1. $\nabla \cdot \mathbf{B} = 0$ so we have a magnetic field.
2. $\mathbf{j} = \frac{B_0}{\mu_0 L_0}(0, 0, j_{sep})$ so the current is constant and is directed along the separator.
3. $\mathbf{B} = \mathbf{0}$ at $x = y = z = 0$ and at $x = y = 0, z = L$ only so we have two nulls a distance L apart.
4. The lower null is positive with a vertical separatrix surface and spine lying in the $z = 0$ plane.
5. The upper null is negative with a vertical separatrix surface and spine lying in the $z = L$ plane.
6. There is only one separator and it lies along the z -axis.

The above conditions lead to the following constraints on the field's parameters

1. $a > 0$,

2. $j_{sep}^2 < 4(1 + aL)$,
3. $4b^2L^2 - j_{sep}^2 > 4(1 + c)(a - c - 1)$,
4. $4b^2L^2 - j_{sep}^2 > -(aL - 2 - 2cL)^2$,
5. $b^2 > c(2a - c) - \frac{(2a - acL - 2c)^2}{(j_{sep}^2 - 4 - 4aL)}$.

The addition of current parallel to the separator should lead to high values of j_{\parallel} , the component of current which is parallel to the magnetic field, being found along the separator and hence high values of E_{\parallel} , the component of the electric field which is parallel to the magnetic field, should also be found here. This field is used in the remaining chapters of this thesis to investigate the currents which form in the model through non-resistive MHD relaxation and the subsequent reconnection which occurs at these current features.

Chapter 3

Non-resistive MHD relaxation to form a separator current layer: high plasma-beta experiments

In this chapter, we study MHS equilibria involving current accumulations that form from the non-resistive relaxation of a non-potential magnetic field which contains two 3D nulls connected by a separator. The analytical magnetic field discussed in Chapt. 2 is used as a starting point for the numerical experiments that are run to create the MHS equilibria. We allow our magnetic field to relax over time to form the MHS equilibria. In this way we gain equilibria with stored magnetic energy. This method of gaining MHS equilibria has been used before in Fuentes-Fernández et al. [2011] who gained a MHS equilibrium at a 2D X-point.

We focus firstly on the relaxation of one specific magnetic field configuration (detailed in the next section) and study the properties of the current accumulation which form during the experiment. We then go on to analyse how varying the value of our initially uniform current affects the properties of the current layer. In the following chapters, we explore the effects of varying other parameters in our magnetic plasma system and analyse properties of the magnetic reconnection which can occur at these equilibria current layers when in a resistive regime.

To carry out the experiments in this chapter, we have used the Lare3d code described in Chapt. 1. The dimensions of the box used, for all experiments in this chapter, are $-L_0$ to L_0 in the x and y -directions and $-L_0$ to $L_0 + L$ in the z -direction and the resolution of the grid is 512^3 . The ratio of specific heats is $\gamma = \frac{5}{3}$, the background physical resistivity is $\eta = 0.0$ (the background numerical resistivity is estimated to be ≈ 0.04) and the viscosity is $\nu = 0.01$. This value, of the background viscosity, corresponds to a characteristic viscous speed of $v_\nu = 2.555$. This value is calculated from the equation which defines the Reynold's number, $R_e = v_\nu \delta l / \nu$ where R_e is the Reynold's number (equal to 1 to calculate this value), δl is the size of a cell ($2/511$) and $\nu = 0.01$. This characteristic viscous speed indicates the speed at which a viscous wave will move in the system, so waves travelling slower than this speed will be damped.

The boundary conditions are chosen such that no energy may leave or enter the domain and so the magnetic field is line tied at the boundaries and the scalar quantities (internal

energy per unit mass and density) have a maximum or minimum on the boundary. This means the derivative across the boundary of all three components of \mathbf{B} , ρ and ϵ is set to zero. All components of the velocity, (v_x, v_y, v_z) , are set to zero on all the boundaries.

3.1 Initial setup

3.1.1 Magnetic field

The initial analytical, non-potential magnetic field containing a single separator which we use for our non-resistive relaxation experiment is that which is discussed in Chapt. 2

$$\begin{aligned} B_x &= \frac{B_0}{L_0}(x + cxz + byz - \frac{1}{2}j_{sep}y), \\ B_y &= \frac{B_0}{L_0}((2a - c)yz - (1 + La)y + bxz + \frac{1}{2}j_{sep}x), \\ B_z &= \frac{B_0}{L_0}(a(Lz - z^2) + \frac{1}{2}cx^2 + (a - \frac{1}{2}c)y^2 + bxy). \end{aligned} \quad (3.1)$$

For the experiments discussed in this chapter we define the magnetic field and length scaling factors as $B_0 = 1$, $L_0 = 1$ and set the initial length of the separator to $L = 1$. The first experiment which will be discussed here has parameter values $a = 0.5$, $b = 0.75$, $c = 0.25$ and $j_{sep} = 1.5$. These values were chosen to satisfy all magnetic field constraints detailed in Sect. 2.3.3.

Here we begin by discussing properties of the plasma and the magnetic field before the relaxation begins. Then in Sect. 3.2 we provide a detailed description of the forces acting on the model, the magnetic skeleton and the energetics of the system before a discussion of the pressure and current accumulations in the relaxed state. We then explore the effects of varying the value of the initial current j_{sep} in Sect. 3.3.

The initial and equilibrium states of the case with initial uniform current $j_{sep} = 1.5$ will be discussed in detail here but, note, the final equilibrium configurations of all experiments discussed in this chapter have current accumulations with the same basic nature and characteristics as that of the case initially discussed.

3.1.2 Plasma

All experiments discussed in this chapter have an initial normalised uniform density of $\rho_0 = 1.5$, an initial normalised internal energy per unit mass of $\epsilon_0 = 1.5$ and an initial normalised velocity of $\mathbf{v}_0 = \mathbf{0}$ (a subscript “0” indicates an initial value). The normalised pressure is $p = \rho\epsilon(\gamma - 1)$, and hence the initial normalised pressure is

$$\begin{aligned} p_0 &= \rho_0\epsilon_0(\gamma - 1) \\ &= (1.5)(1.5)(\frac{5}{3} - 1) \\ &= 1.5. \end{aligned}$$

We normalise time in this chapter to the time it takes a fast-magnetoacoustic pulse to travel from the lower null to the upper null (i.e., to travel the length of the separator)

$$t_f = \int_0^L \frac{1}{\sqrt{c_s^2 + c_A^2(z)}} dz, \quad (3.2)$$

Table 3.1: Fast-magnetoacoustic crossing times.

	Boundary at $x = 1.0$	Boundary at $y = 1.0$	Nearest z boundary
Lower null	$t_f = 0.71$	$t_f = 0.67$	$t_f = 0.74$
Upper null	$t_f = 0.65$	$t_f = 0.74$	$t_f = 0.74$

where c_s is the sound speed ($\sqrt{\epsilon\gamma(\gamma-1)} = \sqrt{5/3}$ initially) and $c_A(z)$ is the Alfvén speed ($\sqrt{B(z)^2/\rho}$) which initially can be written analytically along the separator as $c_A(z) = B_0(a(Lz - z^2))/(L_0\sqrt{\rho})$. Hence, using the magnetic field parameters listed previously, this leads to a fast-magnetoacoustic speed, initially, of $t_f = 0.78$. We have chosen to integrate along this path as the separator is of great interest to us in this work. However, we also provide the value of t_f integrated along the path from the lower and upper nulls to the boundary at $x = 1.0$, to the boundary at $y = 1.0$ and to the nearest z boundary (which is $z = -1.0$ for the lower null and $z = 2.0$ for the upper null) for comparison (Table 3.1). Using $t_f = 0.78$ we find that the average fast-magnetoacoustic speed along the separator is equal to $c_f = 1.28$. This value is lower than the characteristic viscous speed and hence the viscosity should act to damp these waves in the system.

The mean value of the plasma beta over the entire domain is initially $\bar{\beta} = 7.8$ and the plasma beta half-way along the separator (i.e., at $x = y = 0$, $z = 0.5$) in the initial state is $\beta_L = 192$. This value is so high due to the infinite value of the plasma beta at the null points (where $\mathbf{B} = \mathbf{0}$). We require a high initial pressure ($p_0 = 1.5$), which makes the plasma beta value high, to ensure only two nulls exist in the model during the relaxation. It is possible to achieve a lower plasma beta by either increasing the initial length of the separator, L , or increasing the magnetic field scaling factor, B_0 . We have found the latter leads to an increase in null number soon after the relaxation begins. We investigate the outcome of increasing L , and hence beginning with a lower plasma beta, in Chapt. 6.

Fig. 3.1a displays contours of the plasma beta in a cut perpendicular to the separator at $z = 0.5$ at $t = 0t_f$. From this figure, and in particular from Fig. 3.1b, which displays an isosurface of the plasma beta drawn at $\beta = 50$ with the magnetic skeleton of the model, it is clear that the plasma beta is large close to the nulls and separator but is smaller away from these regions. We have also plotted, in Fig. 3.1a, the intersection of the lower and upper null’s separatrix surfaces with this cut. It is clear that these intersections are initially fairly straight. The properties of these intersections, once the relaxation has taken place, will be discussed later.

3.1.3 Initial field properties

The magnetic field of the main case, which we discuss here, contains two improper radial nulls with the following eigenvalues and eigenvectors

$$\begin{aligned} \lambda_{sl} &= -1.25, \lambda_{f_1l} = 0.5, \lambda_{f_2l} = 0.75, \mathbf{e}_{sl} = (\frac{1}{3}, 1, 0)^T, \mathbf{e}_{f_1l} = (0, 0, 1)^T, \mathbf{e}_{f_2l} = (3, 1, 0)^T, \\ \lambda_{su} &= 1.25, \lambda_{f_1u} = -0.5, \lambda_{f_2u} = -0.75, \mathbf{e}_{su} = (\frac{4}{3}, 1, 0)^T, \mathbf{e}_{f_1u} = (0, 0, 1)^T, \mathbf{e}_{f_2u} = (0, 1, 0)^T, \end{aligned}$$

where the subscripts “ s, f_1, f_2 ” refer to the spine, minor and major separatrix-surface eigenvalues and “ l, u ” refer to the lower (positive) and upper (negative) nulls, respectively.

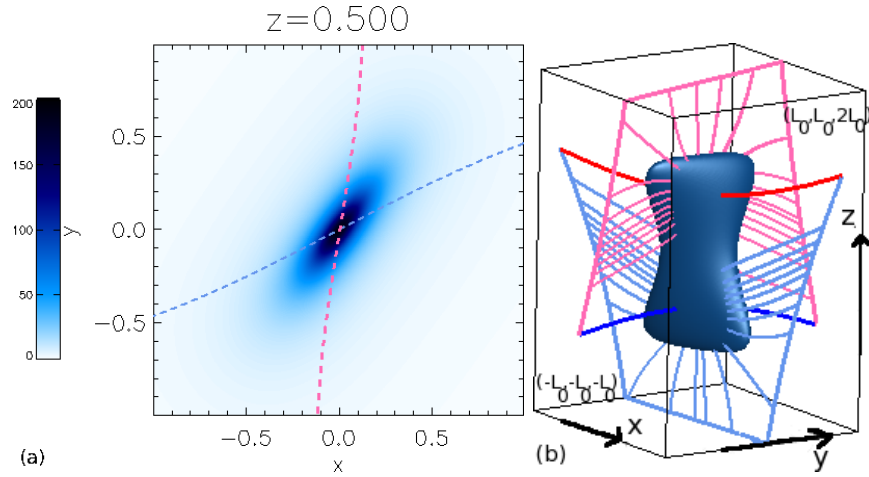


Figure 3.1: (a) Contours of the plasma beta in a cut perpendicular to the separator at $z = 0.5$ at $t = 0t_f$. Pale-blue and pink dashed lines highlight the intersection of the lower and upper null's separatrix surfaces, respectively, with these cuts. (b) Isosurface of the plasma beta, drawn at $\beta = 50$, in the initial state. The blue/red lines are the spines of the lower/upper nulls and the pale-blue/pink lines are the separatrix-surface field lines of the lower/upper nulls respectively. The solid pale-blue/pink lines indicate where the separatrix-surfaces of the nulls meet the boundaries of the box. The nulls and separator are hidden by the isosurface.

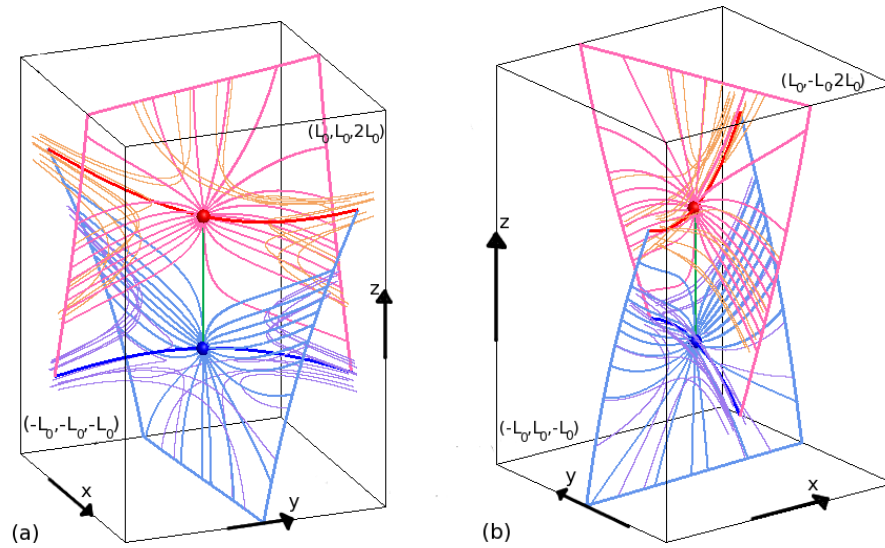


Figure 3.2: (a) and (b) display the skeleton of the initial field. The lower/upper nulls are shown as blue/red spheres with blue/red spines and pale-blue/pink separatrix-surface field lines. The nulls are joined by a green separator. General field lines are drawn around the lower/upper null's spines (lilac/orange). The pale-blue/pink thick lines indicate where the separatrix surfaces from the lower/upper null intersect the walls of the box.

The magnetic skeleton, of the initial configuration of the case with an initial uniform current $j_{sep} = 1.5$, is shown in Figs. 3.2a and 3.2b. The skeleton was found using methods described in Haynes and Parnell [2007] and Haynes and Parnell [2010] which have been discussed in Chapt. 1. General magnetic field lines (thin lilac or orange lines) are drawn from around the ends of the null's spines (thick blue or red lines) to show that the magnetic field near to the spines/separatrix surfaces run parallel to the spines/separatrix surfaces.

3.2 Results

There is an initial non-zero Lorentz force, for all the initial magnetic fields examined in this chapter, which acts perpendicular to the separator, which will cause the separatrix surfaces to fold towards each other as soon as the system is modelled numerically in a MHD experiment. In order to study the behaviour of the system, we use Lare3d (explained earlier in Chapt. 1). Since the system is not in force balance, as soon as the experiment starts, waves are launched and the system evolves under non-resistive MHD (i.e., there is no reconnection and so there is no transfer of flux between the four flux domains about the separator). The system relaxes ideally, save for the damping of waves via viscous effects. This relaxation causes current accumulations to form along the separator and on the separatrix surfaces both close to the separator and close to the boundaries at the top and bottom of the box. The latter form due to the boundary conditions which prevent the separatrix surfaces moving on them. The system evolves to what appears to be an equilibrium state by $t = 51.28t_f$ for the main experiment discussed in this chapter which has initial uniform current $j_{sep} = 1.5$.

We begin here by comparing the initial and equilibrium forces in the main experiment (Sect. 3.2.1) before discussing the skeleton of the model in the equilibrium state (Sect. 3.2.2). We then analyse the energetics of the main experiment (Sect. 3.2.3) and examine the pressure (Sect. 3.2.4) and current (Sect. 3.2.5) of the equilibrium field. In Sect. 3.3 we explore the effects that varying the value of j_{sep} has on the current layer dimensions (Sect. 3.3.1), the twist of the current layer (Sect. 3.3.2) and the behaviour of the pressure (Sect. 3.3.3) and total force (Sect. 3.3.4) along the separator, through the depth and across the width of the current layer. Finally we examine how the growth rate of the current layer varies with the value of j_{sep} (Sect. 3.3.5) before ending this chapter with a summary of our results (Sect. 3.4).

3.2.1 Comparison of the initial and final total forces

The total force, in our experiments, is the sum of the pressure force, the Lorentz force and the viscous force

$$\text{total force} = -\nabla p + \mathbf{j} \times \mathbf{B} + \mathbf{F}_\nu. \quad (3.3)$$

However, at $t = 0t_f$, the pressure is uniform everywhere and the velocity is zero so the only force acting on the field is the Lorentz force. This force is presented in Fig. 3.3, for the case with initial uniform current $j_{sep} = 1.5$, by arrows whose colour and size reflect the strength of the Lorentz force, and also its direction, in planes across the separator. The Lorentz force will act in towards the separatrix surfaces, which are also plotted in this plane at $t = 0t_f$ as dashed pale-blue and pink lines, and causes them to fold towards each

other as the experiment proceeds. Note, in Fig. 3.3b only small parts of the upper nulls separatrix surface (pink lines) intersect this cut forming only two small segments visible near the top and the bottom.

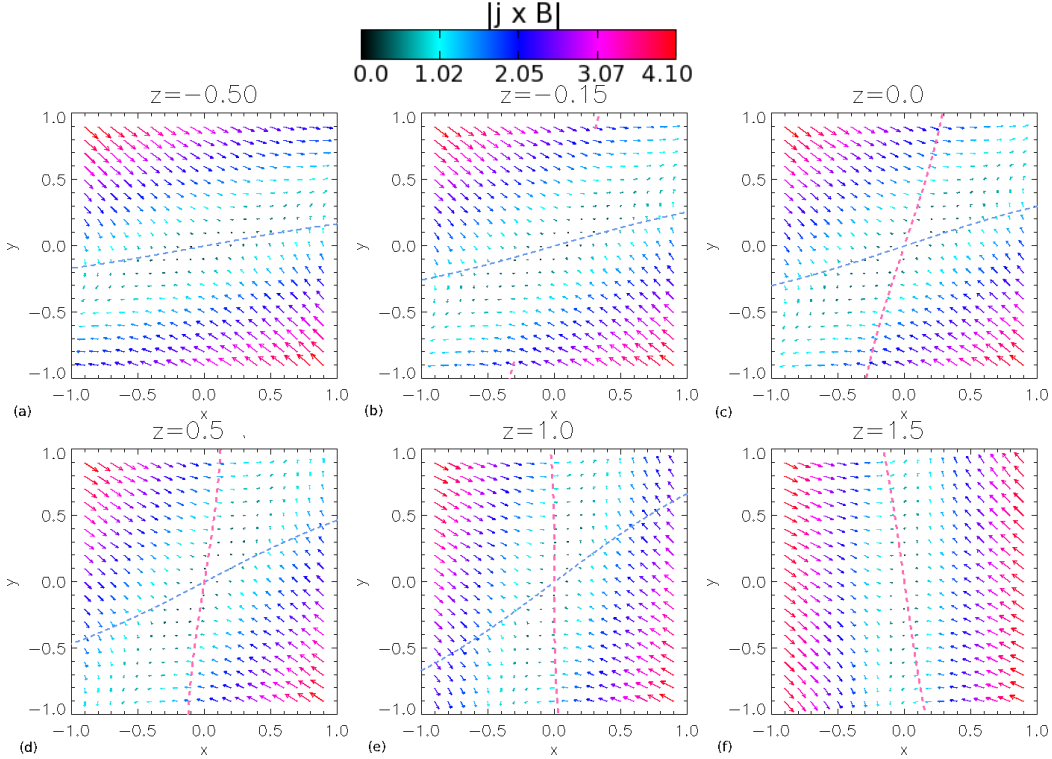


Figure 3.3: Arrows displaying the initial Lorentz force in the planes at (a) $z = -0.5$, (b) $z = -0.15$, (c) $z = 0.0$, (d) $z = 0.5$, (e) $z = 1.0$ and (f) $z = 1.5$. The arrows indicate the strength (by their size and colour) and direction of the Lorentz force in the plane. The length of the arrows has been normalised to the maximum value of $|\mathbf{j} \times \mathbf{B}|$ in the domain. The pale-blue/pink dashed lines indicate the locations where the initial separatrix surfaces from the lower/upper nulls intersect the given plane, respectively.

Fig. 3.4 displays contours of the total force in the final equilibrium which are drawn in planes perpendicular to the separator. The total force is equal to the Lorentz force plus the pressure force here. The viscous force is negligible since the velocities are small in the equilibrium. The intersections of the lower and upper null's separatrix surfaces with this cut are plotted here also for the initial magnetic field (dashed lines) and the equilibrium magnetic field (solid lines). The separatrix surfaces have folded towards each other and, particularly at the times plotted in Figs. 3.4c, 3.4d and 3.4e, the separatrix surfaces in the equilibrium field have clearly curved towards each other in agreement with the initial non-zero Lorentz force. Indeed, the two-dimensional cuts, perpendicular to the separator, reveal that the separatrix surfaces form a cusp exactly like that seen in the collapse of the magnetic field about a 2D null point [e.g., Craig and Litvinenko, 2005, Pontin and Craig, 2005, Fuentes-Fernández et al., 2011]. The cusp regions form due to the nature of the pressure which is initially uniform but is changed through the relaxation. This is

discussed in Sect. 3.2.4.

From the contours of the total force we see that the total force is zero everywhere except near the separator and along the separatrix surface of the nearest null to the plane and that the magnitude of these forces are small in comparison to the initial forces shown in Fig. 3.3 ($\sim 4\%$ of the maximum initial Lorentz force). This result is not surprising. A lack of exact force-balance in the local vicinity of topological features is found in the equilibrium field associated with collapsed 2D and 3D null points and an infinite-time collapse is seen [e.g., Klapper, 1998, Craig and Litvinenko, 2005, Fuentes-Fernández et al., 2011]. Therefore, the highly-localised, residual forces that we find suggest that separators also undergo an infinite time collapse. This is discussed further in Sect. 3.3.5.

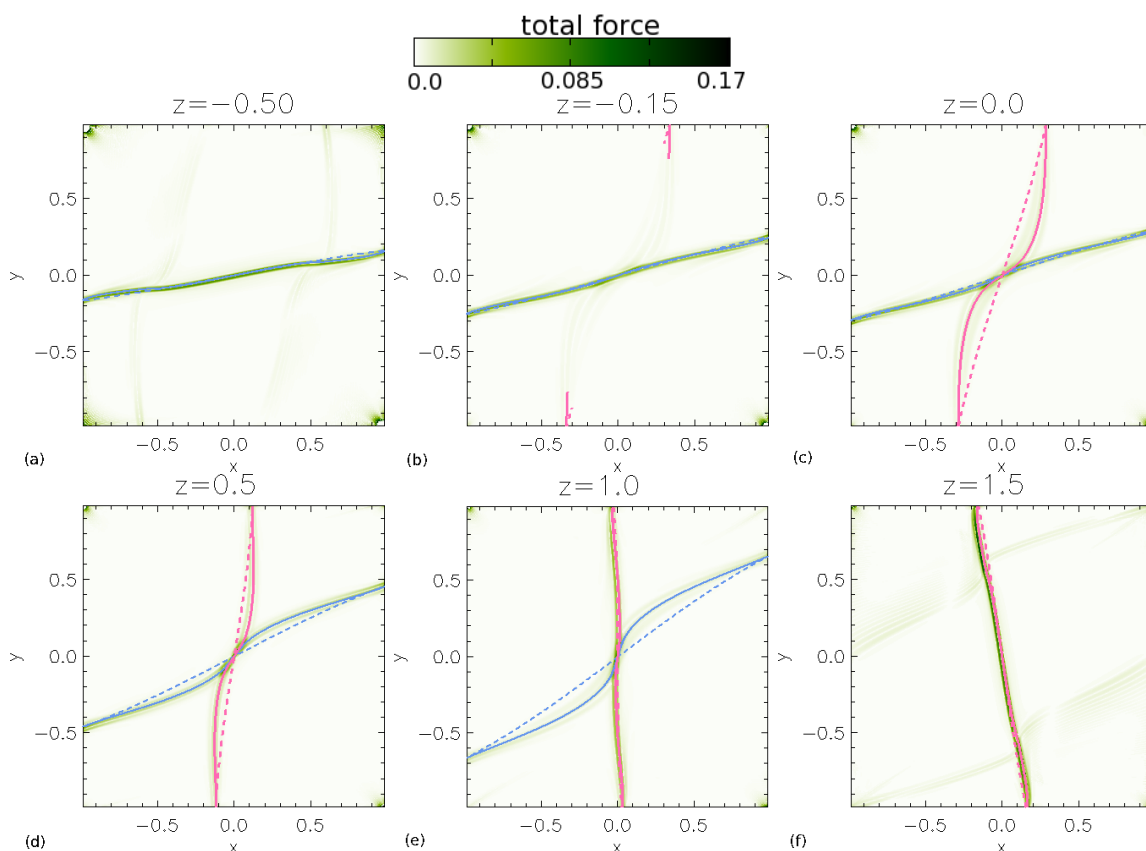


Figure 3.4: Contours of the equilibrium total force in the planes (a) $z = -0.5$, (b) $z = -0.15$, (c) $z = 0.0$, (d) $z = 0.5$, (e) $z = 1.0$ and (f) $z = 1.5$. The pale-blue/pink dashed lines indicate where the initial separatrix surfaces from the lower/upper nulls intersect the plane. The solid lines represent the positions of these separatrix surfaces once the system has reached its final equilibrium.

In the equilibrium state, the Lorentz force is zero along the z -axis (Figs. 3.5a and 3.5b) and hence along the separator (since \mathbf{j} remains parallel to the z -axis). Therefore, the total force along the separator is made up only of the pressure force, which is plotted along the z -axis in Figs. 3.5c and 3.5d. The plots in Figs. 3.5e and 3.5f confirm that the total force along the separator itself is indeed made up only of the z -component of the pressure force

along the z -axis. This force acts outwards towards the nulls from a point just over half way along the separator at $z = 0.58$.

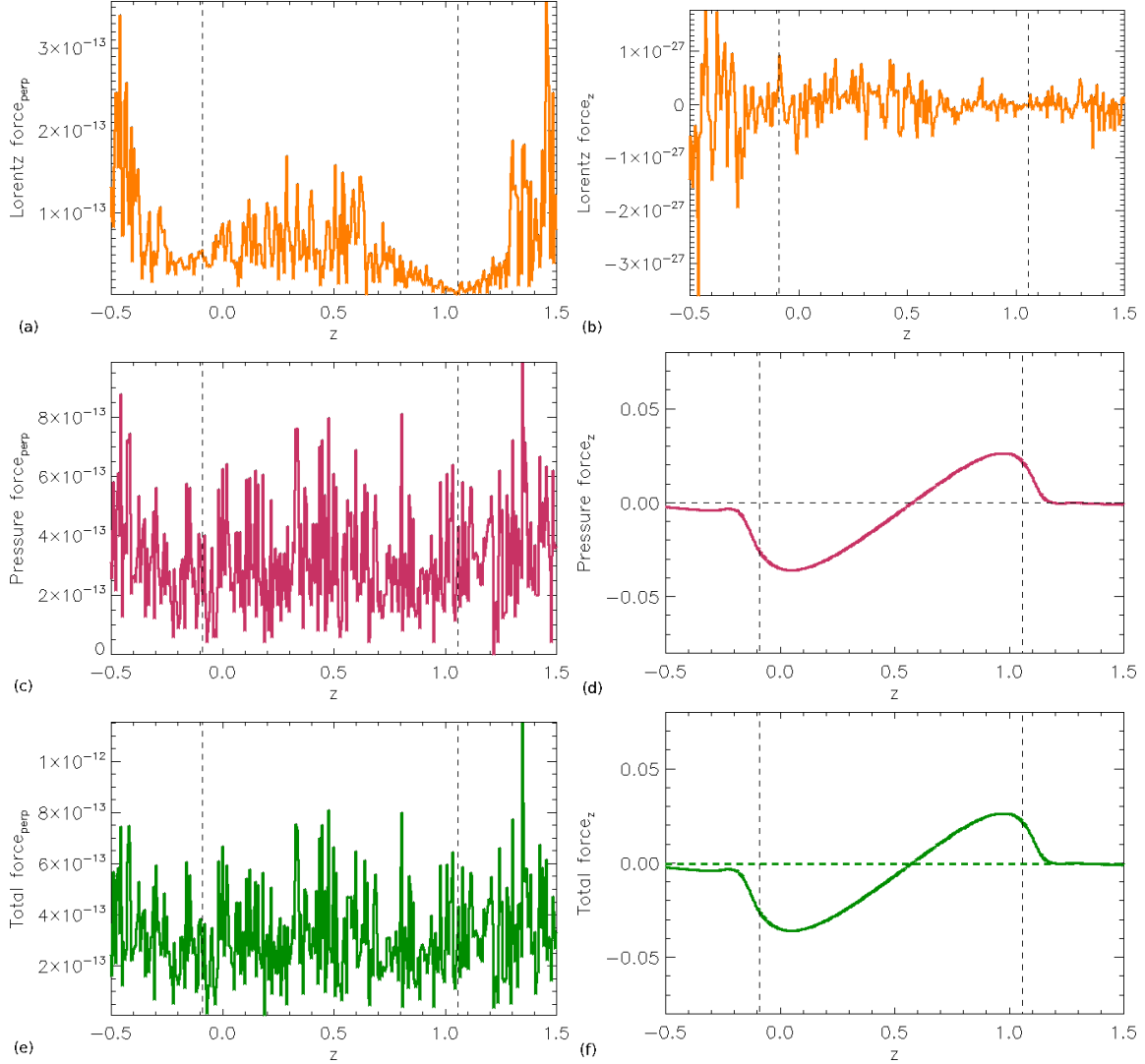


Figure 3.5: The perpendicular (left column) and parallel (right column) components of the Lorentz force ((a) and (b)), the pressure force ((c) and (d)) and the total force ((e) and (f)) along the z -axis (including the separator) of the equilibrium field.

We have investigated the total force along the length of the current layer, but also want to check its behaviour through the depth and across the width of the current layer. Along these cuts we will analyse the behaviour of various plasma parameters in a number of the following sections. Fig. 3.6 displays a cut perpendicular to the separator in the $z = 0.5$ plane through the separator current layer in the equilibrium state with filled contours of $|\mathbf{j}|$ (details of this current layer are discussed in Sect. 3.2.5) along with white lines which are plotted through the depth (solid) and across the width (dashed) of the current layer. It is along these lines, in this plane, that we will plot various parameters.

Fig. 3.7 shows that the Lorentz and pressure forces behave similarly in magnitude, but opposite in sign, through the depth and across the width of the current layer, leading

to the total force almost vanishing here, except as it crosses the current layer. These small residual net forces at the current layer indicate that the current here is still growing, as expected in the case of an infinite-time singularity. Fuentes-Fernández et al. [2011] show similar cuts displaying the total force across the width of the current layer formed after the collapse of a 2D null. These plots have the same profile as Fig. 3.7c. Residual forces for the collapse of a 2D null or a 3D separator are therefore found to lie along the current layer.

The velocities in the domain increase sharply from a value of zero at $t = 0t_f$ to a maximum value of $|\mathbf{v}| = 0.28$ throughout the domain at $t = 1.28t_f$. The mean velocity at this time is $|\bar{\mathbf{v}}| = 0.09$. The maximum and mean velocities in the system decrease after this time with the maximum value equal to $|\mathbf{v}| = 0.009$ and the mean value equal to $|\bar{\mathbf{v}}| = 0.003$ at $t = 12.82t_f$. In the equilibrium state the maximum velocity is $|\mathbf{v}| = 6 \times 10^{-4}$ and the mean value is $|\bar{\mathbf{v}}| = 9 \times 10^{-6}$.

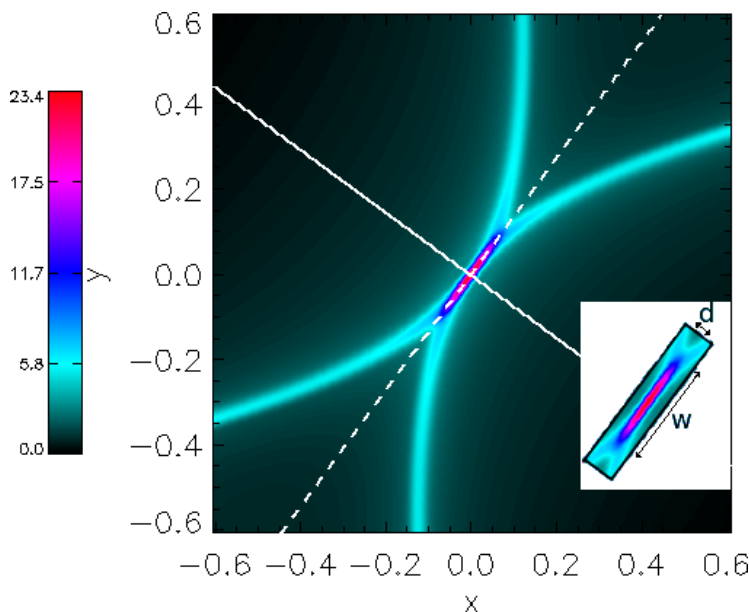


Figure 3.6: Contours of $|j|$ in a cut perpendicular to the separator at $z = 0.5$ in the equilibrium state. The strong current layer is highlighted here at the centre. Here also, a line is drawn through the depth of the current layer (solid white) and across the width of the current layer (dashed white). The inserted image highlights the depth, d , and width, w , of the current layer in this plane.

3.2.2 Equilibrium skeleton

In Fig. 3.8 the magnetic skeleton of the equilibrium field is shown along with the current layer that has formed along the separator (purple isosurface of current drawn at 20% of the maximum value of j_{\parallel} in the domain in Figs. 3.8a and 3.8b and at $j_{\parallel} = 10$ in Figs. 3.8c and 3.8d) which is discussed in Sect. 3.2.5.

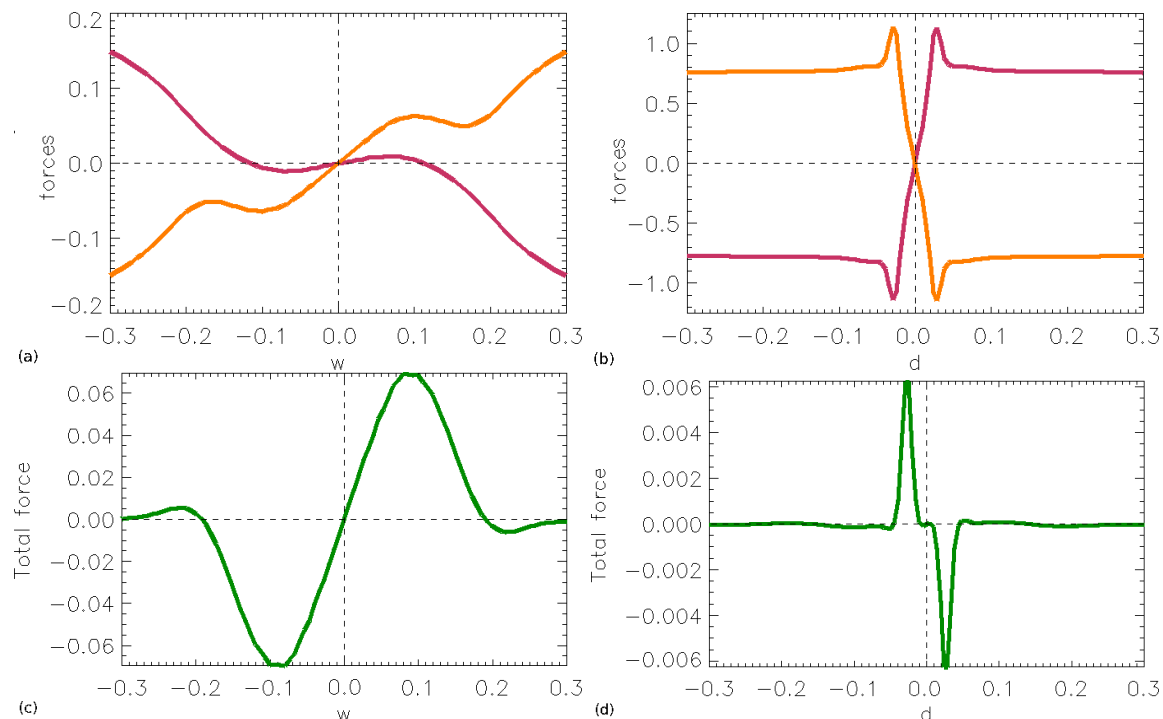


Figure 3.7: The Lorentz force (orange lines) and plasma pressure force (red lines) ((a) and (b)) and the total force ((c) and (d)) in a 1D cut across the width (left column) and through the depth (right column) of the equilibrium current layer, at $z = 0.5$.

From the isosurfaces of the current accumulation seen in Fig. 3.8 we can see a number of interesting characteristics including the fact that it is twisted and that it has the beginnings of “wing-like” features where the current enhancement extends out along one or both separatrix surfaces. These extended enhancements along the separatrix surfaces were also found in the current layers formed following the collapse of a 2D null [e.g. Fuentes-Fernández et al., 2011]. In Sect. 3.2.5, the characteristics of the current layer are studied in detail.

Only two nulls are found to exist at each time step during the relaxation and the topology of the system remains unchanged which is one indication that no numerical dissipation has occurred. The nulls initially move away from each other along the z -axis, but then come back towards each other briefly before slowly moving apart along the z -axis towards the end of the relaxation (Fig. 3.9). The rate of movement after the first oscillations die down is $1.1 \times 10^{-3} L_0/t_f$ and is $4.3 \times 10^{-4} L_0/t_f$ at the end of the relaxation. This very slow lengthening of the separator suggests that this system is following an asymptotic profile towards an equilibrium as was seen in the formation of current layers at 2D and 3D nulls, i.e., it suggests that the collapse of the separator follows an infinite-time singularity as it does for 2D and 3D nulls [e.g., Klapper, 1998, Craig and Litvinenko, 2005, Pontin and Craig, 2005, Fuentes-Fernández et al., 2011, Fuentes-Fernández and Parnell, 2012, 2013]. To check the nature of the equilibrium in our system we now look at the energetics.

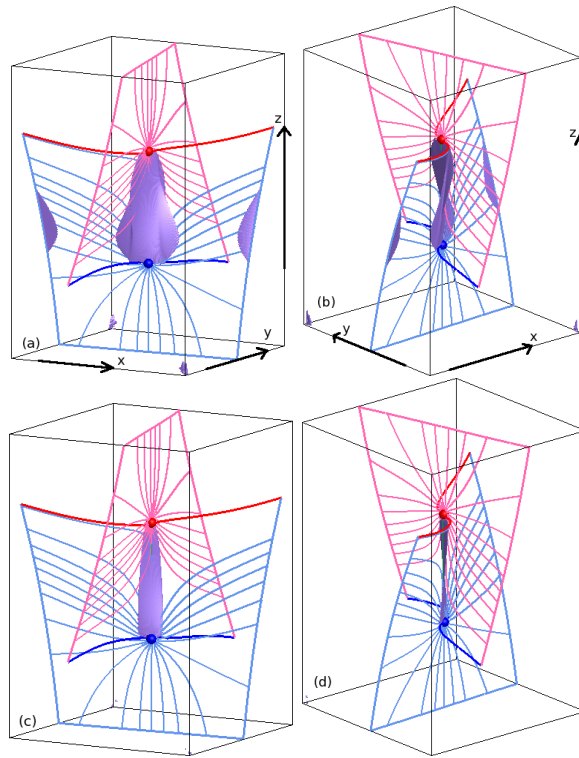


Figure 3.8: The skeleton of the equilibrium field shown from two different angles, with a purple isosurface of current drawn at (a) and (b) 20% of the maximum value of j_{\parallel} in the domain and (c) and (d) at $j_{\parallel} = 10$. The lines drawn are as detailed in Fig. 3.2. The axis for (c) is the same as shown in (a) and the axis for (d) is the same as shown in (b).

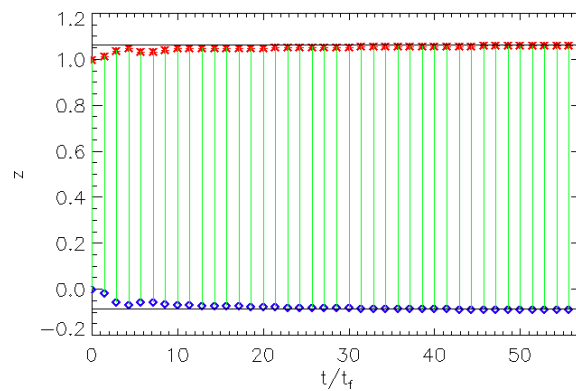


Figure 3.9: The time evolution of the locations on the z -axis of the lower (blue diamonds) and upper (red asterisks) nulls. The green solid lines represent the separator at each time and the black solid lines highlight the equilibrium z positions of the lower and upper nulls.

3.2.3 Energetics

Fig. 3.10 displays the kinetic, magnetic, internal and total energies, as well as the viscous and adiabatic heating terms integrated over the whole 3D domain as a function of time. All parameters in this figure (except the kinetic energy) have been shifted on the y -axis for representational purposes. Hence, the total energy sits at one and the internal and magnetic energies have been shifted such that the initial value of the magnetic energy matches the final value of the internal energy. This highlights the fact that all of the magnetic energy lost has, by the end of the experiment, been converted into internal energy and, hence, no magnetic energy (within the limit of numerical error) is lost due to numerical diffusion. As can be seen in Fig. 3.10 the energy conversion is equivalent to the sum of the viscous and adiabatic heating terms. To highlight this the viscous heating term is shifted on the y -axis so it starts at the same value as the internal energy and the adiabatic term is shifted to start at the final value of the viscous heating term. The viscous heating term is three times bigger than the adiabatic term indicating that most of the relaxation comes from the viscous damping of waves rather than their compression. The relaxation of

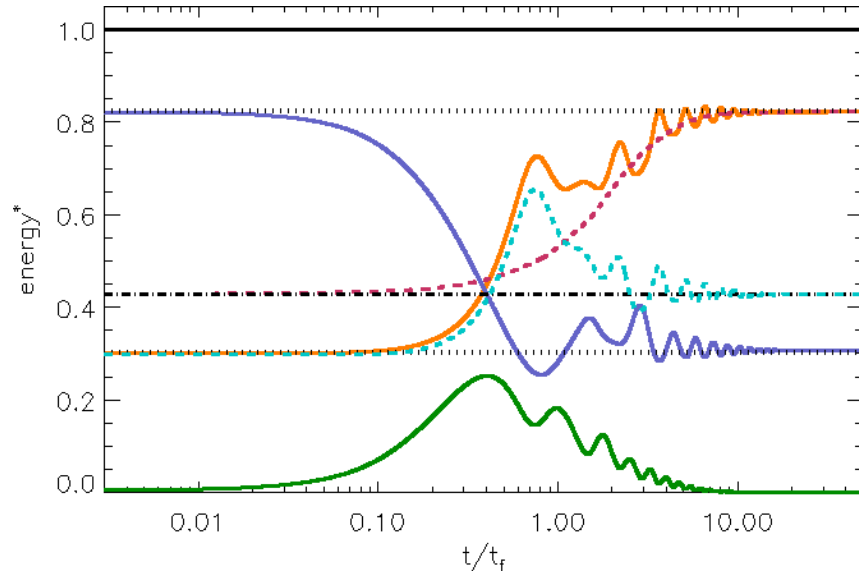


Figure 3.10: Plot of the kinetic (green), magnetic (blue), internal (orange) and total (black) energies along with the viscous (red) and adiabatic (cyan) heating terms for the relaxation with $j_{sep} = 1.5$. These energies have been scaled such that the total energy is 1.0, the initial/final magnetic energy values match the final/initial internal energy values and the adiabatic heating starts at the same value as the internal energy, and the viscous heating term starts from the final value of adiabatic heating.

the system takes place through the viscous damping of waves caused by the sudden collapse of the initial state which is not in force balance. Thus, the energy curves in Fig. 3.10 behave qualitatively as expected: magnetic energy is first converted into kinetic energy which in turn is converted into internal energy. The oscillations seen in the first 10-20 fast-mode crossing times have periods of $1t_f$ for the kinetic energy (which is proportional to v^2) and double this for the magnetic and internal energies, and since the width of the box

is $2L_0$, this suggests that the waves, launched as soon as the experiment starts, move at the fast-magnetoacoustic speed. By $t = 20t_f$, the oscillations in the different energies are basically completely damped. After this, all the energy curves maintain constant values, indicating that the system has essentially achieved an equilibrium state. The total energy is conserved throughout the run, with a standard deviation of just 0.002% of the mean, indicating that any energy losses through the boundaries or via numerical dissipation during the relaxation are negligible.

3.2.4 Pressure

In the equilibrium state, the separatrix surfaces curve creating cusp shapes about the separator, within which lie regions of high pressure and outwith which lie regions of low pressure. These cusps are shown in Fig. 3.11 which displays the pressure difference (the pressure minus the initial pressure, $p - p_0$) in various planes perpendicular to the separator. Fig. 3.12 shows (for the equilibrium of the experiment with initial current $j_{sep} = 1.5$) the 3D extent of the regions of enhanced (yellow) and diminished (blue) pressure that occur inside and outside the cusp regions about the separator, respectively.

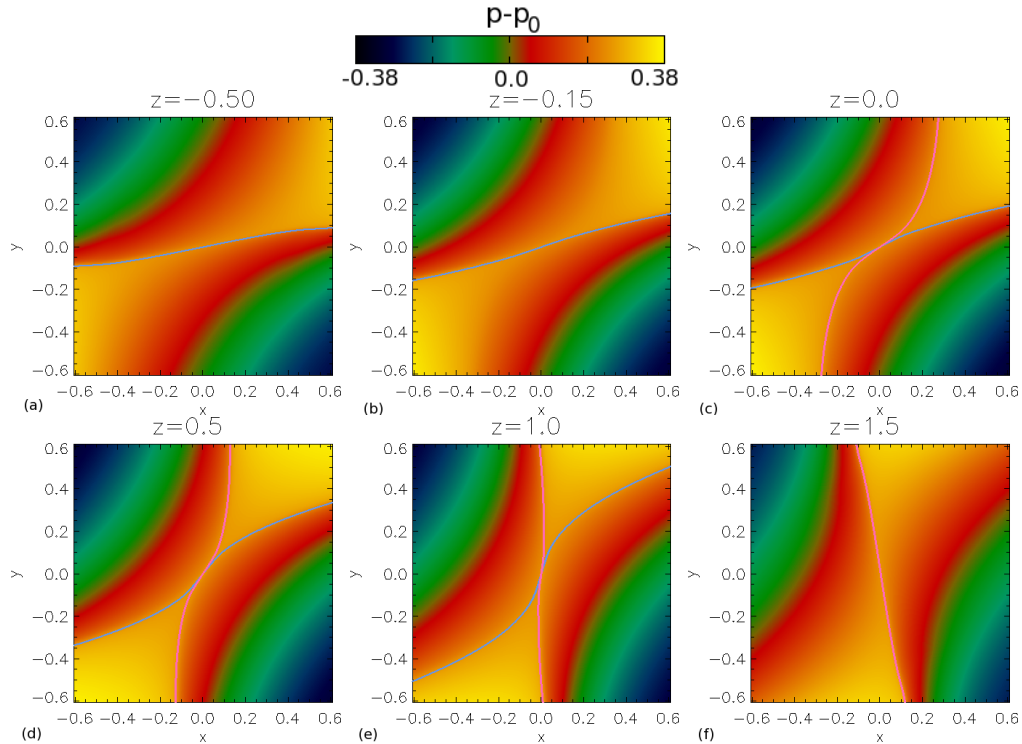


Figure 3.11: Contours of the pressure difference ($p - p_0$) in the equilibrium state in the planes (a) $z = -0.5$, (b) $z = -0.15$, (c) $z = 0.0$, (d) $z = 0.5$, (e) $z = 1.0$ and (f) $z = 1.5$. The pale blue/pink lines indicate where the separatrix surfaces from the lower/upper nulls intersect the plane.

The deformation of the separatrix surfaces into a cusp formation about the separator to create the current layer is analogous to that seen in 2D when the separatrices of a 2D null

collapse to form a current layer, [e.g., Klapper, 1998, Craig and Litvinenko, 2005, Fuentes-Fernández et al., 2011]. The formation of these cusps is due to the requirement that the total pressure (the plasma pressure plus the magnetic pressure) must balance across the separator current layer. In the two smaller domains shown in Fig. 3.11, the magnetic field approaching the current layer tends to zero whereas in the other two domains, the magnetic field approaching the current layer tends to a finite value. Therefore, it is required that the plasma pressure must be higher in the first two domains than in the other two.

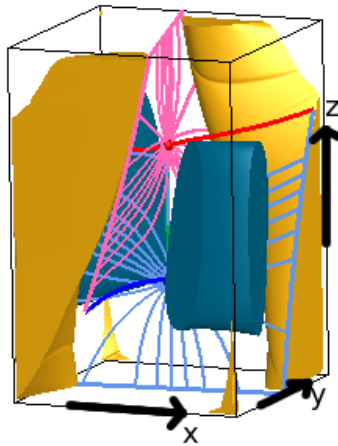


Figure 3.12: 3D plot of the skeleton of the equilibrium field with yellow/blue isosurfaces of pressure difference ($p - p_0$) drawn at 70% of the maximum positive/negative values.

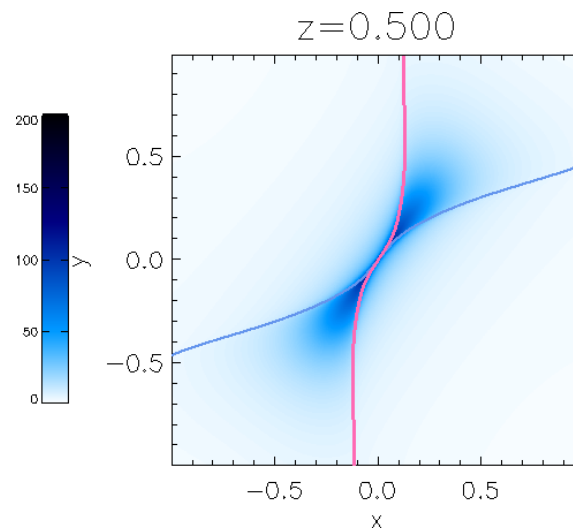


Figure 3.13: Contours of the plasma beta in the equilibrium state in a cut perpendicular to the separator at $z = 0.5$.

The variations in plasma pressure in the relaxed state lead to the value of the plasma beta varying here too. Contours of the plasma beta, drawn in a cut at $z = 0.5$ across the separator (Fig. 3.13), indicate that the plasma beta is higher within the cusp regions close

to the separator (where the pressure was higher) than outwith the cusps. The mean value of the plasma beta throughout the domain in the relaxed state is $\bar{\beta} = 6.9$ which is smaller than the initial mean value of the plasma beta ($\bar{\beta} = 7.8$).

3.2.5 Current

The value of $|\mathbf{j}|$ is strongest along, and in the vicinity of, the separator, but is also enhanced on the separatrix surfaces near the separator and at the domain boundaries (due to the boundary condition), but is small everywhere else (Fig. 3.14). The peak current in the current layer lies on the separator as shown in Fig. 3.14. Figs. 3.14a and 3.14b are drawn in planes between the bottom boundary and the lower null, Figs. 3.14c, 3.14d and 3.14e are drawn in planes perpendicular to the separator where the current layer lies and Fig. 3.14f is drawn above the upper null point. The enhanced current on both separatrix surfaces, and the sharp peak in current at the separator is clearly shown in Fig. 3.14d where the plane is about half-way along the separator. In Figs. 3.14a, 3.14b and 3.14c the current is stronger along the separatrix surface of the lower null than on the separatrix surface of the upper null. This is because the z -planes shown are just below, or close to, the lower null. Conversely, in Figs. 3.14e and 3.14f the current is stronger along the separatrix surface of the upper null than that of the lower null, as the z -planes shown are close to, or above, the upper null.

The strong current which forms the current layer and lies along the collapsed separator is visible in the contour plots of $|\mathbf{j}|$ drawn on the separatrix surfaces of the lower and upper nulls in Fig. 3.15. The value of $|\mathbf{j}|$ is clearly shown to be highest between the nulls along the collapsed separator which has formed through the non-resistive relaxation.

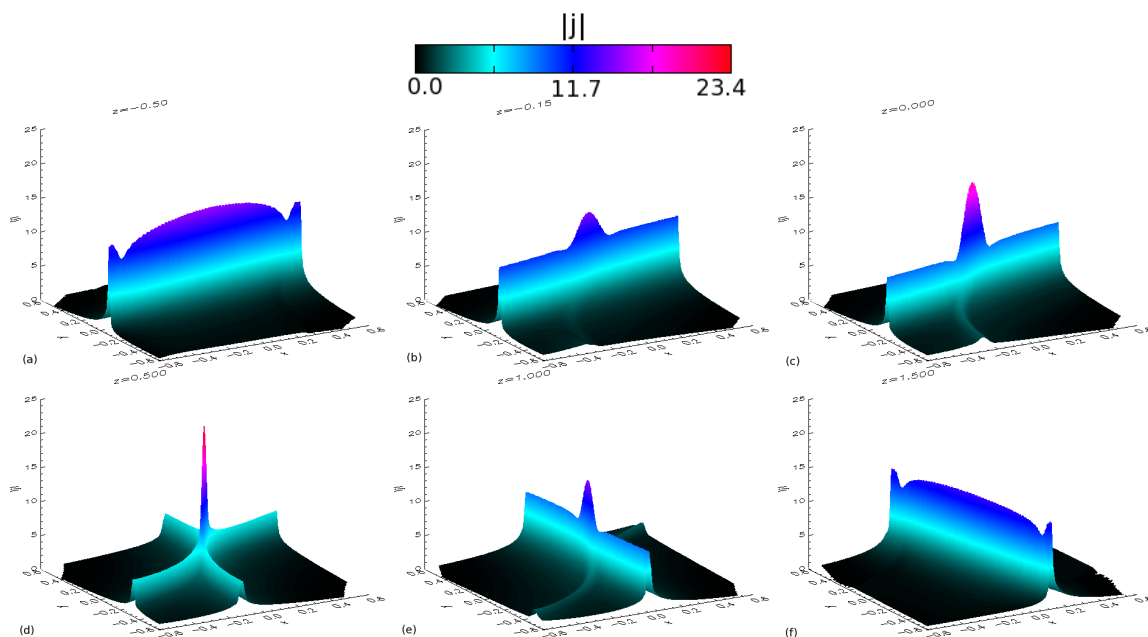


Figure 3.14: Surface plots of $|\mathbf{j}|$ in the equilibrium in the planes (a) $z = -0.5$, (b) $z = -0.15$, (c) $z = 0.0$, (d) $z = 0.5$, (e) $z = 1.0$ and (f) $z = 1.5$ for the experiment with initial uniform current $j_{sep} = 1.5$.

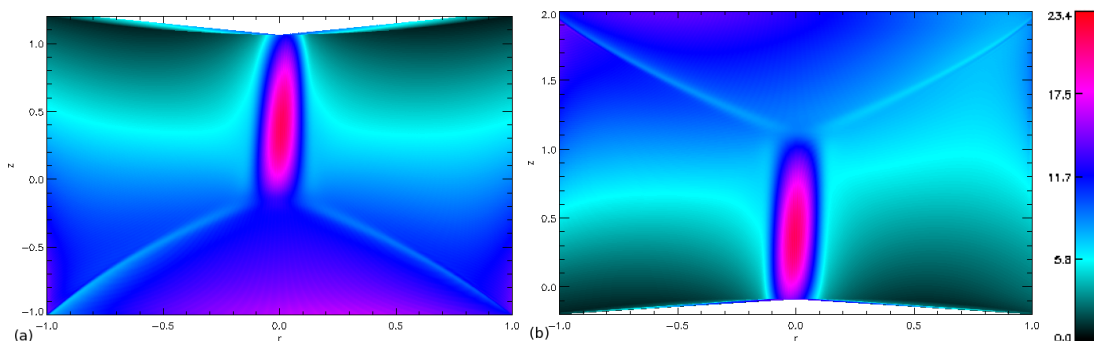


Figure 3.15: Contours of the equilibrium $|\mathbf{j}|$ on the (a) lower and (b) upper null's separatrix surfaces for the experiment with initial uniform current $j_{sep} = 1.5$.

3.3 The effects of varying j_{sep}

We now investigate the effects of varying the uniform current j_{sep} , of the initial system, where the other magnetic field parameters are $a = 0.5$, $b = 0.75$ and $c = 0.25$, and j_{sep} varies from $j_{sep} = 0.75$ up to $j_{sep} = 1.75$ (where $j_{sep} = 1.5$ has already been discussed in Sect. 3.2). The plasma parameters are the same as before, namely $\rho_0 = p_0 = 1.5$, $\epsilon_0 = 1.5$ and $\mathbf{v}_0 = \mathbf{0}$ and all times are normalised to $t_f = 0.78$. We found that values of the initial current j_{sep} which were smaller than 0.75 were too small to produce noticeable results in the final equilibrium state, and higher values than $j_{sep} = 1.75$ caused the model to suffer from the effects of numerical diffusion before the system had relaxed to an equilibrium, leading to the creation of more than two nulls. All values of j_{sep} we use here result in systems that relax through magnetic configurations that contain just two nulls at all times. In all cases, the initial nulls are improper radial nulls ($\lambda_{f1l} \neq \lambda_{f2l}$ and $\lambda_{f1u} \neq \lambda_{f2u}$).

The magnetic skeleton of the initial configurations for the four new experiments (with initial uniform currents equal to $j_{sep} = 0.75, 1.0, 1.25$ and 1.75) discussed in this section are shown in Fig. 3.16. All four experiments follow the same relaxation as that described for the case where $j_{sep} = 1.5$, which we have discussed in Sect. 3.2, with only two nulls being found in every frame and the topology remaining unchanged throughout the relaxation. The nulls move apart initially, come back towards each other slightly before slowly moving further apart through the relaxation as in the case discussed in Sect. 3.2. This indicates that all four new experiments are likely to be undergoing the same type of infinite-time collapse seen in the case already discussed.

The final equilibrium skeletons of the four new experiments, found after the systems have undergone non-resistive MHD relaxation, are shown in Fig. 3.17. The top row in this figure shows the MHS equilibrium skeletons with an isosurface of j_{\parallel} drawn on at 20% of the maximum value in each case. This highlights that a twisted current layer has formed in the final equilibrium of all four new experiments, the twistedness of which appears to depend on the initial current j_{sep} (see Sect. 3.3.2 for more details). There is also some enhanced current on the separatrix surfaces near the boundaries, but the values of j_{\parallel} here are small. The lower row in Fig. 3.17 shows the MHS equilibrium skeletons with an isosurface of current drawn at $j_{\parallel} = 10$ for comparison. Fig. 3.17e does not contain any

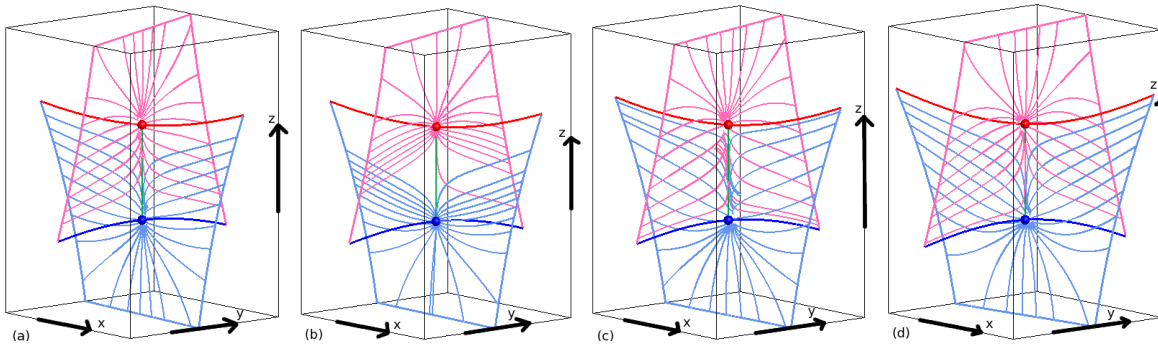


Figure 3.16: Skeleton of the initial magnetic fields for the experiments with initial uniform current (a) $j_{sep} = 0.75$, (b) $j_{sep} = 1.0$, (c) $j_{sep} = 1.25$ and (d) $j_{sep} = 1.75$. All lines are as detailed in Fig. 3.2.

isosurface since the value of j_{\parallel} never reaches 10 in this experiment. The isosurfaces of $j_{\parallel} = 10$ are shown to grow stronger along the separator as j_{sep} is increased indicating that the strength of the current in the current layer increases with j_{sep} .

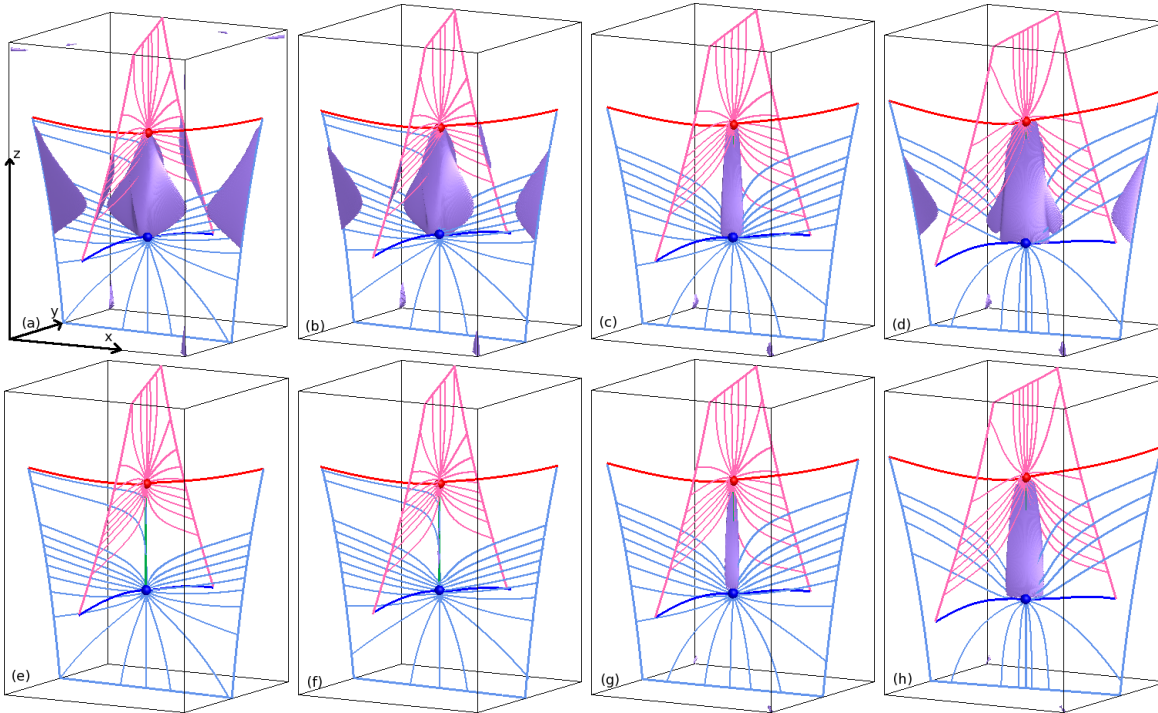


Figure 3.17: Skeletons of the final equilibrium magnetic fields for experiments with initial current (a) and (e) $j_{sep} = 0.75$, (b) and (f) $j_{sep} = 1.0$, (c) and (g) $j_{sep} = 1.25$ and (d) and (h) $j_{sep} = 1.75$. All lines are as detailed in Fig. 3.2. The top row have purple isosurfaces drawn at 20% of the maximum value of j_{\parallel} in each domain and the bottom row have purple isosurfaces drawn at $j_{\parallel} = 10$, except for (e) since j_{\parallel} never reaches this value in this experiment. The axis drawn in (a) applies to all plots here.

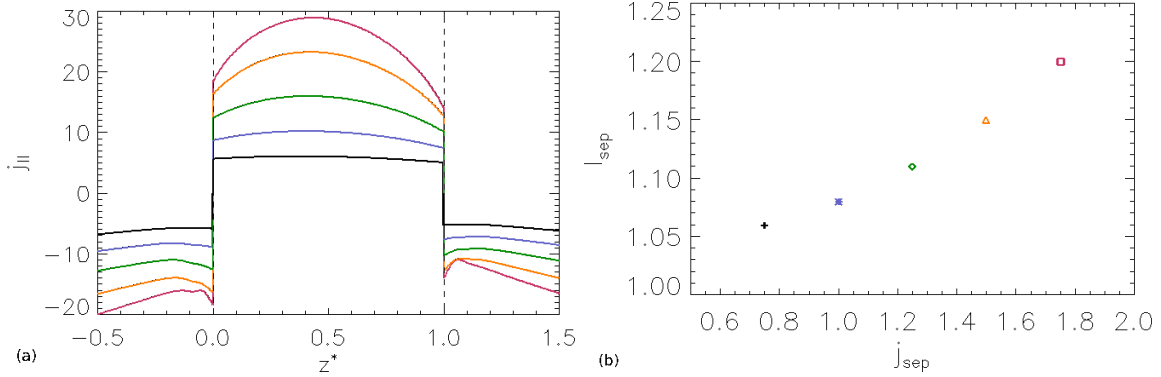


Figure 3.18: Plots of (a) j_{\parallel} along the z^* -axis (the z -axis normalised such that the separator lies between $z^* = 0$ and $z^* = 1$) and (b) the length of the equilibrium skeleton against j_{sep} for experiments with $j_{sep} = 0.75$ (black), $j_{sep} = 1.0$ (blue), $j_{sep} = 1.25$ (green), $j_{sep} = 1.5$ (orange) and $j_{sep} = 1.75$ (red).

3.3.1 Current layer dimensions

In order to determine the dimensions of the current layer, we need to define where it starts and ends. In Fig. 3.18a, the distribution of the parallel current in the equilibrium along the z^* -axis for all five experiments is plotted. The z -axis has been normalised in this figure, and in subsequent figures, for each experiment so the nulls are located at $z^* = 0$ and $z^* = L(= 1)$ in every case. Thus, the separator always has a length of one according to $z^* = (z - z_{ln})/l_{sep}$ where z_{ln} is the z -coordinate of the lower null and l_{sep} is the length of the separator in the equilibrium field. The parallel current, j_{\parallel} , along the z^* -axis is positive within the separator, but drops sharply at the nulls becoming negative in sign outside the separator. These negative values increase slightly before decreasing again away from the separator. The strong currents at the top and bottom boundaries are a result of the line-tied boundary conditions on the magnetic field which prevent the separatrix surfaces from moving. The local minima in current magnitude just outside the separator, in the experiments with the largest initial currents, suggest that the separator current layers have reverse currents at their ends. Although not commonly discussed, reverse currents have also been found associated with current layers formed at 2D null points [e.g., Titov and Priest, 1993, Bungey and Priest, 1995].

The parallel current along the z^* -axis (Fig. 3.18a) has an asymmetric profile, with a greater value as you approach the lower null from within the separator than as you approach the upper null from within the separator, in all experiments. We suspect this is due to asymmetries in the initial field and investigate this further in Chapt. 4.

Therefore, the length of the current layer is defined here as the distance between the two null points (i.e., the length of the equilibrium separator). These are also the points at which the current changes sign. This means we do not include the reverse current regions when considering the length of the separator. The equilibrium separator lengthens as the z positions of the lower and upper nulls move further apart as j_{sep} is increased (Fig. 3.18b).

If the initial current tended to zero, the null points would not move apart and the separator would maintain length L . The growth of the current layer indicates that as a current layer is formed the separator itself can be lengthened significantly. The amount

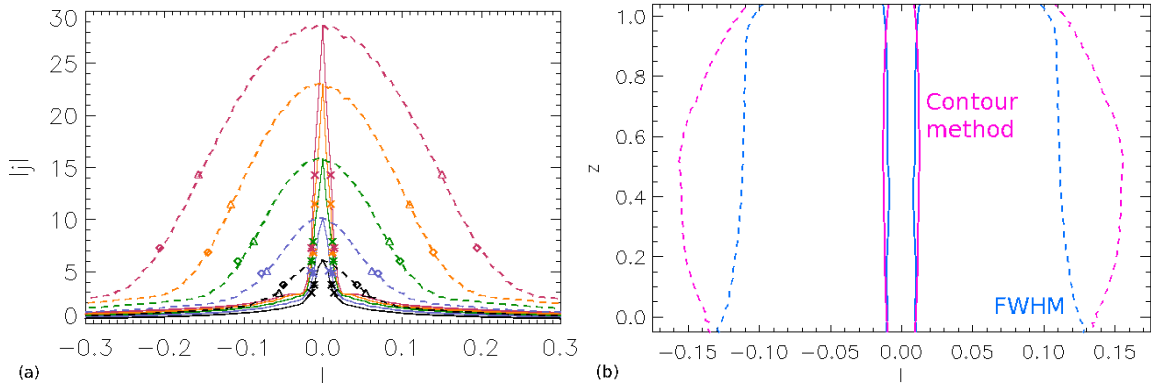


Figure 3.19: Plot of (a) $|j|$ through the depth (solid lines) and across the width (dashed lines) of the current layer, in the cut at $z = 0.5$ across the separator. The asterisks and diamonds represent the values of the current contour used to determine the depth and the width of the current layer at this cut (for the contour method) and the crosses and triangles (for the FWHM method), respectively. The colours represent experiments with initial uniform current $j_{sep} = 0.75$ (black), $j_{sep} = 1.0$ (blue), $j_{sep} = 1.25$ (green), $j_{sep} = 1.5$ (orange) and $j_{sep} = 1.75$ (red). (b) Outline of the width (dashed) and depth (solid) of the current layer using the contour method (pink lines) and the FWHM method (blue lines) for the experiment with $j_{sep} = 1.5$.

by which it extends will depend not just on the current accumulated, but also on the properties of the plasma and the velocity flows within the system.

Defining the width and depth of the current layer is not trivial since the current gradually decreases rather than abruptly stops (Fig. 3.19a). In Fig. 3.19a, 1D slices of $|j|$ are plotted in the $z = 0.5$ plane, through the depth (solid) and across the width (dashed) of the current layer for all five experiments. The 1D slices of $|j|$ through the depth of the current layer show significantly enhanced currents forming a narrow peak about the separator. Elsewhere the current is small.

We consider two approaches for measuring the depth and width of the current layer; counting the current down to the saddle point and using the full width at half maximum. The first method (which we shall call the contour method) involves examining contours of $|j|$, in cuts perpendicular to the separator across the current layer. We then plot a contour in each cut at a value of $|j|$ which only outlines the current layer and not the enhanced current along the separatrix surfaces. This contour looks elliptical in nature and we define the largest diameter of this contour to be the current-layer width, whilst the smallest diameter is defined as the current-layer depth. In other words, we count only the current down to the saddle point of $|j|$ to pick out the current layer. Once the level of the contour has been found for all perpendicular cuts through the separator, the width and depth of the current layer, along the length of the separator, can be determined. The values of the current layer depth and width, at $z = 0.5$, found using this method are highlighted in Fig. 3.19a by the asterisks (depth) and diamonds (width).

The second method uses the full width at half maximum (FWHM) of the current plotted in Fig. 3.19a. Fig. 3.19a displays the values of the current layer depth and width,

in the plane at $z = 0.5$ using this method, plotted as crosses (depth) and triangles (width) but, note, the value of the maximum varies in each cut. Fig. 3.19b compares the current layer widths and depths, found using the contour method and the FWHM method for the experiment where $j_{sep} = 1.5$. We have chosen the contour method as the preferred method to proceed with as it was found that the contour level, using the contour method, in different z -cuts varied less than when using the FWHM method and the contour method accounts for more current in the current layer than the FWHM method.

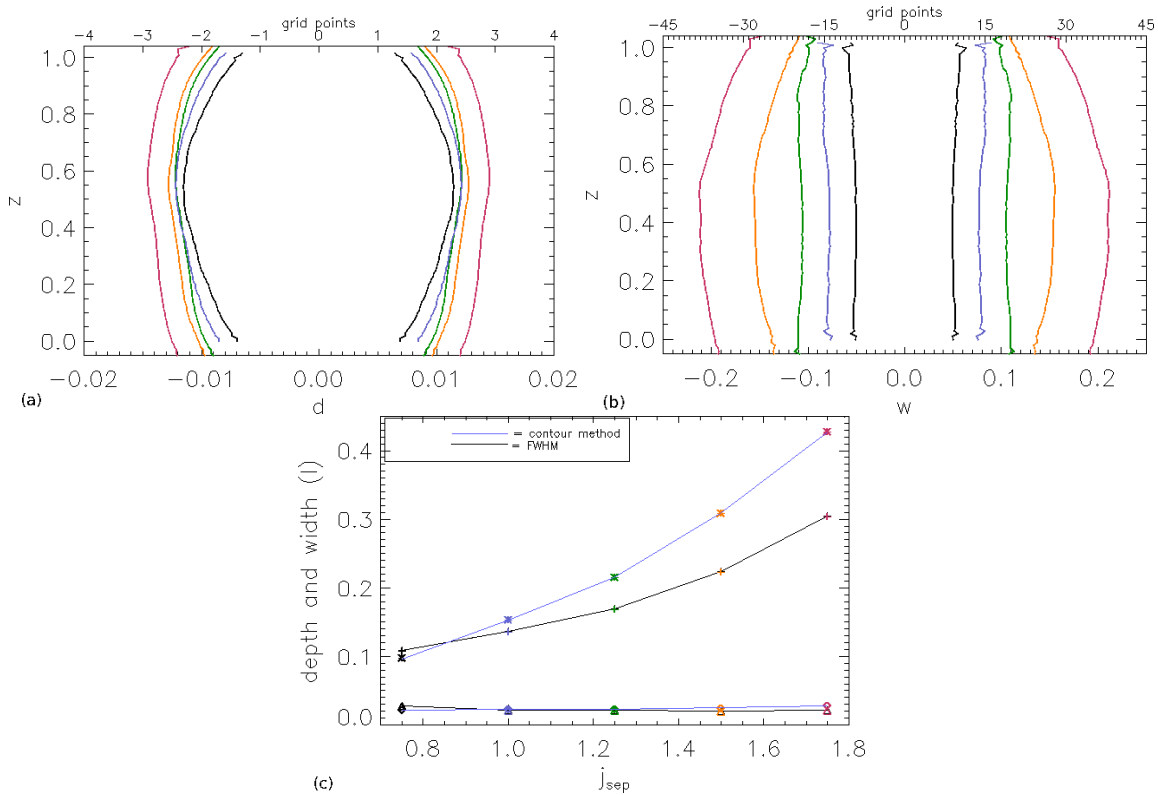


Figure 3.20: Outline of the (a) depth and (b) width of the current layer defined using the contour method. (c) Depth (diamonds) and width (asterisks) of the current layer defined using the contour method at $z = 0.5$. Crosses and triangles represent the width and depth, respectively, found using the FWHM method at $z = 0.5$. The blue/black lines join the widths and depths found using the contour/FWHM methods. The colours represent the results for the experiments with initial current $j_{sep} = 0.75$ (black), $j_{sep} = 1.0$ (blue), $j_{sep} = 1.25$ (green), $j_{sep} = 1.5$ (orange) and $j_{sep} = 1.75$ (red).

In Figs. 3.20a and 3.20b, the edges of the current layer through the depth and across the width determined using the contour method are plotted, against z , for the different experiments. The depths seem to remain pretty constant along the length of the current layer. The widths of the current layers, however, appear to decrease slightly near the nulls at the ends of the separator, for the experiments with higher j_{sep} . The width of the current layer clearly increases with j_{sep} , as does the depth, but by a smaller amount.

In order to determine how the width and depth of the current layers depend on the initial current, we plot the depth and width, as determined in the $z = 0.5$ plane, against

j_{sep} (Fig. 3.20c). The values of the width and the depth calculated using both the contour and the FWHM method are plotted here. While the FWHM method does not pick out a lot of the current seen in the sharp peak near the current layer it does, however, indicate that, the higher the initial current j_{sep} is, the closer the equilibrium current layer appears to be to a singularity, as the depth of the current layer is seen to decrease with increasing initial current.

Using the contour method of counting the current down to the saddle point, the depth of the current layer grows with initial current j_{sep} (Fig. 3.20c). Similar behaviour is observed for $|j|$ across the width of the current layer, but for all finite initial currents j_{sep} , the width of the current layer is much greater than the depth. The rate of increase in width grows with j_{sep} . The width of the current layer is found to be around $5.7j_{sep}$ bigger than the depth for $j_{sep} = 0.75$, $6.3j_{sep}$ bigger for $j_{sep} = 1.0$, $7.2j_{sep}$ bigger for $j_{sep} = 1.25$, around $8.3j_{sep}$ bigger for $j_{sep} = 1.5$ and around $8.7j_{sep}$ times for $j_{sep} = 1.75$ in the plane $z = 0.5$. Note, that the values of width and depth plotted in Fig. 3.20c for the experiment with initial current $j_{sep} = 1.75$, are plotted at an earlier time than for the other experiments so this experiment is not quite as relaxed as the others.

3.3.2 Current layer twist

All the surface plots in Fig. 3.14 have the same orientation, but it is clear that the separatrix surfaces and the current layer are not orientated the same way in each cut. Indeed, as z varies, the current layer rotates, as already mentioned in Sects. 3.2.2 and 3.3. The twisting of the current layer along the separator is highlighted in Figs. 3.8 and 3.17 which show the current layers in 3D as a purple isosurface drawn at 20% of the maximum value of j_{\parallel} in each experiment. The angle through which the current layer twists between the lower and upper nulls increases with j_{sep} (Fig. 3.21) and appears to be tending towards an angle of $\pi/4$ radians as j_{sep} increases. Note, however, that the experiment with $j_{sep} = 1.75$

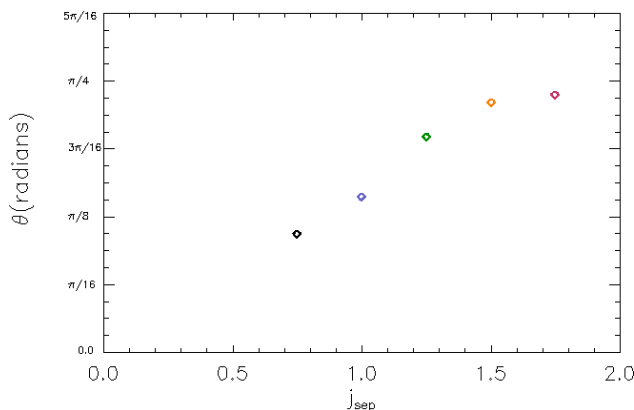


Figure 3.21: Angle, θ , through which the current layer twists for experiments with initial current $j_{sep} = 0.75$ (black), $j_{sep} = 1.0$ (blue), $j_{sep} = 1.25$ (green), $j_{sep} = 1.5$ (orange) and $j_{sep} = 1.75$ (red).

was not relaxed for as long as the other experiments and so the angle of twist for this experiment's current layer may have been greater if it could have been relaxed for longer.

3.3.3 Pressure along the length, through the depth and across the width of the current layer

The MHS equilibria which have formed through the non-resistive MHD relaxation all display the same distribution of plasma pressure: enhanced pressure lies within cusp regions about the current layer and diminished pressure lies outwith these cusps. This distribution comes about due to the need for total pressure balance; the plasma pressure, p , plus the magnetic pressure, $B^2/2$, must be constant across the current layer in an equilibrium state. It is believed in 2D MHS equilibria, that the total pressure must balance across the current layer. Hence, to check for pressure balance across the width and through the depth of our equilibrium current layer, we plot the sum of the plasma and magnetic pressures here. The total pressure balances where the magnetic tension is zero.

Plotting the plasma pressure through the depth of the current layer, in the plane $z = 0.5$, we see a peak at the separator, however, plotting the plasma pressure across its width we see almost constant values (Fig. 3.22a). This behaviour was observed in Fig. 3.11 also. The magnitude of the plasma pressure through the depth and across the width of the current layer increases with the initial value j_{sep} .

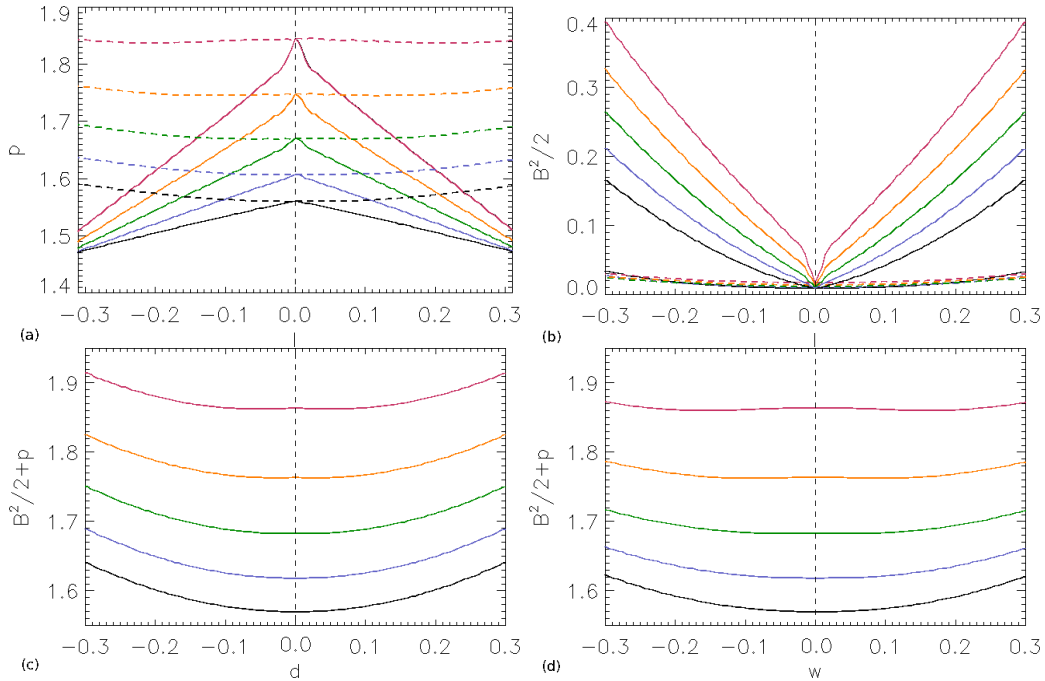


Figure 3.22: Plots of (a) the plasma pressure and (b) the magnetic pressure through the depth (solid lines) and across the width (dashed lines) of the current layer and the sum of the plasma and magnetic pressures (c) through the depth and (d) across the width of the current layer in the cut at $z = 0.5$ across the separator, for experiments with initial uniform current $j_{sep} = 0.75$ (black), $j_{sep} = 1.0$ (blue), $j_{sep} = 1.25$ (green), $j_{sep} = 1.5$ (orange) and $j_{sep} = 1.75$ (red).

The magnetic pressure behaves in an opposite manner to the plasma pressure through

the depth of the current layer where a minimum occurs at the separator (Fig. 3.22b). The magnitude of the magnetic pressure through the depth increases as j_{sep} is increased. Across the width of the current layer, the magnetic pressure is fairly constant, as was the plasma pressure, however, increasing j_{sep} does not greatly vary the magnitude of magnetic pressure here.

Figs. 3.22c and 3.22d display the total pressure (plasma pressure plus magnetic pressure) through the depth and across the width of the current layer, respectively, for all five experiments. Here, although the magnitude of the total pressure increases as j_{sep} increases, pressure balance is achieved across the equilibrium current layer (at the position of the separator) for all five experiments.

We now investigate the plasma pressure, magnetic pressure and the total pressure plotted along the length of the current layer, i.e., along the separator. The value of the plasma pressure in the equilibrium state along the z^* -axis is plotted in Fig. 3.23a for all five experiments where j_{sep} is varied. Here, it is clear that, regardless of the initial value

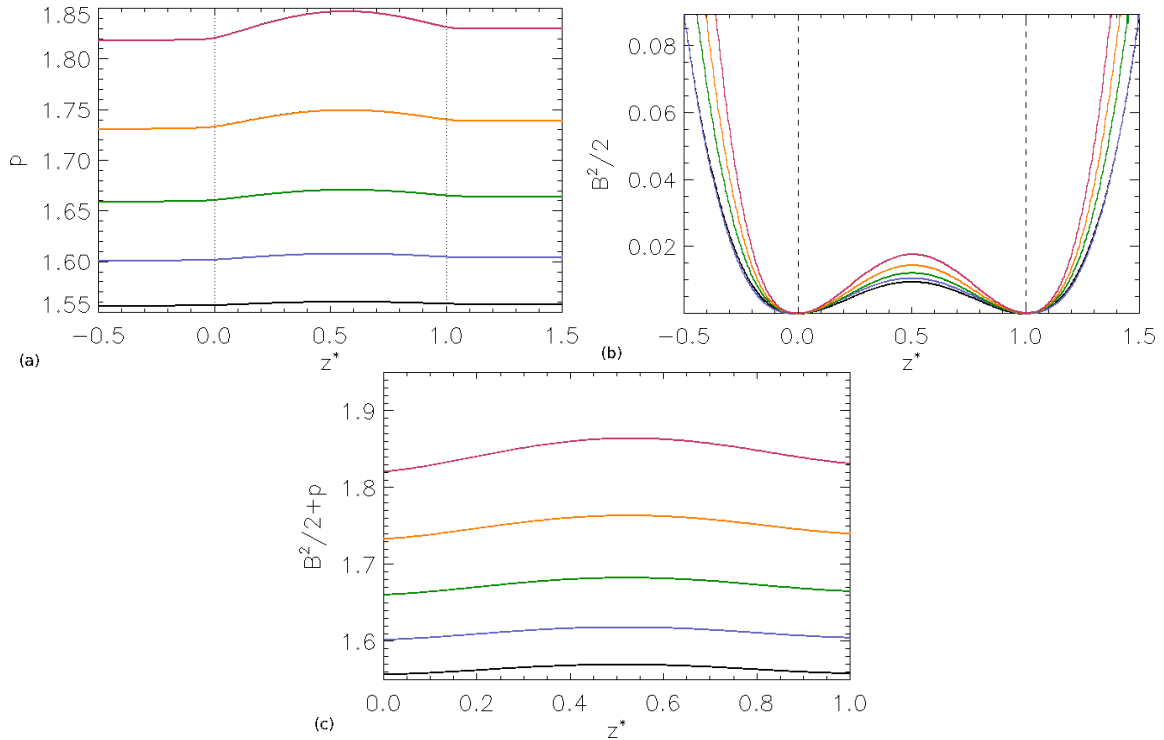


Figure 3.23: Plots of (a) the plasma pressure and (b) the magnetic pressure along the z^* -axis (the z -axis normalised such that the separator lies between $z^* = 0$ and $z^* = 1$) and (c) the sum of the magnetic and plasma pressures along the normalised separator for experiments with initial uniform current $j_{sep} = 0.75$ (black), $j_{sep} = 1.0$ (blue), $j_{sep} = 1.25$ (green), $j_{sep} = 1.5$ (orange) and $j_{sep} = 1.75$ (red).

of j_{sep} , the behaviour of the pressure along the separator is the same: (i) the pressure is largest at some point about half way along the separator; (ii) is higher at the upper null than at the lower null and (iii) is fairly constant outwith the separator. We do note, however, that the magnitude of the final equilibrium pressure increases as the value of the

initial current, j_{sep} , is increased.

We find also that regardless of the initial value of j_{sep} , the magnetic pressure along the separator behaves the same (Fig. 3.23b). The magnetic pressure vanishes at the nulls (where $\mathbf{B} = \mathbf{0}$) and peaks along the separator at $z^* = 0.5$ with the magnitude increasing with the initial value of j_{sep} . Outwith the separator, the magnetic pressure increases away from the nulls towards the boundaries along the z -axis. The plasma pressure is greater than the magnetic pressure for all values of j_{sep} along the separator.

We do not expect there to be pressure balance along the current layer, since a component of the magnetic tension force exists here. The Lorentz force does not have a component parallel to the separator since $\mathbf{B} \cdot (\mathbf{j} \times \mathbf{B}) = \mathbf{0}$, hence, the component of the magnetic pressure force parallel to the magnetic field must balance with the component of the magnetic tension force parallel to the field. Fig. 3.23c shows the plasma pressure plus the magnetic pressure plotted along the normalised separator for all five experiments where j_{sep} is varied. This figure highlights that pressure balance is indeed not achieved along the separator.

3.3.4 Total force along the length, through the depth and across the width of the current layer

As already seen from our discussion of the main experiment (Fig. 3.4), the total force vanishes everywhere except across the separator and on the separatrix surfaces. This holds true for all the experiments here.

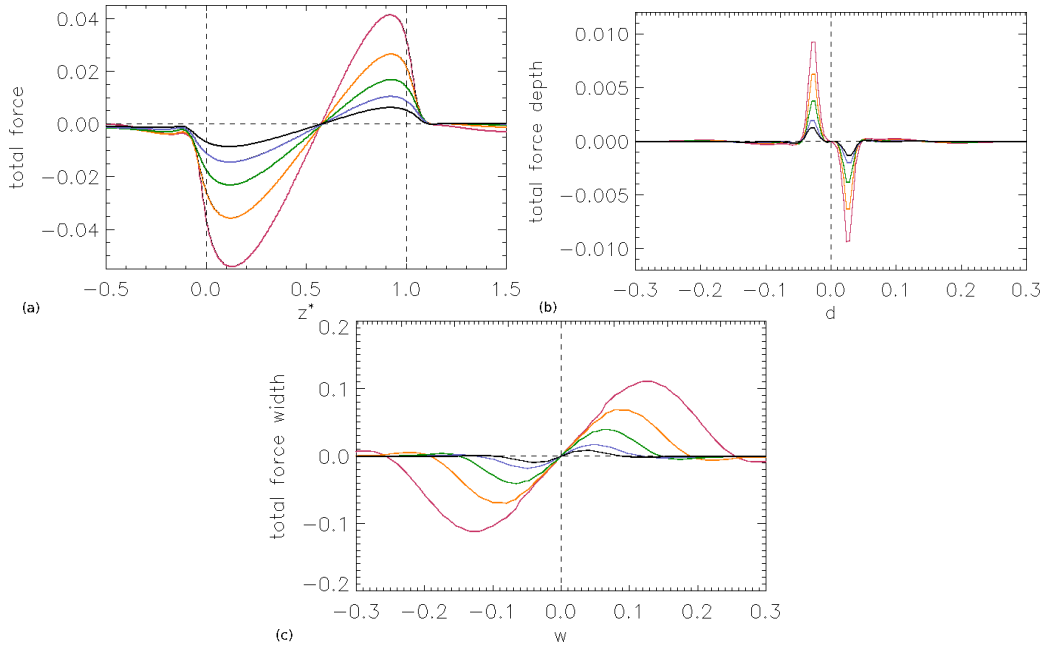


Figure 3.24: The total force (a) along the z^* -axis (the z -axis normalised such that the separator lies between $z^* = 0$ and $z^* = 1$), (b) in a cut through the depth and (c) across the width of the current layer in the plane $z = 0.5$ for initial current $j_{sep} = 0.75$ (black), $j_{sep} = 1.0$ (blue), $j_{sep} = 1.25$ (green), $j_{sep} = 1.5$ (orange) and $j_{sep} = 1.75$ (red).

As already mentioned, the Lorentz force vanishes along the separator which means that the total force here is equivalent to the pressure force (Fig. 3.24a). The behaviour of the total force along the z^* -axis in the final equilibrium state is the same for each initial j_{sep} , but the magnitude of the maxima and minima increase with j_{sep} . Indeed, the total force along the separator acts outwards, from the same point, just over half way along the separator (i.e. from the location of the plasma-pressure maxima), towards both nulls in all experiments.

Fig. 3.24b shows that in all the experiments the total force through the depth of the current layer acts inwards towards the separator such as to squeeze the current layer thinner. From Fig. 3.24c, we can see that the total force across the width acts outwards away from the separator, thus acting to widen the current layer. Naturally, the total force increases with increasing initial current j_{sep} . The behaviour of the total force in the perpendicular cut through the separator is the same as that seen in current layers formed from the collapse of a 2D null [Fuentes-Fernández et al., 2011].

3.3.5 Growth rate of the current layer

The current layer is not yet in equilibrium, as evidenced by the small, non-zero, and highly localised forces about the separator. It is possible that the current layer is undergoing an infinite-time collapse. This type of collapse has been seen in the collapse of 2D and 3D null points [Klapper, 1998, Pontin and Craig, 2005, Fuentes-Fernández et al., 2011, Fuentes-Fernández and Parnell, 2012, 2013].

In Fig. 3.25 we have plotted the maximum value of $|\mathbf{j}|$ along the separator at each time step, for all five experiments examined in this chapter. This figure shows that the current slowly grows in time throughout the relaxation, and evolves according to

$$|\mathbf{j}| = j_{sep} \left(1 + a_0 \frac{t}{t_f} \right)^{a_1}. \quad (3.4)$$

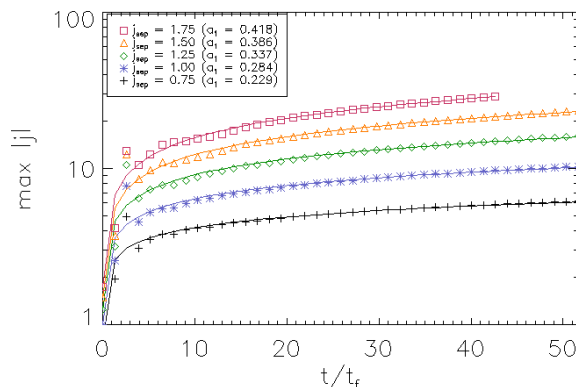


Figure 3.25: Maximum values of $|\mathbf{j}|$ along the separator as a function of time with curves of Eq. 3.4 for experiments with initial current $j_{sep} = 0.75$ (black), $j_{sep} = 1.0$ (blue), $j_{sep} = 1.25$ (green), $j_{sep} = 1.5$ (red) and $j_{sep} = 1.75$ (orange).

This is the same form of growth seen in the collapse of 2D and 3D nulls. Since we have only followed the time evolution for one order of magnitude increase in time, we can

not say definitely that the system is undergoing an infinite-time collapse but the form of growth is suggestive of this. The growth rate, a_1 , is proportional to j_{sep} and is less than 0.5 for all cases investigated here. The same trend is found for the growth of the minimum value of $|\mathbf{j}|$ along the separator. The maximum value of $|\mathbf{j}|$ occurs around $z = 0.4$ for all experiments and the minimum values occur around the upper null.

3.4 Summary

In this chapter, we have performed a non-resistive MHD relaxation, using Lare3d, on five initially non-equilibrium magnetic fields which each contain two null points with spines and separatrix surfaces, and a single-separator linking the nulls. The separator is formed, in each experiment, by the intersection of the separatrix surfaces of the nulls. The initial value of the uniform current, j_{sep} , which is directed parallel to the separator, is varied in each experiment. In all experiments, the main current layers form along the separator and are twisted. The current, which is initially uniform and directed along the separator, causes the separatrix surfaces to fold about the separator which leads to the twistedness of the current layer. The degree of twist increases with j_{sep} . Along with the strong current on the separator, enhanced currents form on the separatrix surfaces of the nulls during the experiment.

The current, which accumulates along the separator and increases with initial value j_{sep} , is not symmetric, possibly due to the initial asymmetries of the magnetic skeleton. Reverse currents, which have been observed in some 2D current sheets, were found along the z -axis below the lower null and above the upper null. The length, depth and width of the equilibrium current layers increase with initial value j_{sep} .

The separatrix surfaces of the nulls collapse, during the non-resistive relaxation, to form cusps in planes perpendicular to the separator. The plasma pressure, which was initially uniform throughout the domain, becomes enhanced within the cusp regions and falls off outwith them. The cusps, which have been observed in the collapse of 2D nulls, are necessary to provide total pressure balance (plasma pressure plus magnetic pressure being constant) across the equilibrium current layer.

The separator and separatrix surfaces have small residual forces acting on them which act to strengthen the current, to lengthen and widen the current layer and to make it thinner. This slow evolution suggests all five experiments are approaching an infinite-time singularity, indicating an infinite time would be required to achieve a true MHS equilibrium, as has been observed in the collapse of 2D and 3D nulls [e.g., Fuentes-Fernández et al., 2011, Fuentes-Fernández and Parnell, 2012]. Elsewhere in the domains of each experiment, there is force balance.

As already mentioned, asymmetries are found in the distribution of the plasma pressure and the current in our non-resistive relaxation experiments. In the next chapter, we vary the analytical magnetic field (Eq. 3.1) parameters a , b and c to see how they affect the asymmetries found in this chapter and properties of the plasma and magnetic field.

Chapter 4

The effects of varying the initial separator magnetic field on the MHS equilibrium and its current layer

In Chapt. 3, MHS equilibria were formed through the non-resistive MHD relaxation of an analytical single-separator model. This analytical magnetic field, which models two nulls linked by a single-separator, is detailed in Chapt. 2. It contains five parameters which, if varied, alter the magnetic configuration of the field,

$$\begin{aligned} B_x &= \frac{B_0}{L_0}(x + cxz + byz - \frac{1}{2}j_{sep}y), \\ B_y &= \frac{B_0}{L_0}((2a - c)yz - (1 + aL)y + bxz + \frac{1}{2}j_{sep}x), \\ B_z &= \frac{B_0}{L_0}(-a(z^2 - zL) + \frac{1}{2}cx^2 + (a - \frac{1}{2}c)y^2 + bxy). \end{aligned} \quad (4.1)$$

These five parameters are:

- a , b and c , which can determine the geometry of the field lines from each of the nulls, or change the relative orientation of the separatrix surfaces from the two nulls,
- j_{sep} , which is the uniform current directed parallel to the separator ($\mathbf{j} = (0, 0, j_{sep})$),
- L , the initial length of the separator.

The effects on the MHS equilibria of varying the initial uniform current, j_{sep} , have already been discussed in Chapt. 3. Here, we consider what effect changing the parameters a , b and c have on any MHS equilibria formed.

In order to investigate the effects of starting from a different initial non-potential magnetic field on the final MHS equilibrium, we consider three separate sets of experiments, each starting with a different initial magnetic field. In the first set of initial fields, we consider five experiments where a is varied ($a = 0.15$, $a = 0.25$, $a = 0.5$, $a = 0.75$ and $a = 0.85$), but all other parameters are held fixed. In the second set we consider five initial fields in which only b is varied ($b = 0.5$, $b = 0.75$, $b = 1.0$, $b = 1.5$, $b = 2.0$) and in the third

set we consider fields where only c is varied ($c = -0.25$, $c = 0.0$, $c = 0.25$, $c = 0.5$ and $c = 0.75$). In all of the new experiments, the two parameters which are not being varied take on the values used throughout Chapt. 3, i.e., $a = 0.5$, $b = 0.75$ and $c = 0.25$. Thus, there is one experiment in common between all three sets of experiments: the experiment described in detail in Chapt. 3 (value italicised in the above lists, and throughout this chapter). The results of all the new experiments will be compared with the results of the main experiment discussed in Chapt. 3. The values of a , b and c which we explore here, have been chosen such that each experiment initially has two improper radial nulls and satisfies all the constraints discussed in Chapt. 2. The initial current $j_{sep} = 1.5$, and the scale factors $B_0 = L_0 = L = 1$ are the same in all the magnetic fields.

All these non-potential fields discussed above are used as initial magnetic configurations for the experiments that undergo non-resistive MHD relaxation in the same manner as that discussed in Chapt. 3. The plasma parameters are the same in all cases. It is just the magnetic field parameters, a , b and c , that are varied in each case, as discussed above.

We begin here by discussing the running time of each experiment and explain why all magnetic configurations are not relaxed for the same length of time, before discussing the energetics of each experiment (Sect. 4.1). We then discuss how the initial Lorentz force varies between all of the twelve new experiments, plus the main experiment discussed in Chapt. 3 (Sect. 4.2).

This chapter is then split into three sections, namely Sects. 4.3, 4.4 and 4.5, where we focus, in turn, on the effects of varying the parameters a , b and c on the equilibrium magnetic field, respectively. In each of these sections we begin by detailing the initial magnetic field properties and comparing the initial and equilibrium skeletons of each series of experiments. Next, we discuss differences in the strength, dimensions and twist of the current layers which have formed through the non-resistive relaxation and look at the behaviour of the pressure and the total force in the MHS equilibria. In Sect. 4.6 we compare the growth rate of the current along the separator throughout each of the thirteen experiments and we summarise our findings in Sect. 4.7.

Note, in all figures which compare experiments throughout this chapter, the results for the main experiment discussed in Chapt. 3, are plotted as black lines/symbols.

4.1 Evolution of each experiment

Before discussing the results of each experiment, we first note that the point at which each experiment considered here underwent non-negligible numerical diffusion is different. One of the first clear signs of non-negligible numerical diffusion was a change in the magnetic skeleton of the magnetic field, in particular, an increase in the number of null points. Such a change can occur without any noticeable effect on the energetics of the system. This is because the reconnection often occurs without creating any enhanced velocities.

Throughout the non-resistive MHD relaxation, we monitored the number of nulls present in the system and found that the topology did not remain fixed for the same length of time in each experiment: any change in topology indicates that reconnection has occurred, which, of course, violates our assumption of non-resistive relaxation. Therefore, by analysing the null number we could ascertain at which point each experiment should be ended at (such that numerical diffusivity effects had not yet come in to play) and hence

attained the final equilibrium state for each experiment (Table 4.1).

Table 4.1: The running time, the initial and final values of the magnetic energy (E_b), the difference between the initial and final magnetic energy values, the percentage contributions of the viscous and adiabatic heating terms and the mean total energy for all experiments discussed in this chapter. Note, the main experiment discussed in Chapt. 3, where $a = 0.5$, $b = 0.75$ and $c = 0.25$, appears in all three sets of values here for comparison.

Experiment	Running time (t_f)	Initial E_b	Final E_b	Initial E_b - final E_b	% visc/adia heating	Mean E_{tot}
$a = 0.15$	51.28	10.11	9.57	0.54	72/28	37.14
$a = 0.25$	51.28	10.32	9.79	0.53	73/27	37.34
$a = 0.50$	<i>51.28</i>	<i>11.67</i>	<i>11.16</i>	<i>0.51</i>	<i>77/23</i>	<i>38.76</i>
$a = 0.75$	37.18	14.20	13.69	0.51	80/20	41.22
$a = 0.85$	33.33	15.54	15.03	0.51	81/19	42.56
$b = 0.50$	51.28	10.21	9.72	0.49	76/24	37.27
$b = 0.75$	<i>51.28</i>	<i>11.67</i>	<i>11.16</i>	<i>0.51</i>	<i>77/23</i>	<i>38.76</i>
$b = 1.00$	51.28	13.71	13.17	0.54	76/24	40.78
$b = 1.50$	51.28	19.55	18.95	0.6	76/24	46.56
$b = 2.00$	21.79	27.72	27.06	0.66	78/22	54.72
$c = -0.25$	51.28	11.31	10.82	0.49	77/23	38.33
$c = 0.00$	51.28	11.23	10.73	0.5	76/24	38.26
$c = 0.25$	<i>51.28</i>	<i>11.67</i>	<i>11.16</i>	<i>0.51</i>	<i>77/23</i>	<i>38.76</i>
$c = 0.50$	51.28	12.66	12.11	0.55	77/23	39.76
$c = 0.75$	32.05	14.18	13.59	0.59	77/23	41.22

The running times in Table 4.1 have all been normalised to the time it would take a fast-magnetoacoustic wave to travel along the separator from the lower to the upper null in each experiment (t_f). In each experiment $t_f = 0.78$.

It is clear from Table 4.1 that as a , b and c are increased, the running time of the experiment decreases, however, it is not a linear relation. It appears that when $a > 0.5$ or when $b > 1.5$ or when $c > 0.5$ (while all other parameters are held constant) that diffusion effects come into play earlier than in the other experiments. The validity of calling the final frame of each experiment an equilibria is discussed throughout this chapter.

Each experiment detailed in this chapter undergoes non-resistive MHD relaxation which causes the collapse of the initial state, which is not in force balance. This creates fast-magnetoacoustic waves in the system. In each experiment the creation of these waves signifies that magnetic energy has been converted into kinetic energy. The initial and final values of the magnetic energy, for each experiment, are given in Table 4.1. Clearly, from Table 4.1, the initial values of the magnetic energy increase as a , b and c increase, as do the final values. We note that increasing a , b and c raises the amount of magnetic energy that remains in the final MHS equilibria.

The waves travel throughout the domains of the experiments, expanding or compressing the plasma which gives rise to adiabatic cooling or heating, respectively. These waves are then damped by viscosity, which gives rise to viscous heating. The proportion of the

viscous and adiabatic heating, which contribute to the conversion of magnetic to internal energy either via kinetic energy or directly, respectively, in the experiments, is found to vary with varying the initial parameter a , but not b or c (Table 4.1). The amount of viscous heating occurring in the system is always greater than adiabatic heating for all experiments, but as a is increased, the contribution of viscous heating increases. This suggests more wave damping is occurring for the experiments with relatively higher a .

The total energy remains constant throughout each of the experiments indicating there are no significant losses of energy through the boundaries or due to numerical dissipation. The mean value of the total energy is given in Table 4.1 for each experiment and it is clear from here that the total energy increases with a , b and c .

4.2 Initial Lorentz force

Each of the twelve new experiments have an initial non-zero Lorentz force, as did the main experiment discussed in Chapt. 3, which acts to collapse the separatrix surfaces towards each other as soon as the relaxation begins

$$\begin{aligned}(\mathbf{j} \times \mathbf{B})_x &= 1.5((2a - c)yz - (1 + a)y + bxz + 0.75x), \\(\mathbf{j} \times \mathbf{B})_y &= 1.5(x + cz + byz - 0.75y).\end{aligned}\tag{4.2}$$

Here we have taken $B_0 = L_0 = L = 1$ and $j_{sep} = 1.5$ as they are in each of the experiments. The magnitude of the Lorentz force is changed by the choice of a , b and c and so will affect the outcome of the thirteen relaxation experiments. The maximum and mean values of the magnitude of the Lorentz force, calculated throughout the entire domain of each experiment, are given in Table 4.2. Here, we see that the peak in the maximum value of $|\mathbf{j} \times \mathbf{B}|$ goes through a minimum as a and c are increased, however, the maximum value of $|\mathbf{j} \times \mathbf{B}|$ increases as b increases. The mean values increase as a , b and c are increased.

For convenience we write the components of the Lorentz force as $(\mathbf{j} \times \mathbf{B})_x = \alpha x + \beta y$ and $(\mathbf{j} \times \mathbf{B})_y = \gamma x + \delta y$, where $\alpha = 1.5(bz + 0.75)$, $\beta = 1.5((2a - c)z - 1.5(1 + a))$, $\gamma = 1.5(1 + cz)$ and $\delta = 1.5(bz - 0.75)$.

If we let b and c take on the values of the main experiment discussed in Chapt. 3, and vary a , we find that α is always positive, but $\beta \geq 0$ if $a > (z + 4)/(8z - 4)$ hence the sign of $(\mathbf{j} \times \mathbf{B})_x$ can be changed by a . On the other hand, γ is always positive and δ is always less than or equal to zero in $(\mathbf{j} \times \mathbf{B})_y$, regardless of the choice of a .

Similarly, if we let a and c take on the values of the main experiment discussed in Chapt. 3, and vary b , we find that α is always negative but $\beta \geq 0$ if $b \geq -3/(4z)$. The term γ is always positive, regardless of the choice of b , but $\delta \geq 0$ if $b \geq 3/(4z)$. Therefore, the signs of both components of the Lorentz force can be altered by varying b .

Finally, if a and b take on the values which they had in the main experiment discussed in Chapt. 3, and c is varied, we find that the terms α and δ are always positive, but $\beta \geq 0$ if $c \geq 1 - 3/(2z)$ and $\gamma \geq 0$ if $c \geq -1/z$. This implies that the sign of both components of the Lorentz force can change by varying the parameter c .

Table 4.2: The maximum and mean values of the magnitude of the Lorentz force, throughout the domain, for all experiments discussed in this chapter. Note, the main experiment discussed in Chapt. 3, where $a = 0.5$, $b = 0.75$ and $c = 0.25$, appears in all three sets of values here for comparison.

Experiment	Max $ \mathbf{j} \times \mathbf{B} $	Mean $ \mathbf{j} \times \mathbf{B} $
$a = 0.15$	5.04	1.64
$a = 0.25$	4.61	1.66
$a = 0.50$	4.74	1.72
$a = 0.75$	5.58	1.81
$a = 0.85$	5.94	1.86
$b = 0.50$	4.77	1.6
$b = 0.75$	4.74	1.72
$b = 1.00$	5.77	1.86
$b = 1.50$	7.87	2.20
$b = 2.00$	9.97	2.58
$c = -0.25$	5.79	1.64
$c = 0.00$	5.26	1.66
$c = 0.25$	4.74	1.72
$c = 0.50$	4.84	1.81
$c = 0.75$	5.50	1.91

4.3 MHS equilibria A: The effects of varying parameter a

In the first series of five experiments we investigate the effects of varying the parameter a . The final equilibrium times for the five experiments in this series are given in Table 4.1 and are all the same ($51.28t_f$) except for the two largest values of a which run for less time ($37.18t_f$ and $33.33t_f$).

4.3.1 Initial and equilibrium magnetic skeleton

The eigenvalues and eigenvectors for the lower and upper nulls, with $b = 0.75$, $c = 0.25$, $j_{sep} = 1.5$ and $B_0 = L_0 = L = 1.0$, are as follows

$$\begin{aligned}
 \lambda_{sl} &= -\frac{a}{2} - \frac{\sqrt{(a+2)^2 - 2.25}}{2}, & \mathbf{e}_{sl} &= \left(\frac{1.5}{a+2 + \sqrt{(a+2)^2 - 2.25}}, 1, 0 \right)^T, \\
 \lambda_{f1l} &= a, & \mathbf{e}_{f1l} &= (0, 0, 1)^T, \\
 \lambda_{f2l} &= -\frac{a}{2} + \frac{\sqrt{(a+2)^2 - 2.25}}{2}, & \mathbf{e}_{f2l} &= \left(\frac{1.5}{a+2 - \sqrt{(a+2)^2 - 2.25}}, 1, 0 \right)^T, \\
 \\
 \lambda_{su} &= 1.25, & \mathbf{e}_{su} &= \left(\frac{3.75}{a-2.5}, 1, 0 \right)^T, \\
 \lambda_{f1u} &= -a, & \mathbf{e}_{f1u} &= (0, 0, 1)^T, \\
 \lambda_{f2u} &= a - 1.25, & \mathbf{e}_{f2u} &= (0, 1, 0)^T.
 \end{aligned} \tag{4.3}$$

Increasing the parameter a brings the spine and the separatrix surface of the lower null closer to being aligned along the y -axis and to the yz -plane, respectively. The spine of the upper null will also become more aligned with the y -axis as a is increased. The plane of the upper null's separatrix surface will vary as a varies since the lower null's spine must bound it.

The skeletons of the initial and equilibrium magnetic fields, for the experiments in Series A, are shown in Fig. 4.1. It is clear from these plots that varying the value of a , changes the initial magnetic field in the manner as expected from looking at the eigenvectors.

The lower row in Fig. 4.1 displays the skeleton for each experiment after the non-resistive MHD relaxation has taken place. An isosurface of $j_{\parallel} = 10$ is also drawn on these graphs, highlighting the twisted current layer that forms along the separator in each case. The strength of this current layer varies with a : this is discussed more in Sect. 4.3.2. Enhanced current also exists on the separatrix surfaces of the nulls for all experiments.

The formation of the strong current, which lies along the separator in all the plots shown in Fig. 4.1, indicates that the magnetic skeleton has been altered through the non-resistive MHD relaxation. The separatrix surfaces become warped through the non-resistive MHD relaxation. In Fig. 4.2a, the intersections of the initial magnetic field's separatrix surfaces (dashed lines) are plotted in a plane perpendicular to the separator, at $z = 0.5$, for all five experiments discussed in Series A. For comparative purposes, on this plot, the intersection of the separatrix surfaces of the equilibrium magnetic field are plotted (solid lines), for the experiments with the lowest and highest values of a , i.e., $a = 0.15$ and $a = 0.85$. Here, slight differences are apparent between the positions at which the separatrix surfaces of the initial magnetic fields intersect this plane. As a is increased, the initial angle between the separatrix surfaces of the nulls enlarges slightly.

The non-resistive MHD relaxation causes the separatrix surfaces of the nulls to curve towards each other, creating cusp regions about the separator (Fig. 4.2b). In this plot the solid lines show where the equilibrium separatrix surfaces (solid lines) intersect the plane at $z = 0.5$ and the dashed lines highlight where the initial magnetic field's separatrix surfaces (dashed lines) with the lowest and highest values of a intersect this plane. We see, from this plot, that the angle within the cusp regions is slightly smaller for larger a . This means that the equilibrium separatrix surfaces collapse slightly more towards each other as the initial value of a is increased. Note, however, that the run times for the experiments with $a = 0.75$ and $a = 0.85$ are not as long as for the other experiments and, hence, the slight enhancements in the curvature of those separatrix surfaces could be due to them not being as relaxed. This explanation for the enhanced curvature of the separatrix surfaces is more likely since the separatrix surfaces initially appear very similar in these cuts regardless of the value of a .

Fig. 4.2 also highlights that the separatrix surfaces, of both nulls, remain stationary on the boundaries, as required by the boundary conditions, throughout the non-resistive MHD relaxation.

In the next sections, we discuss differences in the dimensions and strength of the current layer (Sect. 4.3.2), the twist (Sect. 4.3.3) before analysing the plasma pressure and the magnetic pressure (Sect. 4.3.4) and forces (Sect. 4.3.5) in the equilibrium state of each experiment in Series A.

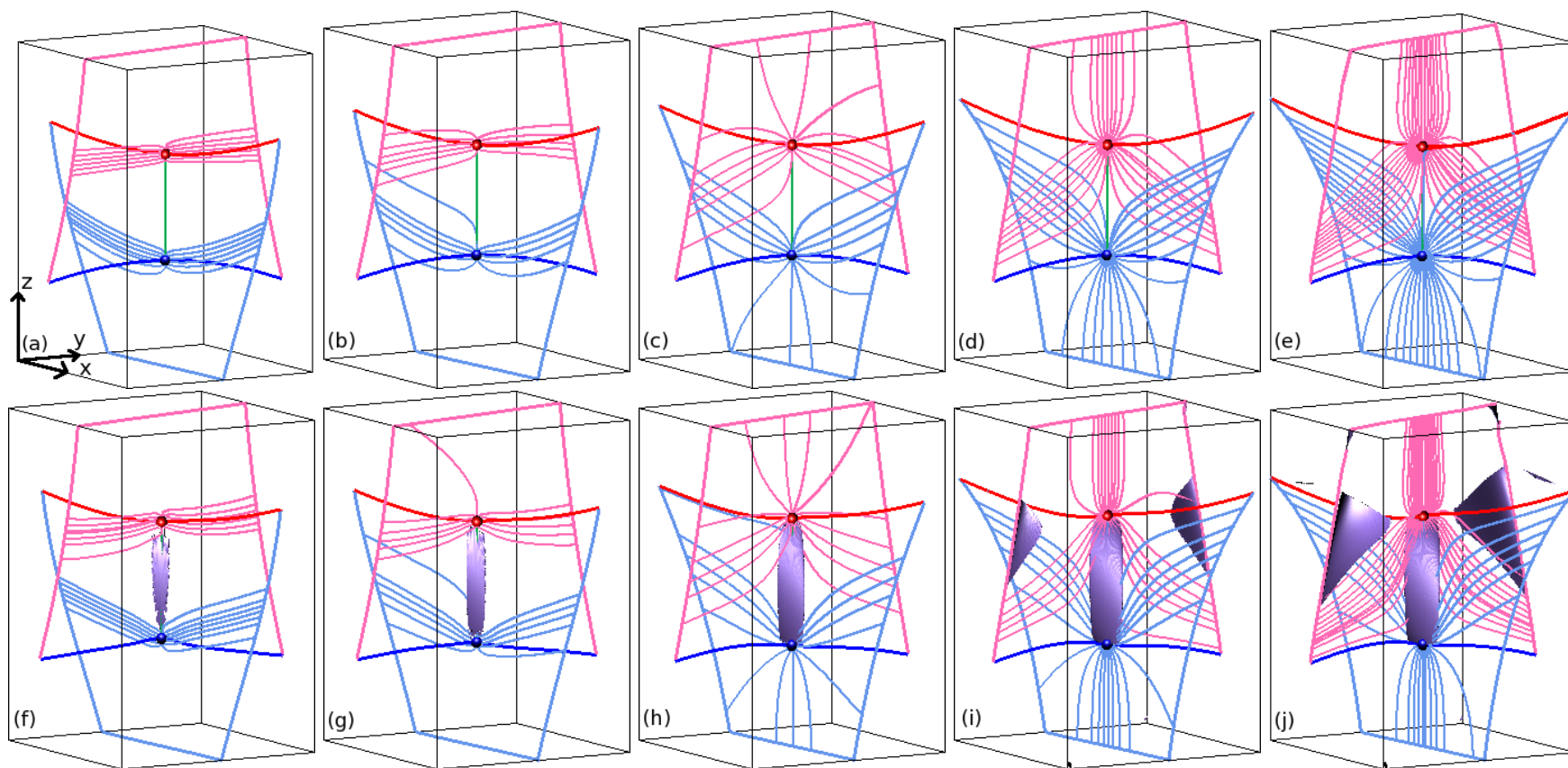


Figure 4.1: Skeletons of the initial (top row) and MHS equilibrium (bottom row) magnetic fields for the experiments whose initial conditions are exactly the same, save for the value of a : (a) and (f) $a = 0.15$, (b) and (g) $a = 0.25$, (c) and (h) $a = 0.5$, (d) and (i) $a = 0.75$ and (e) and (j) $a = 0.85$. Here the lower/upper nulls are blue/red spheres with blue/red spines and pale-blue/pink separatrix surfaces, respectively. The solid pale-blue/pink lines highlight where the separatrix surfaces intersect the boundaries of the box. The separator, green line, links the null points. In the bottom row, a purple isosurface is drawn at $j_{\parallel} = 10$ in each figure. The axes drawn on (a) apply to each skeleton.

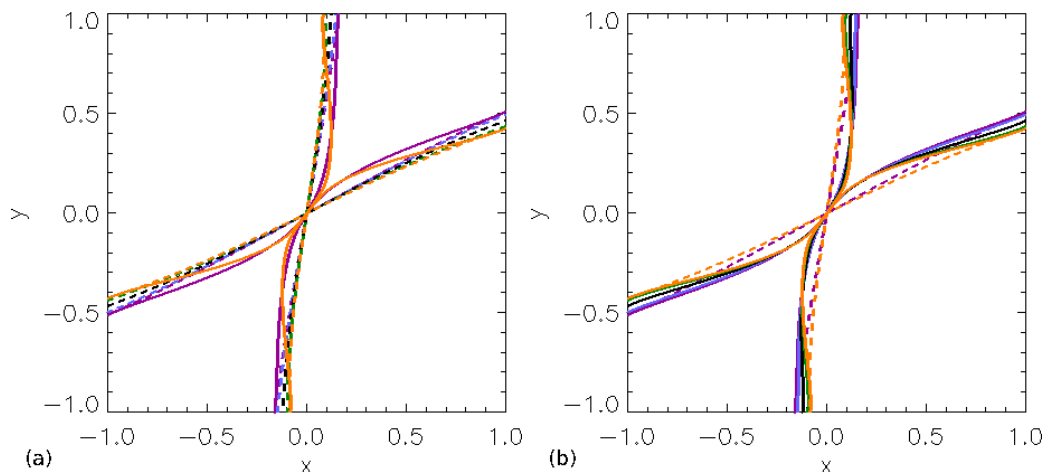


Figure 4.2: Intersections of (a) the initial (dashed lines) and (b) the equilibrium (solid lines) magnetic field's separatrix surfaces with the $z = 0.5$ plane for the experiments with $a = 0.15$ (purple), $a = 0.25$ (blue), $a = 0.5$ (black), $a = 0.75$ (green) and $a = 0.85$ (orange). Over plotted on (a) are the final equilibrium positions (solid lines) of the $a = 0.15$ (purple) and $a = 0.85$ (orange) separatrix surfaces. Similarly, over plotted on (b) are the initial positions (dashed lines) of the separatrix surfaces of these two experiments. The separatrix surface of the lower null spans $x = -1.0$ to $x = 1.0$ and the separatrix surface of the upper null spans $y = -1.0$ to $y = 1.0$.

4.3.2 Properties of the current layer

As we have already seen, a current layer forms along the separator in each experiment. In this section, we quantify the strength of the current in the current layers and analyse the current layer length, width and depth in each experiment's equilibrium state and at $t_c = 33.33t_f$, for comparative purposes.

Length of the current layer

During the relaxation, in all Series A experiments, the two nulls initially move apart from each other along the z -axis before coming back towards each other slightly and then slowly move apart again. This behaviour is shown in Fig. 4.3a which is a plot of the displacement of the nulls from their original position against time. The deflection of the lower null from its original position, is greater for larger a up to $a = 0.5$ after which the position of the lower null throughout the relaxation experiments does not vary greatly. The upper null moves further away from its original position as a is increased, but there is not much distinction in the position of this null while a is small ($a = 0.15$ or $a = 0.25$) or large ($a = 0.75$ or $a = 0.85$).

Fig. 4.3a indicates that the length of the separator in each experiment varies through time with the length dependent on the value of a (Fig. 4.3b). The separator length increases with increasing value a as is shown in Fig. 4.3b until a is large ($a = 0.75$ or $a = 0.85$) when the separator length does not vary significantly. The evolution in time of the separator length does not otherwise depend on the parameter a . The length of the separator at $t_c = 33.33t_f$ and at the equilibrium times are given in Table 4.3. Note, in

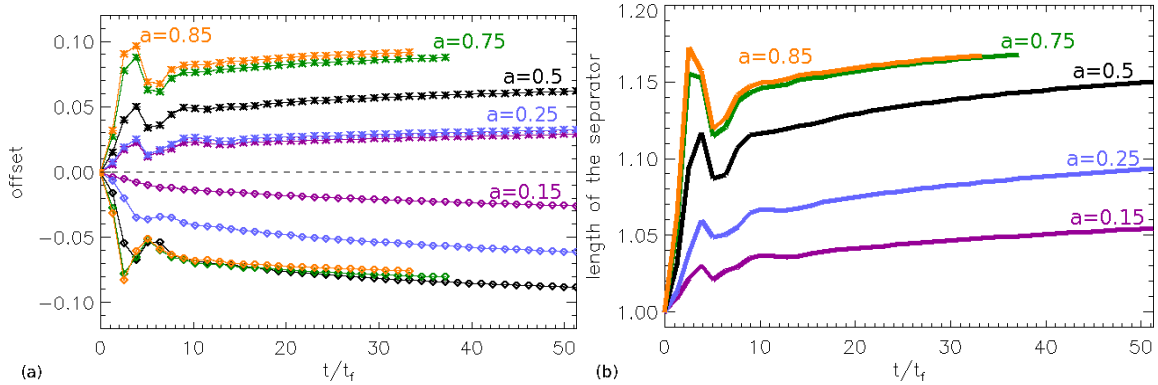


Figure 4.3: (a) The offset in the z -direction, from the null's z -positions at $t = 0t_f$, of the lower nulls (diamonds) and upper nulls (asterisks) against time and (b) the length of the separator against time for the experiments with $a = 0.15$ (purple), $a = 0.25$ (blue), $a = 0.5$ (black), $a = 0.75$ (green) and $a = 0.85$ (orange).

both plots in Fig. 4.3, the values are plotted against each experiment's respective time.

Table 4.3: The length of the current layer, l_{sep} , and its width, w , and depth, d , (both calculated using the contour method) at $z = 0.5$ and the maximum/mean current along the separator at $t_c = 33.33t_f$ for comparison and at the equilibrium times, t_{eq} , for all experiments in Series A, where $b = 0.75$ and $c = 0.25$.

Exp.	l_{sep}		w at $z = 0.5$		d at $z = 0.5$		Max $ \mathbf{j} $		Mean $ \mathbf{j} $	
	a	t_c	t_{eq}	t_c	t_{eq}	t_c	t_{eq}	t_c	t_{eq}	t_c
0.15	1.05	1.06	0.284	0.264	0.038	0.032	15.96	18.19	12.03	13.69
0.25	1.08	1.09	0.286	0.264	0.036	0.030	14.42	16.35	12.85	14.77
0.5	1.14	1.15	0.300	0.292	0.032	0.028	19.52	23.36	17.43	20.52
0.75	1.17	1.17	0.316	0.316	0.024	0.026	29.33	30.85	24.97	26.19
0.85	1.17	1.17	0.324	0.324	0.024	0.024	33.72	33.72	28.56	28.56

Strength of the current layer

Fig. 4.4a shows the value of the component of the current parallel to the magnetic field, j_{\parallel} , plotted along the z^* -axis, for all experiments where a is varied. Here, the z -axis has been normalised, as was done in Chapt. 3, according to the equation $z^* = (z - z_{ln})/l_{sep}$, where z_{ln} is the z -coordinate of the lower null and l_{sep} is the length of the equilibrium separator (as listed in Table 4.3 at $t_c = 33.33t_f$ for comparison and at the equilibrium times, t_{eq}), such that the separator in each experiment lies between $z^* = 0$ and $z^* = 1$.

In Fig. 4.4a, a strong current is shown to exist along the separator of each experiment, as has already been shown in Fig. 4.1. There are also strong currents of opposite sign at the boundaries, as were discussed in Chapt. 3. The maximum value of j_{\parallel} , along the separator grows as a is increased. The maximum value of j_{\parallel} occurs at different values of z depending on the value of a . When a is small ($a = 0.15$ and $a = 0.25$), the maximum value of j_{\parallel} occurs near the upper null. However, when a is larger ($a = 0.5$, $a = 0.75$ and

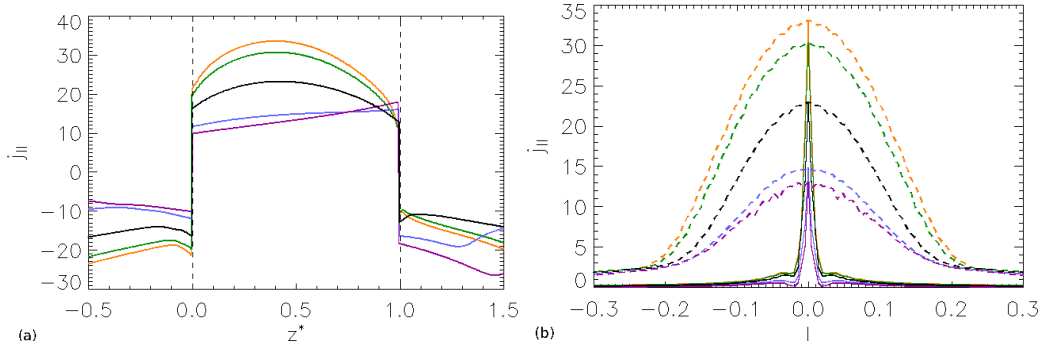


Figure 4.4: Plots of j_{\parallel} (a) along the z^* -axis (normalised such that the separator lies between $z^* = 0$ and $z^* = 1$ and (b) through the depth (solid) and across the width (dashed) of the current layer at $z = 0.5$ for the experiments with $a = 0.15$ (purple), $a = 0.25$ (blue), $a = 0.5$ (black), $a = 0.75$ (green) and $a = 0.85$ (orange).

$a = 0.85$), the maximum value always occurs at roughly $z = 0.4$ regardless of how long the system has relaxed for.

The maximum and mean values of $|j|$ along the separator are given in Table 4.3 at the equilibrium times of each experiment and at t_c for comparative purposes. The maximum value of the current increases with a at t_c and at t_{eq} , except for when a is small ($a = 0.15$). This behaviour is visible in Fig. 4.4a. We find that the mean value of the current along the separator increases with a at both times given in Table 4.3.

The value of j_{\parallel} , across the width and through the depth, of the current layer at $z = 0.5$ is plotted in Fig. 4.4b. For each value of a investigated in this chapter, the behaviour of j_{\parallel} through the depth and across the width is the same: a peak in current lies at the current layer ($l = 0.0$) and the current is small elsewhere. This plot, and that shown in Fig. 4.4a, indicate that the larger the value of a the greater the strength of the current in the current layer formed through the non-resistive relaxation of the system.

Width and depth of the current layer

Fig. 4.5a displays the widths (dashed lines) and the depths (solid lines) of the current layers (found using the contour method which was detailed in Chapt. 3), for all five experiments in Series A. This method finds the width and depth of the current layers by using the last elliptical current contour that can be plotted before the contours become X-shaped. Using this method, the width of the current layer increases as a is increased, but when a is small ($a = 0.15$ and $a = 0.25$), the width does not vary by much (Fig. 4.5a). The depth of the current layer, found using the contour method, appears to be independent of a near the upper null, but decreases with increasing a in the lower half of the separator.

In Table 4.3, we have given the widths and depths of the current layers, in a slice perpendicular to the separator at $z = 0.5$, at t_c and at t_{eq} . These values show that at $z = 0.5$, as a is increased, the width of the current layer increases and the depth of the current layer decreases at both points in time investigated, except for when $a = 0.15$.

The widths and depths of the current layers are also found using the FWHM method, plotted in Fig. 4.5b. Here, the width of the current layer decreases slightly as a increases,

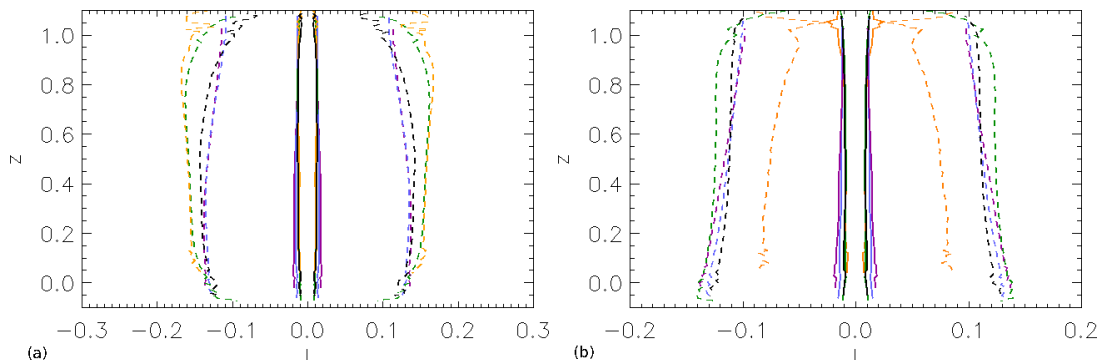


Figure 4.5: The width (dashed) and depth (solid) of the current layer found using (a) the contour method and (b) the FWHM method for the experiments with $a = 0.15$ (purple), $a = 0.25$ (blue), $a = 0.5$ (black), $a = 0.75$ (green) and $a = 0.85$ (orange).

but not surprisingly, the width appears to be affected by the duration of relaxation. The depth of the current layer decreases as a increases near the lower null, as was observed using the contour method.

4.3.3 Current layer twist

The angle through which the current layer twists, from the lower to the upper null, along the length of the separator, increases as the value of a is increased (Fig. 4.6). Note, the

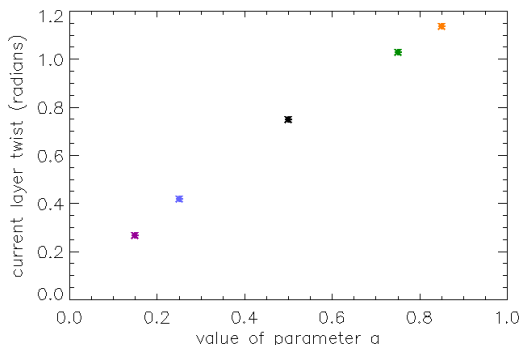


Figure 4.6: The angle (radians) through which the current layer twists from the lower to the upper nulls for the experiments with $a = 0.15$ (purple), $a = 0.25$ (blue), $a = 0.5$ (black), $a = 0.75$ (green) and $a = 0.85$ (orange).

experiments with $a = 0.75$ and $a = 0.85$ are not as relaxed as the other experiments discussed here and so the value of the twist for these two cases may indeed have increased further if these experiments could have been continued.

4.3.4 Pressure along the length, through the depth and across the width of the current layer

As has already been discussed, the non-resistive MHD relaxation causes the field about the separator in each experiment to collapse and the separatrix surfaces to fold towards

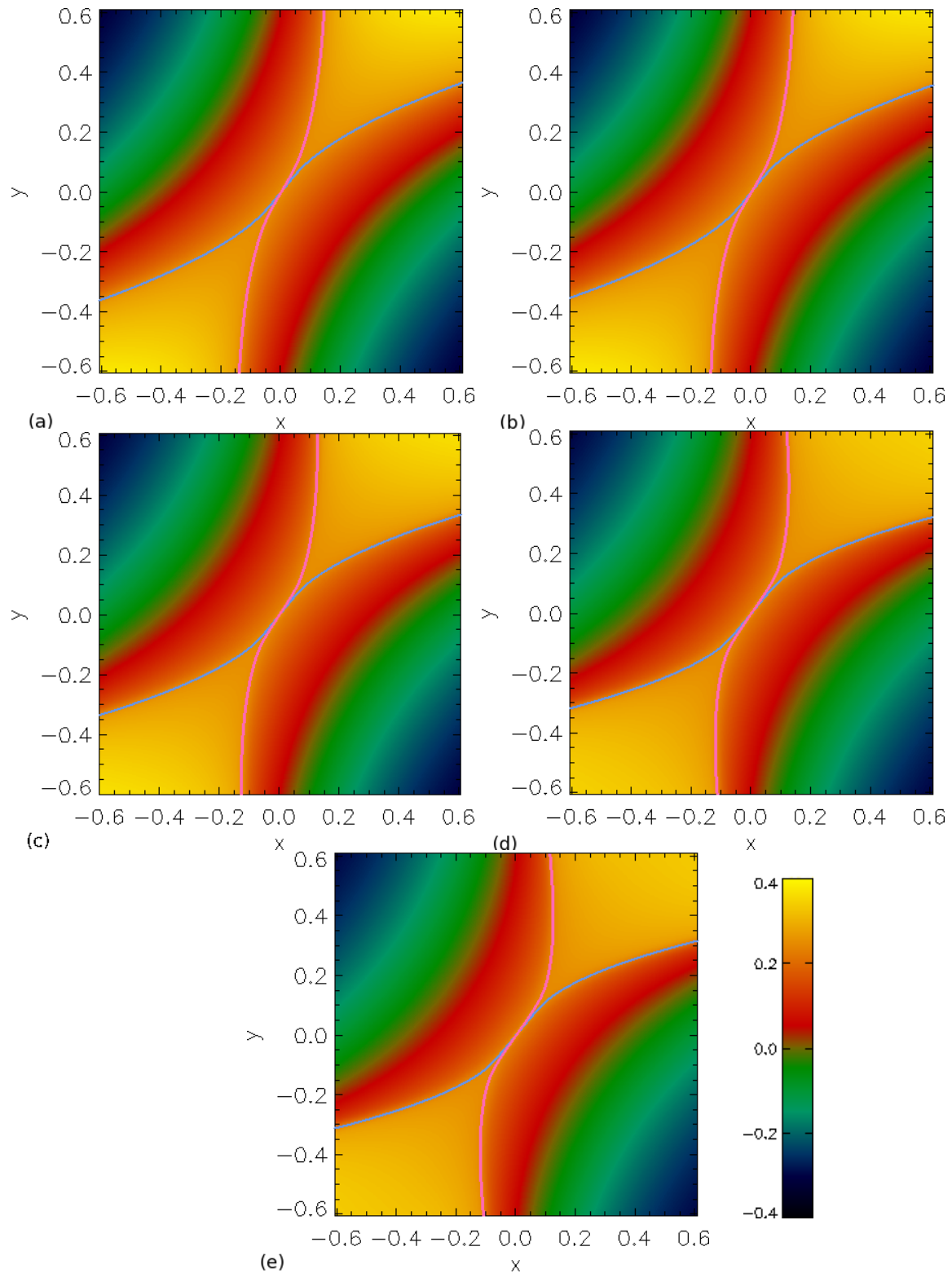


Figure 4.7: Contours of the plasma pressure difference $(p - p_0)$ in the plane perpendicular to the separator at $z = 0.5$ for the experiments with initial parameters (a) $a = 0.15$, (b) $a = 0.25$, (c) $a = 0.5$, (d) $a = 0.75$ and (e) $a = 0.85$. The pale-blue/pink lines highlight where the separatrix surfaces of the lower/upper nulls intersect each cut, respectively.

each other creating cusp regions about the separator. These cusp regions form due to the requirement of pressure balance across the width and through the depth of the current layer in a MHS equilibrium (Chapt. 3). Within the cusp regions, plasma pressure enhancements form, and outwith the cusps the plasma pressure falls off. This is shown in Fig. 4.7 where contours of the plasma pressure difference ($p - p_0$) are plotted in the equilibrium state, in a plane perpendicular to the separator at $z = 0.5$, for all five experiments discussed here in Series A.

These contour plots show that qualitatively there is no difference between the equilibrium plasma pressure as a is varied. We now investigate the pressure balance quantitatively, through the depth and across the width of the current layers and along the length for each of the five experiments where the parameter a is varied.

Fig. 4.8a (solid lines) reveals the quantitative behaviour of the plasma pressure in a slice through the depth of the current layer. As a is increased the plasma pressure decreases. This could not be seen in Fig. 4.7, but is apparent here. Through the depth of the current layer the plasma pressure peaks at $l = 0.0$ as expected (with all experiments having roughly the same value here, $p = 1.75$) and falls off either side of this point. The plasma pressure across the width (dashed lines) is fairly constant across the whole slice, for all values of a , as was observed in Fig. 4.7.

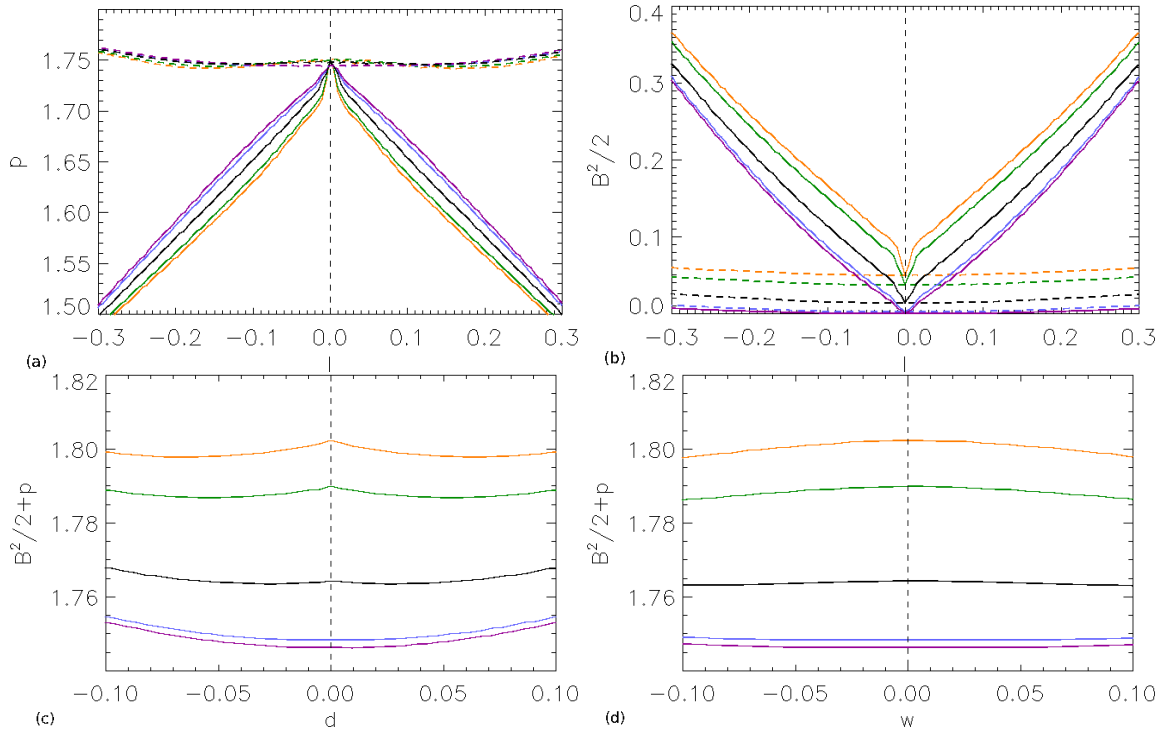


Figure 4.8: The (a) plasma pressure and (b) magnetic pressure plotted through the depth (solid) and across the width (dashed) of the current layer and the sum of the plasma and magnetic pressures plotted (c) through the depth and (d) across the width of the current layer for the experiments with $a = 0.15$ (purple), $a = 0.25$ (blue), $a = 0.5$ (black), $a = 0.75$ (green) and $a = 0.85$ (orange).

The magnetic pressure behaves qualitatively the same, for all values of a investigated here, through the depth and across the width of the current layer (Fig. 4.8b). The magnetic pressure through the depth (solid lines) varies over a greater scale than the plasma pressure but its absolute value is much lower, as expected in a high-beta case. In contrast to the plasma pressure, it has a minimum at the separator through the depth of the current layer. Across the width of the current layer (dashed lines), the magnetic pressure is fairly constant as was seen for the plasma pressure. However, unlike the plasma pressure, the magnitude of the magnetic pressure through the depth and across the width of the current layer increases with a .

For all values of a investigated in this chapter, there is total pressure balance through the depth and across the width of the current layer (Figs. 4.8c and 4.8d, respectively). The magnitude of the total pressure increases with the value of a as expected from the other plots in Fig. 4.8.

Fig. 4.9a displays the plasma pressure plotted along the z^* -axis for all experiments where a is varied. The plasma pressure is higher at the upper null than it is at the lower

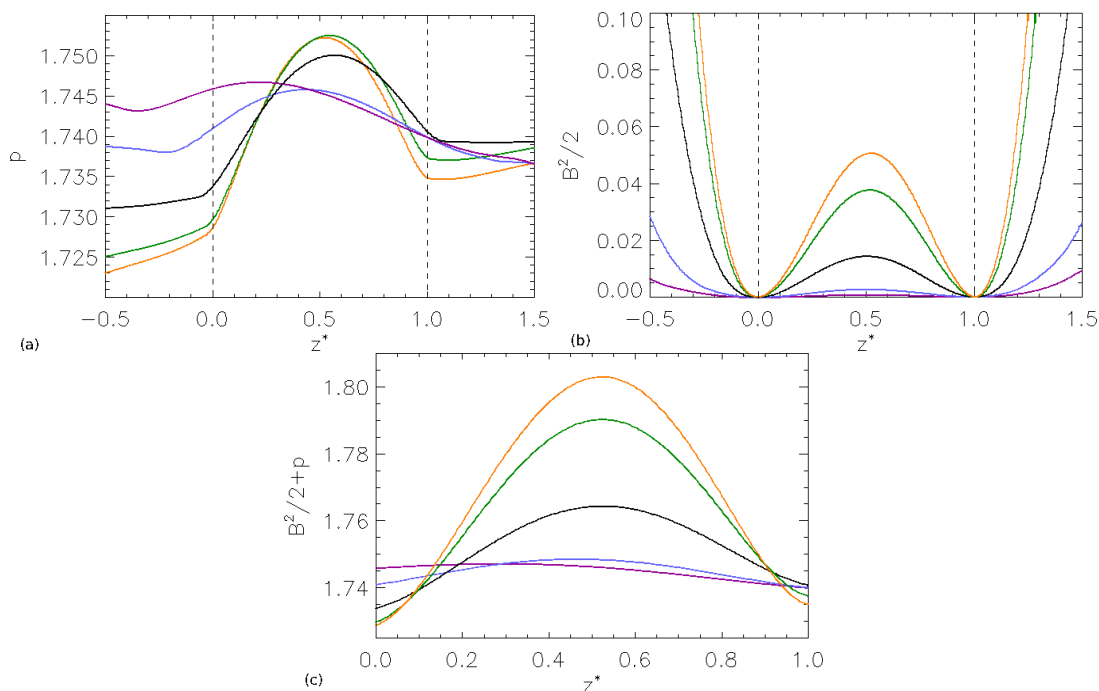


Figure 4.9: Plots along the z^* -axis (the z -axis normalised such that the separator lies between $z^* = 0$ and $z^* = 1$) of (a) the plasma pressure, (b) the magnetic pressure and (c) the sum of the plasma and the magnetic pressures for the experiments with $a = 0.15$ (purple), $a = 0.25$ (blue), $a = 0.5$ (black), $a = 0.75$ (green) and $a = 0.85$ (orange).

null for all experiments except $a = 0.15$ and $a = 0.25$, the smaller values of a we have investigated. In the case where $a = 0.15$, the maximum value of plasma pressure occurs at $z = 0.2$ which is close to the lower null. Excluding this case, the maximum value of plasma pressure increases as a is increased, except in one instance. The maximum plasma pressure is higher when $a = 0.75$ than when $a = 0.85$, but this could be due to the fact that the experiment with $a = 0.75$ is relaxed for slightly longer than the experiment where

$a = 0.85$. The position of the maximum values of plasma pressure are all around $z = 0.56$ when a is greater than or equal to 0.5.

The magnetic pressure vanishes at the null points and has a maximum half way along the separator in each experiment (Fig. 4.9b). The magnitude of the magnetic pressure along the separator is remarkably symmetric in all cases and increases with increasing parameter a . Outwith the separator, the magnetic pressure increases, with the magnitude of the magnetic pressure again, here, increasing with a . The case with $a = 0.15$ has slightly lower magnetic pressure below the lower null than above the upper null. This is the only experiment to show any noticeable asymmetry.

Fig. 4.9c shows the total pressure along the length of the separator, for all five experiments where a is varied. The total pressure is closer to being constant here for the experiments with smaller values of a . We do not expect to see pressure balance along the length of the current layer, i.e., along the separator, since there is a magnetic tension force acting here. The Lorentz force has zero component directed along the separator and so the components of the magnetic pressure force and the magnetic tension force parallel to \mathbf{B} balance along the separator. Hence, pressure balance does not exist along the separator.

4.3.5 Total force along the length, through the depth and across the width of the current layer

In this section, we analyse the equilibrium total force (the plasma pressure force plus the Lorentz force) along the length, through the depth and across the width of the separator current layers, for each of the five experiments where the parameter a is varied.

Fig. 4.10 displays the total force in a cut at $z = 0.5$ across the separator, in the equilibrium states of each experiment where the value of a is varied. These images show that, as expected, the total force is zero everywhere except along the separatrix surfaces and at the separator, where it is strongest. We note here that the experiments with larger a have greater amounts of residual force along these topological regions. This could be due in part to these cases ($a = 0.75$ and $a = 0.85$) not being relaxed for as long as the cases where a is smaller.

Fig. 4.11a shows the total force along the z^* -axis for all five experiments. Here it is clear that the lowest values of the total force occur for the cases which have been relaxed longest ($a = 0.15$ and $a = 0.25$). However, the case where $a = 0.5$ is relaxed for the same time as these two cases, but still displays higher values of total force along the separator, indicating that the value of a does affect the relaxation of the system. This is not surprising since a larger value of a leads to a longer current layer with stronger current in it than a smaller a . The total force acts outwards from some point along the separator ($z = 0.19$, $z = 0.41$, $z = 0.58$, $z = 0.57$ and $z = 0.55$ for the experiments with $a = 0.15$, $a = 0.25$, $a = 0.5$, $a = 0.75$ and $a = 0.85$, respectively) towards the nulls in all experiments and hence acts to lengthen the separator in each case.

The total force through the depth of the current layer behaves as was observed in Chapt. 3, acting in towards the current layer squeezing it thinner for all experiments (Fig. 4.11b). We find here that the magnitude of the total force increases, in the equilibrium state, when the value of a is increased in order to sustain a stronger current in the current layer than found in the small a cases. Note, however, that the experiments with larger a ($a = 0.75$ and $a = 0.85$) were not relaxed for as long as the other three experiments

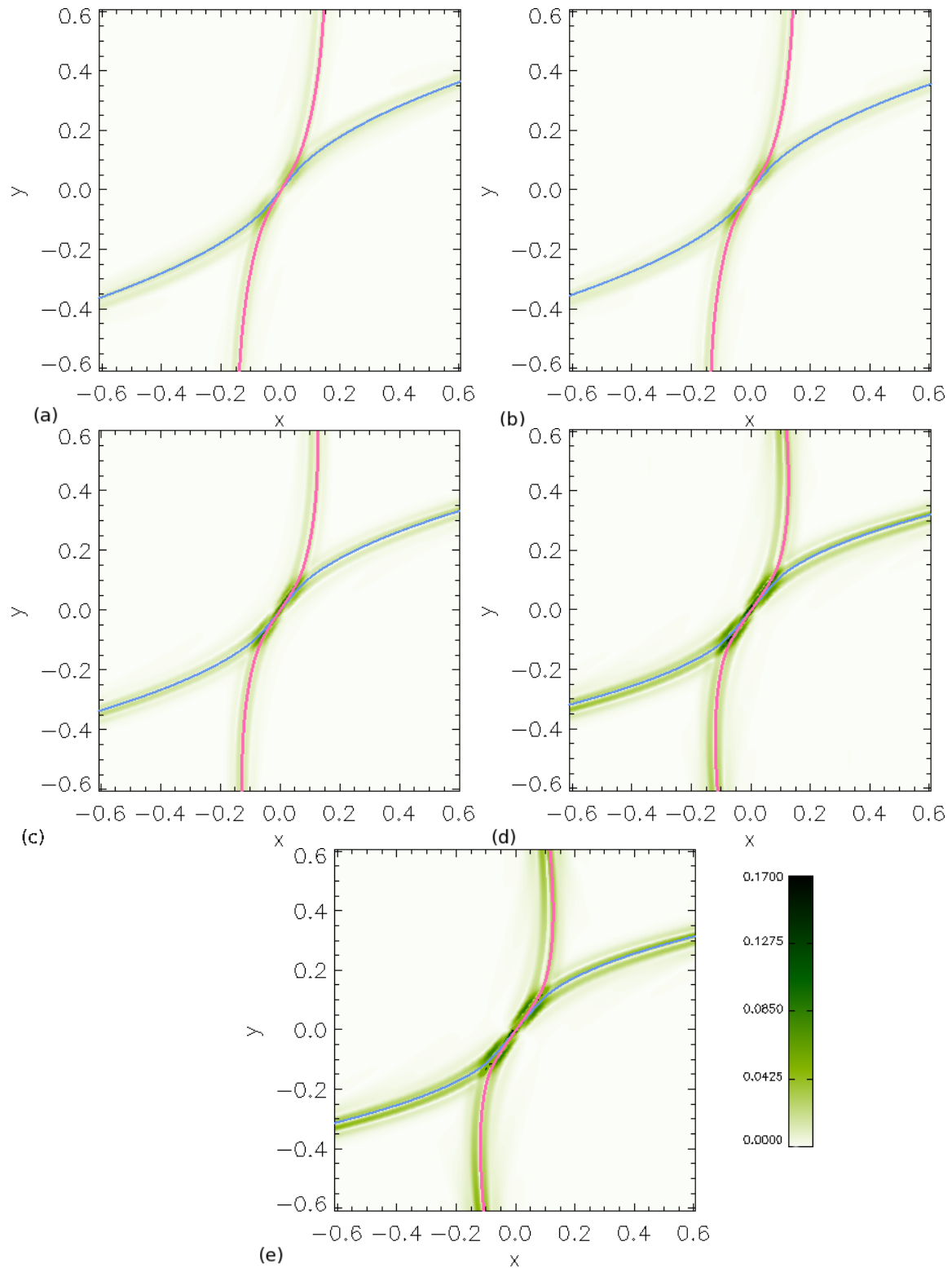


Figure 4.10: Contours of the total force in planes perpendicular to the separator at $z = 0.5$ for the experiments with initial parameters (a) $a = 0.15$, (b) $a = 0.25$, (c) $a = 0.5$, (d) $a = 0.75$ and (e) $a = 0.85$. The pale-blue/pink lines highlight where the separatrix surfaces of the lower/upper nulls intersect each cut, respectively.

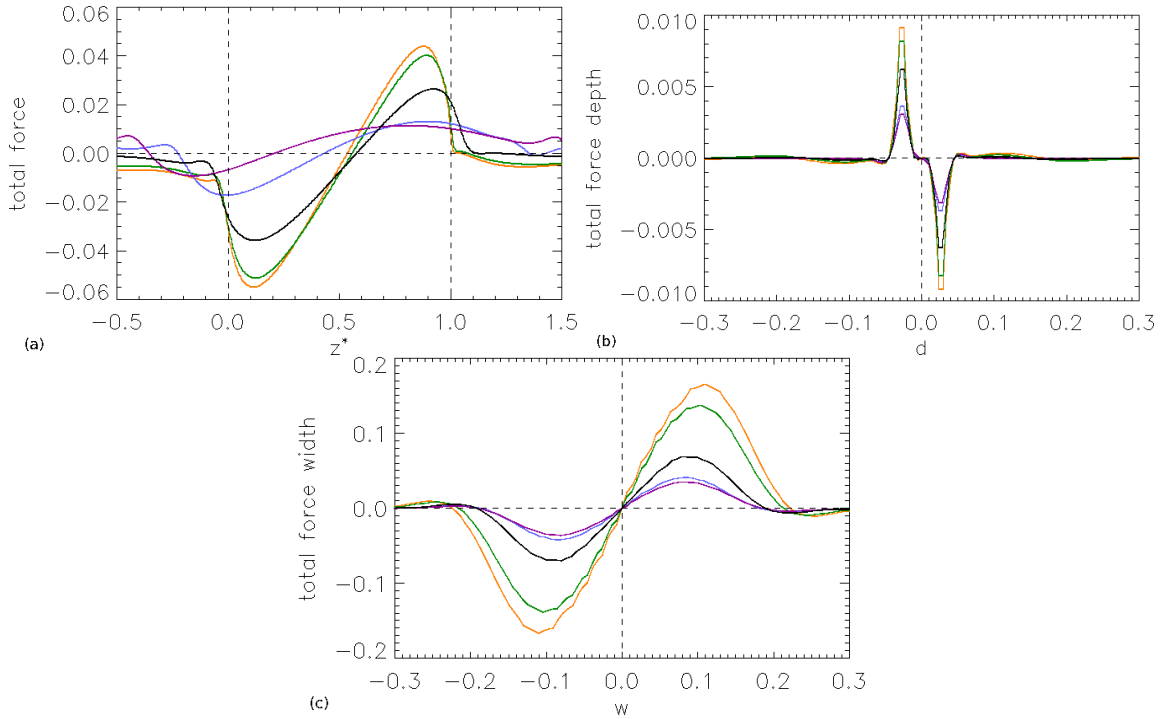


Figure 4.11: Plots of the total force (a) along the z^* -axis, (b) through the depth and (c) across the width of the current layer for the experiments with $a = 0.15$ (purple), $a = 0.25$ (blue), $a = 0.5$ (black), $a = 0.75$ (green) and $a = 0.85$ (orange).

discussed here and so this may contribute to the higher values of total force observed in those cases. However, the experiments with slightly smaller values of a ($a = 0.15$, $a = 0.25$ and $a = 0.5$) were relaxed for roughly the same amount of time and still there is a clear increase in total strength as a is increased between these values.

The same relationship between the value of a and the strength of the total force is displayed in Fig. 4.11c where the total force is plotted across the width of the current layer. The total force acts outwards from the separator (at $w = 0.0$) and therefore widens the current layer. The total force appears to widen the current layer of the experiment with the largest a by the greatest amount.

We note, from Table 4.3, that the widths of the current layers at t_c were either slightly larger than or the same as the values at t_{eq} . This is in contrast to the findings of Fig. 4.11c. However, from studying the evolution of the current in a 1D slice across the width of the current layers we see that, although the width of the current layer decreases slightly over time near the base of the profile, the current profile broadens over time around its middle. Fig. 4.12a shows the value of $|\mathbf{j}|$ in a 1D slice across the width of the current layer at each time step throughout the relaxation, in a cut at $z = 0.5$, for the main experiment where $a = 0.5$, $b = 0.75$ and $c = 0.25$. The different colours represent the value of $|\mathbf{j}|$, plotted across the width of the current layer, evolving through time.

On this plot are two green lines (drawn at $t = t_c$) and two red lines (drawn at $t = t_{eq}$). The dotted lines represent the value of the contour found using the contour method at $t = t_c$ (green line) and at $t = t_{eq}$ (red line). These lines highlight that using these values

to work out the width of the current layer at $t = t_c$ or at $t = t_{eq}$ would show that the current layer becomes less wide over time. The dashed lines are drawn at the value of half of the maximum of $|\mathbf{j}|$ at $t = t_c$ (green dashed line) and $t = t_{eq}$ (red dashed line). Therefore, using these values to work out with width of the current layer at $t = t_c$ and at $t = t_{eq}$ would show that the current layer was widening over time.

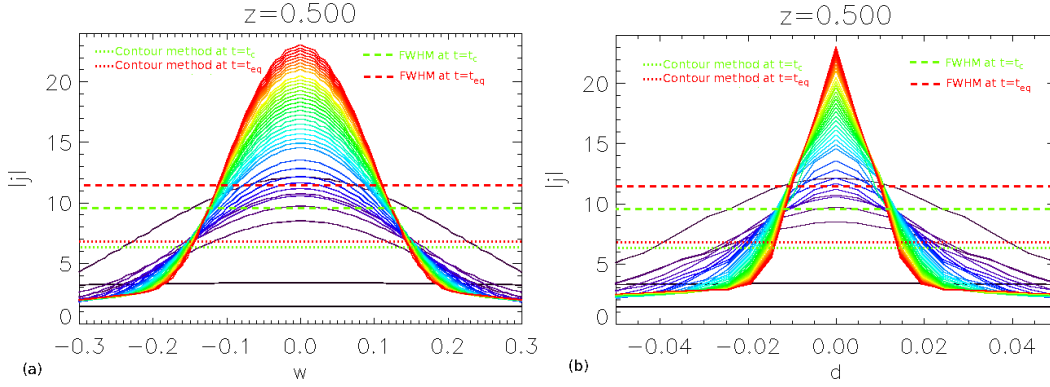


Figure 4.12: Plots of $|\mathbf{j}|$ evolving through time (a) across the width and (b) through the depth of the current layer at $z = 0.5$ for the experiment with $a = 0.5$, $b = 0.75$ and $c = 0.25$. The dotted lines represent the value of the contour used in the contour method to find the width and depth of the current layer at $t = t_c$ (green line) and at $t = t_{eq}$ (red line). The dashed lines represent the value of the contour used in the FWHM method to find the width and depth of the current layer at $t = t_c$ (green line) and at $t = t_{eq}$ (red line). The colours represent $|\mathbf{j}|$ evolving through the experiment where black is drawn at $t = 0t_f$, then time increases as the colours change to purple, blue, green, yellow, orange and red.

Fig. 4.12b shows a similar figure for the current plotted through the depth of the current layer. Here, the depth of the current layer decreases over time (as expected from Fig. 4.11b) regardless of using the level found by the contour method or the FWHM method at $t = t_c$ and at $t = t_{eq}$.

4.4 MHS equilibria B: The effects of varying parameter b

The second series of five experiments we look at now examine the effects of varying the parameter b . From Table 4.1 we see that the equilibrium times of these five experiments are identical ($t = 51.28t_f$), except for the experiment with the highest value, $b = 2.0$ ($t = 21.79t_f$). Since the time of this experiment is less than half of the length of the other experiments its magnetic field/plasma will be less relaxed than the other ones, and so the results for this experiment may not follow the same trend as the other experiments.

4.4.1 Initial and equilibrium magnetic skeleton

The eigenvalues and eigenvectors of the lower and upper nulls, with $a = 0.5$, $c = 0.25$, $j_{sep} = 1.5$ and $B_0 = L_0 = L = 1$, are

$$\begin{aligned} \lambda_{sl} &= -\frac{5}{4}, & \mathbf{e}_{sl} &= \left(\frac{1}{3}, 1, 0\right)^T, \\ \lambda_{f_1l} &= \frac{1}{2}, & \mathbf{e}_{f_1l} &= (0, 0, 1)^T, \\ \lambda_{f_2l} &= \frac{3}{4}, & \mathbf{e}_{f_2l} &= (3, 1, 0)^T, \\ \lambda_{su} &= \frac{1 + 2\sqrt{1.75 + 4b^2}}{4}, & \mathbf{e}_{su} &= \left(\frac{2b - 1.5}{-2 + \sqrt{1.75 + 4b^2}}, 1, 0\right)^T, \\ \lambda_{f_1u} &= -\frac{1}{2}, & \mathbf{e}_{f_1u} &= (0, 0, 1)^T, \\ \lambda_{f_2u} &= \frac{1 - 2\sqrt{1.75 + 4b^2}}{4}, & \mathbf{e}_{f_2u} &= \left(\frac{2b - 1.5}{-2 - \sqrt{1.75 + 4b^2}}, 1, 0\right)^T. \end{aligned} \quad (4.4)$$

From these values, we see that varying the parameter b will affect both nulls. Although the lower null's spine and separatrix-surface eigenvectors do not contain the parameter b , varying b affects the upper null's spine and separatrix surface. Therefore, if the spine of the upper null changes position, the separatrix surface of the lower null will move so that it remains bounded by the upper null's spine. Also, if b is varied, the upper null's separatrix surface plane changes, hence, the position of the spine of the lower null will move so that it bounds the separatrix surface of the upper null. The skeletons of the initial and equilibrium magnetic fields for all the experiments in Series B (with $b = 0.5$, $b = 0.75$, $b = 1.0$, $b = 1.5$ and $b = 2.0$) are shown in Fig. 4.13.

The skeletons of the initial magnetic fields show that the angle between the null's separatrix surfaces becomes greater as b is increased (Figs. 4.13a to 4.13e). We also see from this figure that the field lines of the lower null's separatrix surface (and hence the eigenvalues) are not affected by the value of b . The geometry of the upper null's field lines are, however, altered by the value of b .

The MHS equilibrium skeletons found at the end of the experiments, are shown in Figs. 4.13f to 4.13j. Here, a purple isosurface, drawn at $j_{\parallel} = 10$, shows that a twisted current layer has formed as a result of the relaxation of each experiment, the strength and dimensions of which appear to vary with the value of b . This will be investigated further in Sect. 4.4.2.

As in all the previous relaxation experiments, the skeleton changes due to the non-resistive MHD relaxation (Fig. 4.13). As mentioned previously, the angle at which the separatrix surfaces intersect in the initial field varies depending on b . The parameter b also effects how much the separatrix surfaces of the nulls fold towards each other during the non-resistive MHD relaxation. Fig. 4.14a shows where the separatrix surfaces of the initial magnetic field's separatrix surfaces (dashed lines) intersect the plane at $z = 0.5$.

Over plotted, for comparative purposes, are two solid lines which show where the equilibrium field's separatrix surfaces intersect this cut for the experiments with the lowest and highest values of b ($b = 0.5$ and $b = 2.0$). Clearly, the location of the separatrix surface

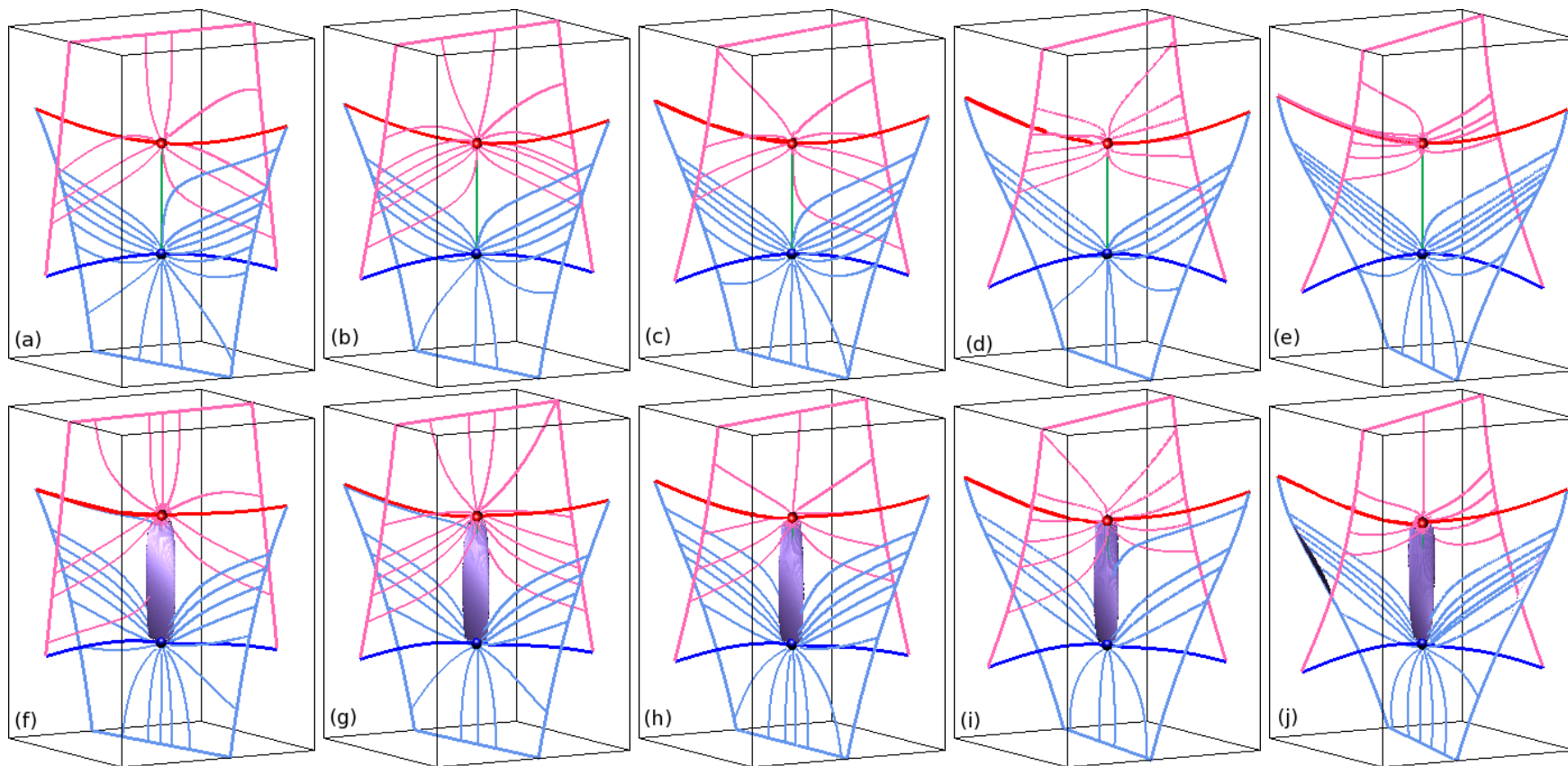


Figure 4.13: Skeletons of the initial (top row) and MHS equilibrium (bottom row) magnetic fields for the experiments whose initial conditions are exactly the same, save for the value of b : (a) and (f) $b = 0.5$, (b) and (g) $b = 0.75$, (c) and (h) $b = 1.0$, (d) and (i) $b = 1.5$ and (e) and (j) $b = 2.0$. Here the lower/upper nulls are blue/red spheres with blue/red spines and pale-blue/pink separatrix surfaces, respectively. The solid pale-blue/pink lines highlight where the separatrix surfaces intersect the boundaries of the box. The separator, green line, links the null points. In the bottom row, a purple isosurface is drawn at $j_{\parallel} = 10$ in each figure.

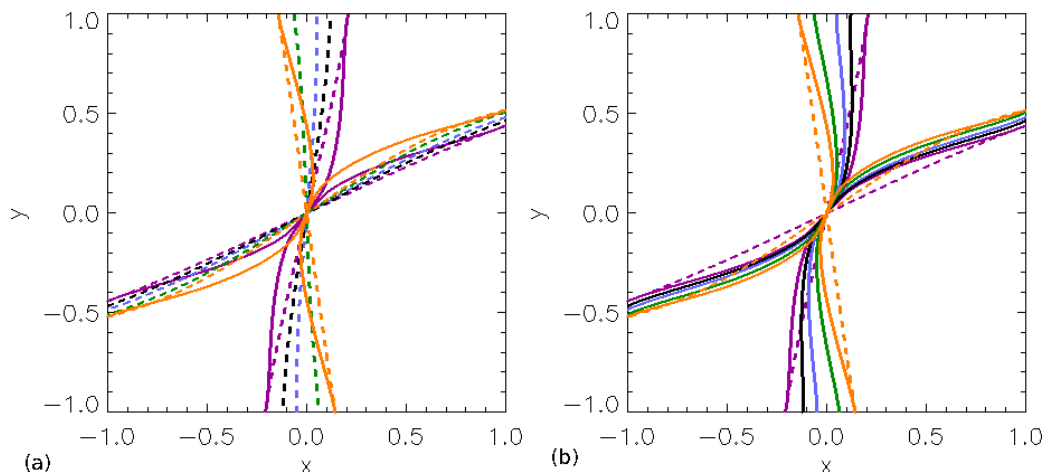


Figure 4.14: Intersections of (a) the initial (dashed lines) and (b) the equilibrium (solid lines) magnetic field's separatrix surfaces with the $z = 0.5$ plane for the experiments with $b = 0.5$ (purple), $b = 0.75$ (black), $b = 1.0$ (blue), $b = 1.5$ (green) and $b = 2.0$ (orange). Over plotted on (a) are the final equilibrium positions (solid lines) of the $b = 0.5$ (purple) and $b = 2.0$ (orange) separatrix surfaces. Similarly, over plotted on (b) are the initial positions (dashed lines) of the separatrix surfaces of these two experiments. The separatrix surface of the lower null spans $x = -1.0$ to $x = 1.0$ and the separatrix surface of the upper null spans $y = -1.0$ to $y = 1.0$.

of the upper null rotates significantly as b increases (most noticeable by looking at where the upper null's separatrix surfaces intersect this plane near the boundaries at $y = -1.0$ and $y = 1.0$). The lower null's separatrix surface vary slightly as b increases, as expected.

Fig. 4.14b shows where the separatrix surfaces of the equilibrium field (solid lines) intersect this plane, at $z = 0.5$, with two dashed lines included to show where the initial field's separatrix surfaces intersect this plane for the experiments with $b = 0.5$ and $b = 2.0$.

As b is increased, the solid lines show that the separatrix surfaces of the equilibrium magnetic field are perturbed more than for small b in such a way as to form a very definite (highly curved) cusp-like shape about the separator. This occurs because the angle between the initial separatrix surfaces is greater for larger values of b . As required by the boundary conditions, the separatrix surfaces do not move on the boundaries throughout the relaxation.

From Fig. 4.14b, the angle between the equilibrium cusps appears to increase as b increases. We investigate the angle through which the current layer twists after the next section, in which we examine the effects that varying b has on the current layer dimensions and the strength of the current in the separator current layer.

4.4.2 Properties of the current layer

The current layers, which form due to the relaxation, lie along the length of the separator. In this section we will analyse how the length, strength, width and depth of the current layer varies between all the experiments we investigate in Series B.

Length of the current layer

As soon as the experiment begins the two nulls move away from each other along the z^* -axis, hence, the length of the separator, in each experiment, increases from its initial length of $L = 1.0$. The displacement, in the z -direction, of the nulls through time for all five Series B experiments, is shown in Fig. 4.15a. Firstly, we note that varying b moves the nulls a smaller distance away from their initial positions than varying a . This plot also shows us that the two nulls behave differently as b is varied. As b is increased, the lower nulls move further away from their initial z -coordinates along the z -axis through the experiment. However, the upper nulls move furthest away from the initial z -coordinate for values of b which are smaller. This same sort of asymmetry was not seen when varying the parameter a .

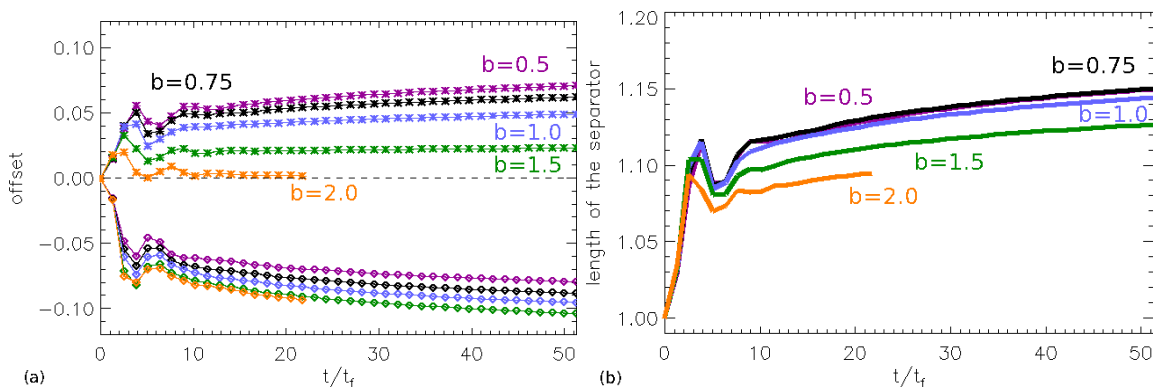


Figure 4.15: (a) The offset in the z -direction, from the null's z -positions at $t = 0t_f$, of the lower nulls (diamonds) and upper nulls (asterisks) against time and (b) the length of the separator against time for the experiments with $b = 0.5$ (purple), $b = 0.75$ (black), $b = 1.0$ (blue), $b = 1.5$ (green) and $b = 2.0$ (orange).

The lengths of the separator, for each of the five experiments, are plotted in Fig. 4.15b. Here, we see that the length of the separator increases with decreasing parameter b (the opposite of what was seen when a was varied). Even if the experiment with $b = 2.0$ was evolved further, it does not appear that this separator's length would exceed that of the experiments with lower values of b . The rate at which the separator lengthens appears to be unaffected by the value of the parameter b .

The length of the separators at $t_c = 21.97t_f$ and at the equilibrium times, t_{eq} , of each experiment are given in Table 4.4. The behaviour of these values is the opposite of that found in Sect. 4.3 where the parameter a was varied. In this section we begin by looking at how the strength of the current in the current layer varies with b and then investigate how varying the parameter b affects the width and depth of the current layer.

Strength of the current layer

Fig. 4.16a displays j_{\parallel} plotted along the z^* -axis (the z -axis normalised such that the separator lies between $z^* = 0$ and $z^* = 1$) for all experiments investigated in this series. For values of $b \leq 1.0$, there is little distinction between the curves of j_{\parallel} along the separator are outwith the separator. For these values of b , j_{\parallel} has a maximum value just under half-way

Table 4.4: The length of the current layer, l_{sep} , and its width, w , and depth, d , (measured using the contour method) at $z = 0.5$ and the maximum/mean current along the separator at $t_c = 21.79t_f$ for comparison and at the equilibrium times, t_{eq} , for all experiments in Series B, where $a = 0.5$ and $c = 0.25$.

Exp.	l_{sep}		w at $z = 0.5$		d at $z = 0.5$		Max $ \mathbf{j} $		Mean $ \mathbf{j} $	
	b	t_c	t_{eq}	t_c	t_{eq}	t_c	t_{eq}	t_c	t_{eq}	t_c
0.5	1.13	1.15	0.312	0.304	0.036	0.024	16.52	23.74	14.79	20.76
0.75	1.13	1.15	0.310	0.292	0.036	0.028	16.33	23.36	14.79	20.52
1.0	1.13	1.14	0.302	0.262	0.036	0.026	16.80	23.93	15.51	21.36
1.5	1.11	1.13	0.272	0.240	0.032	0.024	24.99	31.8	18.78	25.43
2.0	1.10	1.10	0.256	0.256	0.030	0.030	42.79	42.79	24.27	24.27

along the separator and the value of j_{\parallel} outwith the separator, along the z -axis, is fairly constant. When $b = 1$, a slight change is seen in the value of j_{\parallel} near the upper null. This change becomes more significant as b is increased further. For values of $b > 1.0$, the profile of j_{\parallel} along the separator changes. The maximum value of j_{\parallel} is no longer greatest at around $z = 0.4$, but instead peaks at the upper null. It appears that the limited relaxation time of the experiment with $b = 2.0$ has led to the current at the lower null not being as large as it should be.

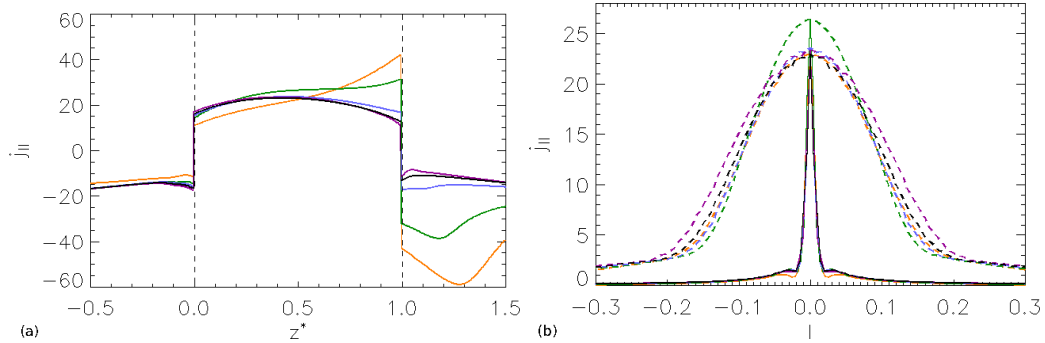


Figure 4.16: Plots of j_{\parallel} (a) along the z^* -axis and (b) through the depth (solid) and across the width (dashed) of the current layer, in the plane perpendicular to the separator at $z = 0.5$, for the experiments with $b = 0.5$ (purple), $b = 0.75$ (black), $b = 1.0$ (blue), $b = 1.5$ (green) and $b = 2.0$ (orange).

The maximum and mean values of $|\mathbf{j}|$ found along the separator at $t_c = 21.97t_f$, for comparison, and at the equilibrium times of each experiment are given in Table 4.4. These values highlight that the strength of the current layer does not vary greatly for smaller values of b ($b \leq 1.0$) but increases sharply when $b > 1.0$.

The highest value of j_{\parallel} achieved, in a slice through the depth and across the width of the current layer in the $z = 0.5$ plane, is around $j_{\parallel} = 26.3$ when $b = 1.5$ (Fig. 4.16b). Here we see in all experiments that there is a peak in current at the current layer, where $l = 0.0$, and the current falls off in value away from this point. The maximum value of the current found through the depth and across the width of the current layer varies slightly

as b increases and increases significantly when $b = 1.0$. We expect that the experiment with $b = 2.0$ (orange lines) would also show a significant increase in the strength of the current in the current layer, if it were relaxed for longer.

Width and depth of the current layer

The depths of the current layers (solid lines in Fig. 4.17a), measured using the contour method, are similar for all values of b , except for when $b = 2.0$ which is the experiment which was not relaxed for as long as the other experiments. Using the contour method, the width of the current layer (dashed lines in Fig. 4.17a) decreases, with increasing b , except, again, for when $b = 2.0$.

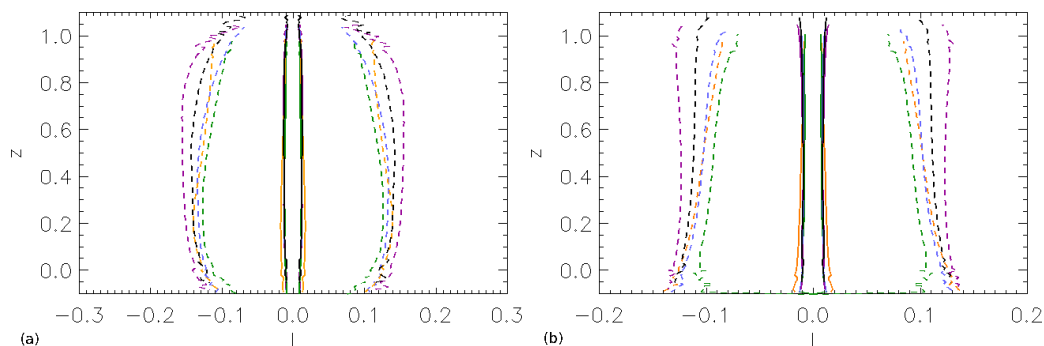


Figure 4.17: The width (dashed) and depth of the current layer using (a) the contour method and (b) the FWHM method for the experiments with $b = 0.5$ (purple), $b = 0.75$ (black), $b = 1.0$ (blue), $b = 1.5$ (green) and $b = 2.0$ (orange).

The values of the widths and depths of the current layer, in a cut perpendicular to the separator at $z = 0.5$, are given in Table 4.4 at $t_c = 21.97t_f$ and at t_{eq} . We see from this table that the width of the current layer decreases with increasing b at t_c and at the equilibrium times of each experiment. The value of the depth remains unchanged at $t = t_c$ as b increases until $b \geq 1.5$ where the depth decreases as b continues to increase. At t_{eq} no clear relationship can be deduced between the value of the depth and the value of b .

Using the FWHM method, the depths of the current layers (solid lines in Fig. 4.17b) do not vary greatly as b is altered (except when $b = 2.0$ due to this experiment not being fully relaxed), but the width of the current layer (dashed lines in Fig. 4.17b) increases steadily as b is increased. Again, this does not hold when $b = 2.0$ since this system is not fully relaxed.

4.4.3 Current layer twist

The angle through which the current layer twists, from the lower null to the upper null along the z -axis, increases slowly as the value of b increases (Fig. 4.18). Moreover, the value of the twist increases more slowly here than when the parameter a was varied (Sect. 4.3). The angle through which the current layer twists, decreases between the experiments with $b = 1.5$ and $b = 2.0$. We suspect this is because the experiment with $b = 2.0$ is not relaxed for as long as the other experiments.

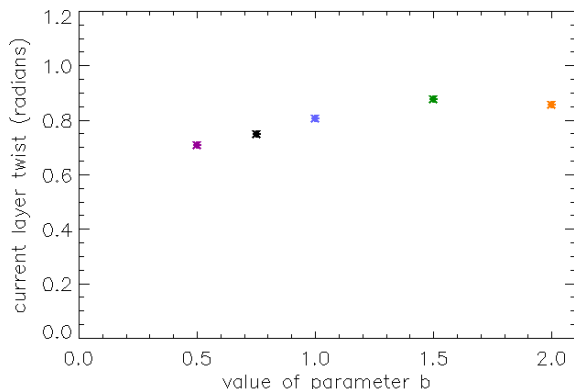


Figure 4.18: The angle (radians) through which the current layer twists, from the lower to the upper null, for the experiments with $b = 0.5$ (purple), $b = 0.75$ (black), $b = 1.0$ (blue), $b = 1.5$ (green) and $b = 2.0$ (orange).

4.4.4 Pressure along the length, through the depth and across the width of the current layer

Fig. 4.19 shows contours of the plasma pressure difference ($p - p_0$), in planes perpendicular to the separator at $z = 0.5$, for all five experiments where b is varied. In all contours, we see, again, that the separatrix surfaces have collapsed towards each other and formed cusp regions within which lies enhanced plasma pressure. Outwith the cusp regions the plasma pressure falls off in value. The results here are similar to those found in Sect. 4.3.

In order to determine the quantitative difference between the pressure in the different experiments, we analyse the plasma pressure and the magnetic pressure in cuts through the current layer.

Fig. 4.20a displays the plasma pressure plotted through the depth (solid lines) and across the width (dashed lines) of the current layer, for all five experiments where b is varied. As expected, from the contours of the plasma pressure difference in Fig. 4.19, the plasma pressure peaks through the depth of the current layer at the separator. We see here that the magnitude of the plasma pressure, through the depth of the current layer, decreases as b increases. The magnitude of the plasma pressure here appears to be approaching a limit as b is decreased. Across the width the plasma pressure is shown to be fairly constant, again, as expected from Fig. 4.19.

The magnetic pressure, plotted through the depth of the current layer, behaves inversely to the plasma pressure here (solid lines in Fig. 4.20b) and has a minimum at the separator for all five experiments investigated here where b is varied. A minimum magnitude of magnetic pressure through the depth of the current layer appears to be approached as the value of b is lowered here. The magnetic pressure is fairly constant across the width of the current layer (dashed lines Fig. 4.20b).

Figs. 4.20c and 4.20d show the total pressure (the plasma pressure plus the magnetic pressure) plotted through the depth and across the width of the current layer, respectively. We see that the total pressure is fairly constant over the current layer for all five experiments, and, the values of the total pressure are much more similar between experiments here than was seen for Series A in Sect. 4.3.

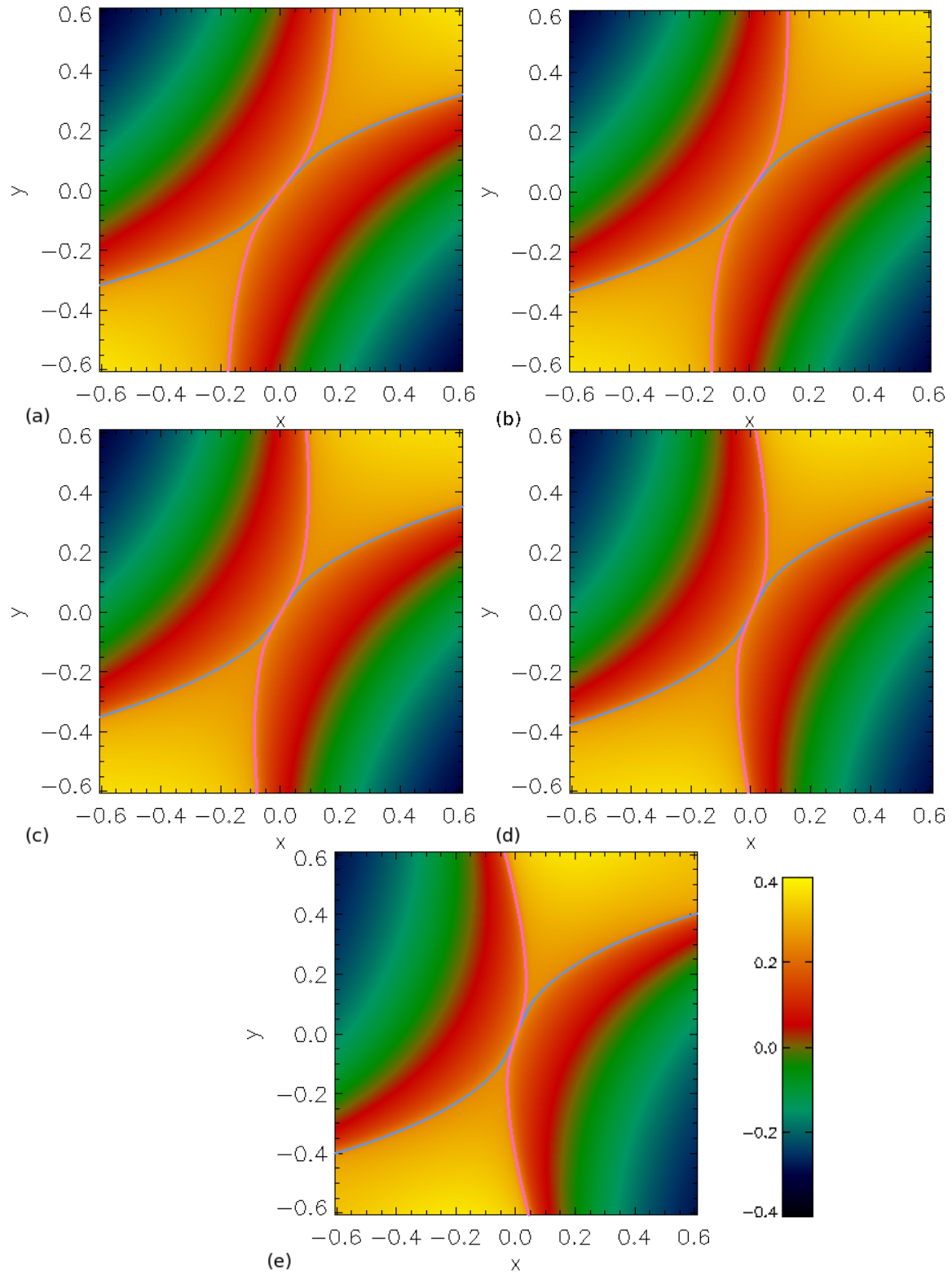


Figure 4.19: Contours of the plasma pressure difference $(p - p_0)$ in planes perpendicular to the separator at $z = 0.5$ for the experiments with (a) $b = 0.5$, (b) $b = 0.75$, (c) $b = 1.0$, (d) $b = 1.5$ and (e) $b = 2.0$. The pale-blue/pink lines highlight where the separatrix surfaces of the lower/upper nulls intersect each cut, respectively.

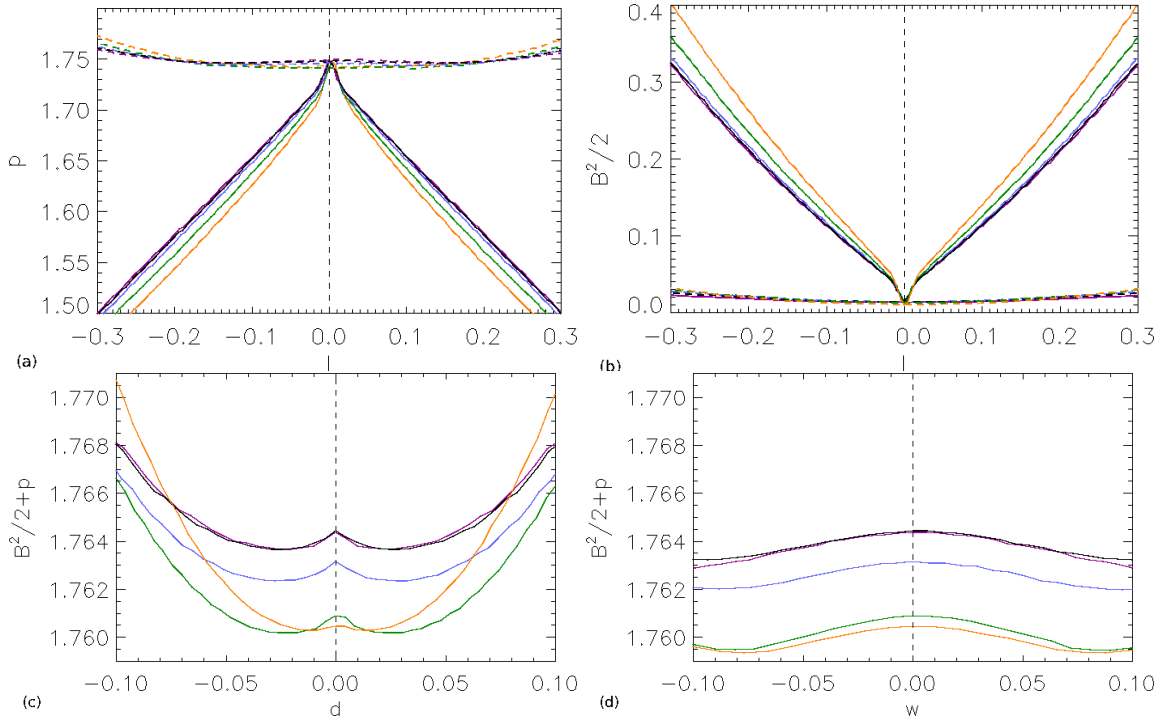


Figure 4.20: The (a) plasma pressure and the (b) magnetic pressure plotted across the width (dashed) and through the depth (solid) of the current layer in planes perpendicular to the separator at $z = 0.5$ and the sum of the magnetic and plasma pressures plotted (c) through the depth and (d) across the width of the current layer, in planes perpendicular to the separator at $z = 0.5$, for the experiments with $b = 0.5$ (purple), $b = 0.75$ (black), $b = 1.0$ (blue), $b = 1.5$ (green) and $b = 2.0$ (orange).

The plasma pressure along the z^* -axis always has a maximum around half-way along the separator for all experiments where b is varied, except when $b = 2.0$ (Fig. 4.21a). When $b = 2.0$ the maximum value of plasma pressure occurs near the upper null. We believe if this experiment had been able to relax for longer then the maximum would have shifted to be in line with the other four experiments. Excluding this case, as b is increased, the maximum value of plasma pressure found along the separator, decreases. This is the opposite of what was found when a was increased. Below the lower null the plasma pressure is fairly constant for all five experiments, but this is not so above the upper null along z .

Fig. 4.21b shows how the magnetic pressure behaves along the z^* -axis for all the experiments where b is varied. The magnetic pressure vanishes at the nulls and has a maximum along the separator at $z^* = 0.5$ for all experiments (except when $b = 2.0$). Outwith the separator, the magnitude of the magnetic pressure increases in strength away from the nulls. Above the upper null, along the z -axis, the magnitude of the magnetic pressure increases with increasing b , but below the lower null, no variation like this is observed (except for when $b = 2$).

The total pressure (the plasma pressure plus the magnetic pressure) is plotted along the normalised length of the separator in Fig. 4.21c. The total pressure is almost identical,

along the separator, for all experiments where b is varied (apart from the experiment with $b = 2.0$). The value of the total pressure varies less along the separator for differing values of b than it did when a was varied (Sect. 4.3). We do not expect the total pressure to be constant along the separator since there is a component of magnetic tension along the separator.

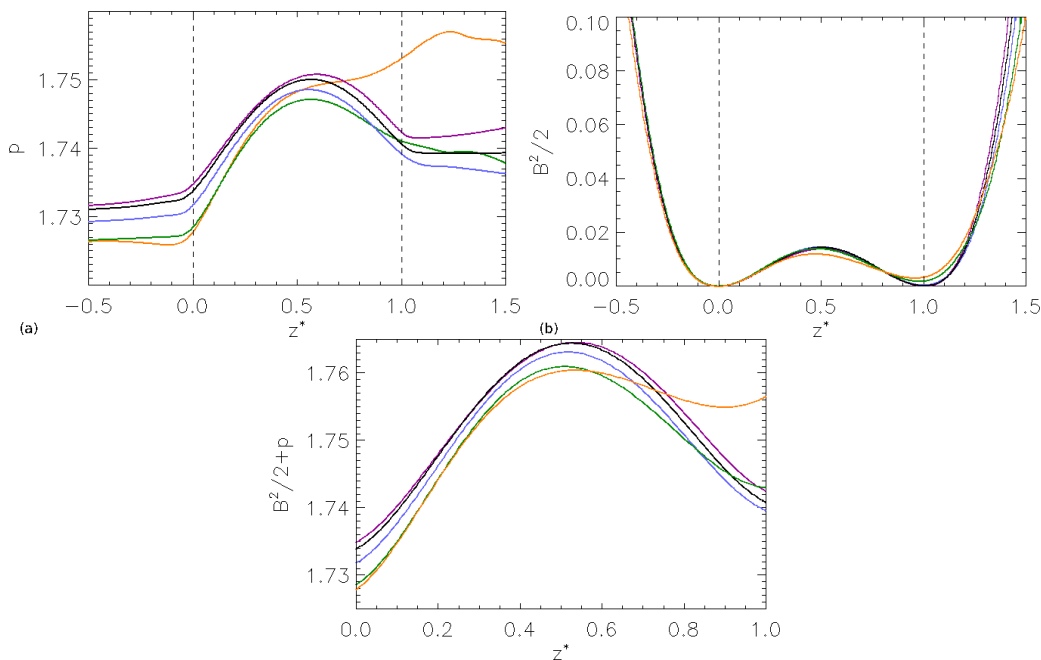


Figure 4.21: Plots along the z^* -axis of (a) the plasma pressure, (b) the magnetic pressure and (c) the sum of the plasma and magnetic pressures for the experiments with $b = 0.5$ (purple), $b = 0.75$ (black), $b = 1.0$ (blue), $b = 1.5$ (green) and $b = 2.0$ (orange).

4.4.5 Total force along the length, through the depth and across the width of the current layer

Due to the fact that the magnetic field about a separator takes an infinite time to collapse (Chapt. 3), the total force in the equilibrium of each experiment where b is varied is small everywhere except along the separatrix surfaces and at the separator (Fig. 4.22). The total force is strongest when $b = 2.0$ (Fig. 4.22e) but this could be due to this experiment not being relaxed for as long as the other four experiments were. There appears to be slightly more residual force along the separatrix surfaces of the experiment with $b = 1.5$ than those with $b = 0.5$ and $b = 1.0$ and so the value of b does appear to affect the magnitude of the residual forces in the equilibrium state of the experiments. This is tested by taking 1D cuts through the width and depth of the separator in the $z = 0.5$ plane.

The total force acts outwards from around half-way along the separator towards the nulls for all experiments, except when $b = 2.0$, which was relaxed for less time (Fig. 4.23a). The magnitude of the total force, acting towards the lower null, increases slightly as b is increased. The total force pushing towards the upper null is fairly constant for low values

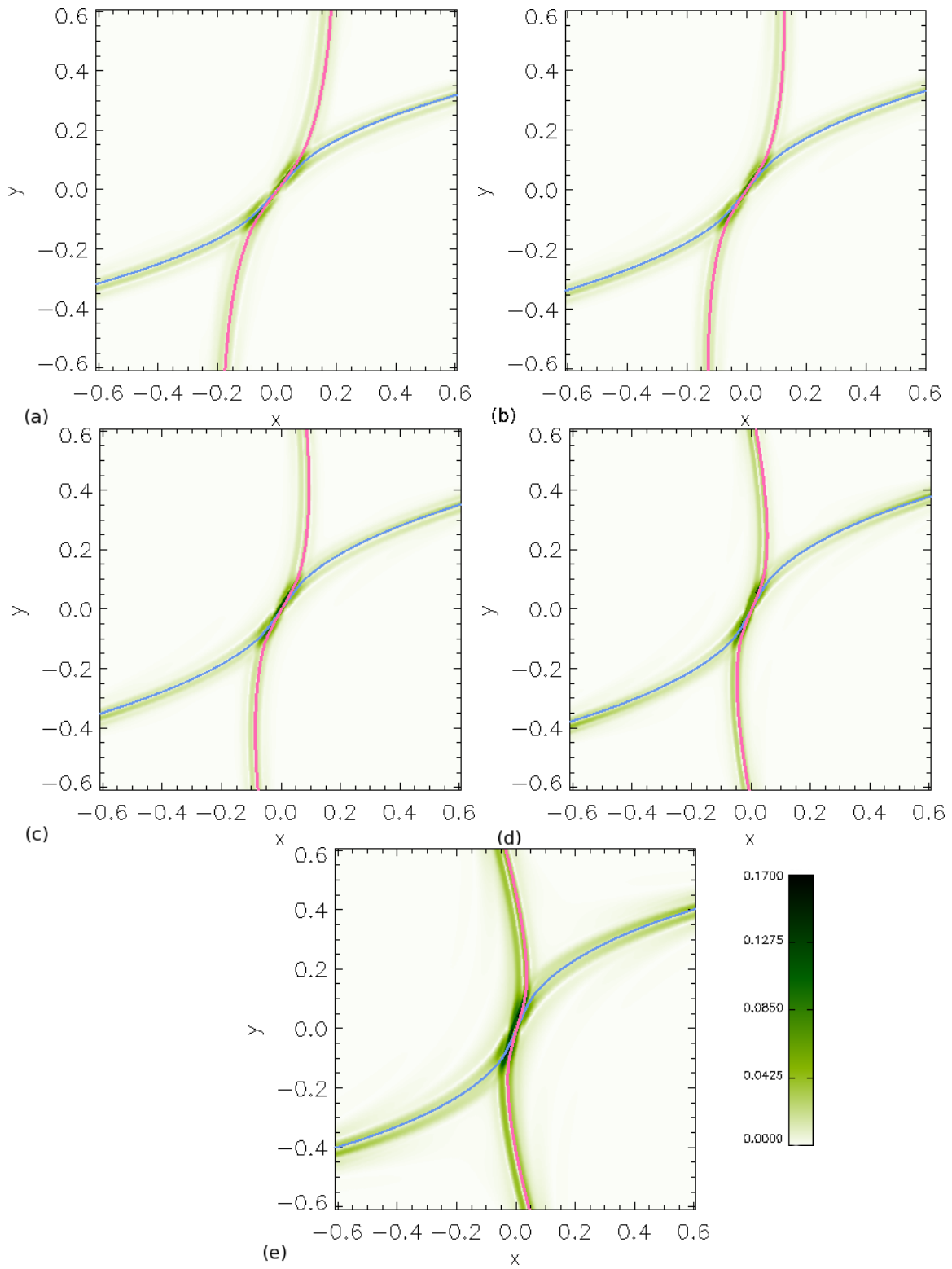


Figure 4.22: Contours of the total force in planes perpendicular to the separator at $z = 0.5$ for the experiments with (a) $b = 0.5$, (b) $b = 0.75$, (c) $b = 1.0$, (d) $b = 1.5$ and (e) $b = 2.0$.

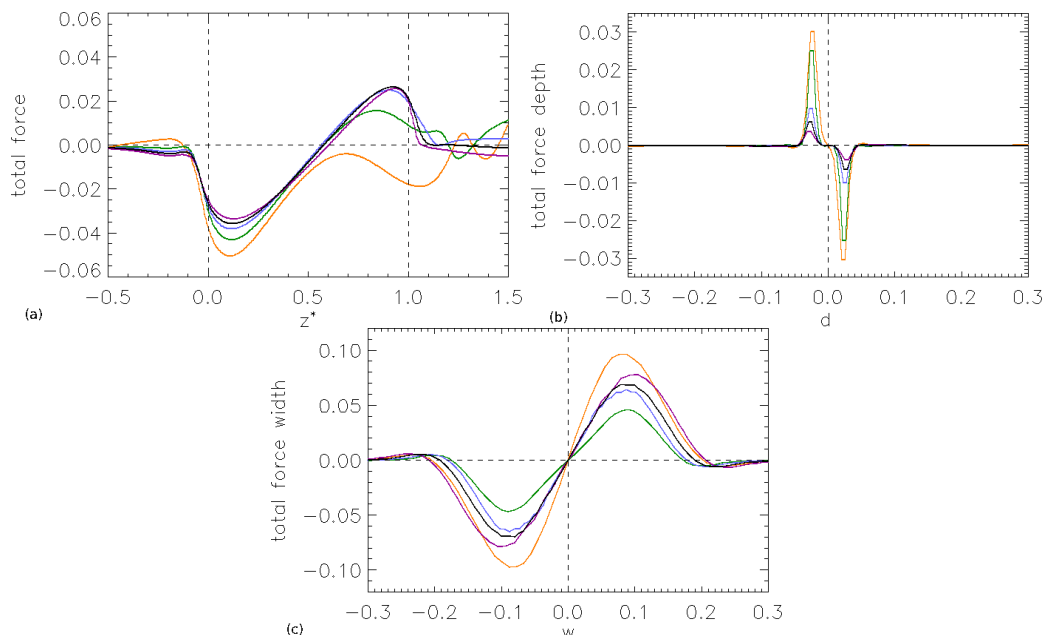


Figure 4.23: Plots of the total force (a) along the z^* -axis, (b) through the depth and (c) across the width of the current layer for the experiments with $b = 0.5$ (purple), $b = 0.75$ (black), $b = 1.0$ (blue), $b = 1.5$ (green) and $b = 2.0$ (orange).

of b , but when $b > 1$ the total force here decreases. The magnitude of the total force here is comparable with that found in the experiments where a was varied (Sect. 4.3).

The total force, through the depth of the current layer, acts inwards towards the separator, at $d = 0.0$, for all experiments where b is varied (Fig. 4.23b). This implies that the total force, in all experiments where b is varied, is acting to make the current layer thinner through its depth. The magnitude of the total force increases as the value of b is increased. We note, from this plot, that the magnitude of the total force increases sharply when $b > 1.0$. This trend, of sharply increasing past a certain value of the parameter being varied, was also observed in Sect. 4.3 where a was varied.

Across the width of the current layer, the total force decreases in magnitude as b increases, except when $b = 2.0$ which has the greatest magnitude here (Fig. 4.23c). This is the opposite of what was observed when a was varied and indicates that the total force (which acts outwards from the separator, in all experiments and hence widens the current layer) is stronger here for a low value of b . This is the opposite of what was observed in a slice through the depth of the current layer.

4.5 MHS equilibria C: The effects of varying parameter c

Finally, we discuss the effects on the MHS equilibrium formed through non-resistive relaxation experiments in which the magnetic field parameter c has been varied. The parameter c , like a , can alter the geometry of the field lines in the separatrix-surface planes, as we will show in this section. Results from five experiments will be discussed here where $c = -0.25$, $c = 0.0$, $c = 0.25$, $c = 0.5$ and $c = 0.75$. The equilibrium times of each of these experi-

ments (Table 4.1) are $t = 51, 28t_f$ for all but the experiment with $c = 0.75$ which has a shorter time of $t = 32.05t_f$.

4.5.1 Initial and equilibrium magnetic skeleton

The eigenvalues and eigenvectors of the lower null are the same here as those given in Sect. 4.4, where b was varied, but those of the upper null are different

$$\begin{aligned}
 \lambda_{sl} &= -\frac{5}{4}, & \mathbf{e}_{sl} &= \left(\frac{1}{3}, 1, 0\right)^T, \\
 \lambda_{f_1l} &= \frac{1}{2}, & \mathbf{e}_{f_1l} &= (0, 0, 1)^T, \\
 \lambda_{f_2l} &= \frac{3}{4}, & \mathbf{e}_{f_2l} &= (3, 1, 0)^T, \\
 \lambda_{su} &= 1 + c, & \mathbf{e}_{su} &= \left(1 + \frac{4}{3}c, 1, 0\right)^T, \\
 \lambda_{f_1u} &= -\frac{1}{2}, & \mathbf{e}_{f_1u} &= (0, 0, 1)^T, \\
 \lambda_{f_2u} &= -\frac{1}{2} - c, & \mathbf{e}_{f_2u} &= (0, 1, 0)^T.
 \end{aligned} \tag{4.5}$$

Therefore, varying the parameter c will affect the geometry of the lower null since it varies \mathbf{e}_{su} . If the spine of the upper null moves, the separatrix surface of the lower null must move such that it is still bounded by this spine. The spine of the upper null should become more aligned with the x -axis as c is increased. The skeletons of the initial magnetic fields are shown in Figs. 4.24a to 4.24e. The field lines in the separatrix-surface plane of the upper null, are more aligned with the x -axis for higher values of c , as expected. In Figs. 4.24f to 4.24j, the equilibrium magnetic skeletons are shown with a purple isosurface drawn at $j_{\parallel} = 10$ in each case. These images show that a twisted current layer has formed along the length of the separator throughout the non-resistive MHD relaxation of each experiment.

The intersections of the initial magnetic field's separatrix surfaces (dashed lines) with the plane at $z = 0.5$, for all experiments discussed in this series, are shown in Fig. 4.25a. In this plot, the solid lines show where the equilibrium separatrix surfaces of the experiments with $c = -0.25$ and $c = 0.75$ intersect this plane. The position of the lower null's separatrix surface moves slightly as c is varied, but the upper null's separatrix surface is fairly stationary. This suggests that the angle between the separatrix surfaces of the nulls increases as c is increased.

Fig. 4.25b shows where the equilibrium magnetic field's separatrix surfaces (solid lines) intersect this plane, and also shows the intersections of the initial separatrix surfaces (dashed lines) for the experiments with $c = -0.25$ and $c = 0.75$. The amount, by which the separatrix surfaces have folded towards each other through the non-resistive MHD relaxation, increases slightly as c decreases. Both Figs. 4.25a and 4.25b indicate that the separatrix surfaces do not move on the boundaries throughout the relaxation, as required.

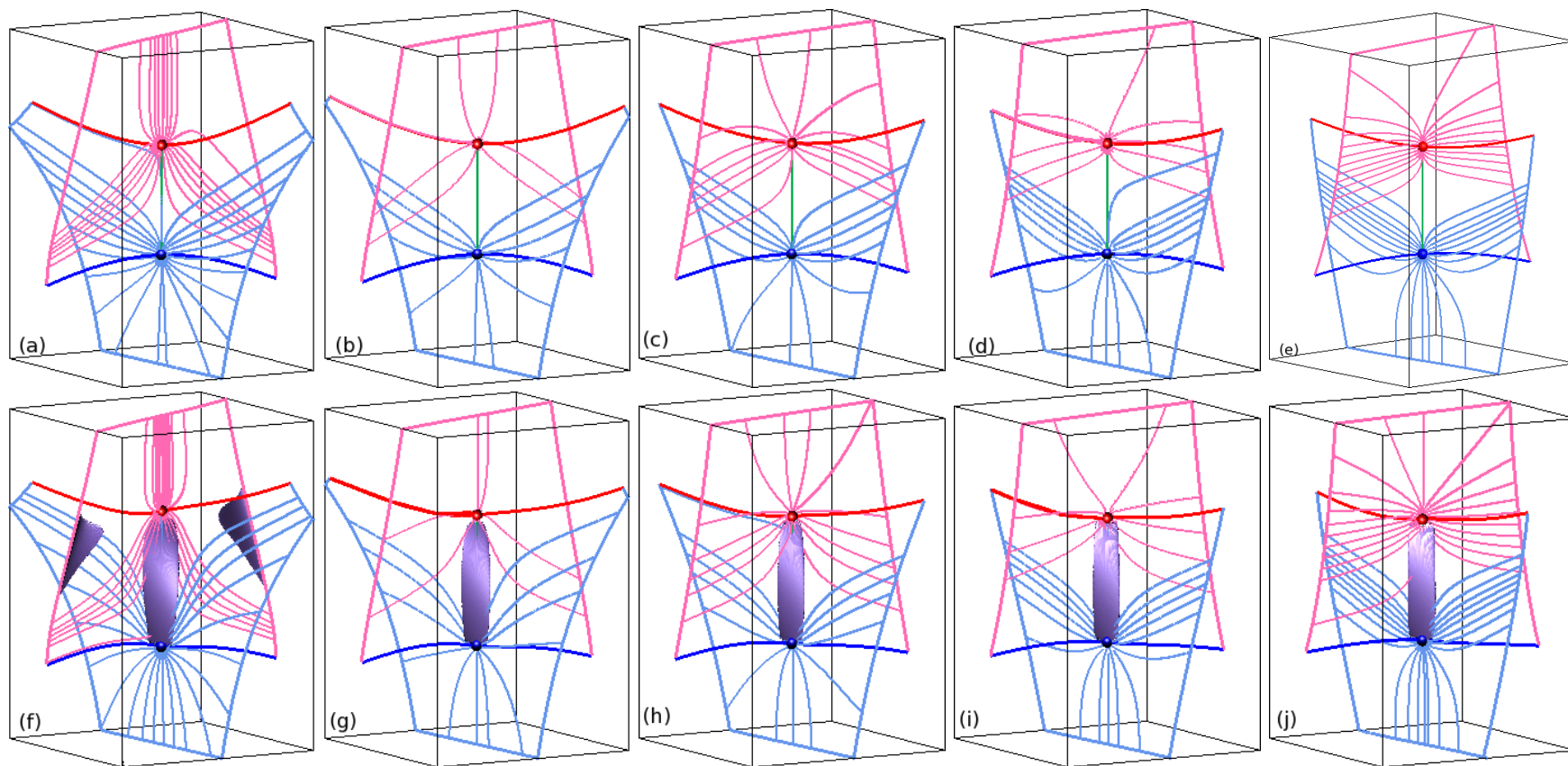


Figure 4.24: Skeletons of the initial (top row) and MHS equilibrium (bottom row) magnetic fields for the experiments whose initial conditions are exactly the same, save for the value of c : (a) and (f) $c = -0.25$, (b) and (g) $c = 0.0$, (c) and (h) $c = 0.25$, (d) and (i) $c = 0.5$ and (e) and (j) $c = 0.75$. Here the lower/upper nulls are blue/red spheres with blue/red spines and pale-blue/pink separatrix surfaces, respectively. The solid pale-blue/pink lines highlight where the separatrix surfaces intersect the boundaries of the box. The separator, green line, links the null points. In the bottom row, a purple isosurface is drawn at $j_{\parallel} = 10$ in each figure.

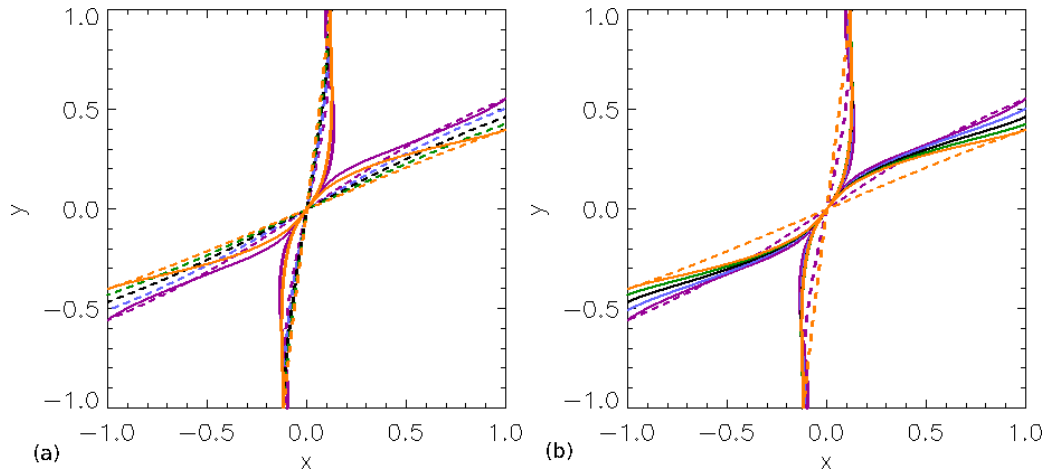


Figure 4.25: Intersections of (a) the initial (dashed lines) and (b) the equilibrium (solid lines) magnetic field's separatrix surfaces. The solid/dashed lines in (a)/(b) show the intersections of the equilibrium/initial separatrix surfaces with this plane for the experiments with $c = -0.25$ (purple) and $c = 0.75$ (orange). The separatrix surface of the lower null spans $x = -1.0$ to $x = 1.0$ and the separatrix surface of the upper null spans $y = -1.0$ to $y = 1.0$. The coloured lines represent the experiments with $c = -0.25$ (purple), $c = 0.0$ (blue), $c = 0.25$ (black), $c = 0.5$ (green) and $c = 0.75$ (orange).

4.5.2 Properties of the current layer

We now discuss how various properties of the equilibrium current layers, i.e., the dimensions and strength, are affected by varying the parameter c .

Length of the current layer

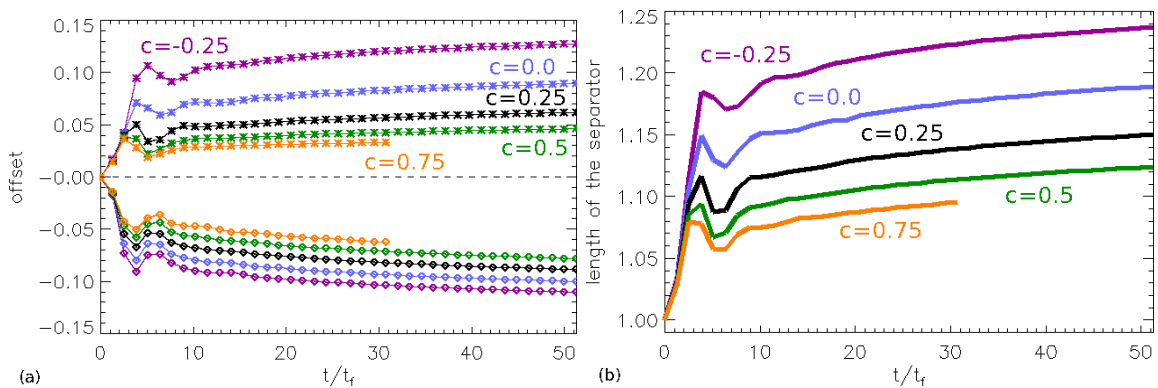


Figure 4.26: (a) The offset in the z -direction, from the null's z -positions at $t = 0t_f$, of the lower nulls (diamonds) and upper nulls (asterisks) against time and (b) the length of the separator against time for the experiments with $c = -0.25$ (purple), $c = 0.0$ (blue), $c = 0.25$ (black), $c = 0.5$ (green) and $c = 0.75$ (orange).

Table 4.5: The length of the current layer, l_{sep} , its width, w , and depth, d , (measured using the contour method) at $z = 0.5$ and the maximum/mean current along the separator at $t_c = 32.05t_f$ for comparison and at the equilibrium times, t_{eq} , for all experiments in Series C where $a = 0.5$ and $b = 0.75$.

Exp.	l_{sep}		w at $z = 0.5$		d at $z = 0.5$		Max $ \mathbf{j} $		Mean $ \mathbf{j} $	
	c	t_c	t_{eq}	t_c	t_{eq}	t_c	t_{eq}	t_c	t_{eq}	t_c
-0.25	1.23	1.24	0.312	0.320	0.026	0.022	17.79	22.07	15.53	18.94
0.0	1.18	1.19	0.314	0.312	0.032	0.028	17.86	21.83	15.59	18.75
0.25	1.14	1.15	0.306	0.292	0.032	0.028	19.20	23.36	17.16	20.52
0.5	1.11	1.12	0.290	0.266	0.030	0.026	21.81	26.39	20.01	23.92
0.75	1.10	1.10	0.280	0.280	0.026	0.026	26.45	26.45	24.32	34.32

As the experiments begin, the nulls move apart along the z -axis and oscillate a little before slowly moving away from each other, along this direction, throughout the experiment. The offset from the null's original z -positions are shown in Fig. 4.26a. The lower and upper nulls move further away from their initial z -coordinates, along the z -axis, as c decreases. This is a different result to that discussed in Sects. 4.3 and 4.4. The separator length, plotted against time for all five experiments where c is varied, is shown in Fig. 4.26b. The lengths of the current layers are given in Table 4.5 at $t_c = 32.05t_f$ for comparison and at the equilibrium times. We see from Fig. 4.26b, and the values Table 4.5, that the length of the separator increases as c decreases and the length of equilibrium separator for the experiment with $c = -0.25$, exceeds the length of all separators considered in this chapter. We also note that as c is increased, the length of the separator appears to be approaching a minimum. The opposite behaviour was observed in Sects. 4.3 and 4.4 where a maximum length of separator was approached as a and b were increased, respectively.

Strength of the current layer

Fig. 4.27a shows the value of j_{\parallel} plotted along the z^* -axis for the five experiments where the parameter c is varied. The maximum value of j_{\parallel} , along the separator, for the experiment with $c = -0.25$ is greater than the maximum found when $c = 0.0$. Other than this exception, the maximum value of j_{\parallel} along the separator increases as c increases. The value of j_{\parallel} is always positive along the separator and negative outwith the separator, along the z -axis. This was also found to be the case in Sects. 4.3 and 4.4. The position at which the maximum value of j_{\parallel} occurs is shifted further to the right as the magnitude of c increases with the maximum occurring at $z = 0.37$, $z = 0.4$, $z = 0.48$ and $z = 0.75$ for the experiments where the magnitude of c is $c = 0.0$, $c = 0.25$, $c = 0.5$ and $c = 0.75$, respectively.

The value of j_{\parallel} , plotted through the depth and across the width of the current layer in the $z = 0.5$ plane, peaks at the separator (Fig. 4.27b). We see a similar trend in this plot to that seen in Fig. 4.27a: the magnitude of j_{\parallel} increases at the separator ($l = 0.0$) as c increases, but when $c = -0.25$ the peak value achieved exceeds that of $c = 0.0$. We have already seen that the length of the separator, and hence by our definition, the length of the current layer, increases as c increases.

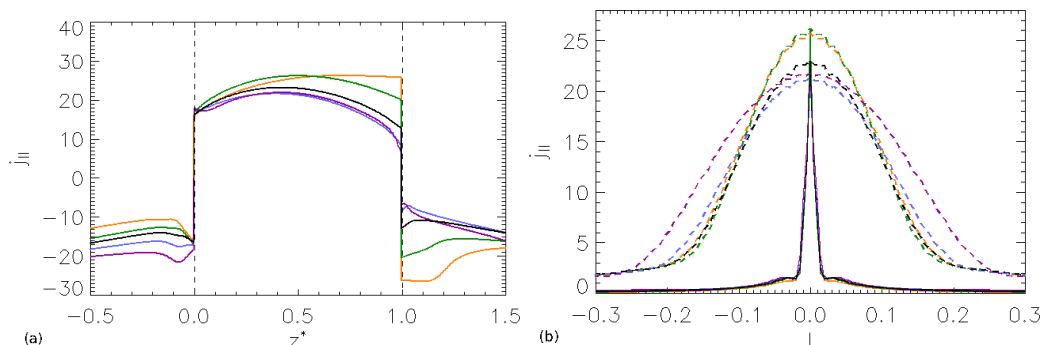


Figure 4.27: Plots of j_{\parallel} (a) along the z^* -axis and (b) through the depth (solid) and across the width (dashed) of the current layer in the plane perpendicular to the separator at $z = 0.5$ for the experiments with $c = -0.25$ (purple), $c = 0.0$ (blue), $c = 0.25$ (black), $c = 0.5$ (green) and $a = 0.75$ (orange).

The maximum and mean values of $|\mathbf{j}|$ are given in Table 4.5 at $t_c = 32.05t_f$ and at the equilibrium times. At t_c the maximum and mean values of $|\mathbf{j}|$ increase as c increases, but not linearly. At the equilibrium times, the mean and maximum values of $|\mathbf{j}|$ increase as c increases except between $c = -0.25$ and $c = 0.0$.

Width and depth of the current layer

Using the contour method, discussed in Chapt. 3, we find that the depth of the current layer remains fairly constant as c is varied (Fig. 4.28a). The depths of the current layers, measured at $z = 0.5$, are given in Table 4.5 at t_c and t_{eq} . Near the upper null, the depth of the current layer curves in slightly for the experiment with $c = -0.25$ indicating that the current layer thins here.

As c is increased from $c = -0.25$ the width of the current layer (measured using the contour method) decreases until $c > 0.5$ where the width increases. Note, the experiment with $c = 0.75$ was not run for as long as the other experiments though. The widths, measured at $z = 0.5$, are given in Table 4.5 at t_c and t_{eq} . Near the nulls there is no clear relationship between the width of the current layers and the value of c .

Using the FWHM method, Fig. 4.28b, the depth of the current layer does not vary greatly near to the lower null and around the middle of the separator, as c is altered, but close to the upper null the depth of the current layer decreases as c increases. The width of the current layer, calculated using the FWHM method, decreases as c increases. This behaviour holds for all values of c investigated here, except when $c = 0.75$. Note, however, this experiment was not relaxed for as long as the other four and so this might account for the current layer being wider in this case than in the experiments with lower values of c .

4.5.3 Current layer twist

In Sects. 4.3 and 4.4, where the parameters a and b were varied, respectively, the angle through which the current layers twists increased as a and b were increased. Here, when

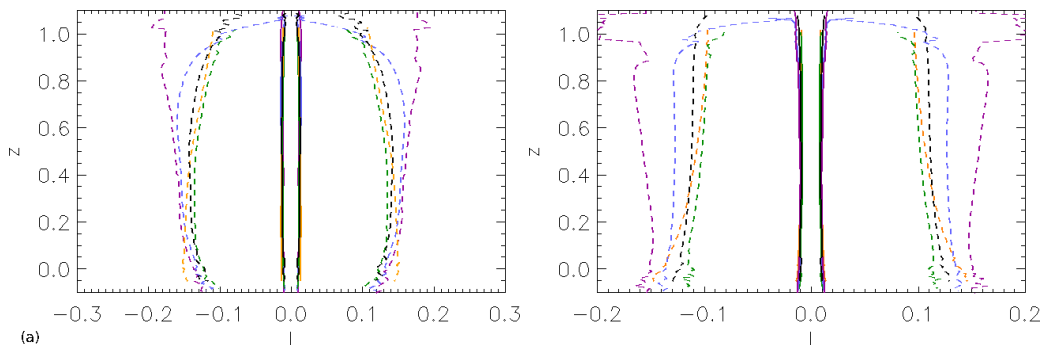


Figure 4.28: The width (dashed) and depth (solid) of the current layer found using (a) the contour method and (b) the FWHM method for the experiments with $c = -0.25$ (purple), $c = 0.0$ (blue), $c = 0.25$ (black), $c = 0.5$ (green) and $c = 0.75$ (orange).

the value of c is increased, the angle through which the current layer twists, from the lower to the upper null, decreases (Fig. 4.29).

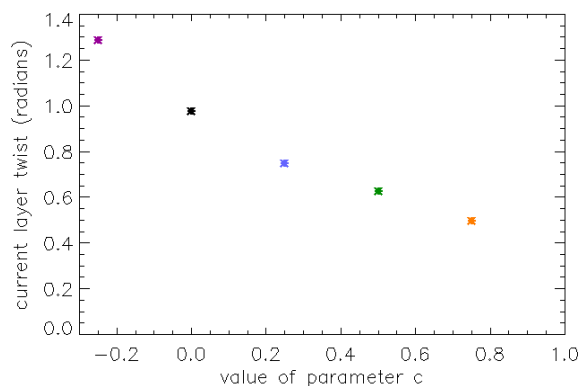


Figure 4.29: The angle (radians) through which the current layer twists from the lower to the upper null for the experiments with $c = -0.25$ (purple), $c = 0.0$ (blue), $c = 0.25$ (black), $c = 0.5$ (green) and $c = 0.75$ (orange).

4.5.4 Pressure along the length, through the depth and across the width of the current layer

As with the experiments already discussed in this chapter, where the parameters a and b were varied, the non-resistive MHD relaxation of the magnetic skeletons, which have varying parameter c , causes cusp regions to form about the separator (Fig. 4.30). Within these cusps lie regions where the plasma pressure has become enhanced, and outwith the cusps, the plasma pressure falls off in value (Fig. 4.30). In this figure, contours of the plasma pressure difference (the plasma pressure minus the initial plasma pressure) are drawn in a cut across the separator at $z = 0.5$. The plasma pressure difference appears to be very similar here in all five experiments. To analyse the effects that varying c has on both the plasma pressure and the magnetic pressure, we now examine these properties plotted through the depth, across the width and along the length of the current layer.

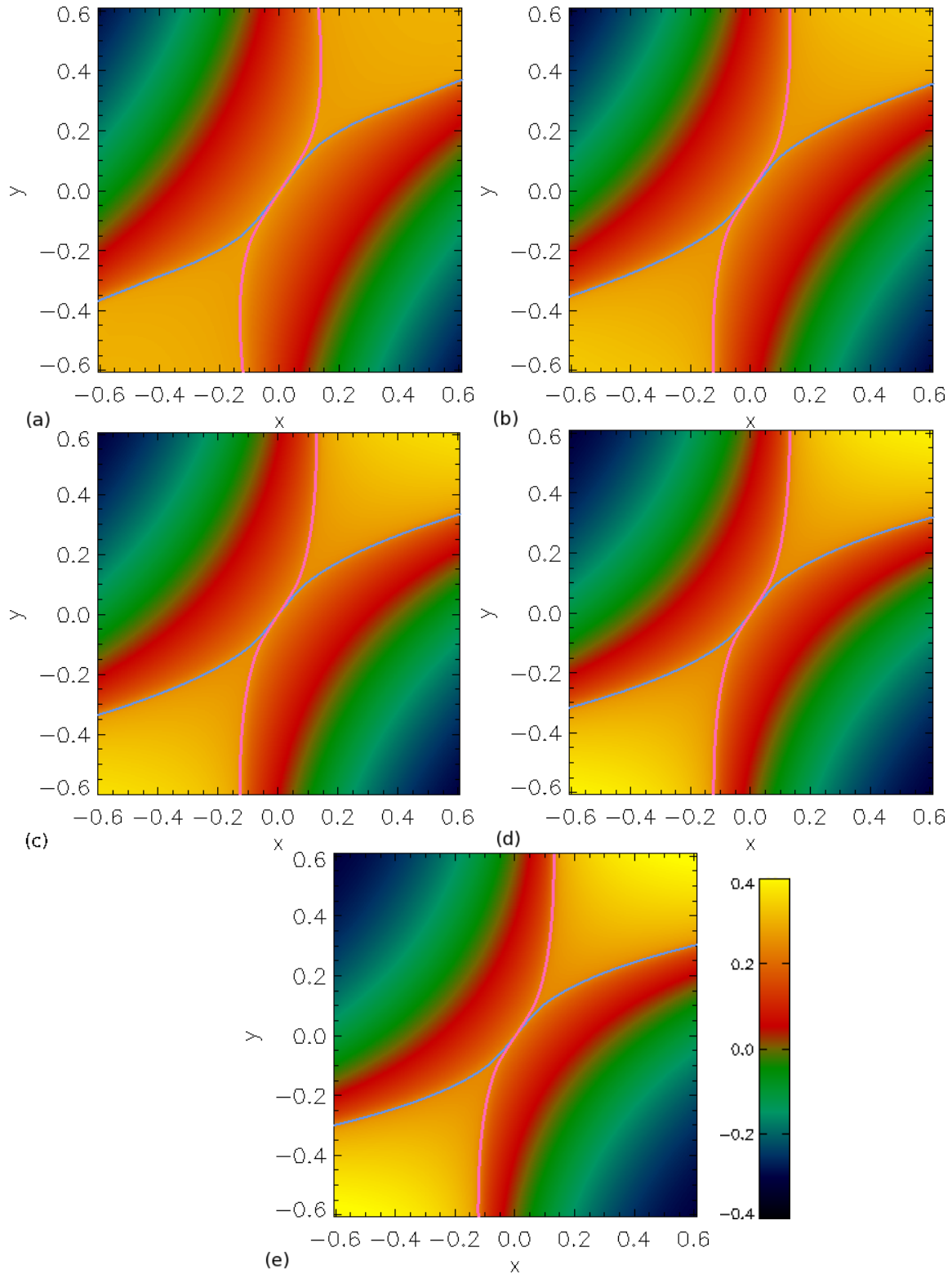


Figure 4.30: Contours of the plasma pressure difference $(p-p_0)$, in planes perpendicular to the separator at $z = 0.5$ for the experiments with (a) $c = -0.25$, (b) $c = 0.0$, (c) $c = 0.25$, (d) $c = 0.5$ and (e) $c = 0.75$. The pale-blue/pink lines highlight where the separatrix surfaces of the lower/upper nulls intersect each cut, respectively.

As c is increased, the value of the plasma pressure, through the depth and across the width of the current layer, decreases (Fig. 4.31a). This was also found in the experiments where a and b were varied (Sects. 4.3 and 4.4). There is a visible spread between the value of the plasma pressure across the width of the current layer (where the plasma pressure is fairly constant) which was not visible when varying the value of a and b . Hence, varying c leads to a bigger distinction between the values of the equilibrium plasma pressure than varying the parameters a or b . The plasma pressure peaks at the current layer ($l = 0.0$) in a slice through the depth of the current layer and falls off either side of it. The difference between the plasma pressure when $c = 0.5$ and when $c = 0.75$ is not as great as that seen between the other values. This is probably due to the fact that the experiment with $c = 0.75$ was not relaxed for as long as the other experiments.

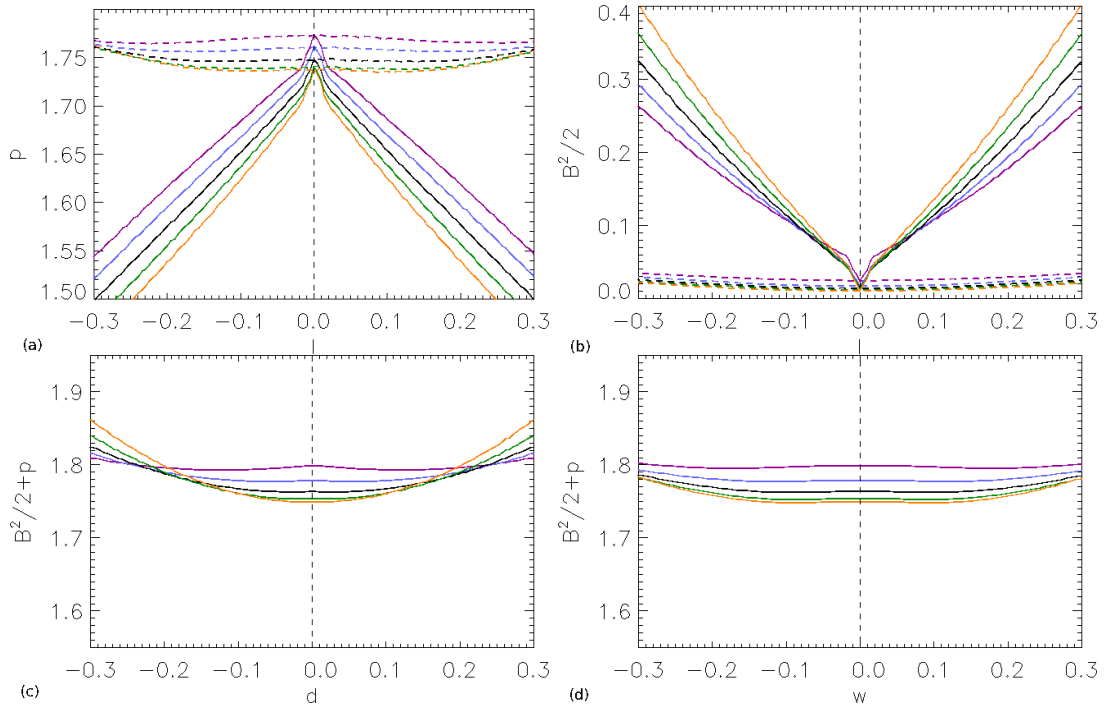


Figure 4.31: Plots of (a) the plasma pressure and (b) the magnetic pressure across the width (dashed) and through the depth (solid) of the current layer in the plane perpendicular to the separator at $z = 0.5$ and the total pressure (c) through the depth and (d) across the width of the current layer in the plane perpendicular to the separator at $z = 0.5$ for the experiments with $c = -0.25$ (purple), $c = 0.0$ (blue), $c = 0.25$ (black), $c = 0.5$ (green) and $c = 0.75$ (orange).

The magnetic pressure behaves inversely to the plasma pressure through the depth of the current layer (solid lines Fig. 4.31b). The magnetic pressure has a minimum value at the separator, through the depth and the magnitude of the magnetic pressure increases as c is increased. Note, the profile of the magnetic pressure close to the separator, for the experiment with $c = -0.25$, becomes much narrower than the profiles for the other experiments where c is varied. This may suggest that the magnetic pressure is more concentrated around the separator, for this experiment, than in the other experiments.

Across the width of the current layer, the magnetic pressure is fairly constant for all experiments.

The total pressure is constant through the depth and across the width of the current layer, for all experiments investigated here where c is varied (Figs. 4.31c and 4.31d).

Unlike in Sect. 4.3, where an increase in a led to an increase in the plasma pressure along the z -axis, we find here that as c is increased, the plasma pressure along the z -axis decreases, as was found when b was varied (Fig. 4.32a). The distinction between the different experiments in this plot is the clearest out of all series of experiments where we have varied a , b or c . This trend occurs regardless of c being negative or positive. The position of the maximum plasma pressure moves to towards lower values of z as c is increased, with the position occurring at $z = 0.66$, $z = 0.65$, $z = 0.56$, $z = 0.48$ and $z = 0.41$ for the experiments with $c = -0.25$, $c = 0.0$, $c = 0.25$, $c = 0.5$ and $c = 0.75$, respectively.

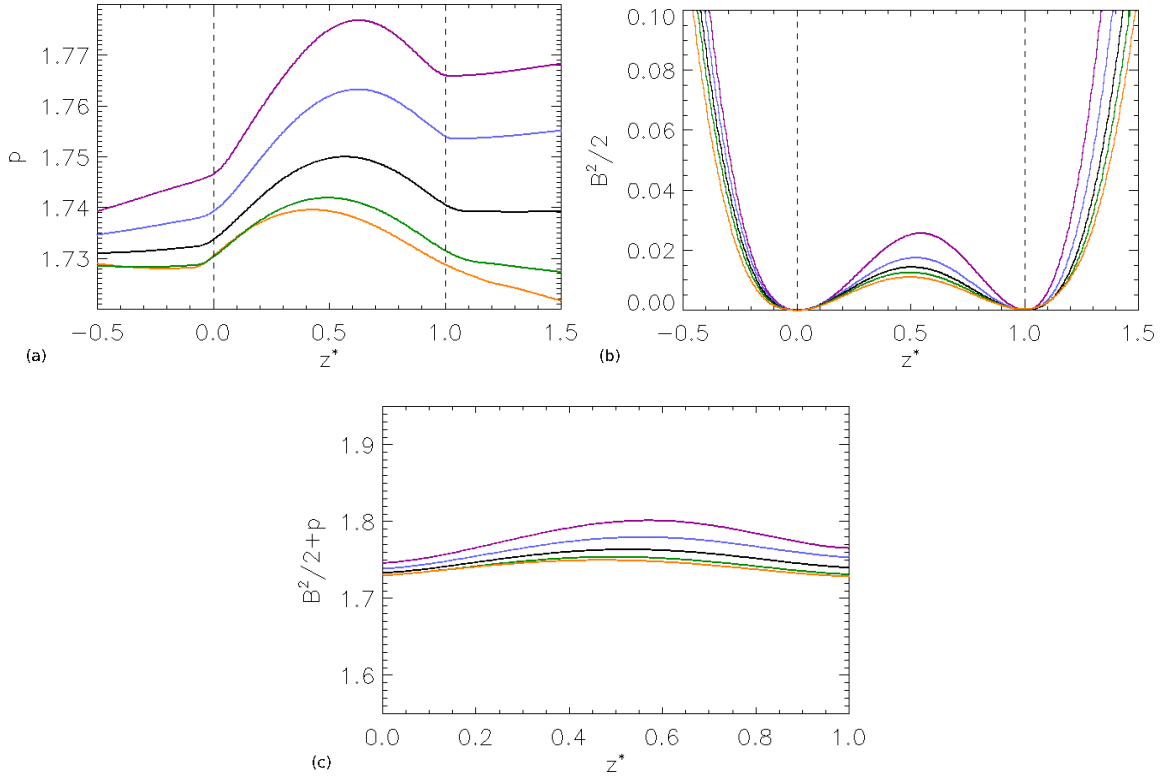


Figure 4.32: Plots along the z^* -axis of (a) the plasma pressure, (b) the magnetic pressure and (c) the total pressures for the experiments with $c = -0.25$ (purple), $c = 0.0$ (blue), $c = 0.25$ (black), $c = 0.5$ (green) and $c = 0.75$ (orange).

This means that the maximum value of plasma pressure always occurs along the separator. Outwith the separator, along the z -axis, the plasma pressure increases beyond the upper null for low values of c , and decreases here for larger values of c . The value of the plasma pressure decreases away from the lower null, along the z -axis, for the experiments with low values of c , but is fairly constant for the experiments where c is high ($c = 0.5$ and $c = 0.75$).

Fig. 4.32b shows the magnetic pressure along the normalised z -axis, z^* . As expected, the magnetic pressure vanishes at the null points and has a maximum half-way along the separator, for all five experiments in this Series where c is varied. The magnitude of the magnetic pressure, along the separator, decreases as c increases. The plasma pressure shows the same behaviour along the separator, but when a was varied the opposite behaviour occurs.

The total pressure, which is not expected to be zero along the length of the separator, varies less along the separator as c increases (Fig. 4.32c).

4.5.5 Total force along the length, through the depth and across the width of the current layer

In a cut half-way across the separator (at $z = 0.5$) the total force is observed to be small everywhere except along the separatrix surfaces and is strongest at the current layer (Fig. 4.33). The residual forces along the separatrix surfaces, and at the current layer, are strongest for the experiments with $c = -0.25$ (Fig. 4.33a) and $c = 0.75$ (Fig. 4.33e). The latter experiment has not been relaxed for as long as the other four and hence it is expected to have larger residual forces in the equilibrium state.

The magnitude of the total force plotted along the separator, decreases slightly as c is increased (Fig. 4.34a). This indicates that the smaller c is initially, the less relaxed the system is. This was observed also in the contours of the total force shown in Fig. 4.33. Here, in all experiments, the total force acts outwards from some point along the separator towards the nulls, acting to lengthen the current layer. The position at which the total force changes sign along the z -axis decreases as c is increased with the position occurring at $z = 0.68$, $z = 0.66$, $z = 0.58$, $z = 0.48$ and $z = 0.39$ for the experiments with $c = -0.25$, $c = 0.0$, $c = 0.25$, $c = 0.5$ and $c = 0.75$, respectively.

The total force through the depth of the current layer behaves qualitatively as expected, with the total force pushing in on either side of the current layer, acting to squeeze it thinner (Fig. 4.34b). The magnitude of the total force here follows the trend of increasing with the initial value of c . This holds for all experiments investigated here, except the experiment where $c = -0.25$. It appears that having a negative value for c leads to greater residual forces acting to diminish the depth of the current layer.

Across the width of the current layer, the total force acts outwards from the separator, widening the current layer, in each experiment where c is varied (Fig. 4.34c). The magnitude of the total force here appears to slightly decrease as c increases, except when $c = 0.75$. This experiment was not relaxed for as long as the other four experiments, hence, the residual forces here are, as expected, larger.

4.6 Growth rate of the current layer

We have already seen that in all three series of experiments, the maximum current along the length of the current layer grows as a , b and c are increased. We find that the maximum current along the separator evolves according to the equation

$$|j| = j_{sep} \left(1 + a_0 \frac{t}{t_f} \right)^{a_1}, \quad (4.6)$$

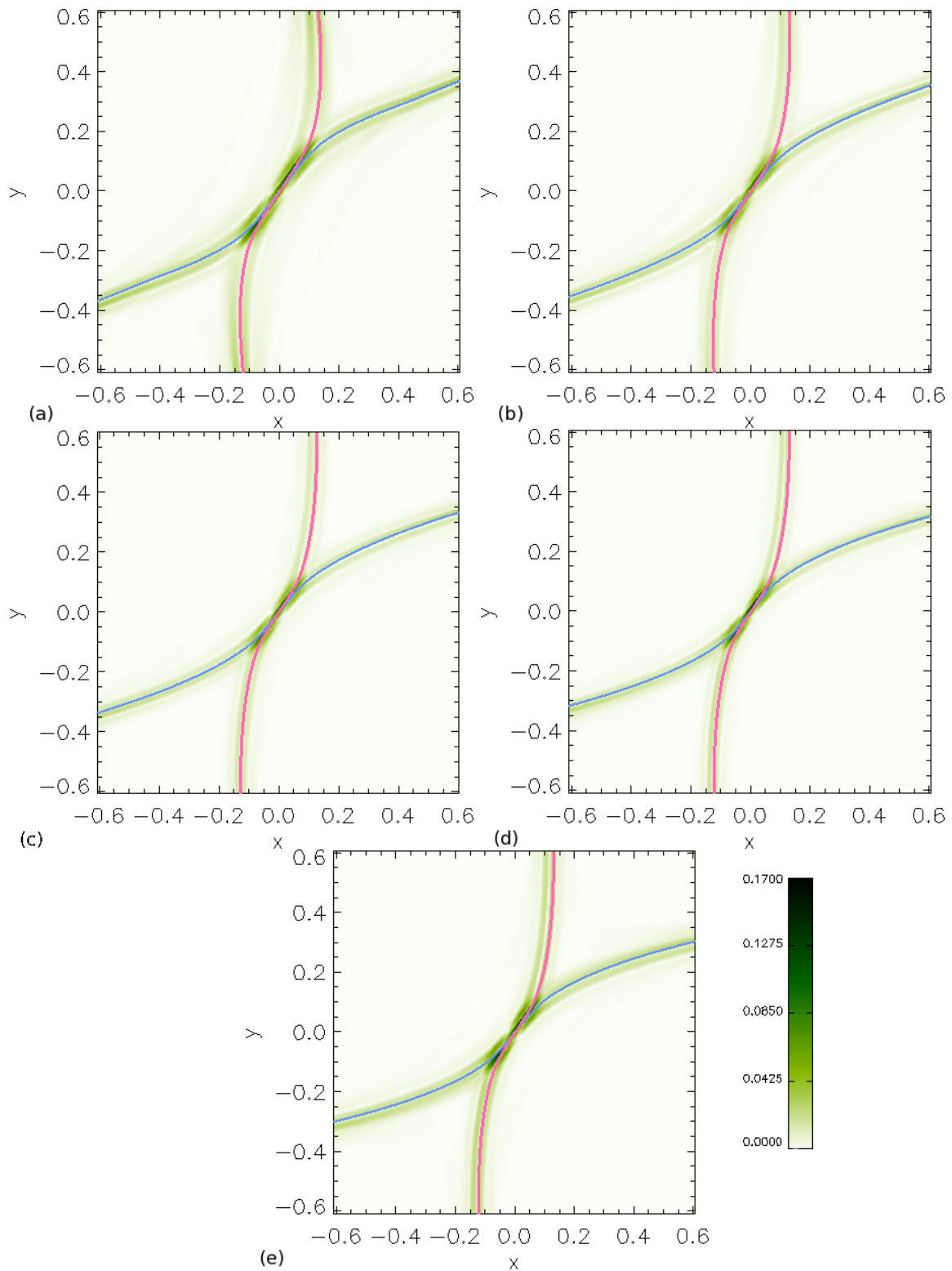


Figure 4.33: Contours of the total force in planes perpendicular to the separator at $z = 0.5$ for the experiments with (a) $c = -0.25$, (b) $c = 0.0$, (c) $c = 0.25$, (d) $c = 0.5$ and (e) $c = 0.75$.

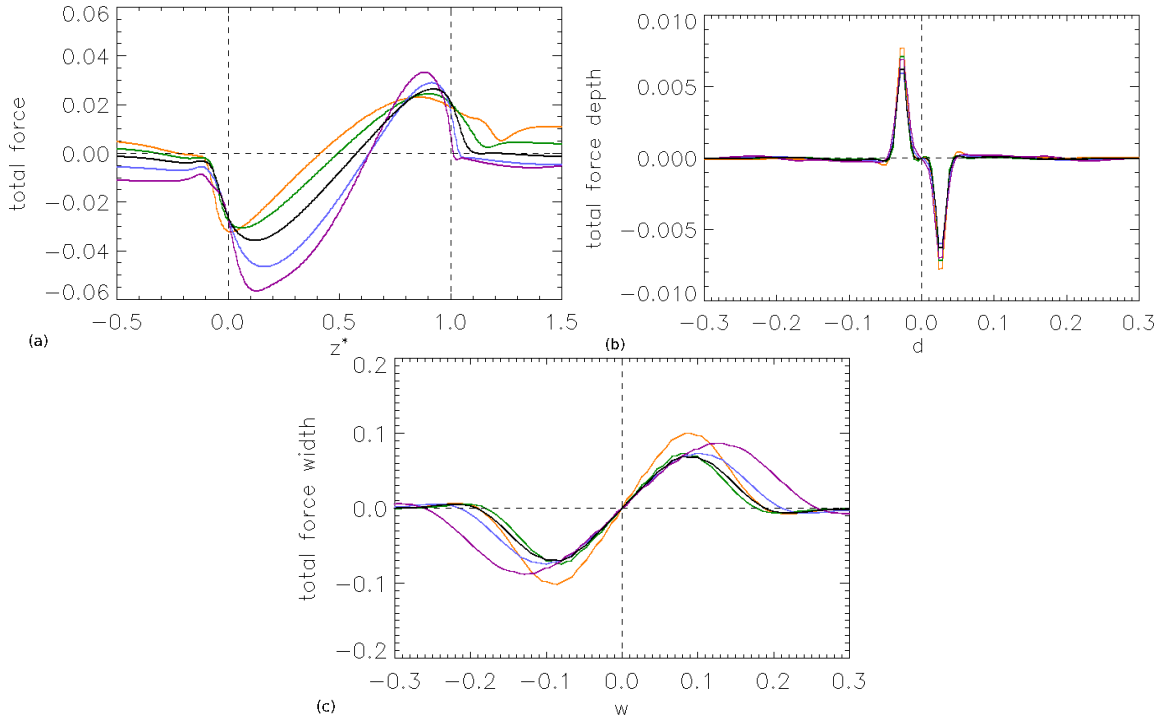


Figure 4.34: Plots of the total force (a) along the z^* -axis, (b) through the depth and (c) across the width of the current layer in planes perpendicular to the separator at $z = 0.5$ for the experiments with $c = -0.25$ (purple), $c = 0.0$ (blue), $c = 0.25$ (black), $c = 0.5$ (green) and $a = 0.75$ (orange).

where $j_{sep} = 1.5$ in all experiments discussed in this chapter. Here, we examine how the maximum value of $|\mathbf{j}|$ along the separator evolves through each series of experiments and quantify the parameters a_0 (amplitude) and a_1 (growth rate) in Eq. 4.6 for all experiments.

Fig. 4.35a displays the maximum value of $|\mathbf{j}|$, found along the separator, for all experiments in Series A with curves of Eq. 4.6 over plotted where the values of a_0 and a_1 , for each experiment, are given in Table 4.6. Here, it is clear that as a increases, the maximum value of $|\mathbf{j}|$ and the growth rate of the current in the separator current layer, increase. The only exception to this is that the strength of the current in the current layer, the growth rate and the amplitude are greater when $a = 0.15$ than when $a = 0.25$. This figure also shows that there is no linear relationship between the value of a and the maximum current in the current layer.

The maximum current found along the separator varies little over time when $b < 1.0$ but increases sharply in size when $b > 1.0$ (Fig. 4.35b). This suggests there is some threshold, over which b begins to affect the strength of the current along the separator. Curves of Eq. 4.6 are over plotted in Fig. 4.35b, with the values of a_0 and a_1 given in Table 4.6, for each experiment in Series B. The rate of growth, and the amplitude, are fairly constant as b increases until $b > 1.0$. After this value of b , the amplitude rises sharply when $b = 1.5$, but then decreases when $b = 2.0$. The growth rate of the current decreases when $b = 1.5$ but then increases when $b = 2.0$, as evidenced from Fig. 4.35b. This experiment had to be ended much sooner than the other experiments due to the

Table 4.6: The amplitude, a_0 , and the growth rate, a_1 , associated with Eq. 4.6, for all experiments in Series A, B and C.

Experiment	a_0	a_1
$a = 0.15$	18.265	0.369
$a = 0.25$	16.378	0.360
$a = 0.5$	23.362	0.386
$a = 0.75$	30.853	0.427
$a = 0.85$	33.721	0.440
$b = 0.5$	23.74	0.386
$b = 0.75$	23.362	0.386
$b = 1.0$	23.929	0.388
$b = 1.5$	150.5	0.346
$b = 2.0$	85.1	0.452
$c = -0.25$	22.072	0.378
$c = 0.0$	21.829	0.378
$c = 0.25$	23.362	0.386
$c = 0.5$	26.393	0.397
$c = 0.75$	26.448	0.429

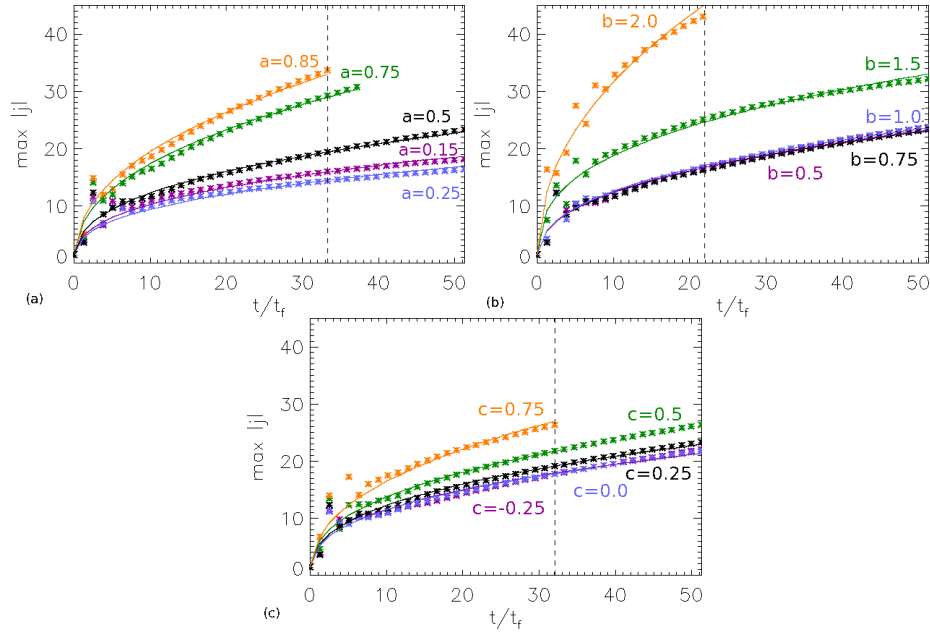


Figure 4.35: The maximum value of $|j|$ found along the separator, through time, for all the experiments discussed in (a) Series A, (b) Series B and (c) Series C. The value of the parameter that distinguishes each experiment is shown in the same colour as the line it matches on each plot. Over plotted are curves of Eq. 4.6 with values of a_0 and a_1 given in Table 4.6. The black dashed vertical lines highlight the run time of the experiment which ended first within each series.

effects of numerical diffusion. The rapid growth rate seen in this experiment causes a strong current increasing the chance of numerical diffusion making a significant effect. We note, however, that the experiment with $c = 0.75$ also had to be stopped early, but the value of the maximum current along the separator at its equilibrium time is about 1.5 times smaller than that of the experiment with $b = 2.0$

Finally, Fig. 4.35c displays how the maximum current along the separator evolves through all the experiments in Series C. The maximum current does not vary much when c is small ($c < 0.25$), but does increase more noticeably when $c > 0.5$. This behaviour is reflected in the amplitude and growth rate of the maximum current in the current layer (Table 4.6). This suggests that c only starts to affect the properties of the current along the separator once it has a larger value.

4.7 Summary

We have investigated the effects of varying the magnetic field parameters a , b and c that appear in the analytical magnetic field equation, Eq. 4.1. In all experiments discussed in this chapter, the initial non-potential magnetic field, with current directed parallel to the separator, is allowed to relax non-resistively over time using the Lare3d code.

All experiments undergo the same energy conversion, with magnetic energy being converted into internal energy through kinetic energy. The amount of magnetic energy available in each experiment increases as all the magnetic parameters (a , b and c) are increased. We have also found that the amount of magnetic energy that remains in the MHS equilibrium increases as a , b and c increase and is significantly higher in the experiment with $b = 2.0$ than in all other experiments. Waves travel in the systems of each experiment, caused by the collapse of the separator, which give rise to adiabatic and viscous heating. We find that in most experiments discussed here, the conversion from magnetic to internal energy occurs from $\sim 76\%$ viscous heating and $\sim 24\%$ adiabatic heating, except for the experiments where a is varied. In this series of experiments, the contribution from the viscous heating increases, and hence the adiabatic heating contribution decreases, as the parameter a increases.

All experiments discussed in this section undergo the same initial collapse of the separatrix surfaces towards each other, due to the initial non-zero Lorentz force, the mean value of which increases with increasing a , b and c . Through the relaxation of each experiment, the nulls initially move apart along the z -axis. Unlike the series of experiments in which increasing the parameters a and b led to greater equilibrium separator lengths, decreasing values of c increase the separator length to values exceeding that found in all other experiments investigated in this chapter.

Throughout the non-resistive relaxation of each high plasma-beta experiment a twisted current layer forms along the separator. The maximum value of current found along the separator was shown to (mostly) follow the same trend for varying a , b and c : the maximum current along the separator increases as a , b or c is increased. The strongest current, in the separator current layer, occurred in the experiment with the largest b value, $b=2.0$.

The widths of the current layer, found in each experiment, were shown, overall, to increase as a increases and decrease as b and c increase. The depths of the current layer, found in each experiment, were shown to decrease as a increases. No clear correlation

could be determined between the value of the depth and the parameters b and c .

Table 4.7: The length of the current layer, l_{sep} , and its width, w , and depth, d , (measured using the contour method) at $z = 0.5$, mean plasma beta, $\bar{\beta}$, the plasma beta half-way along the equilibrium separator, $\beta_{l_{sep}/2}$, and the parameters a_0 and a_1 from Eq. 4.6. The parameters which are not being varied take the values $a = 0.5$, $b = 0.75$ and $c = 0.25$.

Exp.	l_{sep}	w at $z = 0.5$	d at $z = 0.5$	$\bar{\beta}$	$\beta_{l_{sep}/2}$	a_0	a_1
$a = 0.15$	1.06	0.264	0.032	12.21	1869.8	18.265	0.369
$a = 0.25$	1.09	0.264	0.030	9.65	607.31	16.378	0.360
$a = 0.5$	1.15	0.292	0.028	6.85	120.44	23.362	0.386
$a = 0.75$	1.17	0.316	0.026	5.85	46.41	30.853	0.427
$a = 0.85$	1.17	0.324	0.024	5.56	34.65	33.721	0.440
$b = 0.5$	1.15	0.304	0.024	8.26	124.99	23.74	0.386
$b = 0.75$	1.15	0.292	0.028	6.85	120.44	23.362	0.386
$b = 1.0$	1.14	0.262	0.026	5.92	119.42	23.929	0.388
$b = 1.5$	1.13	0.240	0.024	4.68	124.43	150.5	0.346
$b = 2.0$	1.10	0.256	0.030	3.92	145.87	85.1	0.452
$c = -0.25$	1.24	0.320	0.022	8.90	70.04	22.072	0.378
$c = 0.0$	1.19	0.312	0.028	7.89	100.23	21.829	0.378
$c = 0.25$	1.15	0.292	0.028	6.85	120.44	23.362	0.386
$c = 0.5$	1.12	0.266	0.026	6.25	136.75	26.393	0.397
$c = 0.75$	1.10	0.280	0.026	6.05	155.55	26.448	0.429

We have recapped the widths and depths of the current layers for all thirteen experiments in Table 4.7, at the respective equilibrium time of each experiment. This table also gives the mean plasma beta, $\bar{\beta}$, and the plasma beta half-way along the separator in the equilibrium states of each experiment, $\beta_{l_{sep}/2}$. The value of $\bar{\beta}$ decreases as a , b and c increase, leading to higher growth rates, but the value of the plasma beta half-way along the separator does not behave in this way. We note that the trend in the value of $\bar{\beta}$ is not the same as that of the plasma beta at $l_{sep}/2$.

We have seen, that as a increases, the plasma pressure increases along the separator. Therefore, since as a increases $\beta_{l_{sep}/2}$ decreases, increasing a implies that the magnetic field pinches in more around the separator. Also, increasing a leads to a stronger current layer, which is longer, wider and thinner with a higher growth rate (see value a_1 in Table 4.7).

The value of $\beta_{l_{sep}/2}$ decreases as b increases until $b > 1.0$ when $\beta_{l_{sep}/2}$ starts to increase. The strongest current layer was formed when $b = 2.0$, even though this experiment has the highest $\beta_{l_{sep}/2}$ of all the experiments in Series B. A high plasma-beta value indicates that the plasma pressure dominates over the magnetic pressure and so the separatrix surfaces of the nulls can not collapse as much when the plasma beta here is lower. This high value of the plasma beta causes the width and depth of the current layer in this experiment, to not follow the same trend as in the other experiments in Series B.

As c increases, $\beta_{l_{sep}/2}$ increases. Since increasing c leads to weaker plasma pressure along the separator, this implies that as c increases the magnetic field pinches in less tightly around the separator.

The angle through which the equilibrium current layer twists increases as a and b

increase, but decreases as c increases. The maximum amount of twist was achieved for the experiment with $c = -0.25$ (1.3 radians).

In all experiments, the folding of the separatrix surfaces towards each other creates cusp regions about the equilibrium separator, within which plasma pressure enhancements lie and outwith which the plasma pressure falls off. The plasma pressure through the depth and across the width of the current layer behave quantitatively the same in all experiments, as does the magnetic pressure. Again, the experiments where b is varied, appear to be closest to achieving pressure balance through the depth and across the width of the separator. We check for pressure balance across the width and through the depth of the MHS equilibrium current layer, since the magnetic tension force here should be negligible and hence the sum of the plasma and magnetic pressures should be constant. In all the experiments discussed here, we acknowledge that true MHS equilibria can not be achieved in a finite time, hence, it would take an infinite time for true pressure balance to be achieved everywhere across the equilibrium separator.

We found that in the series of experiments where b and c were varied, the value of the plasma pressure along the separator decreased overall as these parameters were increased. The opposite effect was seen when a was varied. Series C showed the clearest distinction between value of parameter and plasma pressure found along the separator. A similar behaviour was observed here for the magnetic pressure. The total pressure along the separator, which should not be constant since there is a magnetic tension force here, was most constant for Series B indicating that these experiments have the weakest magnetic tension force along the separator.

The total force gives a measure of how relaxed the equilibrium state is. Through the depth of the current layer, the magnitude of the total force, which acts here to squeeze the current layer thinner, increases as a , b and c increase. Across the width of the current layer, similar results were found when a and c were increased, however, increasing b decreases the strength of the total force, meaning that it takes longer for a true MHS equilibrium to be reached for the experiments with low b . This is also clear from the steepness of the growth rate curves, which are clearly still rising in Series B, but are fairly flat in Series A and C.

The maximum current along the separator increases as all three magnetic field parameters are increased. However, the strongest current layers formed in each of the three series were all formed in experiments which had to be stopped early due to the effects of numerical diffusion introducing excess nulls into our domain. We have recapped the values of a_0 , which represents the amplitude, and a_1 , which is the growth rate, in Eq. 4.6 for all experiments discussed here in Table 4.7. We note that the experiment which produces the strongest current layer, $b = 2.0$, is also the experiment which has the smallest β (see Table 4.7). This small value of the plasma beta may also contribute to this experiment gaining significant numerical diffusion.

Finally, we have also investigated the separatrix-surface eigenvalues and eigenvectors, of the lower null (Table 4.8) and the upper null (Table 4.9), at $t = 0t_f$ and at the equilibrium times of each experiment, $t = t_{eq}$. In all experiments considered in Series A, B and C, the separatrix-surface eigenvalue, e_{f1} , of both nulls is aligned along the z -axis at $t = 0t_f$ and at $t = t_{eq}$. This is the eigenvector associated with the minor eigenvalue, λ_{f1} , in most of the experiments considered here. This means that the separator current layer forms along the minor axes of the separatrix surfaces in all experiments.

Table 4.8: The ratio of the lower null's separatrix-surface eigenvalues ($\lambda_{f_{2l}}/\lambda_{f_{1l}}$) and the eigenvector $\mathbf{e}_{f_{2l}}$ at $t = 0t_f$ and at $t = t_{eq}$. The parameters which are not being varied take the values $a = 0.5$, $b = 0.75$ and $c = 0.25$.

Exp.	$\lambda_{f_{2l}}/\lambda_{f_{1l}}$		$\mathbf{e}_{f_{2l}}$	
	$t = 0t_f$	$t = t_{eq}$	$t = 0t_f$	$t = t_{eq}$
$a = 0.15$	4.634	60.674	$(2.461, 1, 0)^T$	$(0.821, 0.570, -0.001)^T$
$a = 0.25$	2.854	40.188	$(2.618, 1, 0)^T$	$(0.862, 0.506, -0.001)^T$
$a = 0.5$	1.5	21.22	$(3, 1, 0)^T$	$(0.913, 0.407, -0.006)^T$
$a = 0.75$	1.037	12.988	$(3.370, 1, 0)^T$	$(0.931, 0.365, -0.001)^T$
$a = 0.85$	0.925	12.105	$(3.516, 1, 0)^T$	$(0.937, 0.35, -0.001)^T$
$b = 0.5$	1.5	17.351	$(3, 1, 0)^T$	$(0.900, 0.436, -0.002)^T$
$b = 0.75$	1.5	21.22	$(3, 1, 0)^T$	$(0.913, 0.407, -0.006)^T$
$b = 1.0$	1.5	28.776	$(3, 1, 0)^T$	$(0.920, 0.378, -0.001)^T$
$b = 1.5$	1.5	58.830	$(3, 1, 0)^T$	$(0.928, 0.325, -0.001)^T$
$b = 2.0$	1.5	78.426	$(3, 1, 0)^T$	$(0.950, 0.311, -0.014)^T$
$c = -0.25$	1.5	12.654	$(3, 1, 0)^T$	$(0.915, 0.404, -0.002)^T$
$c = 0.0$	1.5	14.942	$(3, 1, 0)^T$	$(0.916, 0.401, -0.006)^T$
$c = 0.25$	1.5	21.22	$(3, 1, 0)^T$	$(0.913, 0.407, -0.006)^T$
$c = 0.5$	1.5	30.251	$(3, 1, 0)^T$	$(0.902, 0.433, -0.006)^T$
$c = 0.75$	1.5	34.325	$(3, 1, 0)^T$	$(0.89, 0.455, -0.003)^T$

In Table 4.8, we have given the ratio of the major eigenvalue to the minor eigenvalue of the lower null ($\lambda_{f_{2l}}/\lambda_{f_{1l}}$), and the major eigenvalues associated eigenvector, $\mathbf{e}_{f_{2l}}$, at $t = 0t_f$ and at $t = t_{eq}$ for all experiments where a , b and c are varied. The ratio of the separatrix-surface eigenvalues gives a measure of how strongly the field lines are aligned along the major axis of the separatrix surface. We call $\lambda_{f_{2l}}$ the major eigenvalue and $\lambda_{f_{1l}}$ the minor eigenvalue, however, these labels flip if the ratio of these values is smaller than one.

As a increases, the major axis of the separatrix surface of the lower null becomes less dominant over the minor axis, at $t = 0t_f$ and at $t = t_{eq}$. At $t = 0t_f$, the minor axis actually becomes the major axis when $a = 0.85$. However, looking at how this ratio varies as each experiment in Series A relaxes, the major axis becomes more dominant. The values of the eigenvector $\mathbf{e}_{f_{2l}}$ implies that as a increases, the major axis becomes more aligned along the $y = x/3$ line, at $t = 0t_f$ and at $t = t_{eq}$. As each experiment in Series A relaxes the major axis becomes less strongly aligned along the x -axis. The experiments with $\mathbf{e}_{f_{2l}}$ most aligned along the x -axis, at $t = t_{eq}$, correspond to the experiments with the smallest $\bar{\beta}$ at this time. Also, in Series A the values of $\bar{\beta}$ and $\beta_{l_{sep}/2}$ were smallest for $a = 0.85$.

As b increases, the initial ratio between the separatrix-surface eigenvalues of the lower null remain fixed as do the associated eigenvectors (Table 4.8). As the models relax, the ratio of the separatrix-surface eigenvalues indicates that the separatrix surface is becoming more aligned with the major axis, and as b increases so too does the severity of the alignment at $t = t_{eq}$. This is also evident from the values of $\mathbf{e}_{f_{2l}}$ at $t = t_{eq}$ shown in Table 4.8 for the Series B experiments. At $t = t_{eq}$, as b increases, $\mathbf{e}_{f_{2l}}$ becomes more aligned along the $y = x/3$ line and the experiments where this alignment is best achieved

Table 4.9: The ratio of the upper null's separatrix-surface eigenvalues ($\lambda_{f_{2u}}/\lambda_{f_{1u}}$) and the eigenvector $\mathbf{e}_{f_{2u}}$ at $t = 0t_f$ and at $t = t_{eq}$. The parameters which are not being varied take the values $a = 0.5$, $b = 0.75$ and $c = 0.25$.

Exp.	$\lambda_{f_{2u}}/\lambda_{f_{1u}}$		$\mathbf{e}_{f_{2u}}$	
	$t = 0t_f$	$t = t_{eq}$	$t = 0t_f$	$t = t_{eq}$
$a = 0.15$	7.333	5.691	$(0, 1, 0)^T$	$(0.352, 0.936, -0.002)^T$
$a = 0.25$	4.0	3.472	$(0, 1, 0)^T$	$(0.283, 0.959, -0.002)^T$
$a = 0.5$	1.5	1.430	$(0, 1, 0)^T$	$(0.07, 0.998, -0.001)^T$
$a = 0.75$	0.667	0.577	$(0, 1, 0)^T$	$(-0.210, 0.977, -0.003)^T$
$a = 0.85$	0.471	0.390	$(0, 1, 0)^T$	$(-0.296, 0.955, -0.003)^T$
$b = 0.5$	1.158	1.127	$(0.137, 1, 0)^T$	$(0.119, 0.993, -0.002)^T$
$b = 0.75$	1.5	1.430	$(0, 1, 0)^T$	$(0.07, 0.998, -0.001)^T$
$b = 1.0$	1.898	1.961	$(-0.114, 1, 0)^T$	$(0.05, 1.0, -0.003)^T$
$b = 1.5$	2.779	1.335	$(-0.284, 1, 0)^T$	$(0.085, 0.996, -0.007)^T$
$b = 2.0$	3.713	0.279	$(-0.402, 1, 0)^T$	$(0.106, 0.994, -0.003)^T$
$c = -0.25$	0.5	0.421	$(0, 1, 0)^T$	$(0.453, 0.892, -0.001)^T$
$c = 0.0$	1.0	0.989	$(0, 1, 0)^T$	$(0.985, 0.173, -0.002)^T$
$c = 0.25$	1.5	1.430	$(0, 1, 0)^T$	$(0.07, 0.998, -0.001)^T$
$c = 0.5$	2.0	1.433	$(0, 1, 0)^T$	$(0.230, 0.973, -0.002)^T$
$c = 0.75$	2.5	0.493	$(0, 1, 0)^T$	$(0.349, 0.937, -0.002)^T$

are those which had smaller values of $\bar{\beta}$ at $t = t_{eq}$.

Similarly for the experiments in Series C, the ratio of the lower null's separatrix-surface eigenvalues, and the eigenvector $\mathbf{e}_{f_{2l}}$, are unchanged at $t = 0t_f$ by variations in c . However, at $t = t_{eq}$, the major axis of the separatrix surface dominates strongly over the minor axis, but not as strongly as when b was increased. As c increases the major axis of the upper null becomes more dominant, but unlike the experiments where a and b were varied, increasing c leads to the major eigenvector of the lower null aligning more with the $y = x/2$ line. Hence, the major axis of this null is increasingly dominant over the minor axis for the experiments with higher values of c which also have lower values of $\bar{\beta}$.

Table 4.9 shows similar values for the upper null for all thirteen experiments discussed in this chapter. As a increases, the ratio between the upper null's separatrix-surface major eigenvalue ($\lambda_{f_{2u}}$) and minor eigenvalue ($\lambda_{f_{1u}}$) decreases at $t = 0t_f$ and at $t = t_{eq}$. These ratios also decrease as each experiment in Series A relaxes. This suggests that the major axis becomes less dominant due to the relaxation and as a increases. The major eigenvalue of the upper null's separatrix surface is not $\lambda_{f_{2u}}$, but $\lambda_{f_{1u}}$ for the experiments with $a = 0.75$ and $a = 0.85$. The eigenvector $\mathbf{e}_{f_{2u}}$ is aligned along the y -axis at $t = 0t_f$ regardless of the value of a . The relaxation causes this eigenvector to become more aligned with the x -axis. As a increases, at $t = t_{eq}$, $\mathbf{e}_{f_{2u}}$ becomes more aligned with the y -axis until $a > 0.5$ when this eigenvector becomes more aligned along the $y = -3x$ line. This change coincides with when $\lambda_{f_{1u}}$ becomes the major eigenvalue of the separatrix surface of the upper null. These two experiments ($a = 0.75$ and $a = 0.85$) not only have stronger, wider, thinner and longer current layers than the other experiments in Series A, but also have significantly smaller $\beta_{l_{sep}}/2$.

As b increases the ratio of the upper null's separatrix-surface eigenvalues increase at $t = 0t_f$ (Table 4.9). This indicates that the major eigenvalue dominates more strongly over the minor eigenvalue at this time. At this time, increasing b leads to the eigenvector going from being aligned with the $y = 7x$ line to becoming aligned with the $y = -2.5x$ line. At $t = t_{eq}$ the ratio of the eigenvalues increases as b increases until $b > 1.0$, where it begins to decrease and, when $b = 2.0$, the major eigenvalue becomes λ_{f_1u} . We note that this experiment was not run for as long as the other four experiments in Series B and that some properties of its MHS equilibrium did not follow the trends of the other four Series B experiments. This experiment also had the smallest $\bar{\beta}$ value of all experiments discussed in this chapter. At $t = t_{eq}$, the eigenvector \mathbf{e}_{f_2u} does not vary greatly from being aligned along the y -axis as b increases.

Increasing c leads to the ratio of the separatrix-surface eigenvalues of the upper null increasing at $t = 0t_t$, but at $t = t_{eq}$ this value only increases until $c > 0.5$ at which point it decreases again. At $t = t_{eq}$, λ_{f_1u} is the major eigenvalue for the experiments with $c = -0.25$ and $c = 0.75$. When $c = 0.0$, the ratio of the separatrix-surface eigenvalues is approximately 1 at $t = 0t_f$ and at $t = t_{eq}$. This indicates that neither eigenvalue dominates over the other and hence the null is proper radial. We believe that the eigenvector given for this experiment is not correct because of this fact. Excluding this experiment, as the other experiments in Series C relax, the major axis becomes less dominant. Although the eigenvector, \mathbf{e}_{f_2u} , remains the same regardless of the value of c at $t = 0t_f$, at $t = t_{eq}$ the eigenvector goes from being aligned along the $y = 2x$ line when $c = -0.25$ to being aligned with the $y = 2.7x$ line when $c = 0.75$, so this eigenvector does not vary greatly. We note that the value of $\bar{\beta}$ varied by the smallest amount of this series of experiments.

We have now analysed the effects of varying four of the five magnetic field parameters of Eq. 4.1. In the next chapter, we use a MHS equilibrium similar to the main experiment, discussed in Chapt. 3, as the initial condition for a high plasma-beta separator reconnection experiment in which we analyse the nature of the reconnection that occurs at the twisted separator current layer, and the effects it has on the magnetic field and plasma in the system.

Chapter 5

Spontaneous reconnection at a high plasma-beta separator current layer

So far in this thesis, we have analysed the non-resistive MHD relaxation of a single-separator, which begins with current parallel to the separator. The non-resistive MHD relaxation causes the initial magnetic field, which is not in force balance, to form a MHS equilibrium with a twisted current layer lying along the separator. The MHS equilibrium contains free magnetic energy, which may be released and converted into other forms of energy through the process of magnetic reconnection. In this chapter, we study the properties of the 3D magnetic reconnection which occurs at such a current layer in a high plasma-beta domain. To carry out this experiment, we have again used the Lare3d code, but with a non-zero anomalous resistivity in order to gain magnetic reconnection at the separator current layer.

Many works regarding 3D magnetic reconnection begin with a potential, linear force-free or non-linear force-free magnetic field which is driven such as to gain magnetic reconnection. This driven reconnection method has been used to study reconnection at not only 3D null points [e.g., Craig and Fabling, 1996, Pontin and Craig, 2005, Pontin et al., 2005a, Masson et al., 2009, Pontin et al., 2013], but at separators [e.g., Galsgaard and Nordlund, 1996, Longcope and Cowley, 1996, Haynes et al., 2007, Parnell et al., 2010a,b] and also at quasi-separatrix layers [e.g., Aulanier et al., 2006]. We have chosen not to use this method for various reasons. Potential fields do not contain free energy (the magnetic energy which is excess above the potential energy) so all the energy released in experiments that start from a potential field is injected via the Poynting flux associated with boundary driving of the field. The current layer formed through driven reconnection will be one that is created through the boundary driving, but dissipated immediately (if there is uniform resistivity) or once it reaches a certain strength (if the resistivity is dependent on the strength of the current). So, its properties will not be the same as those found in models created by MHD relaxation (see Chaps. 3 and 4). This type of reconnection is commonly found to depend on the initial configuration and the rate of boundary driving [e.g., Galsgaard and Parnell, 2005]. Hence, the reconnection is in some sense controlled and so is not entirely free to do what it wants. Finally, since there is no equilibrium state, the study of any perturbations

is much harder to perform.

We gain a current layer in our non-potential single-separator model by allowing it to slowly relax such that a current layer builds along the separator (Chapts. 3 and 4). In the solar atmosphere and the Earth’s magnetosphere it is thought that free magnetic energy is built up by the stressing of magnetic structures through the slow driving of the magnetic field. Equilibria can form, with current layers, when topologically complex magnetic fields are stressed. These current layers are not dissipated immediately since the magnetic Reynold’s number is not less than one. We have simulated this slow stressing by allowing our single-separator model to relax non-resistively without any external effects, and we have seen in Chapts. 3 and 4 that this method produces a MHS equilibrium with a current layer lying along the separator with stored free magnetic energy.

Reconnection can occur at such a current layer, in the solar atmosphere or the Earth’s magnetosphere. Once the length scales within the current layer become short enough such that $R_m \leq 1$, this reconnection can be initiated by micro-instabilities. We simulate the effect of these micro-instabilities by applying an anomalous resistivity to our MHS equilibrium which contains a current layer, such that reconnection occurs at the strong current layer, but not elsewhere in the domain. Such an approach (allowing a current layer to form through the non-resistive relaxation of a magnetic field before triggering the reconnection via an anomalous resistivity) has been used before in the study of reconnection at two-dimensional magnetic null points [e.g., Fuentes-Fernández and Parnell, 2012, Fuentes-Fernández et al., 2012].

We begin here by briefly recapping the details of the equilibrium magnetic field, discussed in Chapt. 3, which is used as the initial field in our reconnection experiment, as well as the plasma properties of this system and also the numerical model used to carry out the experiment (Sect. 5.1). In Sect. 5.2 we investigate how the energies, heating terms and reconnection rate behave throughout the experiment before detailing the evolution of the magnetic field and the plasma (Sect. 5.3), and the residual forces in the system (Sect. 5.4). In Sect. 5.5 the properties of waves, which are created as a consequence of reconnection, are investigated. Next, we discuss the vorticity and velocities in the system in Sect. 5.6 before analysing what energy the waves, and the flows set up by these waves, are transporting in Sect. 5.7. Next, in Sect. 5.8, we discuss the effects that varying the strength of the resistivity, the size of the diffusion region and the value of the background viscosity have on the reconnection rate and the energy transfer in the system. We summarise this chapter in Sect. 5.9

5.1 Properties of the equilibrium field and the plasma

The MHS equilibrium field, which we use in this chapter as our initial magnetic field, has the same magnetic field parameters as those used for the main experiment in Chapt. 3 ($a = 0.5$, $b = 0.75$, $c = 0.25$, $j_{sep} = 1.5$, $B_0 = 1.0$, $L_0 = 1.0$, $L = 1.0$). Here, our box has length $-1.0 < x, y < 1.0$ and $-1.75 < z < 2.75$ and has a grid resolution of (512,512,768). Therefore, the only difference between the equilibrium field used in this chapter and the one found in Chapt. 3 is the height of the box. Here, we increased the height of the box to move any boundary currents further away from the main current layer which lies along the separator. The skeleton of this equilibrium field, containing two oppositely signed

nulls with spines and separatrix surfaces which intersect to form a separator, is shown in Fig. 5.1 with an isosurface of current drawn at $j_{\parallel} = 10.0$.

The MHS equilibrium current layer, which lies between the null points at $(0, 0, -0.10)$ and $(0, 0, 1.08)$, twists through an angle of $\theta = 0.79$ rads along the length of the separator from the lower to the upper null. The depth and width of the current layer vary along its length and have the values $d = 0.06$ and $w = 0.24$, respectively, in the cut perpendicular to the separator at $z = 0.4$. The strong current at the separator in the equilibrium field, and enhanced current along the separatrix surfaces of the nulls in the $z = 0.4$ plane are displayed in Fig. 5.2. We follow the consequences of the reconnection by plotting contours of the plasma and magnetic field parameters in the $z = 0.4$ plane in subsequent figures throughout this chapter since this is the position along the separator where the current peaks. In this plot, a yellow contour is drawn on the edge of the current layer at $|j| = 10.0$ and eight black asterisks are plotted in four positions on the edges of the current layer. The significance of the value of the yellow contour and the positions of the black asterisks will be explained in the following sections.

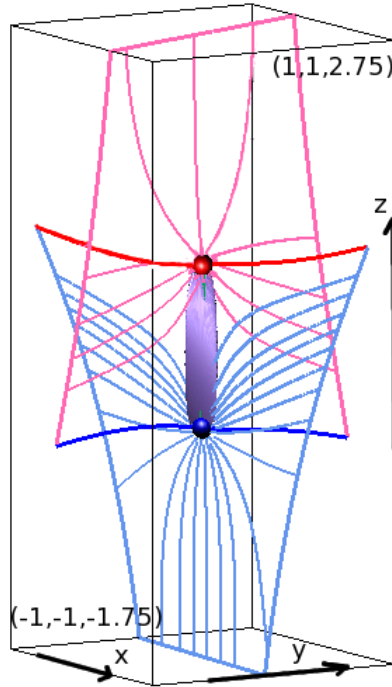


Figure 5.1: The MHS equilibrium skeleton which contains a positive/negative null (blue/red spheres) which have blue/red spines and pale-blue/pink separatrix surfaces associated with them. A green separator links the nulls. The separator is hidden in this image by a purple isosurface drawn at $j_{\parallel} = 10.0$.

All times in this chapter are normalised to the time it would take a fast-mode wave to travel from the lower null to the upper null along the separator

$$t_f = \int_{z_l}^{z_u} \frac{1}{\sqrt{c_A(z)^2 + c_s(z)^2}} dz = 0.92. \quad (5.1)$$

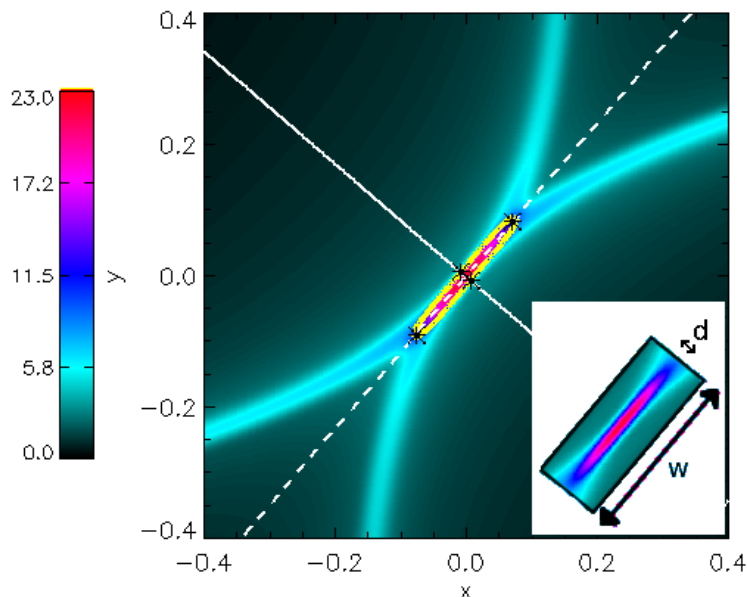


Figure 5.2: Contours of $|\mathbf{j}|$ in the MHS equilibrium field, in the plane perpendicular to the separator at $z = 0.4$. The white dashed and solid lines go across the width and through the depth of the current layer in this cut, respectively. The yellow contour is drawn at $|\mathbf{j}| = 10.0$ and the eight black asterisks, at four positions, sit on the edges of the current layer. The inserted picture highlights the width, w , and depth d , of the current layer in this plane.

Here $z_l = -0.10$ is the z -position of the lower null, $z_u = 1.08$ is the z -position of the upper null, $c_A(z)$ is the Alfvén speed and $c_s(z)$ is the sound speed. The MHS equilibrium magnetic field with twisted current layer is our initial magnetic field for the reconnection experiments and, hence, occurs at $t = 0t_f$ in this chapter.

We apply line-tied boundary conditions here by setting the derivatives of the internal energy per unit mass (ϵ), the density (ρ) and the magnetic field (B_x, B_y, B_z) normal to each boundary to zero. The velocity (v_x, v_y, v_z) is set to zero on the boundaries.

The mean plasma beta of the equilibrium field is $\bar{\beta} = 4.8$. This value is relatively high, but this is not surprising due to the existence of two magnetic null points, at which $\mathbf{B} = \mathbf{0}$, in the model. Fig. 5.3a shows contours of the plasma beta in the plane perpendicular to the equilibrium separator at $z = 0.4$. This figure, and Fig. 5.3b which displays the MHS equilibrium skeleton with an isosurface drawn at $\beta = 100$, show that, although the plasma beta is high near to the separator (and at the nulls), it is small elsewhere in the domain.

The value of the background viscosity, used in the main experiment in this chapter, is $\nu = 0.01$, as in Chaps. 3 and 4. This corresponds to a characteristic viscous speed of $v_\nu = 2.555$ as was found in Chaps. 3 and 4 (using $R_e = v_\nu \delta l / \nu$ where $R_e = 1$, $\delta l = 2/511$ and $\nu = 0.01$). The average fast-magnetoacoustic speed along the separator is $c_f = 1.17$ and so the viscosity should act to damp waves which travel at this speed. Here, we apply a non-uniform resistivity, η , which acts only where the current is greater than a set value,

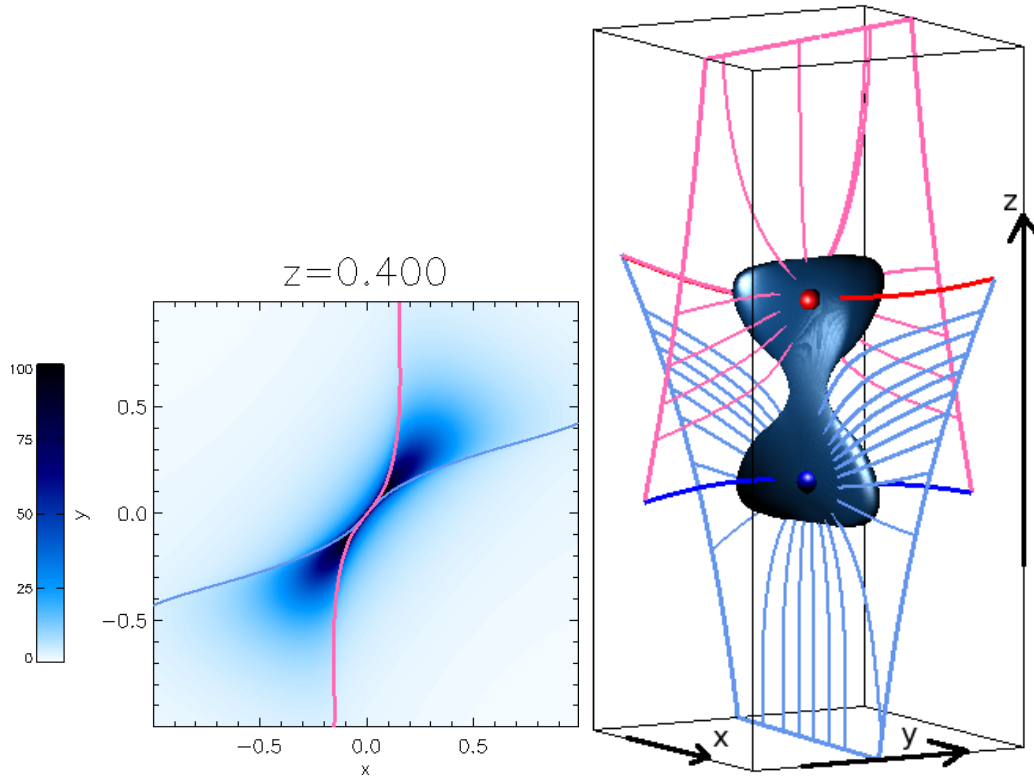


Figure 5.3: (a) Contours of the plasma beta in the MHS equilibrium field, in the plane perpendicular to the separator at $z = 0.4$. The pale-blue and pink lines are the intersections of the equilibrium magnetic field's separatrix surfaces with this plane. (b) The MHS equilibrium skeleton with two null points (blue/red spheres) and associated blue/red spines and pale-blue/pink separatrix surfaces. A green separator links the nulls but this is hidden by a dark blue isosurface drawn at $\beta = 100$.

j_{crit}

$$\eta = \begin{cases} 0 & |\mathbf{j}| < j_{crit}, \\ \eta_d & |\mathbf{j}| \geq j_{crit}. \end{cases}$$

For the main experiment in this chapter we use $\eta_d = 0.001$ and $j_{crit} = 10.0$. In Sect. 5.8 we analyse the effects that varying η_d (the strength of the reconnection), j_{crit} (the size of the diffusion region) and ν (the background viscosity) have on the energetics and the reconnection rate in the experiment.

5.2 Energetics

As soon as the experiment begins magnetic energy is converted into internal energy (99.77%) and kinetic energy (0.23%) (Fig. 5.4a). This figure displays the change in magnetic, internal and kinetic energies normalised to the maximum change in the magnetic energy and the change in total energy against time, on a log scale. The change in kinetic energy has been multiplied by 50 for representational purposes.

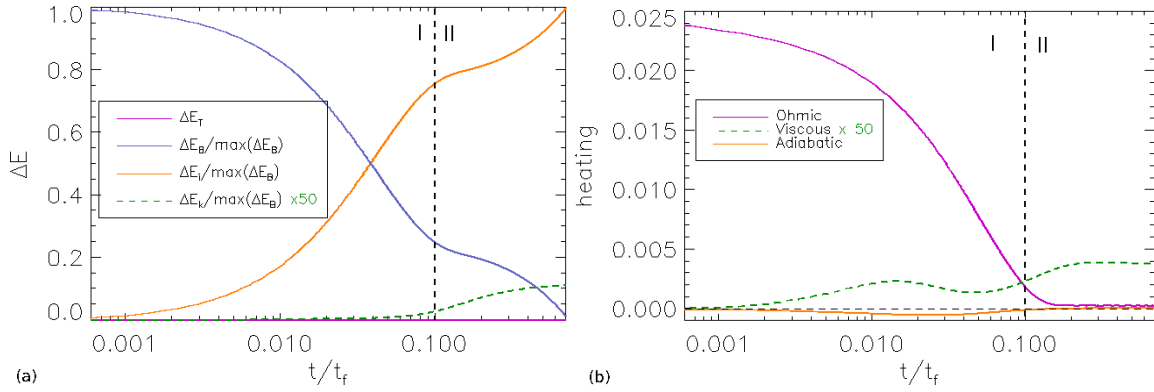


Figure 5.4: Plots of the change in (a) magnetic, internal and kinetic energies normalised to the maximum change in magnetic energy and the change in the total energy and the instantaneous (b) Ohmic, viscous and adiabatic terms plotted against time on a log scale. The kinetic energy and viscous heating terms are multiplied by 50 for representational purposes. The end of phase I and the start of phase II is marked by the black dashed vertical lines and symbols “I” and “II”. The black dashed horizontal line in (b) marks where zero is.

The immediate variations in energy indicate that reconnection occurs as soon as the experiment is started, due to the anomalous resistivity acting where the magnitude of the current is greater than j_{crit} . The rate of change of energies shown in Fig. 5.4a slows at $t = 0.1t_f$. This suggests that at this point in the experiment, the nature of the reconnection may have changed. We indicate this change by the black vertical dashed line and the symbols “I” and “II” on this plot indicating that there are two different phases of reconnection occurring. After this time ($t = 0.1t_f$), a rise in kinetic energy is observed, which is greater than the increase in kinetic energy from $t = 0t_f$ to $t = 0.1t_f$. This indicates that there are waves moving in the system which were launched at the start of the experiment. The total energy is conserved to within a relative error of $2 \times 10^{-5}\%$ and so the energy is well conserved throughout the reconnection experiment.

The magnetic energy is mostly converted via Ohmic heating (94%) with some viscous heating (4%) and adiabatic heating (2%) occurring in the system too (Fig. 5.4b). In Fig. 5.4b, the instantaneous heating terms are plotted against time (on a log scale) where the viscous heating term has been multiplied by 50 so it is visible on this scale. There is a lot of Ohmic heating initially in the system. The value of the Ohmic heating decreases rapidly and is small, but non-zero, towards the end of the experiment. We see from this figure that again the nature of the reconnection evidently changes at $t = 0.1t_f$. We indicate this on the plot by the dashed black vertical line and symbols for phase I and phase II. Phase I is associated with high Ohmic heating, the value of which is greatly reduced in phase II. In phase I the viscous heating term has increased, in line with the increase in kinetic energy at these times. Although the viscous heating increases in phase II, the heating terms are always dominated by the Ohmic heating due to the high plasma-beta. There is also adiabatic cooling occurring in phase I which suggests a rapid expansion happens in the system in this phase.

Fig. 5.5 displays the reconnection rate (solid line) and the total flux reconnected

(dashed line) against time, where time is on a log scale. Here, the change between the two phases of the experiment is very distinct. A lot of reconnection occurs initially but the rate of the reconnection decreases throughout the first phase becoming zero, for the first time, at $t = 0.1t_f$. Through phase II the reconnection rate is small and is zero at times however, these small amounts of reconnection add up such as to increase the total flux reconnected in phase II. The plot of the total flux reconnected grows quickly through phase I, the phase during which most of the reconnection is occurring, and then steadily grows at a slower pace during phase II which suggests these small amounts of reconnection are not just noise.

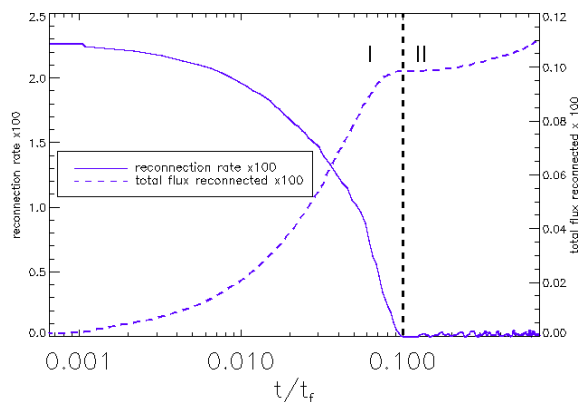


Figure 5.5: Plot of the reconnection rate (solid blue line) and total flux reconnected (dashed blue line), both multiplied by 100. The end of phase I and the start of phase II is marked by the black dashed line and symbols “I” and “II”.

The plots in Fig. 5.4 and 5.5 indicate that this high plasma-beta reconnection experiment occurs in two phases. During the first phase (the fast-reconnection phase) 75% of the total magnetic energy is converted into internal and kinetic energy, high values of Ohmic heating are seen and the velocities in the system are relatively low. This phase lasts from $t = 0t_f$ to $t = 0.1t_f$. Phase II, which is more than six times longer than phase I, lasts from just after $t = 0.1t_f$ to $t = 0.73t_f$. During this phase, the rate of change of energies is reduced compared to phase I, the amount of Ohmic heating is small, the velocities are relatively high and viscous heating of the waves launched from the diffusion site in phase I is observed. This phase is, therefore, associated with slow-steady reconnection. The nature of the reconnection in this phase can be deduced from the kinetic energy and viscous heating plots which level off in phase II (Figs. 5.4a and 5.4b, respectively).

5.3 Evolution of the magnetic field

In a cut perpendicular to a 3D magnetic separator, the reconnection which occurs appears similar to 2D X-point reconnection in that flux is transferred from one pair of topologically distinct flux domains into another pair of topologically distinct flux domains. 2D X-point reconnection requires, however, a stagnation type flow whereas 3D magnetic separator reconnection is associated with a counter-rotating flow. In this section, we firstly analyse the effects that the reconnection has on the magnetic field of our model, before finding the

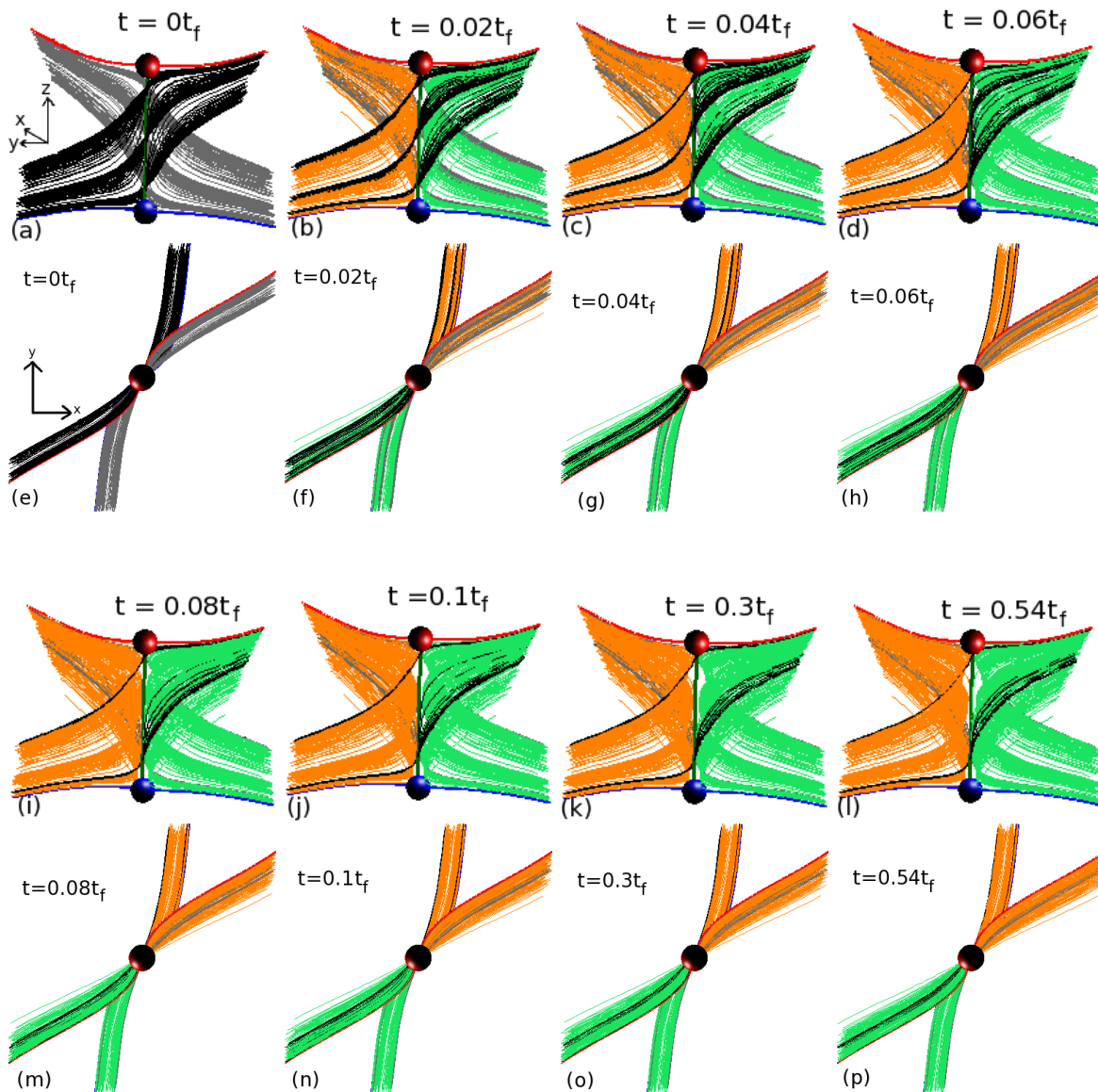


Figure 5.6: Evolution of field lines throughout the reconnection experiment. The positive/negative nulls are displayed as blue/red spheres with blue/red spines. The separatrix surfaces of the nulls are not drawn and the separator is the green line linking the nulls. The first and third rows show side views of the skeleton and the second and fourth rows show top down views. The top down views, which display the field at the same times as the side views, are placed below the corresponding side views. Field lines, drawn initially in oppositely situated flux domains as grey/black lines, at $t = 0t_f$, are coloured green/orange, respectively, once they have been reconnected.

location of the peak reconnection and studying several plasma and field parameters here.

Fig. 5.6 shows the skeleton of the model (excluding the separatrix surfaces) along with some field lines drawn initially in the two domains which lie outwith the cusp regions about the separator. These field lines are coloured grey or black depending on which domain

they inhabit at $t = 0t_f$. The skeleton of the model with these field lines is shown at eight times throughout the experiment from both side and top views. The experiment begins and once these field lines have reconnected they are coloured green or orange, respectively. Fig. 5.6 shows that most of the field lines have been reconnected by $t = 0.1t_f$ which is the end of phase I (Figs. 5.6a to 5.6j and 5.6m and 5.6n). The reconnection of these field lines occurs by the apparent flipping of the field lines about the separator so that they no longer lie in the domains they existed in at $t = 0t_f$. During phase II, the remaining field lines which have not yet reconnected do so slowly over time (Figs. 5.6k, 5.6l, 5.6o and 5.6p).

The separator reconnection causes the current, which has a magnitude greater than $j_{crit} = 10$, to be rapidly dissipated during the first phase of the experiment (Fig. 5.7). Once this current has been dissipated, the contours in Fig. 5.7, which show $|\mathbf{j}|$ do not appear to change, however, we know from the plot of the total flux reconnected, that at some points along the separator there is reconnection in phase II. The enhanced current along the separatrix surfaces is not dissipated by the reconnection since the value of the current here is less than j_{crit} .

To study the reconnection occurring in the system, we look at where the strength of the reconnection is greatest. To check this, we calculate $\int_l E_{\parallel} dl$ and plot contours of this in a plane perpendicular to the separator at $z = 0.4$. We integrate the value of E_{\parallel} along all the field lines which thread the plane at $z = 0.4$ (Fig. 5.8) at a time near the start of phase I. From Fig. 5.8 we see that the strongest reconnection occurs at the separator (the inserted picture in this figure shows the region about the separator close up to highlight this). There is also evidence of weaker reconnection along the separatrix surfaces of the nulls close to the original diffusion site. Note though, as we have already said, reconnection does not actually occur on the separatrix surfaces, so this evidence of reconnection simply indicates that all the field lines with non-zero $\int_l E_{\parallel} dl$ must at some point thread the diffusion region about the separator. As such, we will now examine how various parameters behave along the separator throughout the reconnection experiment.

Throughout the reconnection experiment the nulls move over small distances in the z -direction. Fig. 5.9 shows the offset in the z -direction of both nulls from their respective positions at $t = 0t_f$. The lower null moves from its initial position downwards along the z -axis by $0.1L_0$ in the first $0.03t_f$, whereas the upper null moves a distance of $0.08L_0$ away from its initial position along the z -axis in the first $0.01t_f$ (the domain is $4.5L_0$ long in the z -direction). After these times both nulls move very slowly away from each other (the lower null moves a further distance of $1 \times 10^{-4}L_0$ and the upper null moves a further $5 \times 10^{-5}L_0$ during the rest of the experiment), due to the total force along the separator which is discussed in Sect. 5.4.

In this section we will consider various time slices (where time is on the y -axis and is on a log scale) plotted along the length of the separator. Since, the separator length varies slightly through this experiment, in these time slices the separator is normalised such that it lies between $z^* = 0.0$ and $z^* = 1.0$ throughout the experiment according to $z^* = (z - z_{ln})/l_{sep}$ where z_{ln} is the z -coordinate of the lower null and l_{sep} is the length of the separator in the frame being considered.

Fig. 5.10 shows the value of E_{\parallel} in a time slice plotted along the length of the separator. From this figure we see that at the start of phase I, reconnection is occurring along the entire length of the separator, with the strongest reconnection occurring between the

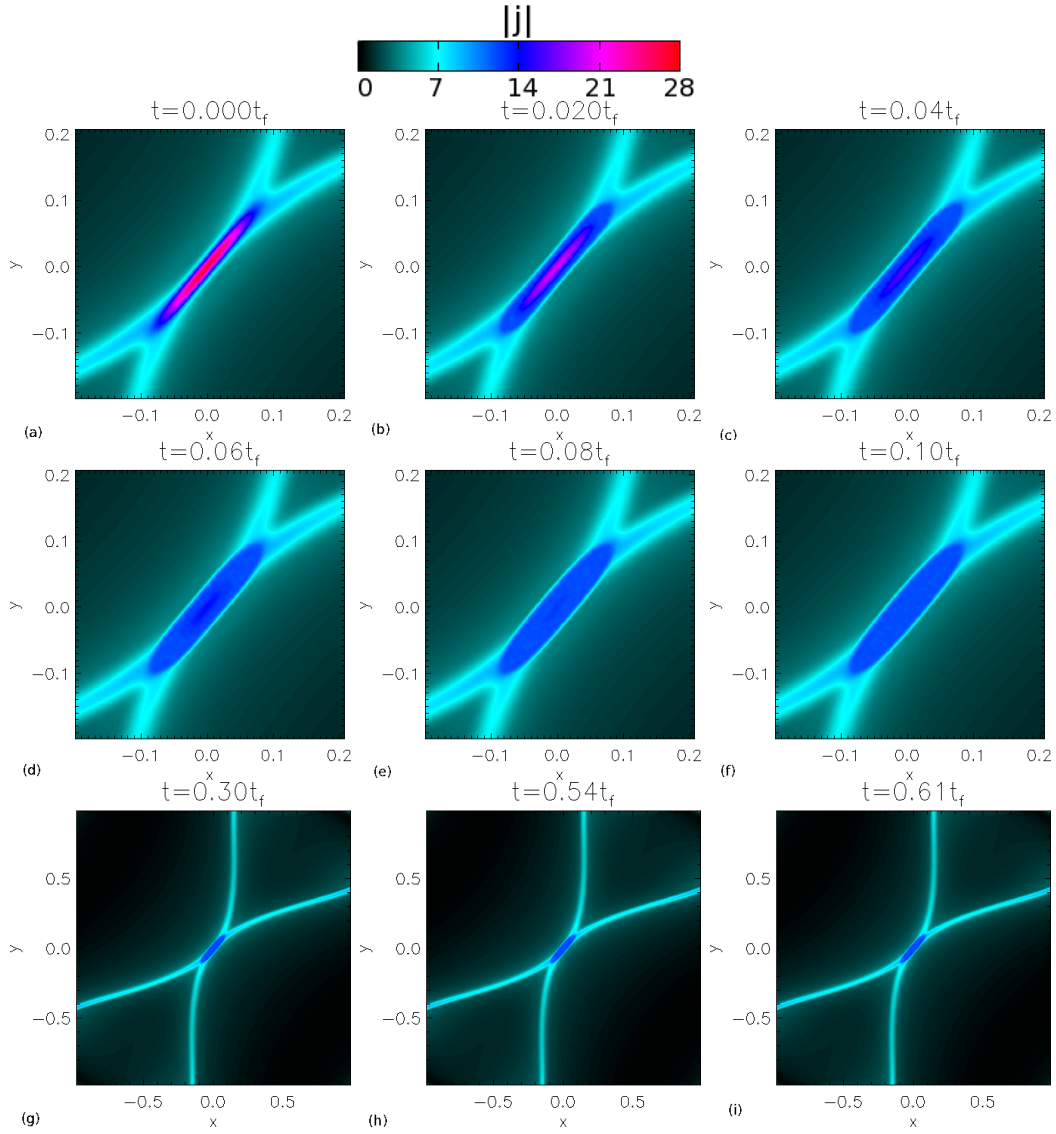


Figure 5.7: Contours of $|\mathbf{j}|$ in the plane perpendicular to the separator at $z = 0.4$ throughout phase I ((a) to (f)) and phase II ((g) to (i)). The last three plots show a larger area than the previous plots.

points $z^* = 0.12$ and $z^* = 0.73$. Half-way between these points is near the location of peak current along the separator in the equilibrium field. Through phase I the strength of the reconnection decreases along the length of the separator and in phase II only small amounts of localised, short-lived reconnection occur. We know that these small reconnection events are sufficiently significant in number to contribute to the total flux reconnected (Fig. 5.5).

On top of the contours of E_{\parallel} , in Fig. 5.10, is the zeroth contour of the discriminant of the perpendicular component of the magnetic field, \mathbf{B}_{\perp} (black lines). The sign of \mathbf{B}_{\perp} indicates if the local magnetic field about the separator is X-type (hyperbolic) or O-type (elliptic), in planes perpendicular to separator. We have annotated this figure

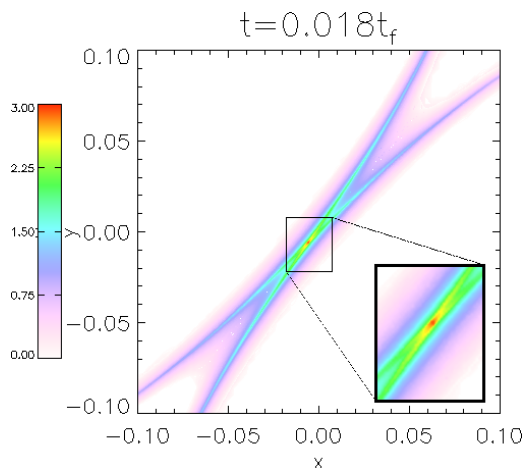


Figure 5.8: Contours of $\int_l E_{\parallel} dl$ in the plane perpendicular to the separator at $z = 0.4$ at $t = 0.018t_f$. The inserted image in this figure shows a close up of the area around the separator.

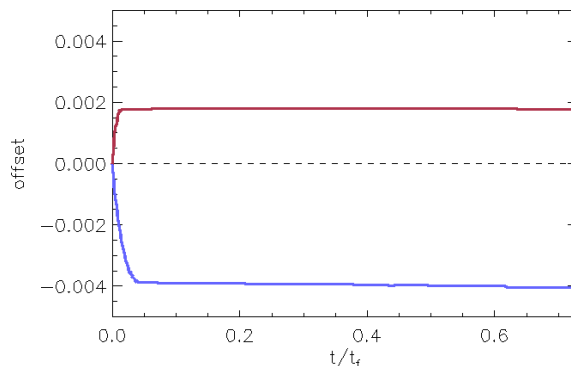


Figure 5.9: The offset in the z -direction, from the null's z -positions at $t = 0t_f$, of the lower null (blue line) and the upper null (red line).

to highlight that the local separator magnetic field, is O-type where the reconnection is strongest in phase I, and is X-type where the reconnection is weaker in phase I and is X-type everywhere on the separator in phase II. This behaviour agrees with the findings of Parnell et al. [2010a] who also study reconnection at magnetic separators.

Fig. 5.11a shows a time slice of the component of the vorticity parallel to the separator, $\omega_z = (\nabla \times \mathbf{v})_z$, plotted along the separator. The sign of ω_z indicates which direction the flow, in planes perpendicular to the separator, is rotating: red contours represent an anti-clockwise flow and blue contours represent a clockwise flow. Therefore, Fig. 5.11a shows that the flow counter-rotates about a point along the separator throughout both phases of the experiment. The point, about which the flow counter-rotates, is initially at $z^* = 0.48$ but moves slightly towards the lower null during phase I and then returns to a point at around $z^* = 0.49$ where it remains throughout the rest of the experiment.

Fig. 5.11b displays a similar time slice where contours of the component of the curl of the magnetic field parallel to the separator, $(\nabla \times \mathbf{B})_z = j_z$, are drawn. This plot shows

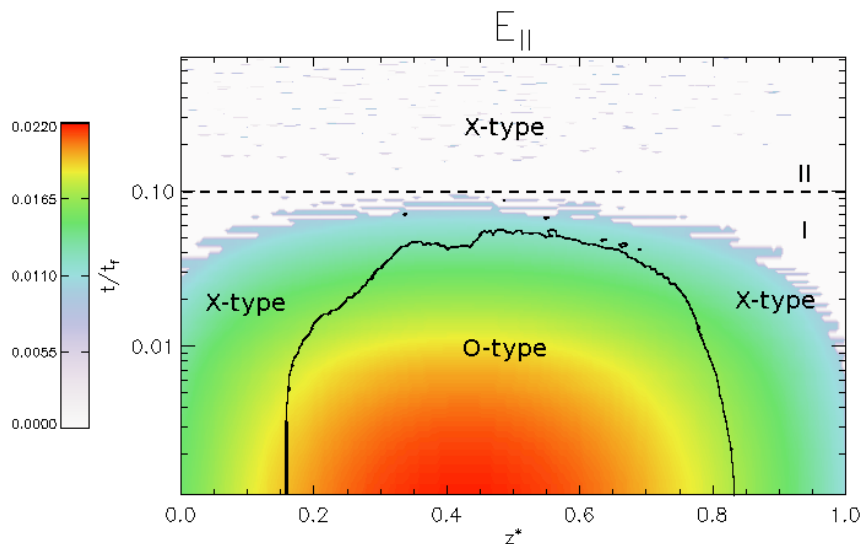


Figure 5.10: Time slice of E_{\parallel} along the separator (normalised such that it lies between $z^* = 0$ and $z^* = 1$) throughout the experiment. Time is plotted here on a log scale. The end of phase I and start of phase II is highlighted by the black dashed line and symbols “I” and “II”. The black lines are the zeroth contour of the discriminant of \mathbf{B}_{\perp} . This plot is annotated to describe the nature of the magnetic field local about the separator.

that the magnetic field lines are untwisting during phase I.

The nature of the flow, in cuts perpendicular to the separator, can be determined by analysing the sign of the discriminant of the perpendicular component of the velocity, \mathbf{v}_{\perp} , along the length of the separator (Fig. 5.11c). This plot infers that, during phase I, the local flow about the separator is O-type in some places (pink-purple regions) and X-type in other places (orange-blue regions). This is different to what is observed in 2D X-point reconnection, where the flow is always X-type. In phase II, the flow is X-type along almost the entire length of the separator.

On top of these contours we have over plotted black lines which represent the contours of E_{\parallel} which were shown as coloured contours in Fig. 5.10. This highlights that where the reconnection is strongest (i.e., where E_{\parallel} is strongest along the separator), the flow is not always X-type. We find that regions where the reconnection is strongest in phase I are generally associated with X-type flow and that regions where the reconnection is weak in phase I are generally associated with O-type flow. This is not a clear-cut relationship, unlike the findings of Parnell et al. [2010a], as some O-type flow exists where the reconnection is strong and some X-type flow exists where the reconnection is weak.

Fig. 5.11d shows similar contours for the discriminant of \mathbf{B}_{\perp} plotted as a time slice, on a log scale, along the length of the separator. These are a coloured contour version of the black lines plotted in Fig. 5.10, and indicate the behaviour of the local magnetic field perpendicular to the separator throughout the experiment. We again see here, that during phase I, the magnetic field lines are elliptic along most of the separator and are hyperbolic near the nulls. Also, the magnetic field lines are hyperbolic along the entire length of the separator in phase II.

Having analysed the nature of the reconnection, the velocity and the magnetic field at

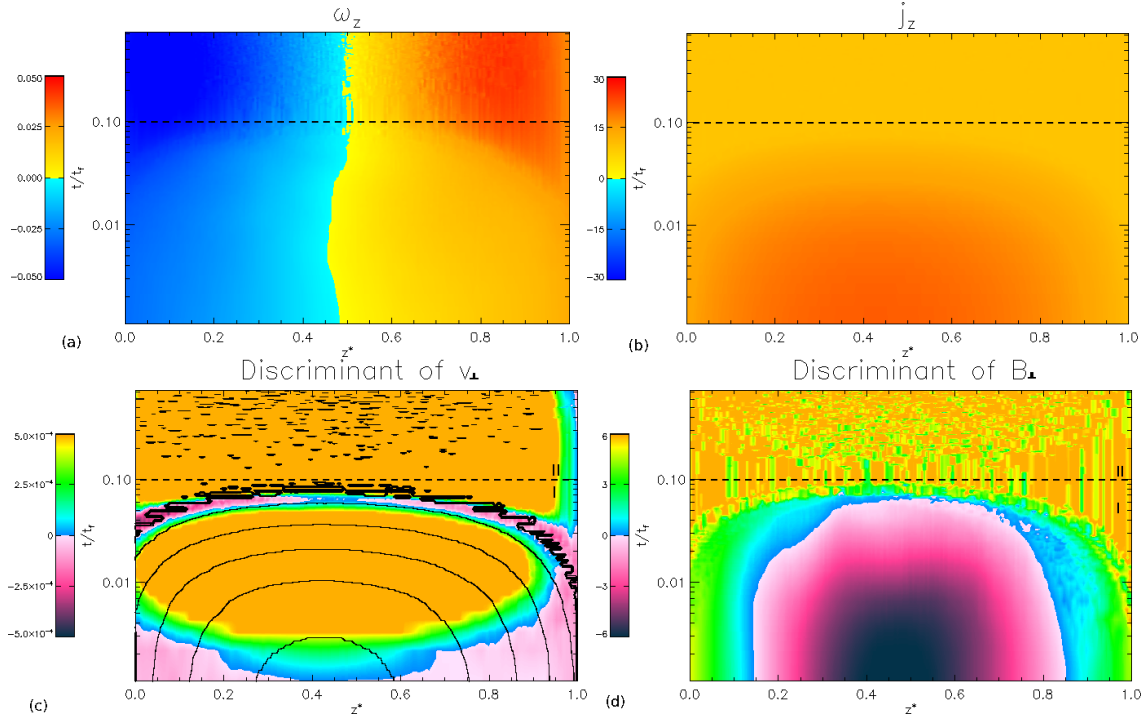


Figure 5.11: Time slices along the length of the separator which has been normalised such that it lies between $0.0 \leq z^* \leq 1.0$ showing contours of (a) $(\nabla \times \mathbf{v})_z = \omega_z$ and (b) $(\nabla \times \mathbf{B})_z = j_z$ and the discriminant of the component of (c) \mathbf{v} and (d) \mathbf{B} perpendicular to the separator. The end of phase I and start of phase II is highlighted by the black dashed line and symbols “I” and “II”.

the separator, which is the location of the peak reconnection, we now examine the residual forces in the system during the reconnection experiment (Sect. 5.4) before investigating the nature of the waves which are launched due to the reconnection (Sect. 5.5).

5.4 Effects of residual forces during the reconnection experiment

In Chapt. 3 and 4, we examined the magnitude and direction of the residual total force along the length, through the depth and across the width of the MHS equilibrium separator current layer and found that the very small residual total force acted to make the current layer longer, wider and thinner.

Throughout the reconnection experiment, the total force along the separator continues to act outwards towards the null points, but the magnitude of the total force decreases through phase I to a value of ~ 0.02 (Fig. 5.12). During phase II this peak value does not change although the position along the separator, from which the total force acts outwards, varies slightly from $z^* = 0.56$, at $t = 0t_f$, to $z^* = 0.62$ in phase II.

The decrease in the magnitude of the residual forces directed along the separator occurs due to the dissipation of the separator current during the reconnection and the subsequent

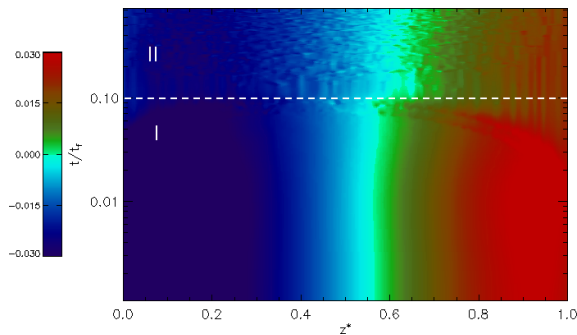


Figure 5.12: Time slice of the total force plotted along the z^* -axis. Note that time is plotted on a log scale. The white dashed line and symbols “I” and “II” indicate where phase I ends and phase II begins.

loss of force balance at the separator. These residual forces cause the nulls to move a little away from each other, along the z -axis, during the experiment, as was detailed in Sect. 5.3.

In perpendicular cuts across the z -axis (at $z = 0.4$) the magnitude of the total force initially decreases due to the loss of current about the separator (Figs. 5.13a to 5.13c). However, as phase I continues, the total force about the separator intensifies (Figs. 5.13d to 5.13f). This indicates that the residual forces start to build up again during phase I when the reconnection rate is slowing. This is linked to the plasma trying to regain force balance (i.e., rebuild the current layer) at the separator. However, due to the resistive nature of the system about the separator, current is immediately dissipated as soon as it gets above $|\mathbf{j}| = 10$ and so the current layer is never reformed.

This behaviour is clarified by the arrows on the plots in Fig. 5.13. These arrows indicate the direction of the x and y -components of the total force in this plane at $z = 0.4$ and show that there is a strong component of the total force pointing outwards from the separator into the cusp regions or, in other words, the total force is still trying to widen the current layer (Figs. 5.13d to 5.13i). Also, arrows are observed to be pointing in towards the separator from the other two flux domains, i.e., outwith the cusps, which highlights that the total force is still acting to make the current layer thinner in cuts perpendicular to the separator. This behaviour of the total force has been seen before in 2D X-point reconnection [Fuentes-Fernández et al., 2012]. In this work the total force was observed to be directed in towards the X-point outwith the cusp regions formed by the separatrices of the nulls, and was directed outwards away from the X-point in the cusp regions.

A circular motion is witnessed about the two strong regions of total force in Figs. 5.13d to 5.13f. The total force appears to be acting from the limits of the current layer (width ways) into the centre of the current layer where it is being squeezed thinner.

Figs. 5.14 and 5.15 show the magnitude of the total force on surfaces which go through the depth and across the width of the current layer from the lower to the upper null, respectively. Therefore, the two surfaces are not straight planes, but twist along the length of the separator, as the current layer itself twists. On top of these contours are arrows which show the direction of the total force in these planes. These arrows are coloured orange where $d < 0$ and $w < 0$ and are coloured black where $d > 0$ and $w > 0$ so that the direction of the arrows is clear. The strength of the total force through the

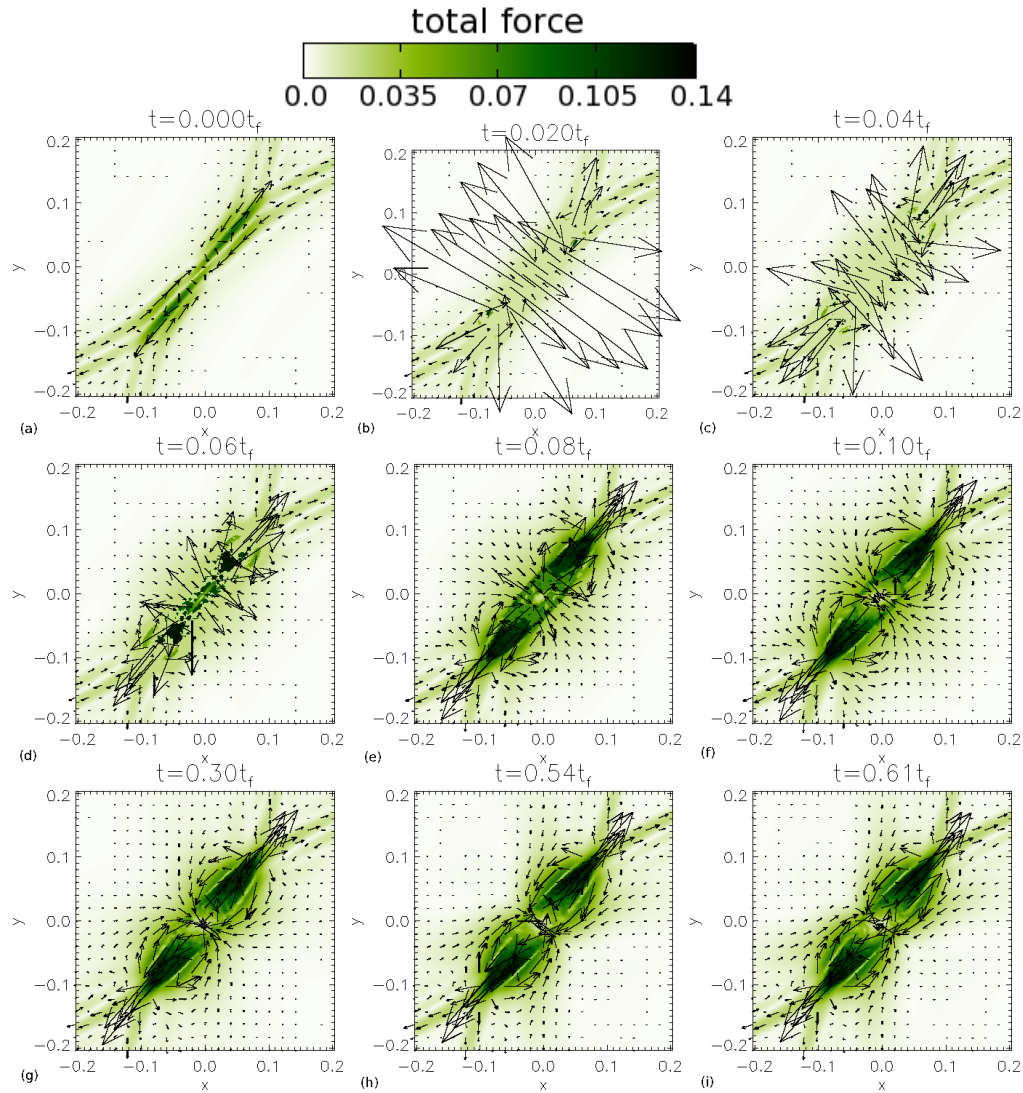


Figure 5.13: Contours of the total force in the plane perpendicular to the separator at $z = 0.4$ at (a) $t = 0t_f$, (b) $t = 0.02t_f$, (c) $t = 0.04t_f$, (d) $t = 0.06t_f$, (e) $t = 0.08t_f$, (f) $t = 0.1t_f$, (g) $t = 0.3t_f$, (h) $t = 0.54t_f$ and (i) $t = 0.61t_f$. Black arrows, normalised to the maximum value on the colour bar, display the direction of the total force in the plane (x and y -components of the total force).

depth is weak and so the arrows here, pointing in towards the separator at $l = 0.0$, are small (Fig. 5.14). Fig. 5.15 shows the total force plotted across the width of the current layer. The total force is stronger here than it is through the depth of the current layer and the arrows indicate that the total force is acting outwards away from the separator as expected from the contours in Fig. 5.13.

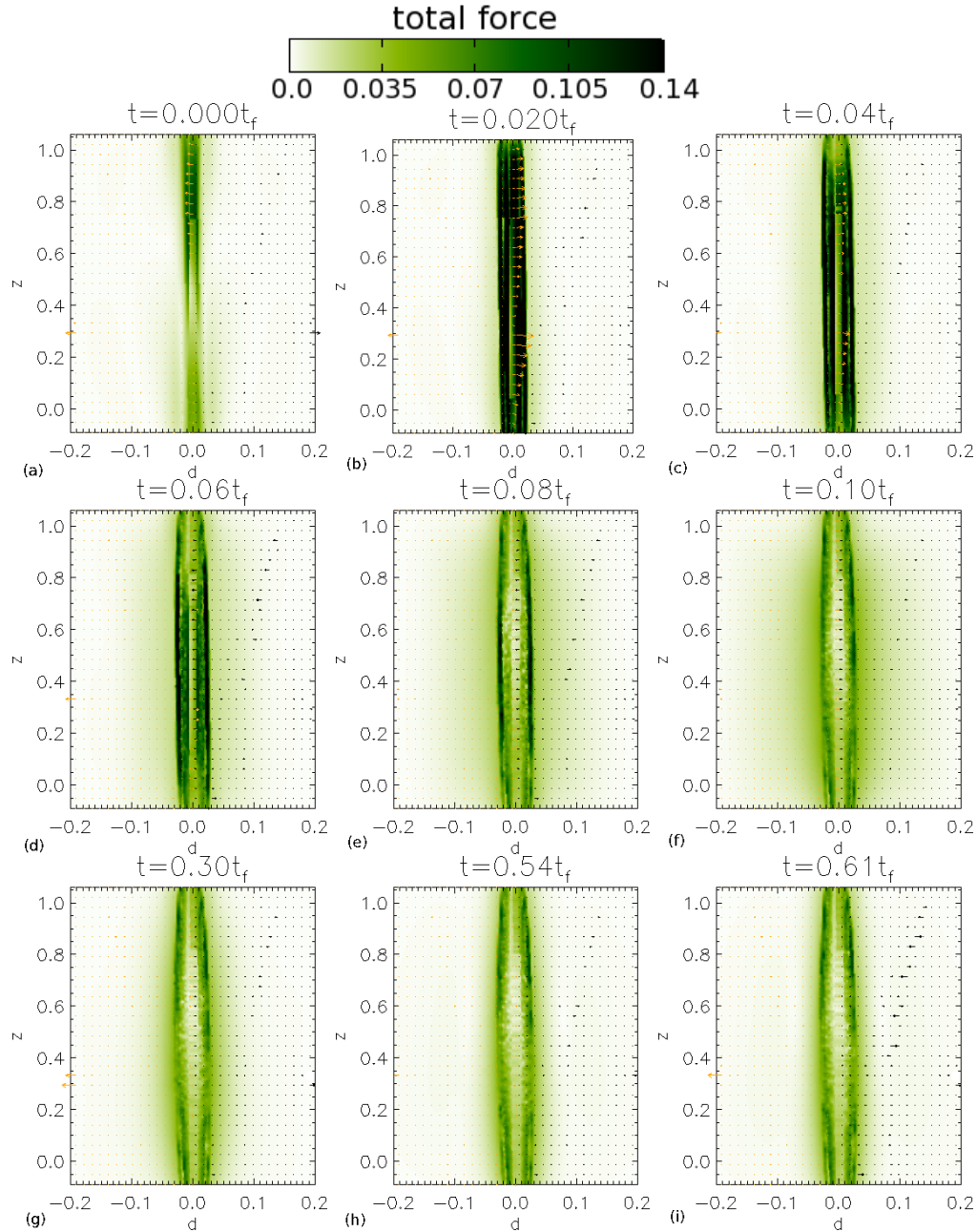


Figure 5.14: Contours of the total force through the depth, d , of the current layer plotted along the length of the separator at (a) $t = 0t_f$, (b) $t = 0.02t_f$, (c) $t = 0.04t_f$, (d) $t = 0.06t_f$, (e) $t = 0.08t_f$, (f) $t = 0.1t_f$, (g) $t = 0.3t_f$, (h) $t = 0.54t_f$ and (i) $t = 0.61t_f$. Arrows, normalised to the maximum value on the colour bar, display the direction of the total force in this plane. The arrows are coloured orange/black where d is less than/greater than 0.

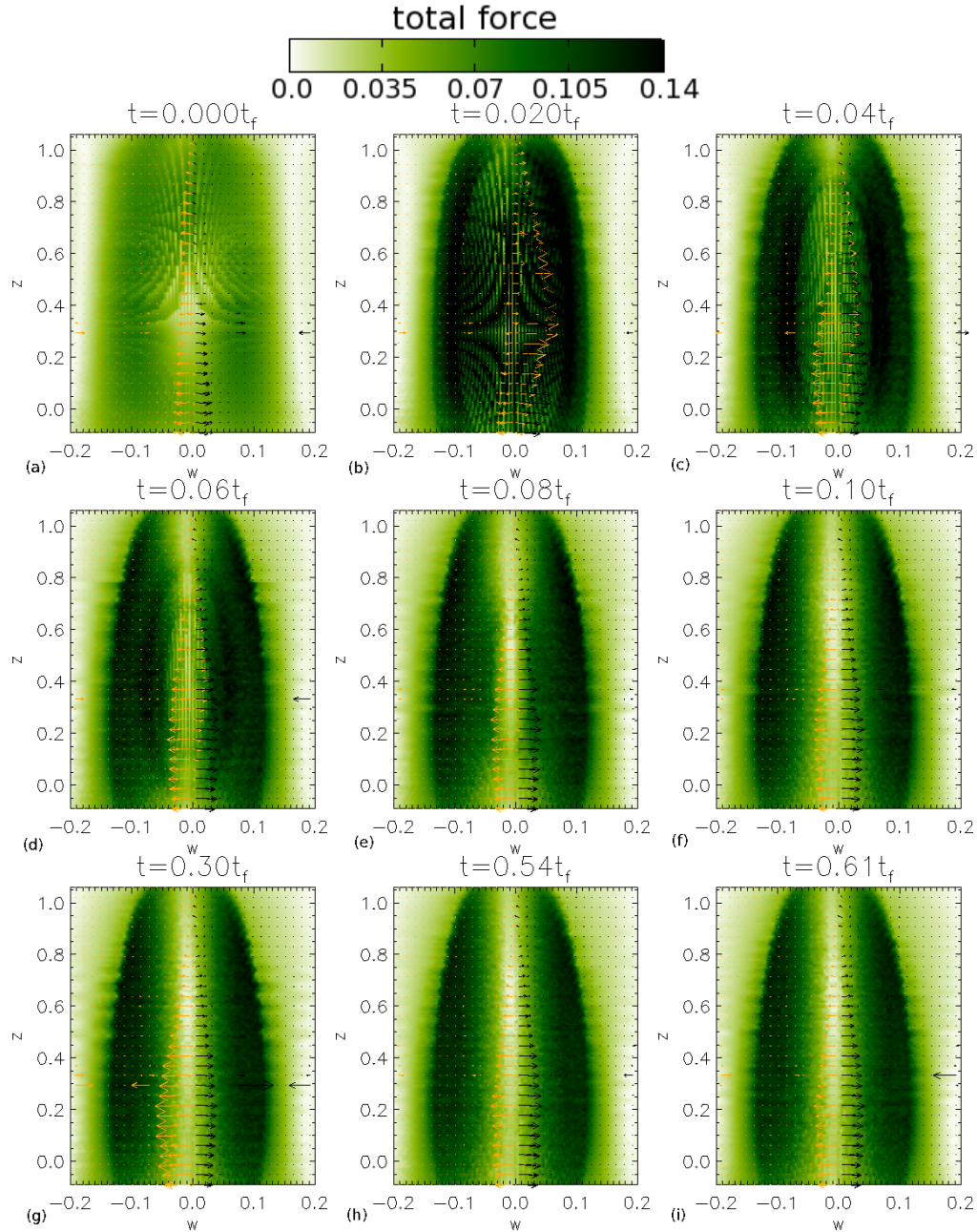


Figure 5.15: Contours of the total force across the width, w , of the current layer plotted along the length of the separator at (a) $t = 0t_f$, (b) $t = 0.02t_f$, (c) $t = 0.04t_f$, (d) $t = 0.06t_f$, (e) $t = 0.08t_f$, (f) $t = 0.1t_f$, (g) $t = 0.3t_f$, (h) $t = 0.54t_f$ and (i) $t = 0.61t_f$. Arrows, normalised to the maximum value on the colour bar, display the direction of the total force in this plane. The arrows are coloured orange/black where w is less than/greater than 0.

5.5 Analysis of waves in the system

In this section, we will look at the effect that waves, launched from the edge of the diffusion site, as soon as the reconnection begins due to the loss of force balance, have on our equilibrium single-separator model. These waves travel out and communicate to the rest of the plasma that reconnection has occurred and that there has been a loss of force balance at the separator current layer. This, in turn, causes the magnetic field and the plasma to change and sets up flows in the system. Sects. 5.5.1 and 5.5.2, examine the perturbed current ($|\mathbf{j}| - |\mathbf{j}_{MHS}|$) and the perturbed plasma pressure ($p - p_{MHS}$), where $|\mathbf{j}_{MHS}|$ and p_{MHS} are the values of the current and the pressure in the MHS equilibrium state, respectively.

To analyse the perturbations, we will look at contours in three planes: (i) a cut perpendicular to the separator at $z = 0.4$, (ii) a surface which goes through the depth of the current layer from the lower to the upper null and (iii) a surface which goes across the width of the current layer from the lower to the upper null as in Figs. 5.14 and 5.15. Further to this, all figures plotted in this way have asterisks over plotted on them which are located on the edge of the contour of $j_{crit} = 10$ at $t = 0t_f$, as was shown in Fig. 5.2 by the black asterisks. There are eight asterisks in Fig. 5.2 at four locations. When the experiment begins four asterisks, one at each of the four locations, will move at the fast-mode speed (c_f) away from the diffusion site. Simultaneously, the other four asterisks, one at each of the four locations, will move at c_f inwards across the current layer. In this way, we can compare the movement of the perturbed current and pressure with the fast-mode speed. We plot only asterisks which move at c_f since in a high plasma-beta system the values of the fast and slow-mode speeds are similar.

5.5.1 Perturbed current $|\mathbf{j}| - |\mathbf{j}_{MHS}|$

As soon as the experiment begins, the non-uniform resistivity causes reconnection to occur at the MHS equilibrium current layer. This reconnection dissipates the current here and leads to waves being launched from the diffusion site. Fig. 5.16 shows the perturbed current at various times throughout phase I and phase II. The amplitude of the current waves are small (on the order of 10^{-3}) due to the high plasma beta which inhibits the formation of large waves. An immediate deficit in current is visible at the current layer (Fig. 5.16b) and as the experiment evolves, enhancements in current, followed by deficits, travel outwards away from the original diffusion site in the regions outwith the cusp which are formed by the separatrix surfaces.

We also see from these contours that on the separatrix surfaces there are further current enhancements on top of those that exist in the equilibrium field. Along the separatrix surfaces, the current is not affected by the reconnection since here $|\mathbf{j}| < j_{crit}$. Instead, an increase in current occurs here since the plasma is still behaving as it did at the end of the non-resistive relaxation experiment discussed in Chapt. 3, i.e., the equilibrium is in force balance everywhere except along the separator where the current layer lies and on the separatrix surfaces where the current is enhanced.

Figs. 5.17 and 5.18 display contours of the perturbed current through the depth and across the width of the current layer, respectively, at the same times as shown in Fig. 5.16. These contours show that the behaviour of the perturbed current in the plane perpendic-

ular to the separator, at $z = 0.4$, occurs along the entire length of the separator.

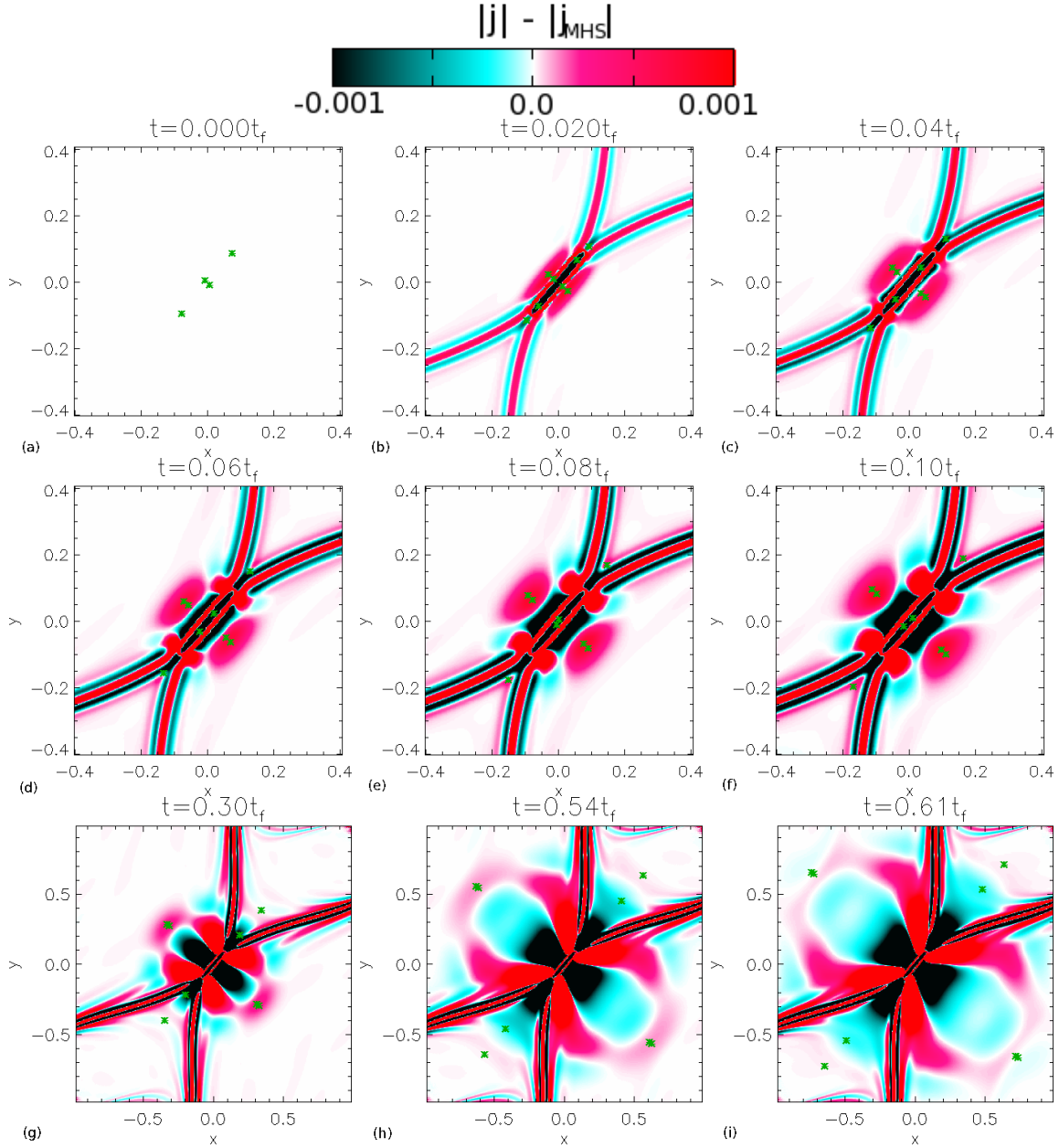


Figure 5.16: Contours of $|\mathbf{j}| - |\mathbf{j}_{MHS}|$ in the plane perpendicular to $z = 0.4$ throughout phase I ((a) to (f)) and phase II ((g) to (i)). Asterisks, which initially lie on the edge of the diffusion region, as shown in Fig. 5.2, move at the fast-magnetoacoustic speed, $c_f(x, y, z, t)$. The last three plots show a larger area than the previous plots.

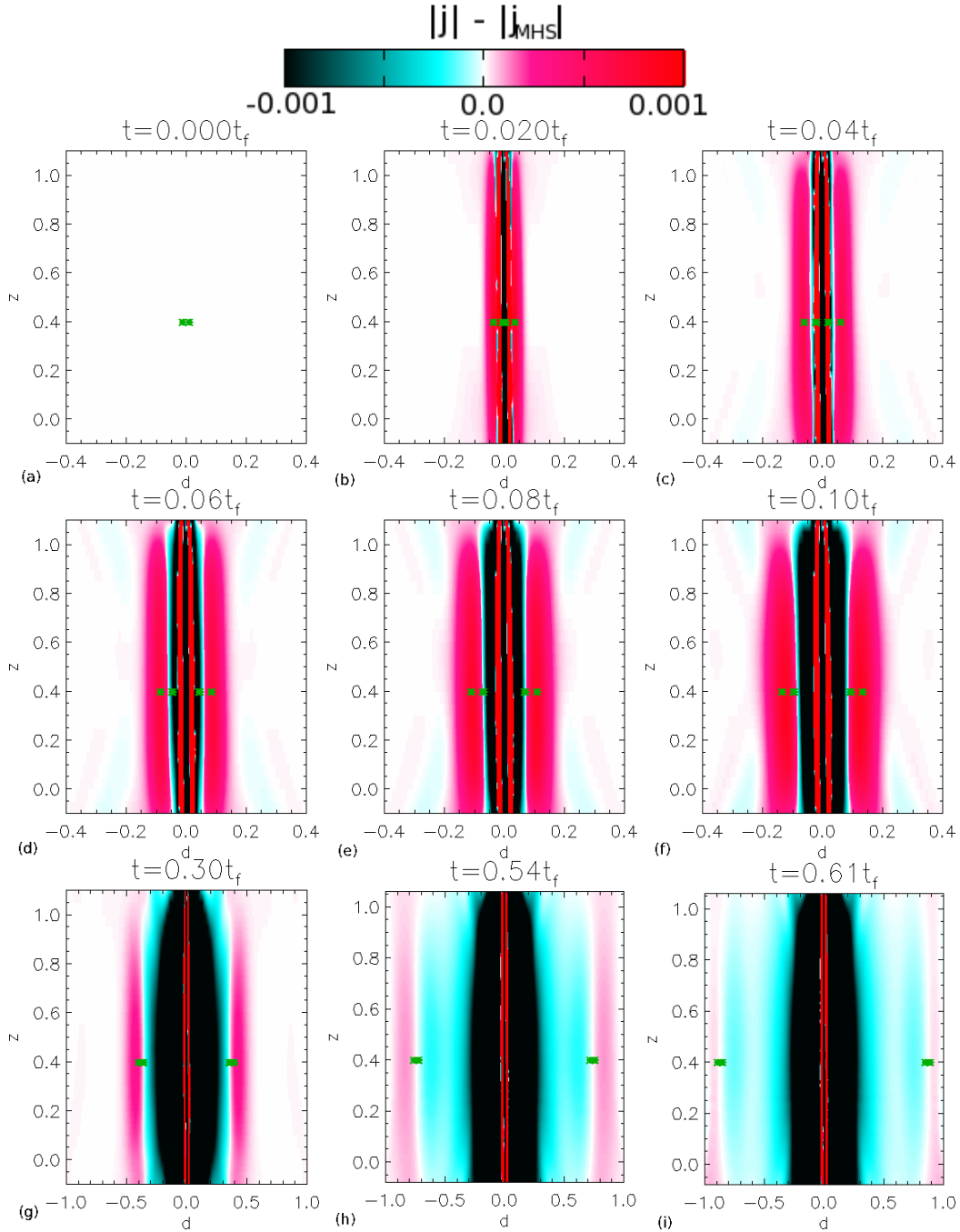


Figure 5.17: Contours of $|j| - |j_{MHS}|$ through the depth of the current layer plotted along the length of the separator throughout phase I ((a) to (f)) and phase II ((g) to (i)). Asterisks, which initially lie on the edge of the diffusion region, as shown in Fig. 5.2, move at the fast-magnetoacoustic speed, $c_f(x, y, z, t)$. The last three plots show a larger area than the previous plots.

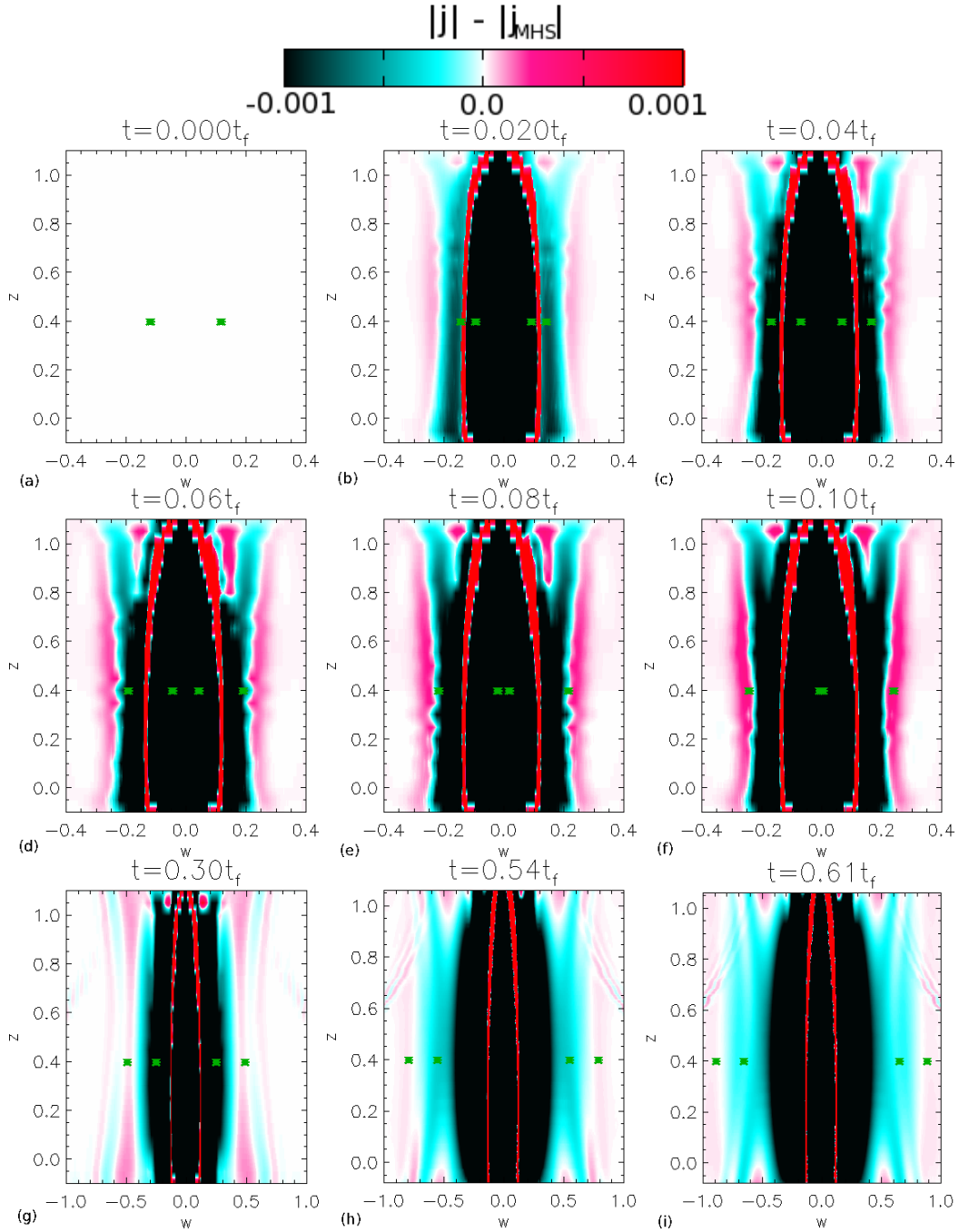


Figure 5.18: Contours of $|j| - |j_{MHS}|$ across the width of the current layer plotted along the length of the separator throughout phase I ((a) to (f)) and phase II ((g) to (i)). Asterisks, which initially lie on the edge of the diffusion region, as shown in Fig. 5.2, move at the fast-magnetoacoustic speed, $c_f(x, y, z, t)$. The last three plots show a larger area than the previous plots.

Once the perturbations have travelled away from the original diffusion site, regions around the separator, where there are current deficits, slowly expand out at no specific wave speed (Figs. 5.16h and 5.16i particularly highlight this). The state of equilibrium is lost within the separator current layer and this causes the non-resistive region around the current layer to attempt to regain force balance. It does this by trying to rebuild the current within the separator current layer. A situation is set up like that found in the MHS equilibrium: (i) outwith the cusp regions the magnetic pressure force, which is directed inwards, is stronger than the outward directed magnetic tension leading to an inflow and (ii) within the cusp regions the magnetic tension force, which is directed outwards, is stronger than the inward directed magnetic pressure force which leads to an outflow. These inflows and outflows are directed towards the separator current layer along the entire length of the separator leading to the current being temporarily built up here. Once the current has values $|\mathbf{j}| \geq j_{crit}$ it is dissipated. This process maintains the flows and prevents a static equilibrium being formed and so we describe phase II as the slow reconnection phase.

Fig. 5.19 displays time slices of the perturbed current through the depth and across the width of the current layer in the $z = 0.4$ plane. In these plots, the y -axis represents time, but it is not on a log scale as many of the previous time slices have been. There are four green lines in Figs. 5.19a and 5.19b which are initially plotted at the position of the asterisks on $|\mathbf{j}| = j_{crit}$ at $t = 0t_f$, in the plane perpendicular to the separator at $z = 0.4$, and represent c_f . Therefore, two of the lines in each plot initially travel away from the diffusion region and the other two lines initially travel towards the diffusion region. These lines highlight that the wave pulses travel at c_f away from the diffusion region. Any discrepancies here could be due to this being a 3D model and hence the waves could move up or down in z , as well as outwards in r .

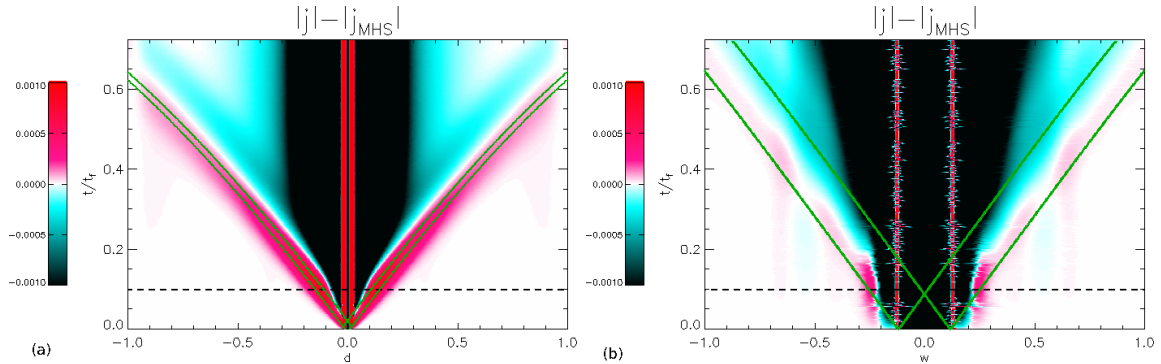


Figure 5.19: Contours of the perturbed current plotted on slices (a) through the depth and (b) across the width of the current layer, in the plane at $z = 0.4$, through time. The black dashed line highlights where the first phase ends. The green lines start on the edge of the current layer and represent c_f .

5.5.2 Perturbed pressure $p - p_{MHS}$

Similar contours, in a plane perpendicular to the separator at $z = 0.4$, show the perturbed pressure throughout the reconnection experiment (Fig. 5.20). Here, unlike the perturbed

current contours which showed an enhancement in current followed by a deficit travelling outwards in the regions outwith the cusps, the perturbed pressure is enhanced moving outwards inside the cusp regions and has a deficit outwith the cusps. In the MHS equilibrium, enhanced pressure existed inside the cusp regions and diminished pressure existed outwith the cusps.

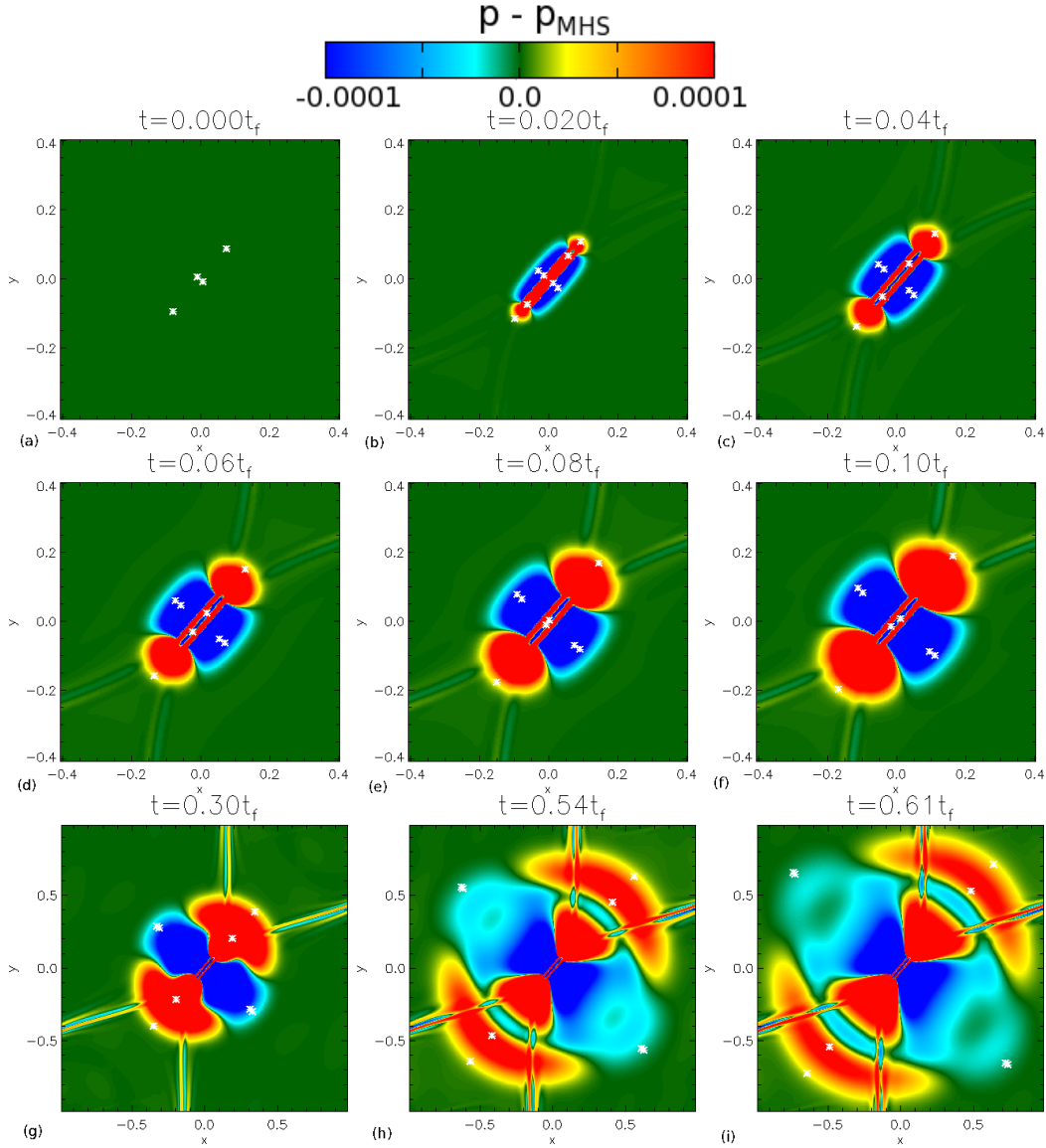


Figure 5.20: Contours of $p - p_{MHS}$ in the plane $z = 0.4$ throughout phase I ((a) to (f)) and phase II ((g) to (i)). Asterisks, which initially lie on the edge of the diffusion region, as shown in Fig. 5.2, move at the fast-magnetoacoustic speed, $c_f(x, y, z, t)$. The last three plots show a larger area than the previous plots.

We see different forms of waves moving out from the edges and ends of the diffusion site. Within the cusp regions the waves appear to launch from a point and propagate out spherically whereas outwith the cusps, the perturbations are more planar in nature and so

move linearly outwards. This pattern, and that shown by the perturbed current, in planes perpendicular to the separator at $z = 0.4$, is very similar to that found about a 2D null at which reconnection has occurred [Fuentes-Fernández et al., 2011].

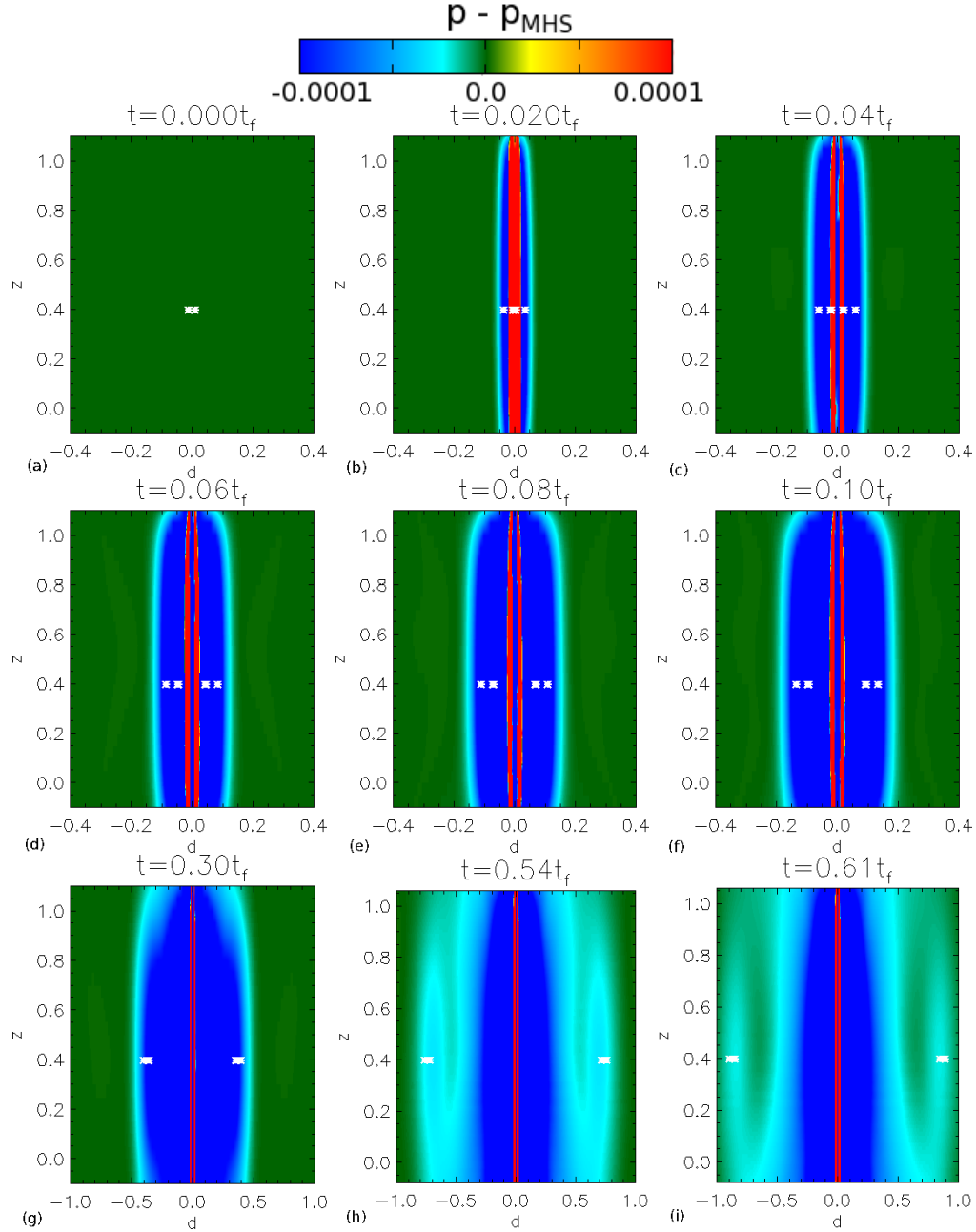


Figure 5.21: Contours of $p - p_{MHS}$ through the depth, d , of the current layer plotted along the length of the separator throughout phase I ((a) to (f)) and phase II ((g) to (i)). Asterisks, which initially lie on the edge of the diffusion region, as shown in Fig. 5.2, move at the fast-magnetoacoustic speed, $c_f(x, y, z, t)$. The last three plots show a larger area than the previous plots.

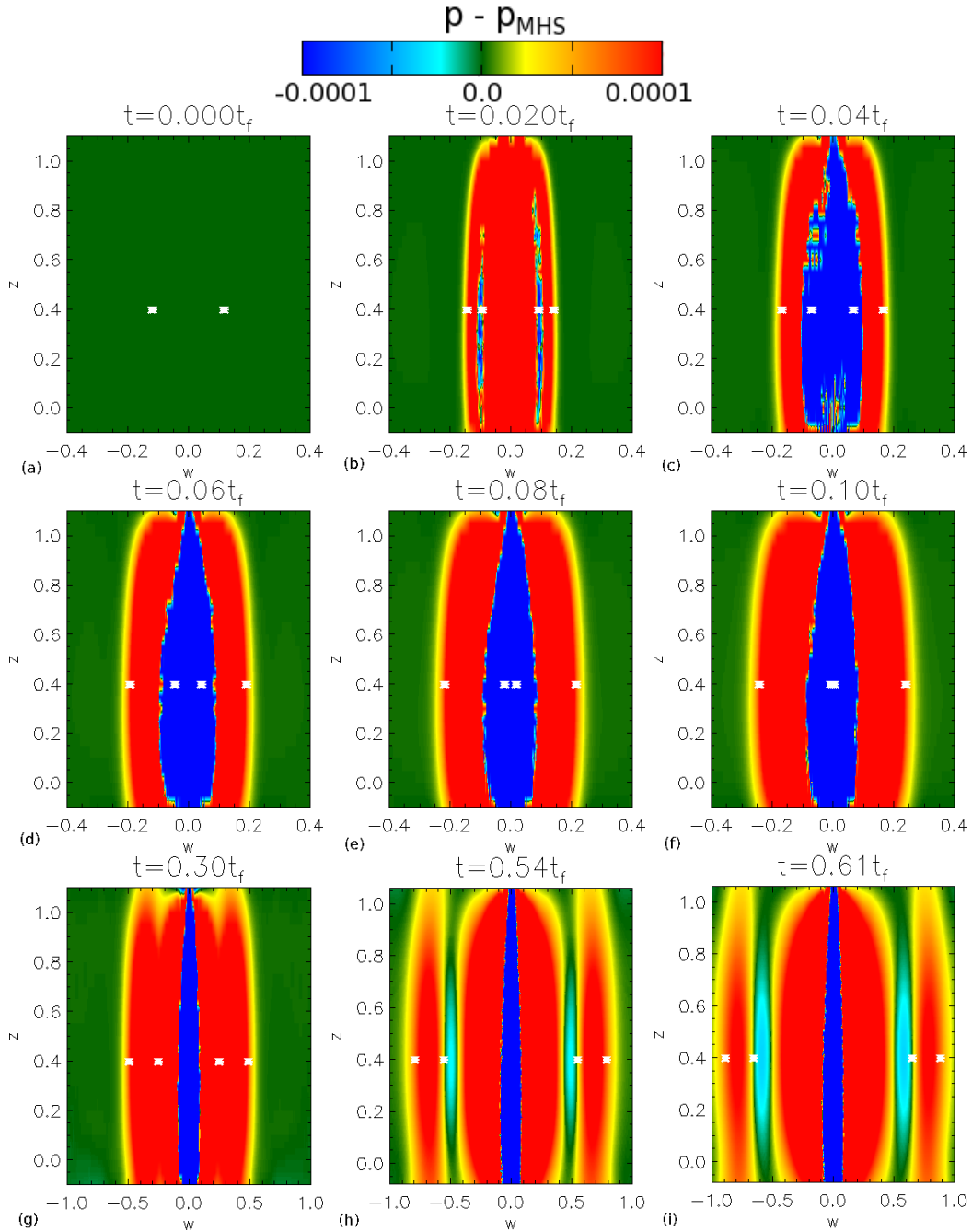


Figure 5.22: Contours of $p - p_{MHS}$ across the width, w , of the current layer plotted along the length of the separator throughout phase I ((a) to (f)) and phase II ((g) to (i)). Asterisks, which initially lie on the edge of the diffusion region, as shown in Fig. 5.2, move at the fast-magnetoacoustic speed, $c_f(x, y, z, t)$. The last three plots show a larger area than the previous plots.

Again, this behaviour of the perturbed pressure, occurs along the entire length of the separator, as shown in the contours through the depth (Fig. 5.21) and across the width

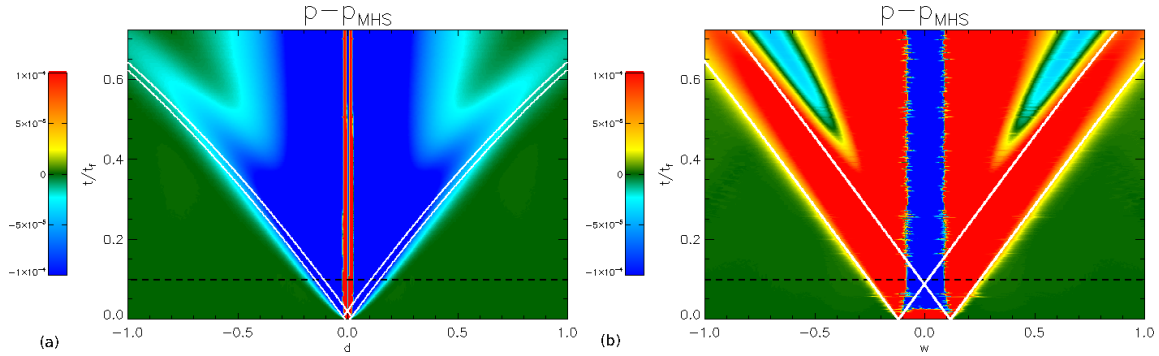


Figure 5.23: Contours of the perturbed pressure plotted on slices (a) through the depth and (b) across the width of the current layer, in the plane at $z = 0.4$, through time. The black dashed line highlights where the first phase ends. The white lines start on the edge of the current layer and represent c_f .

(Fig. 5.22) of the current layer.

Once the perturbations have travelled away from the original diffusion site, regions around the separator where there are pressure enhancements (within the cusps) and pressure deficits (outwith the cusps) slowly expand out at no particular wave speed (Fig. 5.20h and 5.20i). As explained previously, the state of equilibrium is lost within the separator current layer and this causes the non-resistive region around the current layer to attempt to regain force balance.

In Fig. 5.23, time slices of the perturbed pressure are shown, plotted through the depth and across the width of the current layer in the $z = 0.4$ plane. The y -axis represents time on a linear scale in this figure. The four white lines in Figs. 5.23a and 5.23b are initially plotted at the position of the asterisks on $|\mathbf{j}| = j_{crit}$ at $t = 0t_f$, in the plane perpendicular to the separator at $z = 0.4$, and move at the speed c_f . As such, two of the lines in each plot initially travel away from the diffusion region and the other two lines initially travel towards the diffusion region. These lines highlight that the wave pulses travel at c_f away from the diffusion region. Again, any discrepancies here could be due to this being a model with three dimensions.

5.6 Vorticity and velocity

In this section, we consider both the vorticity and the velocity at various times throughout the first and second phases of the experiment, in order to understand the nature of the flows created as a result of the reconnection. The maximum value of the velocity throughout the domain during phase I is $|\mathbf{v}| = 0.016$ and occurs at $t = 0.005t_f$. The mean value of the velocity at this time is $|\bar{\mathbf{v}}| = 1.2 \times 10^{-5}$. The maximum value of the velocity reduces to $|\mathbf{v}| = 0.01$ at the end of phase I at which point the mean velocity is $|\bar{\mathbf{v}}| = 4.9 \times 10^{-5}$. By the end of phase II the maximum velocity is $|\mathbf{v}| = 5.6 \times 10^{-3}$ and the mean velocity throughout the domain is $|\bar{\mathbf{v}}| = 1.4 \times 10^{-4}$.

Here, we again plot the contours in the $z = 0.4$ plane perpendicular to the separator at a range of different times (Fig. 5.24), but also in planes perpendicular to the separator

going from the lower to the upper null at a fixed time (Fig. 5.25). Figs. 5.26 and 5.27 then show the vorticity in the surface through the depth and in the surface across the width of the current layer, respectively. Over plotted on these graphs are arrows which indicate the direction and size of the velocity in these cuts. In Figs. 5.24 and 5.25 these arrows are coloured green regardless of their position, however, in Figs. 5.26 and 5.27, the arrows positioned where $d < 0$ and $w < 0$ are coloured black while the arrows positioned where $d > 0$ and $w > 0$ are coloured green. This is done such that the direction of the flow is clear in these plots.

The contours in Fig. 5.24 show that a very similar pattern to the classical quadrupolar vortex scenario and stagnation flow found in 2D X-point reconnection regimes is formed rapidly once the experiment starts. The main difference is that instead of finding zero vorticity in the vicinity of the separator, an antiparallel flow is found associated with a clockwise (blue) rotating flow pattern in this plane.

Fig. 5.25 shows contours of the vorticity in various planes perpendicular to the separator, starting around the lower null and ending near the upper null at $t = 0.1t_f$. These contours show a similar quadrupole vortex (rotated slightly due to the twisted nature of the current layer and separatrix surfaces about the separator), but in the vicinity of the separator, the flow is clockwise (blue) along the lower half of the separator and anti-clockwise (red) along the upper half of the separator. This agrees with the existence of a counter-rotating flow along the separator shown in Fig. 5.11a.

Due to the nature of the vorticity seen in Fig. 5.25, it is not surprising, therefore, that the directions of the flows change with position along the separator through the depth (Fig. 5.26) and across the width (Fig. 5.27) of the current layer. The velocity arrows (which are coloured black where $d, w < 0$ and are coloured green where $d, w > 0$ such that the direction of the flow is clear) indicate that the dominant flows are directed inwards through the depth, and outwards across the width, for all z . However, superimposed on these are weak stagnation-type flow patterns.

Along the separator, in the cut through the depth (Fig. 5.26), weak flows run towards both nulls from a point 0.6 times the length of the separator from the lower null. The location of this stagnation point, which corresponds to where the flows are purely directed inwards to the current layer through the depth, does not appear to move over time. Its location is a result of the fact that the plasma pressure on the separator is greatest at this point in the MHS equilibrium and so the strongest magnetic pressure force must have existed at this location to counter the largest pressure force that would have been located there.

The cuts across the width of the current layer (Fig. 5.27) show the opposite quadrupolar-vortex pattern close to the separator. This pattern shows that there are weak flows that run in from the nulls along the separator to a point 0.4 times the length of the separator from the lower null. This is the approximate centre of the initial main stagnation outflow across the width of the current layer. This region, within which the flows are oppositely directed to the flows outwith it, disappears through phase I and is not visible in phase II. The flows around this part appear to remove this area within which the flows are oppositely directed. Near the end of phase I a stagnation point starts to form near the lower null and this point moves up, in the z -direction, during phase II and is situated near $z = 0.2$ by the end of the experiment.

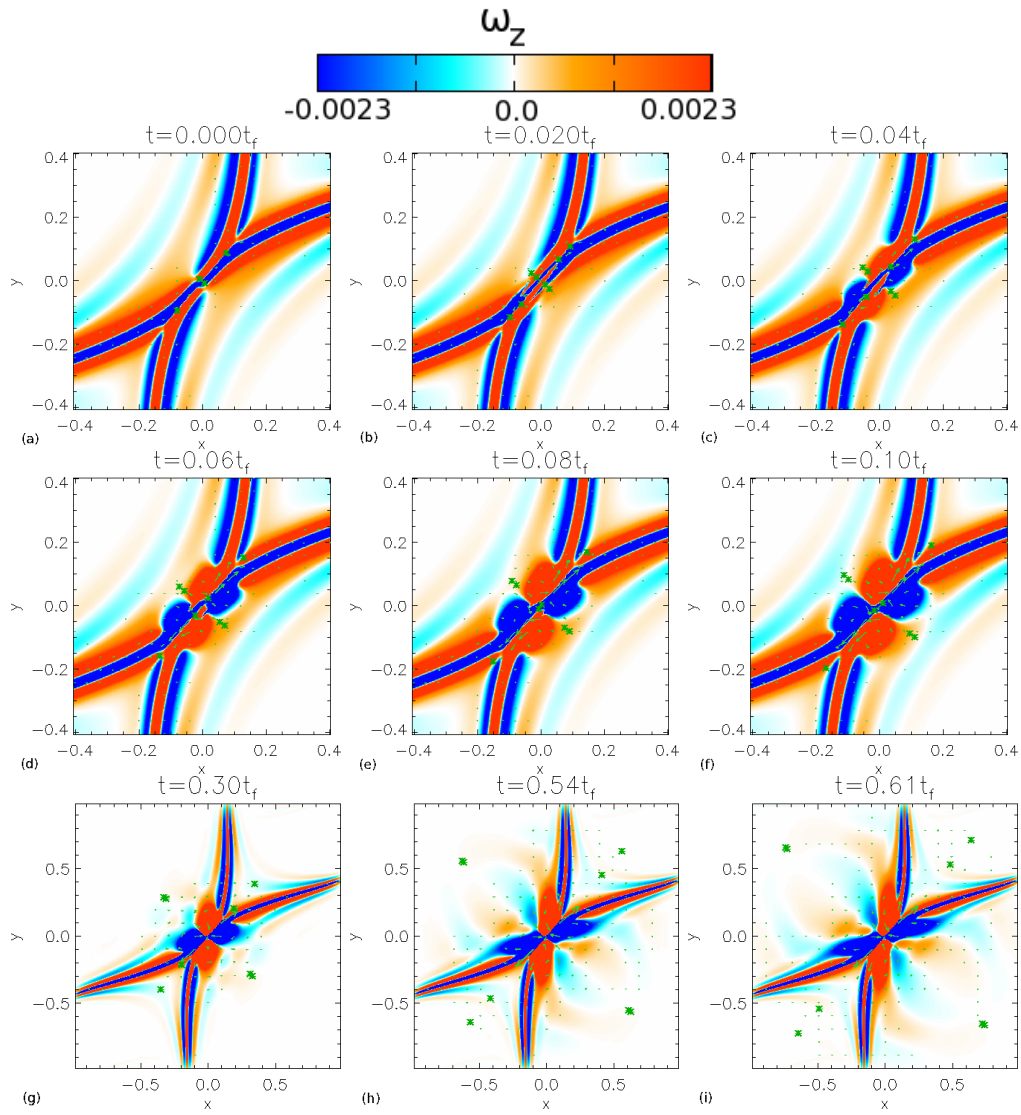


Figure 5.24: Contours of the z -component of the vorticity in the plane $z = 0.4$ throughout phase I ((a) to (f)) and phase II ((g) to (i)). Arrows (normalised to the maximum value of $|\mathbf{v}|$ in the domain at $t = 0.61t_f$, $|\mathbf{v}| = 6 \times 10^{-3}$) display the direction of v_x and v_y . Asterisks, which initially lie on the edge of the diffusion region, as shown in Fig. 5.2, move at the fast-magnetoacoustic speed, $c_f(x, y, z, t)$. The last three plots show a larger area than the previous plots.

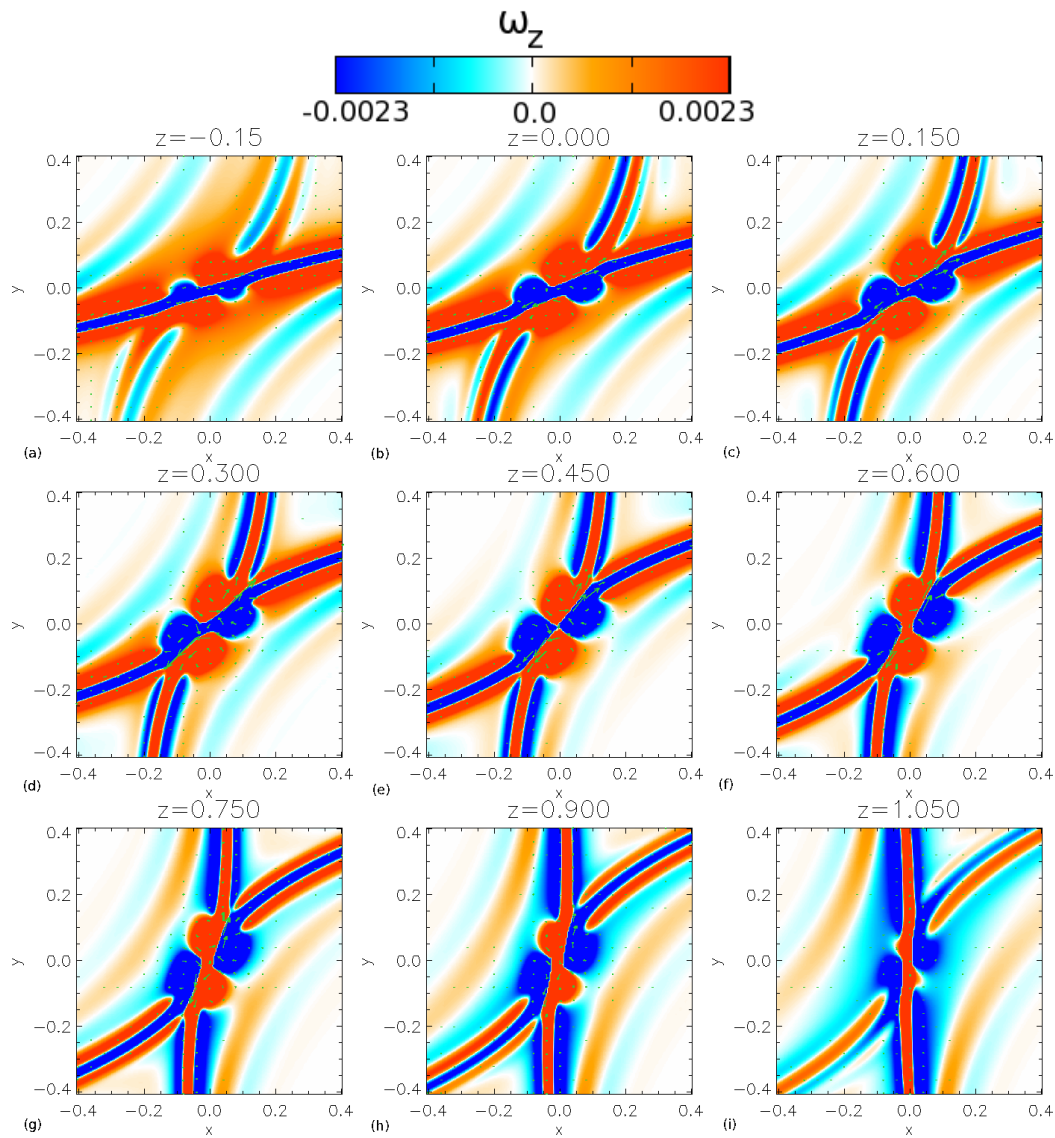


Figure 5.25: Contours of the z -component of the vorticity at $t = 0.1t_f$, in planes perpendicular to the separator at (a) $z = -0.15$, (b) $z = 0.0$, (c) $z = 0.15$, (d) $z = 0.3$, (e) $z = 0.45$, (f) $z = 0.6$, (g) $z = 0.75$, (h) $z = 0.9$ and (i) $z = 1.05$. Arrows (which have been normalised to the maximum value of $|\mathbf{v}|$ in the domain at $t = 0.61t_f$, $|\mathbf{v}| = 6 \times 10^{-3}$) display the direction of v_x and v_y .

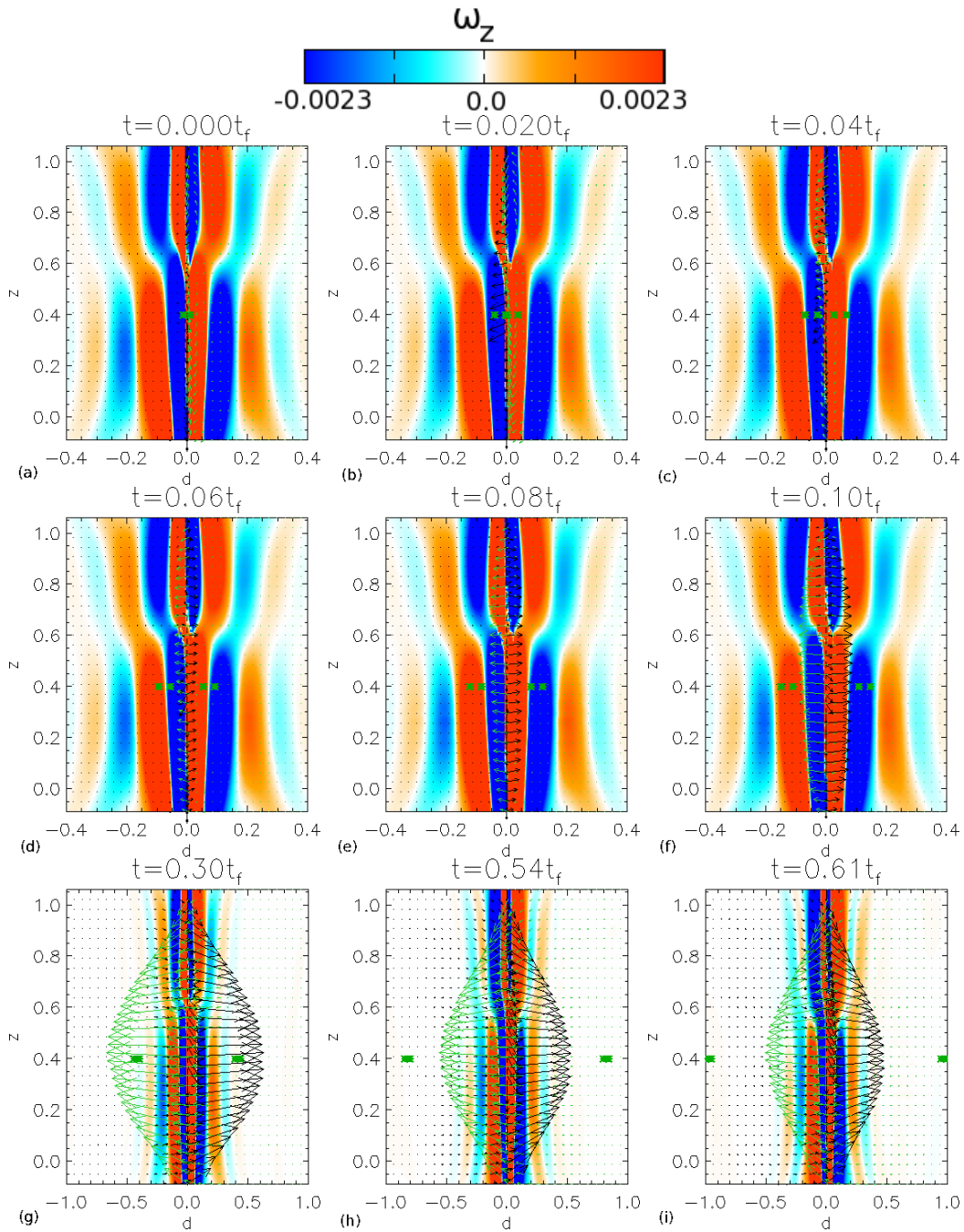


Figure 5.26: Contours of the vorticity through the depth of the current layer plotted along the length of the separator throughout phase I ((a) to (f)) and phase II ((g) to (i)). The last three plots show a larger area than the previous plots. Arrows (normalised to the maximum value of $|\mathbf{v}|$ in the domain at $t = 0.61t_f$, $|\mathbf{v}| = 6 \times 10^{-3}$) display the direction of v_r and v_z in this plane. The arrows are coloured black where $d < 0$ and are coloured green where $d > 0$. Asterisks, which initially lie on the edge of the diffusion region, as shown in Fig. 5.2, move at the fast-magnetoacoustic speed, $c_f(x, y, z, t)$.

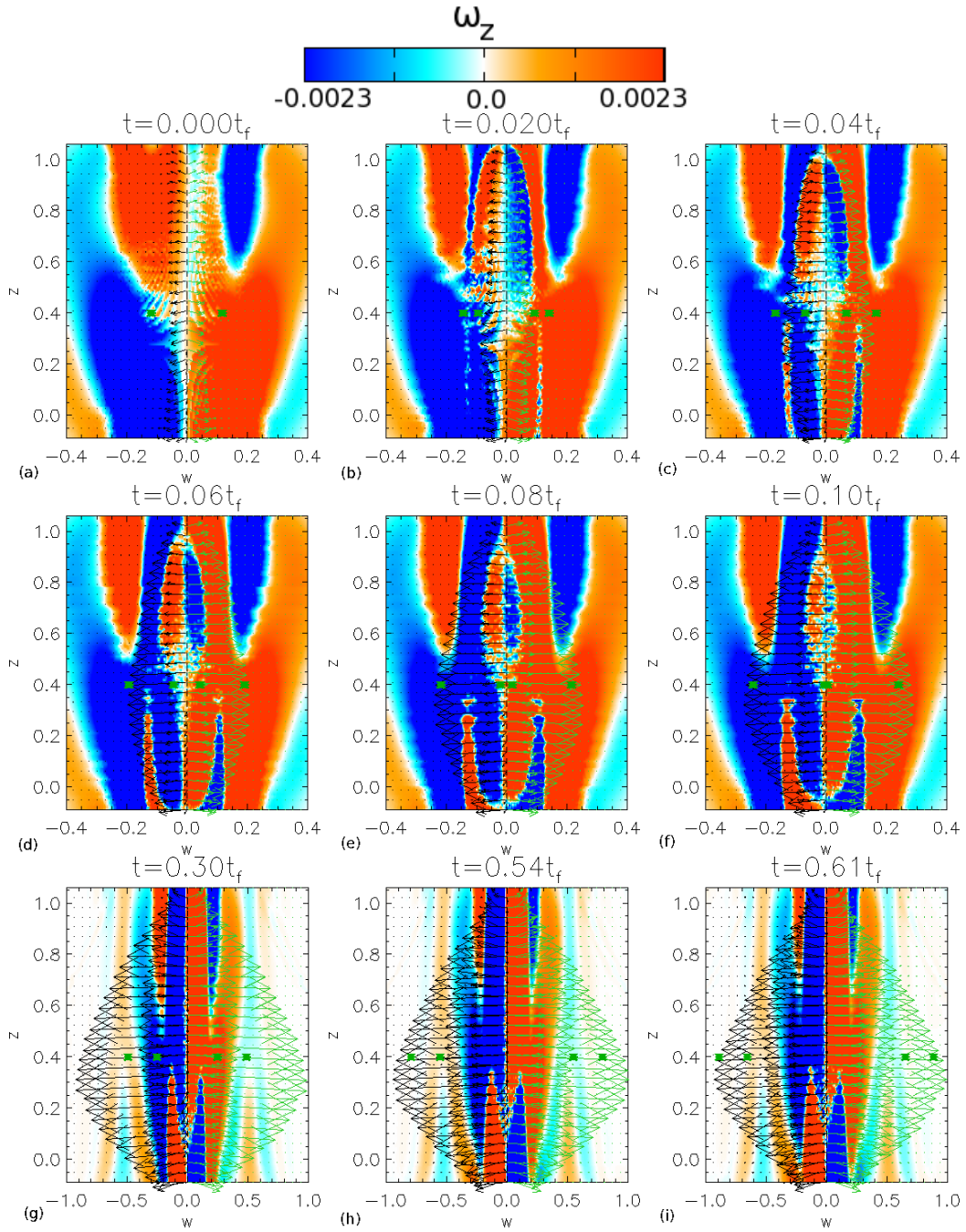


Figure 5.27: Contours of the vorticity across the width of the current layer plotted along the length of the separator throughout phase I ((a) to (f)) and phase II ((g) to (i)). The last three plots show a larger area than the previous plots. Arrows (normalised to the maximum value of $|\mathbf{v}|$ in the domain at $t = 0.61t_f$, $|\mathbf{v}| = 6 \times 10^{-3}$) display the direction of v_r and v_z . The arrows are coloured black where $w < 0$ and are coloured green where $w > 0$. Asterisks, which initially lie on the edge of the diffusion region, as shown in Fig. 5.2, move at the fast-magnetoacoustic speed, $c_f(x, y, z, t)$.

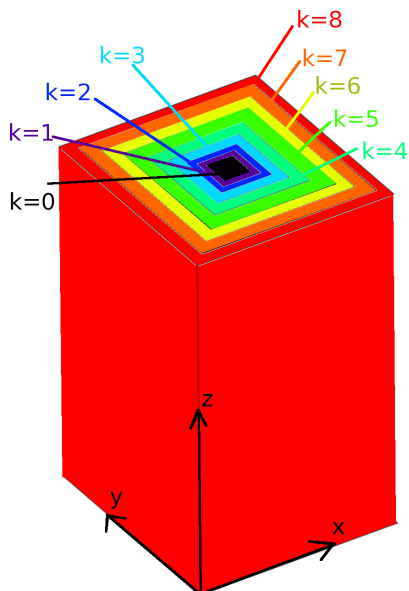


Figure 5.28: Coloured boxes representing the volumes over which the transport of energy equations are integrated. The volumes increase according to $-(0.15 + k/10) \leq x, y \leq (0.15 + k/10)$ and $-0.2 \leq z \leq 1.2$ shown by the colours black ($k = 0$), purple ($k = 1$), blue ($k = 2$), cyan ($k = 3$), lime ($k = 4$), green ($k = 5$), yellow ($k = 6$), orange ($k = 7$) and red ($k = 8$).

5.7 Transport of energy

As has been discussed previously, the separator reconnection which occurs in the system causes waves to be launched from the diffusion site, as a consequence of the sudden lack of force balance. The waves, which travel out causing changes to the magnetic field and plasma, set up flows in the system. We now study the transport of magnetic energy, internal energy and kinetic energy equations, integrated over volumes within our domain, in order to analyse what quantities these waves and flows carry with them.

We integrate the various terms in the transport of energy equations over volumes, of increasing size, within our domain. The smallest volume we integrate over, encloses the separator current layer and has dimensions $-0.15 \leq x, y \leq 0.15$ and $-0.2 \leq z \leq 1.2$. In total there are nine volumes, over which we integrate, with dimensions $-(0.15 + k/10) \leq x, y \leq (0.15 + k/10)$, for $k = 0, 1, 2, \dots, 8$ and the z range is fixed for all volumes. Hence, the largest volume we use is slightly smaller than the size of our domain. A cartoon of these volumes is shown in Fig. 5.28, where the volumes are coloured black, purple, blue, lime, green, yellow, orange and red as they increase in size. Hence, in Fig. 5.29, which shows the terms in the transport of energy equations, there are nine lines, coloured to match the different volumes.

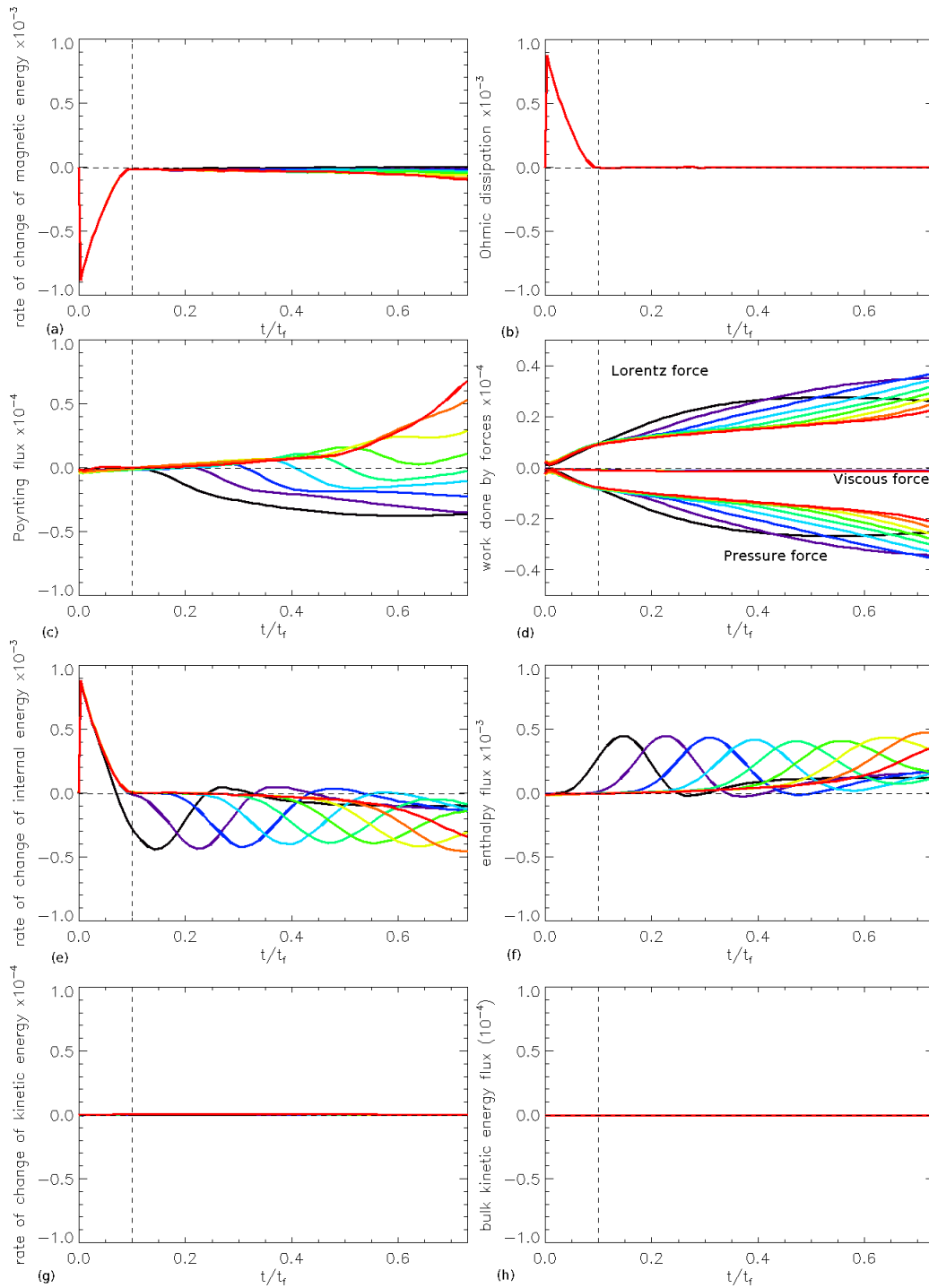


Figure 5.29: Quantities, plotted against time, of (a) the rate of change of the magnetic energy, (b) the Ohmic dissipation, (c) the Poynting flux, (d) the work done by the Lorentz force, the work done by the viscous force and the work done by the pressure force, (e) the rate of change of internal energy, (f) the enthalpy flux, (g) the rate of change of kinetic energy and (h) the bulk kinetic energy flux. The coloured lines represent different volumes over which these quantities have been integrated. The black dashed vertical line highlights where phase I ends and phase II begins and the black dashed horizontal line represents the zero line.

5.7.1 Transport of magnetic energy

Eq. 5.2 is the transport of magnetic energy equation

$$\frac{\partial}{\partial t} \left(\frac{B^2}{2\mu_0} \right) = -\eta j^2 - \nabla \cdot (\mathbf{E} \times \mathbf{B}) - \mathbf{v} \cdot (\mathbf{j} \times \mathbf{B}). \quad (5.2)$$

This equation states that the rate of change of magnetic energy is equivalent to the negative value of the Ohmic dissipation minus the Poynting flux minus the work done by the Lorentz force.

The term on the left hand side of Eq. 5.2 is shown in Fig. 5.29a, plotted throughout the reconnection experiment, integrated over the nine volumes shown in Fig. 5.28. The negative sum of the next three graphs (Figs. 5.29b, 5.29c and 5.29d) make Fig. 5.29a in which an initial sharp drop in the rate of change of magnetic energy is observed. This drop is due to the Ohmic dissipation at this time (Fig. 5.29b) and coincides with phase I where the reconnection rate is high and a lot of Ohmic heating is occurring in the system, as was shown in Fig. 5.4. The value of the Ohmic dissipation integrated over all nine volumes is the same regardless of the size of the volume since the value of η is only non-zero in the smallest box. Hence, the integrals of the Ohmic dissipation within all larger volumes do not make any contribution to the integrated value within the black box. The Ohmic dissipation is fairly constant after $t = 0.1t_f$ which is the slow-steady second phase.

The second term, on the right hand side of value of Eq. 5.2 represents the Poynting flux. Fig. 5.29c shows that the Poynting flux is initially positive indicating that waves are travelling out through the boundaries of our volumes. As has been discussed, these waves lead to flows being set up in the system near to the original diffusion site. These flows bring Poynting flux in through the smaller volumes, over which we integrate, and eventually dominate over the value of the Poynting flux carried out of the five smallest volumes by the waves. However, in the larger volumes the Poynting flux values carried out through the volumes by the waves, become relatively large the further out they travel (see the green to red lines in Fig. 5.29c). Note, however, that the amount of Poynting flux is roughly 25 times smaller than the Ohmic dissipation which peaked in phase I.

The Lorentz force is working to try and regain force balance in the system from the moment the current in the separator current layer begins to be dissipated (positive values in Fig. 5.29d). This figure shows that the work done by the Lorentz force, which is roughly of the order of 3×10^{-5} , is acting out through the sub-volumes, over which we have integrated. The Lorentz force is the sum of the magnetic pressure and tension forces. The magnetic tension force, which acts to straighten the field lines, is directed outwards from the diffusion site both within and outwith the cusp regions which are formed by the separatrix surfaces of the nulls. The magnetic pressure force is directed in towards the diffusion region within the cusps and outwith the cusps. Overall, these forces sum such that the work done by the Lorentz force is acting outwards away from the diffusion region. The magnitude of this term is roughly 30 times smaller than the Ohmic dissipation term.

5.7.2 Transport of internal energy

The transport of internal energy equation can be written as

$$\frac{\partial}{\partial t} (\rho\epsilon) = \eta j^2 - \nabla \cdot \left((p + \rho\epsilon)\mathbf{v} \right) - (-\mathbf{v} \cdot \nabla p), \quad (5.3)$$

where $\rho\epsilon = 3p/2$, since our closure equation is $\epsilon = p/\rho(\gamma - 1)$, and $\gamma = 5/3$ and therefore $p + \rho\epsilon = 5p/2$. Eq. 5.3 states that the rate of change of internal energy is due to the Ohmic heating minus the enthalpy flux minus the work done by the pressure force. Fig. 5.29e shows the rate of change of internal energy, which is of the order of 10^{-3} , integrated over all nine volumes, throughout the experiment. The initial sharp spike in this figure is due to the Ohmic heating (Fig. 5.29b) as was seen in Fig. 5.4a.

After this spike, the rate of change of internal energy decreases and becomes negative. A small travelling wave is seen moving out through all the sub-volumes which comes from the enthalpy flux term (Fig. 5.29f). This term is of the order of 5×10^{-4} and is 2 times smaller than the Ohmic dissipation which occurs in phase I. It remains constant in amplitude except just before it leaves the final volumes. Over a much larger area this term may become more important.

The final term which contributes to Eq. 5.3 is the work done by the pressure force (negative values in Fig. 5.29d), however, the magnitude of this term is about 30 times smaller than that of the Ohmic heating and about 15 times smaller than the enthalpy flux terms and so its contribution is small here. The work done by the pressure force is directed in through the sub-volumes over which we integrate and is acting, like the Lorentz force, to try to regain force balance in the system as soon as the reconnection begins.

5.7.3 Transport of kinetic energy

We now consider the transport of kinetic energy equation

$$\frac{\partial}{\partial t} \left(\frac{\rho v^2}{2} \right) = \mathbf{v} \cdot (\mathbf{j} \times \mathbf{B}) + (-\mathbf{v} \cdot \nabla p) + \mathbf{v} \cdot \mathbf{F}_\nu - \nabla \cdot \left(\frac{\rho v^2}{2} \mathbf{v} \right). \quad (5.4)$$

This equation states that the rate of change of kinetic energy is equal to the work done by the Lorentz force plus the work done by the pressure force plus the work done by the viscous force minus the bulk kinetic energy flux.

Fig. 5.29g shows the term on the left-hand side of Eq. 5.4 integrated over all nine volumes shown in Fig. 5.28. This figure indicates that the rate of change of kinetic energy is very small ($\sim 5 \times 10^{-7}$) throughout the reconnection experiment. These values are so small since the work done by the Lorentz force and the work done by the pressure force are about equal in size, but are acting in opposite directions (Fig. 5.29d). Both the Lorentz and pressure forces are acting to regain force balance in the system after the waves have moved out from the diffusion site. Also, the contribution from the work done by the viscous forces (Fig. 5.29d) is very small ($\sim 5 \times 10^{-7}$) as is the bulk kinetic energy flux term (Fig. 5.29h) since the velocities in the system have small magnitudes.

5.7.4 Main terms involved in the transport of energy

There are five terms which play a significant role in the transport of energy in our high plasma-beta reconnection experiment. Ohmic heating initially causes a lot of the magnetic energy to be converted into internal energy and plays the most significant role in our experiment. This energy is then carried away from the diffusion region by the enthalpy flux, which is half the size of the Ohmic heating term and the Poynting flux, which is roughly 25 times smaller than the peak Ohmic heating. The final two important terms

are the work done by the Lorentz and pressure forces, which are similar in magnitude, but act in opposite directions and are both about 30 times smaller than the Ohmic heating term.

5.8 Parameter analysis: η_d , j_{crit} and ν

In the final section of this chapter, we investigate the effects that three of the plasma parameters have on the reconnection rate (Sect. 5.8.1) and the energetics (Sects. 5.8.2, 5.8.3 and 5.8.4). These parameters are (i) the anomalous resistivity, η_d , (ii) the size of the diffusion region (controlled by the value of j_{crit}) and (iii) the background viscosity, ν . Therefore, we have analysed reconnection experiments with three different values of η_d : $\eta_d = 0.0005$, 0.001 and 0.002 , three different values of j_{crit} : $j_{crit} = 7.5$, $j_{crit} = 8.5$ and $j_{crit} = 10.0$, and three different values of ν : $\nu = 0.001$, $\nu = 0.005$ and $\nu = 0.01$. None of the plasma parameters, nor the initial magnetic field have changed from the original experiment in any of these runs except for the values of η_d , j_{crit} or ν thus, of the three parameters examined here, the two not being varied have the values used in the main experiment detailed in this chapter, i.e., $\eta_d = 0.001$, $j_{crit} = 10.0$ and $\nu = 0.01$. In all figures shown in this section, the solid curves represent the main experiment discussed previously.

5.8.1 Effects of η_d , j_{crit} and ν on the reconnection rate

Fig. 5.30a shows the reconnection rate and the total flux reconnected for three experiments in which η_d is varied. As expected, a higher value of η_d leads to faster reconnection, but a shorter phase I (the fast-reconnection phase). Fig. 5.30a shows that the total amount of reconnected flux increases as η_d increases, except for the experiment with $\eta_d = 0.002$. We believe this occurs since near the start of the experiment with $\eta_d = 0.002$ (the highest value of the anomalous resistivity investigated in this chapter) additional nulls appear in the system. These nulls form in opposite-sign pairs and appear close to the locations of the original nulls leading to the creation of extra intercluster separators that link the two original null points and null-point clusters. Therefore, reconnection may be occurring on all the separators that now exist. The reconnection rate and the total flux reconnected are plotted along the original separator only, in Fig. 5.30a, and so any reconnection that may occur on the other separators will not be picked up. This is the only experiment discussed here which displays this behaviour.

Fig. 5.30b indicates that a smaller diffusion region (i.e., a high value of j_{crit}) leads to a shorter fast-reconnection phase (phase I). This is expected since a smaller diffusion region will contain less flux to reconnect. We also note, that the peak reconnection rate is unaffected by the value of j_{crit} , hence, the total amount of flux reconnected increases as j_{crit} is lowered.

We find that varying the value of ν has little effect on the reconnection rate during the fast-reconnection phase, but a lower viscosity appears to be associated with a marginally shorter duration of phase I (Fig. 5.30c). In addition to this, during phase II a smaller viscosity is associated with a faster reconnection rate since the resulting flows that drive the steady state reconnection of phase II are stronger in a fluid that is less viscous. This leads to more flux being reconnected overall in the case with the lowest viscosity.

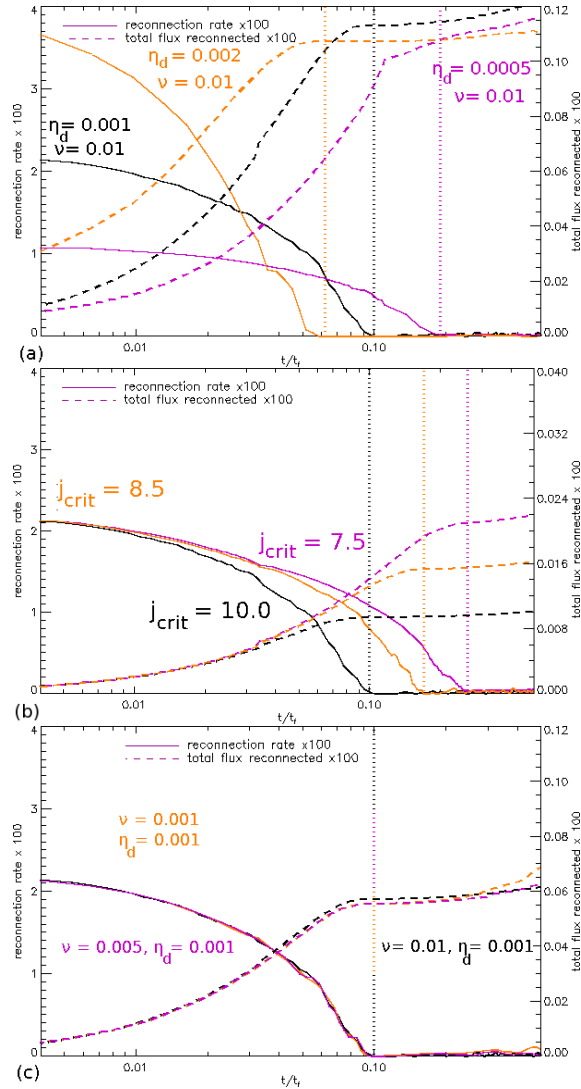


Figure 5.30: Plot of the reconnection rate (solid lines) and the total flux reconnected (dashed lines), multiplied by 100, against time for varying (a) η_d , (b) j_{crit} and (c) ν . In these plots, vertical dotted lines (coloured to match the respective experiment) highlight the time at which phase I ends and phase II begins for each experiment.

5.8.2 Effects of varying the resistivity, η_d

The same basic behaviour of energies is found in this set of experiments, where η_d is varied, as that seen in the main experiment (Fig. 5.31). The change in energies, shown in Fig. 5.31a, are normalised to the maximum change in the magnetic energy of the main experiment (where $\eta_d = 0.001$, $j_{crit} = 10.0$ and $\nu = 0.01$) so that the energy release of all experiments can be compared. The magnetic energy decreases with most of it being converted directly into internal energy and only a little kinetic energy generated. Varying η_d leads to a change in the rate of loss of magnetic energy and, hence, the experiment with the highest η_d experiences the most rapid loss, but also the shortest first phase. Symbols

are positioned on the curves in Fig. 5.31 indicating where phase I ends and phase II begins in each experiment. The total loss of magnetic energy increases as η_d increases. Note as before, the kinetic energy curves have been multiplied by fifty here so they are visible on this scale.

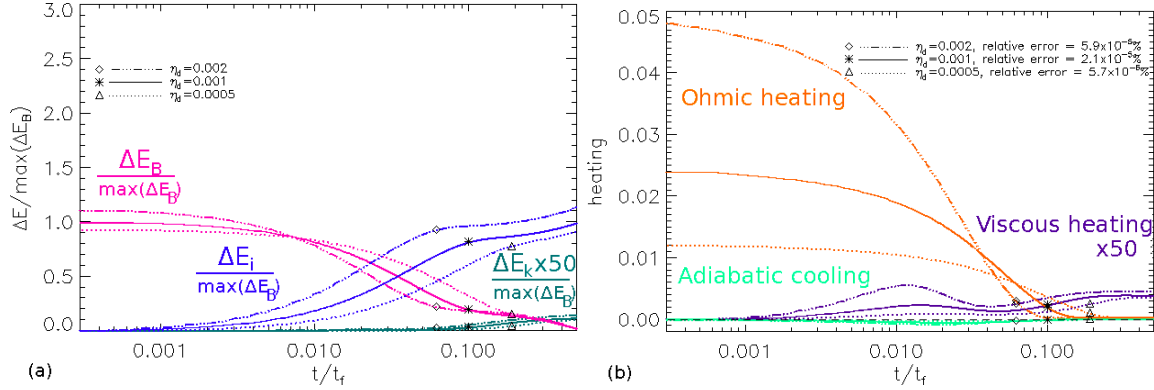


Figure 5.31: Plots of (a) the energy and (b) heating terms for experiments with $\eta_d = 0.0005$, $\eta_d = 0.001$ and $\eta_d = 0.002$ with $j_{crit} = 10.0$ and $\nu = 0.01$. Triangles, asterisks and diamonds indicate where phase I ends and phase II begins for the experiments with $\eta_d = 0.0005$, $\eta_d = 0.001$ and $\eta_d = 0.002$, respectively.

Fig. 5.31b indicates that the conversion of magnetic energy into internal and kinetic energy occurs mostly via Ohmic heating with a small contribution from viscous heating (multiplied by fifty for representational purposes). This shows that there is some wave damping occurring in the system, predominantly during phase II of each experiment. In each experiment, a small amount of adiabatic cooling occurs in the later part of phase I due to the sudden expansion of the field about the separator current layer. The rate of viscous heating is very similar in all three experiments suggesting that a more rapid reconnection does not lead to the creation of larger perturbations.

Although it appears that the peak Ohmic heating rate is basically linearly proportional to η_d , from Fig. 5.31b, the duration of the main Ohmic heating period (which, as shown in Sect. 5.2, is slightly longer than phase I) does not vary in the same way. The relative error in the total energy, is small and of the same order for all three experiments.

5.8.3 Effects of varying j_{crit}

The size of the diffusion region, and hence the amount of current which will be involved in the reconnection, is determined by the value of j_{crit} . We have lowered the value we used in the main experiment ($j_{crit} = 10.0$) to $j_{crit} = 8.5$ and $j_{crit} = 7.5$, while using the same values for the resistivity and background viscosity as were used in the main experiment ($\eta_d = 0.001$ and $\nu = 0.01$) and investigate the effects this has on the energetics and reconnection rate.

A lower value of j_{crit} implies more current in the separator current layer will be involved in the reconnection (Fig. 5.30b) and so, as expected, the length of the first phase, in which fast reconnection occurs, increases as j_{crit} decreases (Fig. 5.32).

The energy plots for the experiments where j_{crit} is varied (Fig. 5.32) have been created

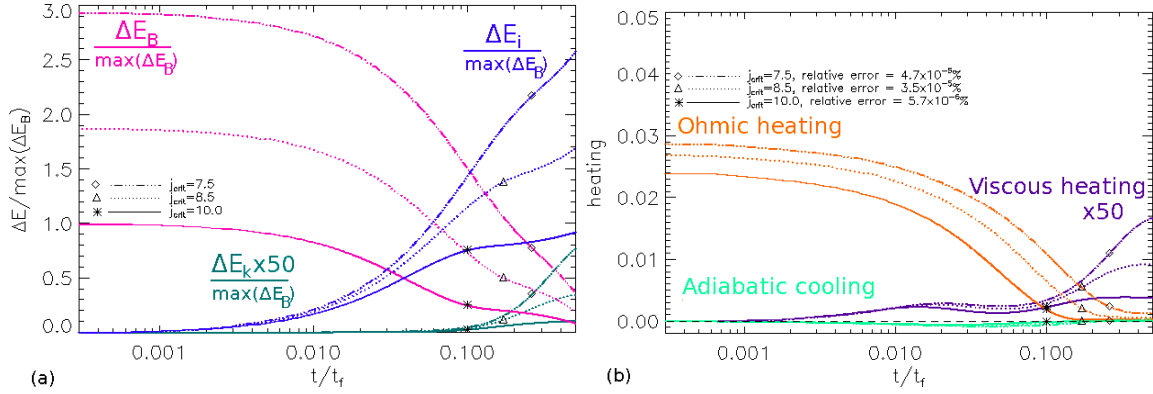


Figure 5.32: Plots of (a) the energy and (b) heating terms for experiments with $j_{crit} = 7.5$, $j_{crit} = 8.5$ and $j_{crit} = 10.0$ with $\eta_d = 0.001$ and $\nu = 0.01$. Diamonds, triangles and asterisks indicate where phase I ends and phase II begins for the experiments with $j_{crit} = 7.5$, $j_{crit} = 8.5$ and $j_{crit} = 10.0$, respectively.

in the same way as those in Fig. 5.31 where the change in energies, normalised to the maximum change in magnetic energy of the main experiment, are plotted. Fig. 5.32a indicates that having a lower value of j_{crit} leads to the total loss in magnetic energy increasing and an increase in the length of phase I. We find that the free energy released, calculated as a percentage of the energy released if a uniform background resistivity was used, in the experiments increases as j_{crit} decreases with 3% of the free energy released when $j_{crit} = 10.0$, 5% of the free energy released when $j_{crit} = 8.5$ and 8% of the free energy released when $j_{crit} = 7.5$.

Fig. 5.32b shows that the initial amount of Ohmic heating increases as j_{crit} decreases. These changes arise because a lower value of j_{crit} encloses more current (more magnetic field) in the diffusion region and, a lower initial j_{crit} leads to the production of larger perturbations produced as a consequence of the greater loss in force balance due to the greater reconnection. This is evident from the viscous heating curves in Fig. 5.32b, which have higher values for lower j_{crit} .

5.8.4 Effects of varying the background viscosity, ν

Finally, we have explored the effects of varying the value of the background viscosity, ν by running experiments which are the same as the main experiment with $\eta_d = 0.001$ and $j_{crit} = 10.0$, but with $\nu = 0.001$, 0.005 and 0.01 . We find that the total loss in magnetic energy does vary as ν is varied (Fig. 5.33a). The Ohmic dissipation (Fig. 5.33b) appears the same in all experiments in phase I but varies slightly in phase II. The proportion of magnetic energy converted to kinetic energy during the experiment depends on ν . Larger values of the background viscosity, correspond to greater viscous heating in the first part of phase I leading to smaller kinetic energy since the waves are damped to a greater extent. Near the end of phase I, and throughout phase II, the kinetic energy is greatest for experiments with lower ν . This occurs since the fluid is less viscous for experiments with lower ν . In phase II, we find that the higher the value of ν is the smaller the Ohmic heating is. The adiabatic cooling term is unaffected by the value of ν .

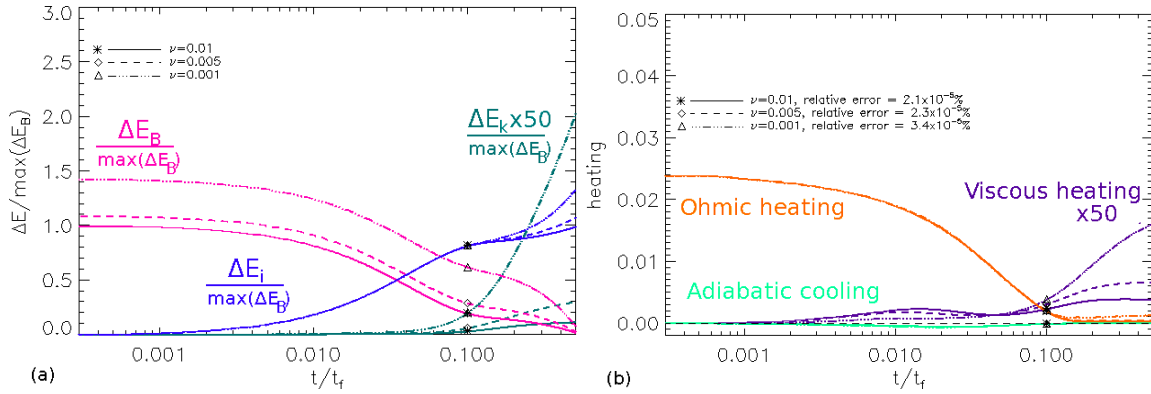


Figure 5.33: Plots of (a) the energy and (b) heating terms for experiments with $\nu = 0.001$, $\nu = 0.005$ and $\nu = 0.01$ with $j_{crit} = 10.0$ and $\eta_d = 0.001$. Asterisks, diamonds and triangles indicate where phase I ends and phase II begins for the experiments with $\nu = 0.01$, $\nu = 0.005$ and $\nu = 0.001$, respectively.

5.9 Summary

In this chapter, we have considered the reconnection, which occurs at a high plasma-beta single-separator model which contains a current layer lying parallel to the separator by using the resistive MHD code Lare3d. The model which we have used as the initial condition for our experiment is very similar to the MHS equilibrium, which is in force balance everywhere except near to the separator and on the separatrix surfaces of the nulls, detailed as the main experiment in Chapt. 3. An anomalous resistivity is applied which works such that the reconnection will only dissipate current that has a magnitude greater than a set amount, i.e., reconnection only occurs at the twisted separator current layer. The onset of the reconnection, as soon as the experiment begins, dissipates the current at the separator and leads to a system, which is no longer in force balance. This lack of force balance causes waves to be launched into the system, which propagate out and cause the magnetic field and plasma to respond to the changes caused by the reconnection.

The experiment occurs in two phases: a fast-reconnection phase in which the Ohmic heating is high and the velocities are relatively low, and a slow-steady reconnection phase in which the Ohmic heating is reduced and the velocities are relatively high indicating the movement of waves in the system. We have seen that the reconnection, in the first phase, occurs asymmetrically along the entire length of the separator, with the null points having little or no involvement in the reconnection. A counter-rotating flow was found to exist about a point half way along the separator, even though the global flow is stagnation type about the separator.

Since this is a high plasma-beta experiment, the waves, which are produced by the reconnection, have small amplitudes, and they travel at the fast-magnetoacoustic speed (which in our high-beta experiment is approximately equal to the slow-magnetoacoustic speed). These waves carry the dissipated current away from the diffusion region and disperse as they travel. Similar work carried out for 2D X-point reconnection has found the same pattern as that found here in all planes parallel to the separator.

Planar-like waves are launched from either side of the edge of the diffusion region and

travel away from the separator current layer. These waves carry current and cause a deficit in pressure to develop outwith the cusp regions. Outwith the cusps, waves are also launched inwards through the depth of the current layer at the same time. These waves end up running closely behind the outwardly-launched waves.

Point-like waves are launched outwards from the narrow ends of the diffusion region. These spread in a spherical pattern carrying current away from the separator current layer and causing an enhancement in pressure. As above, point-like waves also travel inwards across the width of the separator current layer, which is roughly 20 times the size of the depth, thus these waves lag behind the outward waves.

These waves set up flows in the system which bring Poynting flux into the site of the original diffusion region. Within the regions left behind by the perturbations, that have a current deficit and pressure enhancement or deficit, the system attempts to regain force balance. The Lorentz and pressure forces both contribute, but act in opposite directions such that the rate of change of kinetic energy is small. The plasma tries to rebuild the current layer by bringing in more flux to be reconnected, but as soon as the current in the layer reaches the level of j_{crit} the anomalous resistivity dissipates it. This leads to a slow, steady second phase of reconnection which occurs in the regions left behind by the perturbations. The reconnection during this phase is very slow, but the Ohmic dissipation associated with it is still larger than the viscous heating due to the high plasma-beta.

We began by focussing on a single experiment, but have also compared the reconnection rate and energetics of six other experiments where the plasma parameters which control the strength of the resistivity, the size of the diffusion region and the value of the background viscosity have been varied. As expected, higher values of the resistivity lead to faster dissipation of the current layer. We saw that larger diffusion regions, which contain more flux to be reconnected, take longer to reach the end of phase I and, experiments with high viscosities, contain more magnetic energy, which can be converted into internal and kinetic energy.

All the experiments discussed thus far, in this thesis, have dealt with high plasma-beta systems. In the next chapter, we explore how to achieve a low plasma-beta single-separator model, with current parallel to the separator and analyse the magnetic skeleton and the plasma of the model as it undergoes non-resistive MHD relaxation.

Chapter 6

Non-resistive MHD relaxation to form a separator current layer: achieving low plasma-beta

Throughout this thesis, we have studied single-separator systems, which are embedded in a high-beta plasma. In the solar corona, the value of the plasma beta is small, $\beta < 1$, and so the magnetic forces dominate the plasma forces. It is difficult to achieve a low plasma beta in the set up discussed in this thesis, which contains two null points, since at null points $\mathbf{B} = \mathbf{0}$ and in the surrounding area the magnetic pressure is very weak, hence, $\beta \rightarrow \infty$. However, in this chapter we discuss how the plasma beta can be lowered in our analytical single-separator magnetic field model, which was introduced in Chapt. 2. We begin in this chapter by discussing the different ways a low plasma beta can be achieved in our model (Sect. 6.9) and then, after explaining the method, we present the results of a low plasma-beta non-resistive MHD relaxation experiment, using our single-separator model, with current parallel to the separator.

6.1 Approaching a low plasma beta

The single-separator magnetic field, with current parallel to the separator, which has been used throughout this thesis is

$$\begin{aligned} B_x &= \frac{B_0}{L_0}(x + cxz + byz - \frac{1}{2}j_{sep}y), \\ B_y &= \frac{B_0}{L_0}((2a - c)yz - (1 + aL)y + bxz + \frac{1}{2}j_{sep}x), \\ B_z &= \frac{B_0}{L_0}(-a(z^2 - zL) + \frac{1}{2}cx^2 + (a - \frac{1}{2}c)y^2 + bxy). \end{aligned} \quad (6.1)$$

The initial plasma beta can be written as

$$\beta = \frac{2\mu_0 p_0}{B^2}, \quad (6.2)$$

where $\mu_0 = 1.0$ in dimensionless units, p_0 is the initial plasma pressure and B^2 is equal to

$$\begin{aligned}
 B^2 = & \frac{B_0^2}{L_0^2} \left((x + cxz + byz - \frac{1}{2}j_{sep}y)^2 \right. \\
 & + ((2a - c)yz - (1 + aL)y + bxz + \frac{1}{2}j_{sep}x)^2 \\
 & \left. + (-a(z^2 - zL) + \frac{1}{2}cx^2 + (a - \frac{1}{2}c)y^2 + bxy)^2 \right). \quad (6.3)
 \end{aligned}$$

In all experiments discussed in this thesis, thus far, $p_0 = 1.5$, $B_0 = L_0 = L = 1.0$ and the other magnetic field parameters (a, b, c, j_{sep}) have been varied. The initial value of the plasma beta half-way along the separator for the main experiment discussed in Chapt. 3 was $\beta_{L/2} = 192$ and the mean plasma beta was $\bar{\beta} = 7.8$. These values are too high to be found in the corona but were necessary to ensure only two nulls existed in the model throughout the non-resistive MHD relaxation. High plasma-beta values are known to exist in planetary magnetospheres [e.g., Dorelli et al., 2007]. In particular, in the Earth's magnetosphere values of $1 < \beta < 10$ have been found [Trenchi et al., 2008]. There are various ways in which the plasma beta, associated with our analytical magnetic field, can be lowered, which we discuss now.

6.1.1 Lowering the value of the plasma beta

The value of the plasma beta, associated with the magnetic field given in Eq. 6.1, may be reduced by increasing the magnetic field scaling factor, B_0 , or decreasing the magnetic field length scaling factor, L_0 , from one (the value these parameters took in Chaps. 3 and 4). Increasing B_0 (or decreasing L_0) leads to the value of the plasma beta half-way along the separator being reduced. By inserting Eq. 6.3 into Eq. 6.2, with $x = y = 0$ and $z = L/2$, the plasma beta half-way along the separator of the initial magnetic field may be written as

$$\beta_{\frac{L}{2}} = \frac{L_0^2}{B_0^2} \frac{32p_0}{a^2L^4}. \quad (6.4)$$

Various values of B_0 were investigated (e.g., $B_0 = 10$ or 100 with $p_0 = 1.125$ and $B_0 = 4$ or 15 with $p_0 = 1.5$), however, this method always led to the creation of multiple nulls (excess to the two original nulls) in the magnetic field early on during the relaxation indicating that numerical diffusion had occurred in the system and, thus, the relaxation was not non-resistive. Hence, this was not a suitable method to use to reduce the value of the plasma beta.

Next, we tried increasing the length of the separator, L , to achieve a lower plasma beta, while maintaining a uniform pressure. This did lower the value of the plasma beta half way along the separator, as evident from Eq. 6.4, but we found this method also led to multiple nulls appearing in the magnetic field during the relaxation and so again this method was not suitable.

The method which worked (i.e., permitted the non-resistive MHD relaxation of the separator without significant numerical diffusion occurring) involves increasing the initial

length of the separator and introducing an initial non-uniform pressure p_0 of the form

$$p_0 = p_b + p_n \left(e^{-\frac{(\mathbf{r}-\mathbf{r}_0)^2}{2\alpha_0^2}} + e^{-\frac{(\mathbf{r}-\mathbf{r}_L)^2}{2\alpha_L^2}} \right), \quad (6.5)$$

where p_b is the background pressure, p_n is the pressure at the nulls, $\mathbf{r} = (x, y, z)$, $\mathbf{r}_0 = (x_0, y_0, z_0)$ and $\mathbf{r}_L = (x_L, y_L, z_L)$ are the positions of the lower and upper nulls, respectively, and α_0 and α_L control the width of the Gaussians around the lower and upper nulls, respectively.

Thus, the pressure is initially uniform everywhere (with a value of $p_0 = p_b$), except around the null points, located at \mathbf{r}_0 and \mathbf{r}_L , where it peaks (at a value of $p_0 = p_b + p_n$) and then falls off as a Gaussian over x , y and z . The high pressure at the nulls helps maintain low numerical diffusivity throughout the non-resistive relaxation whilst the low pressure elsewhere helps to achieve a low plasma beta, as desired, along the separator away from the nulls and throughout the rest of the domain. Hence, to achieve a stable low plasma-beta experiment, we apply this pressure profile and also increase the initial length of the separator from $L = 1$.

6.2 Low plasma-beta magnetic field and plasma properties

To carry out the non-resistive MHD relaxation of our low plasma-beta model, we use the Lare3d code, detailed in Chapt. 1, with $\eta = 0$. Our domain has dimensions $-1 < x, y < 1$ and $-1 < z < 4$ with a grid resolution of (512, 512, 768). We employ line-tied boundary conditions such that the normal component of the magnetic field (B_x, B_y, B_z), the density (ρ) and the internal energy per unit mass (ϵ) all have a minimum or a maximum on the boundaries. Also, the velocity (v_x, v_y, v_z) is set to zero on the boundaries.

In this chapter, we use the following values for our magnetic field parameters, as were used for the experiments discussed in Chapt. 3: $B_0 = 1.0$, $L_0 = 1.0$, $a = 0.5$, $b = 0.75$ and $c = 0.25$. We use $j_{sep} = 0.75$, which is half the value of the initial current used in the main experiment of Chapt. 3 and all experiments in Chapt. 4, to try and reduce the risk of numerical diffusion occurring during the relaxation due to the build up of a strong current layer along the separator. Also, here we use $L = 3$ so the initial separator is three times the length of the initial separators in the experiments discussed in Chapt. 3 and 4. Therefore, the initial magnetic skeleton consists of two null points, positioned at $(0, 0, 0)$ and $(0, 0, 3)$, which have the following eigenvalues and eigenvectors

$$\lambda_{sl} = -2.46, \quad \mathbf{e}_{sl} = (0.11, 1, 0)^T,$$

$$\lambda_{f_1l} = 0.5, \quad \mathbf{e}_{f_1l} = (0, 0, 1)^T,$$

$$\lambda_{f_2l} = 0.96, \quad \mathbf{e}_{f_2l} = (9.22, 1, 0)^T,$$

$$\lambda_{su} = 3.18, \quad \mathbf{e}_{su} = (1.31, 1, 0)^T,$$

$$\lambda_{f_1u} = -0.5, \quad \mathbf{e}_{f_1u} = (0, 0, 1)^T,$$

$$\lambda_{f_2u} = -1.68, \quad \mathbf{e}_{f_2u} = (-0.55, 1, 0)^T.$$

The skeleton of the initial magnetic field is shown in Fig. 6.1a. The angle between the upper and lower null's separatrix surfaces appears to be greater here than in many of the experiments discussed in Chapt. 4.

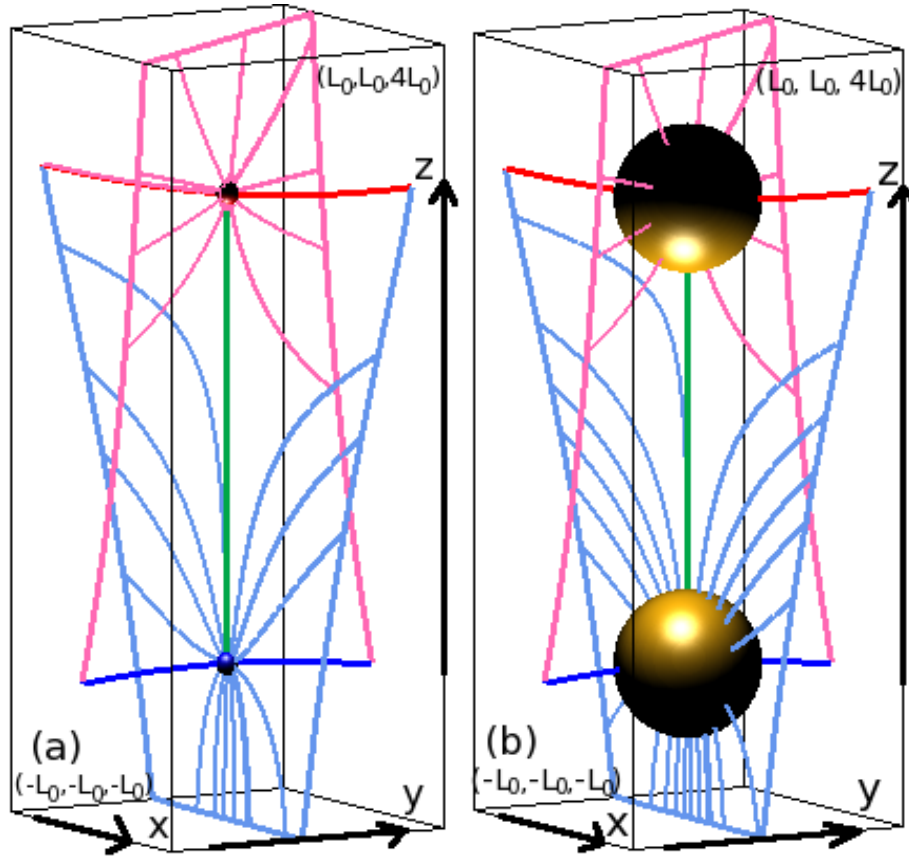


Figure 6.1: (a) Skeleton of the initial magnetic field containing a positive and a negative null, with blue/red spines and pale-blue/pink separatrix surfaces. The solid pale-blue/pink lines indicate where the separatrix surfaces of the nulls intersect the domain boundaries. The separatrix surfaces of the nulls are intersecting to form the separator (green line) which links the nulls. (b) Skeleton of the initial magnetic field with yellow isosurfaces of plasma pressure drawn at $p_0 = 1.0$.

We use an initial uniform internal energy per unit mass of $\epsilon_0 = 1.5$ and the velocity is

initially equal to $\mathbf{v}_0 = \mathbf{0}$. The initial density can be calculated from the closure equation

$$\rho_0 = \frac{p_0}{\epsilon_0(\gamma - 1)}, \quad (6.6)$$

where the initial pressure, p_0 , is of the form shown in Eq. 6.5. Hence, the initial density may be written as

$$\rho_0 = p_b + p_n \left(e^{-\frac{(\mathbf{r}-\mathbf{r}_0)^2}{2\alpha_0^2}} + e^{-\frac{(\mathbf{r}-\mathbf{r}_L)^2}{2\alpha_L^2}} \right), \quad (6.7)$$

since we choose $\epsilon_0(\gamma - 1) = 1$ here. For the experiment discussed in this chapter, we use $p_b = 0.43$, $p_n = 2.0$ and $\alpha_0 = \alpha_L = 0.3$.

Using the values for the magnetic field parameters detailed above, the initial magnetic field satisfies all the constraints detailed in Chapt. 2. Fig. 6.1b shows the skeleton of the initial magnetic field along with isosurfaces of the plasma pressure drawn at $p_0 = 1$. This figure highlights that the pressure is high around the null points, but is small elsewhere in the domain.

The initial value of the mean plasma beta is $\bar{\beta} = 1.07$ and the initial value of the plasma beta half-way along the separator is $\beta_{L/2} = 0.68$. An isosurface, drawn at $\beta = 1.0$, is shown in Fig. 6.2a along with the skeleton of the initial magnetic field. This figure highlights that, although the plasma beta is high ($\beta \rightarrow \infty$) around the null points, it is small elsewhere. Fig. 6.2b shows contours of the plasma beta drawn in a plane perpendicular to the separator at $z = 1.5$, which is half-way along the separator. This plot shows that $\beta < 1$ everywhere in this cut and is slightly higher around the separator than elsewhere.

As in the previous chapters, the times for this experiment are normalised to the time it takes a fast-magnetoacoustic wave to travel from the lower null to the upper null along the path of the separator

$$t_f = \int_{z_l}^{z_u} \frac{1}{\sqrt{c_s^2 + c_A(z)^2}} dz = 1.82, \quad (6.8)$$

where $z_l = 0.0$ is the z -coordinate of the lower null, $z_u = 3.0$ is the z -coordinate of the upper null, $c_s = \sqrt{\epsilon_0\gamma(\gamma - 1)}$ is the sound speed and is equal to $c_s = 5/3$ since, γ , the ratio of specific heats, equals $5/3$ and $c_A(z)$, the Alfvén speed, is equal to

$$c_A(z) = \frac{z^2(3 - z)^2}{1.72 + 8\left(e^{-z^2/0.18} + e^{-(z-3)^2/0.18}\right)}. \quad (6.9)$$

6.2.1 Initial forces on the magnetic field

At $t = 0t_f$, not only is there a non-zero Lorentz force acting on the model (as was seen in the experiments in Chapt. 3 and 4), but due to the initial form of the plasma pressure, a non-zero pressure force is also acting on the model. The strength and direction of this total force (equivalent to the Lorentz force plus the plasma pressure force) is shown in a plane perpendicular to the separator, at $z = 1.5$, in Fig. 6.3a. The total force acts in towards the separatrix surfaces in this plane, indicating that as soon as the experiment begins, the separatrix surfaces will fold towards each other.

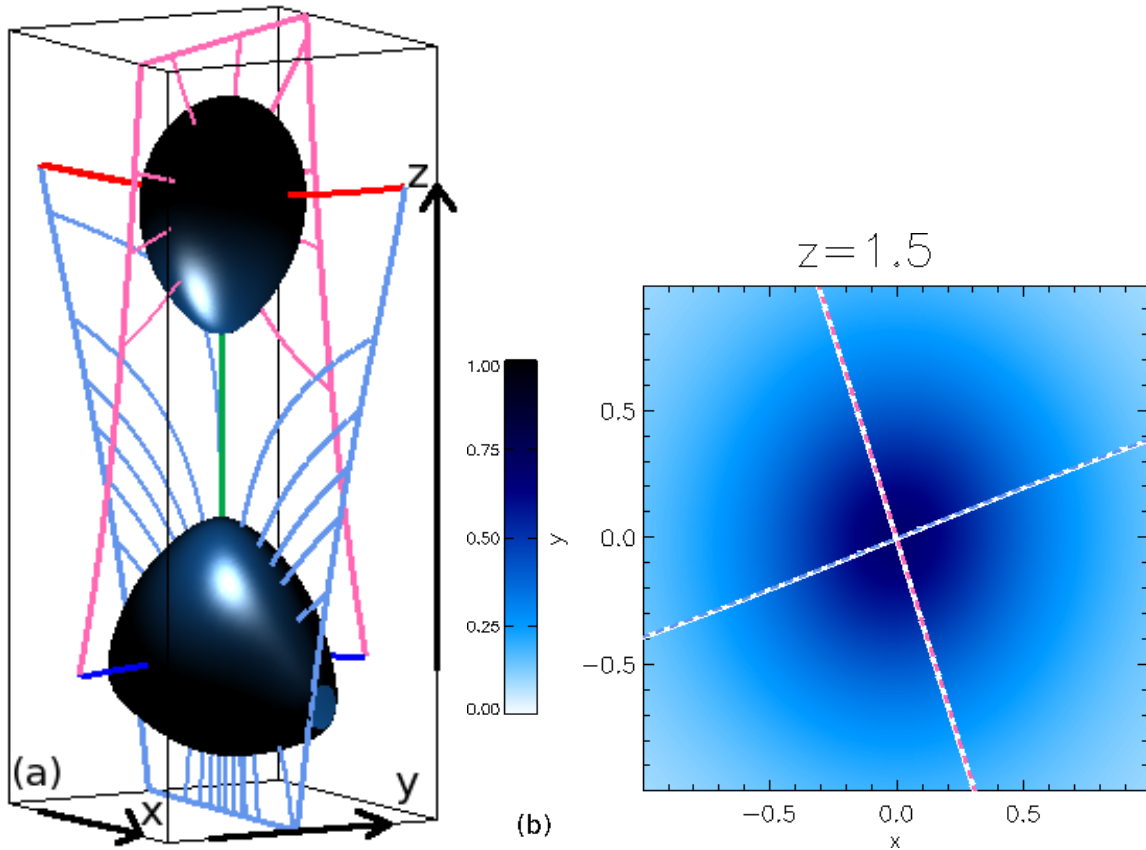


Figure 6.2: (a) The initial magnetic field skeleton which contains a positive/negative null (hidden by isosurfaces) with blue/red spines and pale-blue/pink separatrix surfaces. The solid pale-blue/pink lines indicate where the separatrix surfaces intersect the boundaries. A separator links the nulls (green line). Also, blue isosurfaces are drawn here at $\beta = 1.0$. (b) Contours of the plasma beta drawn in a plane perpendicular to the separator half-way along its length at $z = 1.5$. The pale-blue/pink lines show where the separatrix surfaces of the nulls intersect these cuts. These intersections are plotted on top of thick white lines so they are visible here.

Figs. 6.3b and 6.3c show contours of the total force in planes perpendicular to the y and x -planes, at $y = 0$ and $x = 0$, respectively. In both of these planes the total force is shown to act inwards, from the boundaries, towards the z -axis, except at the null points where, due to the nature of the pressure profile, the total force is directed outwards in the x and y -directions for Figs. 6.3b and 6.3c, respectively. The stronger pressure here acts against the collapsing of the separatrix surfaces towards each other during the relaxation.

The low plasma-beta single-separator model is allowed to relax non-resistively over time using the Lare3d code. We analyse the results found throughout this relaxation in the following sections, starting with a discussion of the energetics of the experiment in Sect. 6.3. Next, we analyse how the magnetic field and plasma evolve (Sect. 6.4) before detailing the properties of the current layer which forms through the relaxation (Sect. 6.5). We then analyse the plasma pressure and the magnetic pressure in the equilibrium state

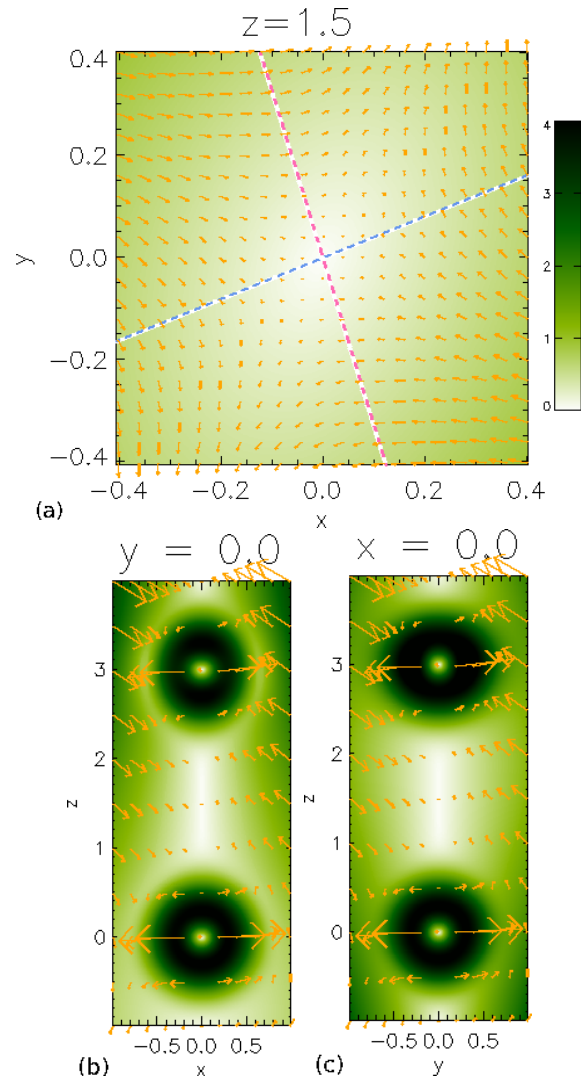


Figure 6.3: Contours of the total force in a plane (a) perpendicular to the separator at $z = 1.5$, (b) perpendicular to the y -axis at $y = 0$ and (c) perpendicular to the x -axis at $x = 0$. The orange arrows show the direction and strength of the (a) x and y , (b) x and z and (c) y and z components of the total force in these planes, respectively.

(Sect. 6.6) and look at the properties of residual forces which exist in the MHS equilibrium (Sect. 6.7). We discuss the growth rate of the current in Sect. 6.8 before detailing how a low mean plasma-beta value can be achieved by using the MHS equilibrium field (Sect. 6.9). Our findings are summarised in Sect. 6.10.

6.3 Energetics

The initial magnetic field is not in force balance and so, as soon as the experiment begins, the separatrix surfaces collapse towards each other. During the experiment, overall, the magnetic energy is converted into kinetic energy, which in turn is converted into internal

energy (Fig. 6.4). However, the path that the energies take to being constant is different to that observed in the high plasma-beta relaxation experiments discussed in Chapt. 3 and 4. The system evolves to what appears to be a MHS equilibrium by $t = 9.34t_f$ which is the end point of the experiment. By this time there have been no significant changes to the energies for almost $7t_f$.

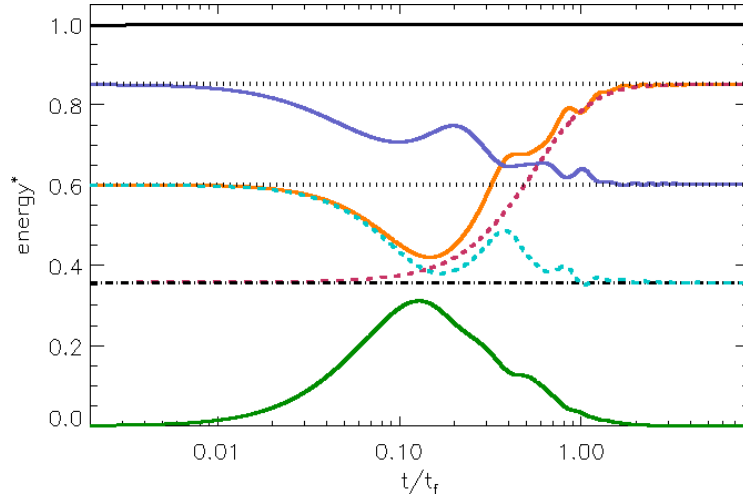


Figure 6.4: Plot of the kinetic (green), magnetic (blue), internal (orange) and total (black solid) energies along with the viscous (red dashed) and adiabatic (cyan dashed) heating terms. These energies have been scaled such that the total energy is 1.0, the initial/final magnetic energy values match the final/initial internal energy values and the adiabatic heating starts at the same value as the internal energy, with the viscous heating term starting from the final value of the adiabatic heating. The dotted and dashed black lines highlight the start and end points of the heating terms.

The curves of the energy and heating terms, in Fig. 6.4, have been shifted on the y -axis, for representational purposes, such that the internal energy starts/finishes at the values at which the magnetic energy finishes/starts. This is to highlight that all the magnetic energy, to within numerical error, is converted into internal energy. The magnetic energy starts to decrease as the experiment begins and the kinetic energy increases, however, rather than an increase in internal energy following this, the internal energy decreases due to the adiabatic cooling and appears to go into both kinetic and magnetic energy at around $t = 0.15t_f$. After this time the magnetic energy increases slightly, due to the adiabatic cooling before decreasing as it is converted into kinetic and internal energy. The internal energy begins to increase after $t = 0.15t_f$ due to the conversion of kinetic energy to internal energy via viscous heating.

This behaviour, from the start of the experiment to $t = 0.15t_f$, occurs since there is a rapid expansion of the plasma in the system as the experiment begins due to the pressure gradients about the nulls. This expansion is adiabatic in nature causing there to be cooling in the system, evident from the drop in the adiabatic term, plotted in Fig. 6.4, near the start of the experiment. The viscous heating term increases throughout the experiment, indicating that waves are being damped. The existence of waves is evident from the oscillations of the curves in Fig. 6.4.

The adiabatic term has been positioned such that it starts at the same point as the internal energy curve and the viscous heating curve starts at the value at which the adiabatic heating term ends. This is to highlight that the energy conversion is solely due to the combined effects of the adiabatic and viscous heating terms although, here, the adiabatic heating term reduces the internal energy by 100% and the viscous heating term increases the internal energy by 200%.

The total energy is well conserved throughout the experiment, with a maximum relative error of $3 \times 10^{-3}\%$.

6.4 Evolution of the magnetic field and plasma

The number of nulls found within the system remains constant at two (one positive improper radial null and one negative improper radial null), with one separator linking the nulls, throughout the non-resistive relaxation. Both nulls remain stationary in the x and y directions (at $x = y = 0$). Along the z -axis, the nulls remain stationary over the first $t = 0.3t_f$, but then move towards each other, along the z -axis, away from their initial z -positions at $z = 0.0$ and $z = 3.0$ (Fig. 6.5a). The nulls then oscillate slightly away from and towards each other throughout the rest of the experiment. This movement, of the nulls towards each other along the z -axis, is different to that seen in all of the high plasma-beta relaxation experiments in which the nulls moved apart along the z -axis.

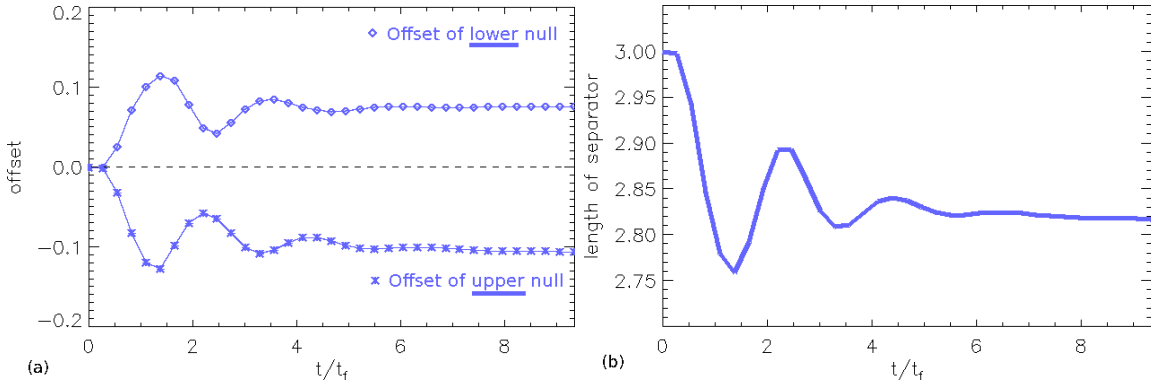


Figure 6.5: The offset, in the z -direction, of the lower (diamonds) and upper (asterisks) nulls, from their positions at $t = 0t_f$ and (b) the length of the separator throughout the relaxation experiment.

This in turn leads to the overall distance between the nulls, and hence the length of the separator, oscillating over time and ending up 6% shorter than the initial value of $L = 3$ (Fig. 6.5b). The length of the separator appears to be approaching a constant value towards the end of the relaxation.

Fig. 6.6a shows the magnetic skeleton of the equilibrium field. Although the magnetic skeleton does not appear to have varied greatly through the relaxation, the initial forces in the system have caused the separatrix surfaces to fold towards each other as the experiment begins. Fig. 6.6b shows that the separatrix surfaces have indeed curved towards each other during the non-resistive relaxation, and appear flatter over the area in which they

intersect than in the high plasma-beta experiments, where the separatrix surfaces of the nulls intersected over a point.

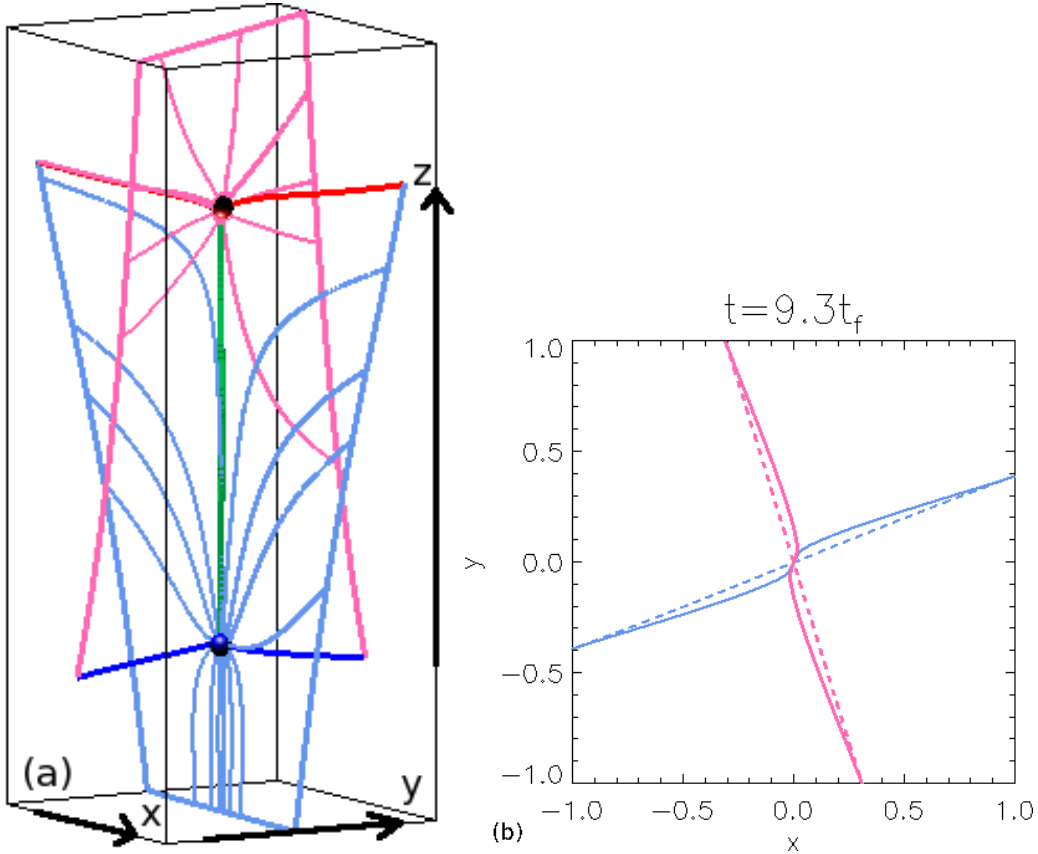


Figure 6.6: (a) The equilibrium magnetic field's skeleton containing a positive and a negative null, with blue/red spines and pale-blue/pink separatrix surfaces. The solid pale-blue/pink lines indicate where the separatrix surfaces of the nulls intersect the domain boundaries. The separatrix surfaces of the nulls are intersecting to form the separator (green line) which links the nulls. (b) The intersections of the lower (pale-blue) and upper (pink) null's separatrix surfaces with the plane perpendicular to the separator, at $z = 1.5$. The initial magnetic field's (dashed lines) and equilibrium magnetic field's (solid lines) separatrix surfaces are both plotted here.

The plasma-beta value changes through the non-resistive relaxation also. Fig. 6.7a shows the equilibrium skeleton of the model along with an isosurface drawn at $\beta = 1$. Comparing this image to Fig. 6.2a, which showed the initial magnetic skeleton with an isosurface drawn at $\beta = 1$, we see that the plasma beta has become greater along the length of the separator and is stronger over a larger area of the separatrix surfaces. This could be a consequence of the plasma pressure changing in the system (this is investigated in Sect. 6.6). Fig. 6.7b shows contours of the plasma beta in the $z = 1.5$ plane perpendicular to the separator in the equilibrium state. This plot indicates that indeed the plasma beta has increased along the separatrix surfaces especially around the separator. The mean plasma beta in the MHS equilibrium is $\bar{\beta} = 1.22$ and the value of the plasma-beta

half-way along the separator is $\beta_{l_{sep}/2} = 2.8$

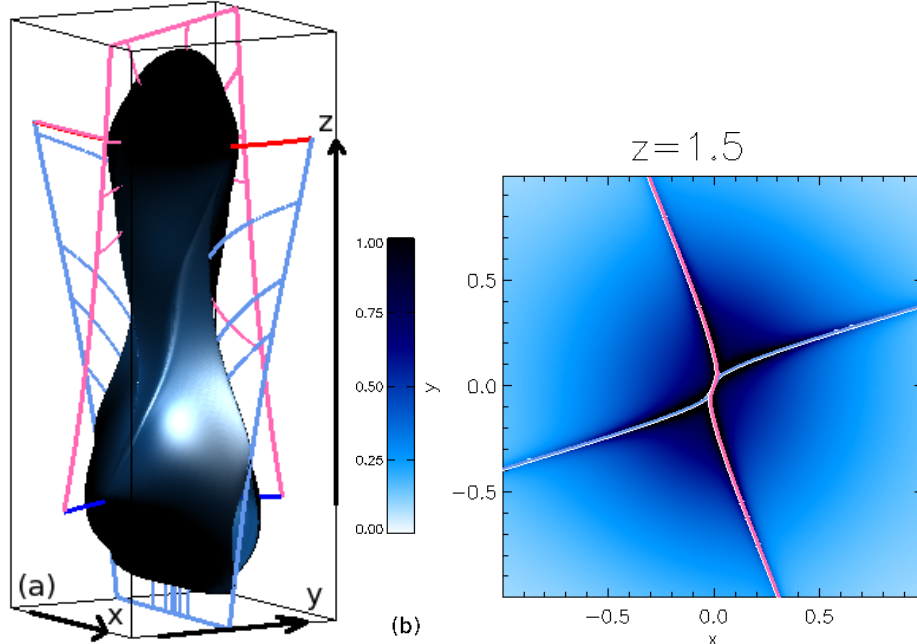


Figure 6.7: (a) The equilibrium magnetic skeleton along with a blue isosurface drawn at $\beta = 1$. Here the pale-blue/pink lines represent field lines in the separatrix surfaces of the lower/upper nulls, the blue/red lines are the spine of the lower/upper nulls and the solid pale-blue/pink lines indicate where the separatrix surfaces of the nulls intersect the boundaries. (b) Contours of the plasma beta drawn in a plane perpendicular to the separator, at $z = 1.5$, in the equilibrium field. The pale-blue/pink lines highlight where the separatrix surfaces intersect this cut.

6.5 Current layer formation

During the non-resistive relaxation, a strong current layer builds along the separator and enhanced current grows along the separatrix surfaces of the null points. Fig. 6.8 shows the MHS equilibrium magnetic skeleton with an isosurface of $j_{\parallel} = 10.0$ from two different angles. In this figure, the current is shown to be stronger along the separator away from the null points and is strong on the separatrix surfaces close to the domain boundaries.

Fig. 6.9 shows surface plots of $|\mathbf{j}|$ in planes perpendicular to the separator in the equilibrium state. These graphs show the strong current which lies along the separator, and is twisted along its length (discussed in more detail below), and the enhanced current which sits on the separatrix surfaces of the nulls. The value of $|\mathbf{j}|$ on the separatrix surfaces is shown in Fig. 6.10 normalised to the same value of $|\mathbf{j}|$ used in Chapt. 3 for the main experiment. We note that, unlike the high plasma-beta experiment where the value of $|\mathbf{j}|$ increased going from the top to the bottom of the lower null's separatrix surface, and vice versa for the upper null's separatrix surface, here the current does not follow as neat a pattern. In Fig. 6.10a, which shows contours of $|\mathbf{j}|$ on the lower null's separatrix surface,

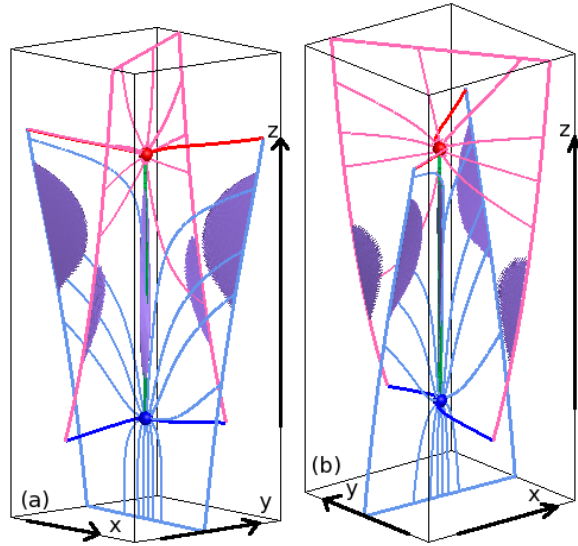


Figure 6.8: (a) and (b) show the MHS equilibrium skeleton with isosurfaces of $j_{\parallel} = 10.0$ from two different angles. The skeleton contains a positive/negative null (blue/red spheres) which have blue/red spines and pale-blue/pink separatrix surfaces. The solid pale-blue/pink lines indicate where the separatrix surfaces intersect the domain. A separator links the nulls (green line).

the current is small near the top of this null's separatrix surface, slightly greater where it is level with the separator, and increases near the positive side of the lower boundary. Similarly for the upper null's separatrix surface (Fig. 6.10b), the current is small near the bottom, is increased around the level of the separator on the positive boundary and has higher boundary currents at the top of the domain. Note that the value of $|\mathbf{j}|$ in the separator current layer is about 1.5 times greater than the maximum value on the colour bar in Fig. 6.10.

This experiment was run for a much shorter time than the high plasma-beta experiments and so the current has not had as long to build up along the separator. After $t = 9.34t_f$, multiple separators existed in the domain which linked the original two null points together. This is an indication that the topology was changed and, hence, we ended the experiment at this point.

We define the length of the current layer as the distance between the null points along the z -axis, i.e., the length of the separator. The equilibrium current layer found in this low plasma-beta experiment is longer than the high plasma-beta current-layer length, since in the initial field the nulls are positioned further apart (but it is not as long as the initial separator in this experiment, as already discussed in Sect. 6.4, Fig. 6.5).

Fig. 6.11a shows the value of j_{\parallel} , along the normalised z -axis, in the MHS equilibrium. The z -axis is normalised here according to the equation $z^* = L(z - z_{ln})/l_{sep}$ where L is the initial length of the separator, z_{ln} is the z -coordinate of the lower null and l_{sep} is the length of the equilibrium separator. The value of j_{\parallel} is positive along the length of the separator, and is negative outwith it along the z^* -axis (Fig. 6.11a), however, the profile of j_{\parallel} along the separator is different to that seen in the high plasma-beta relaxation

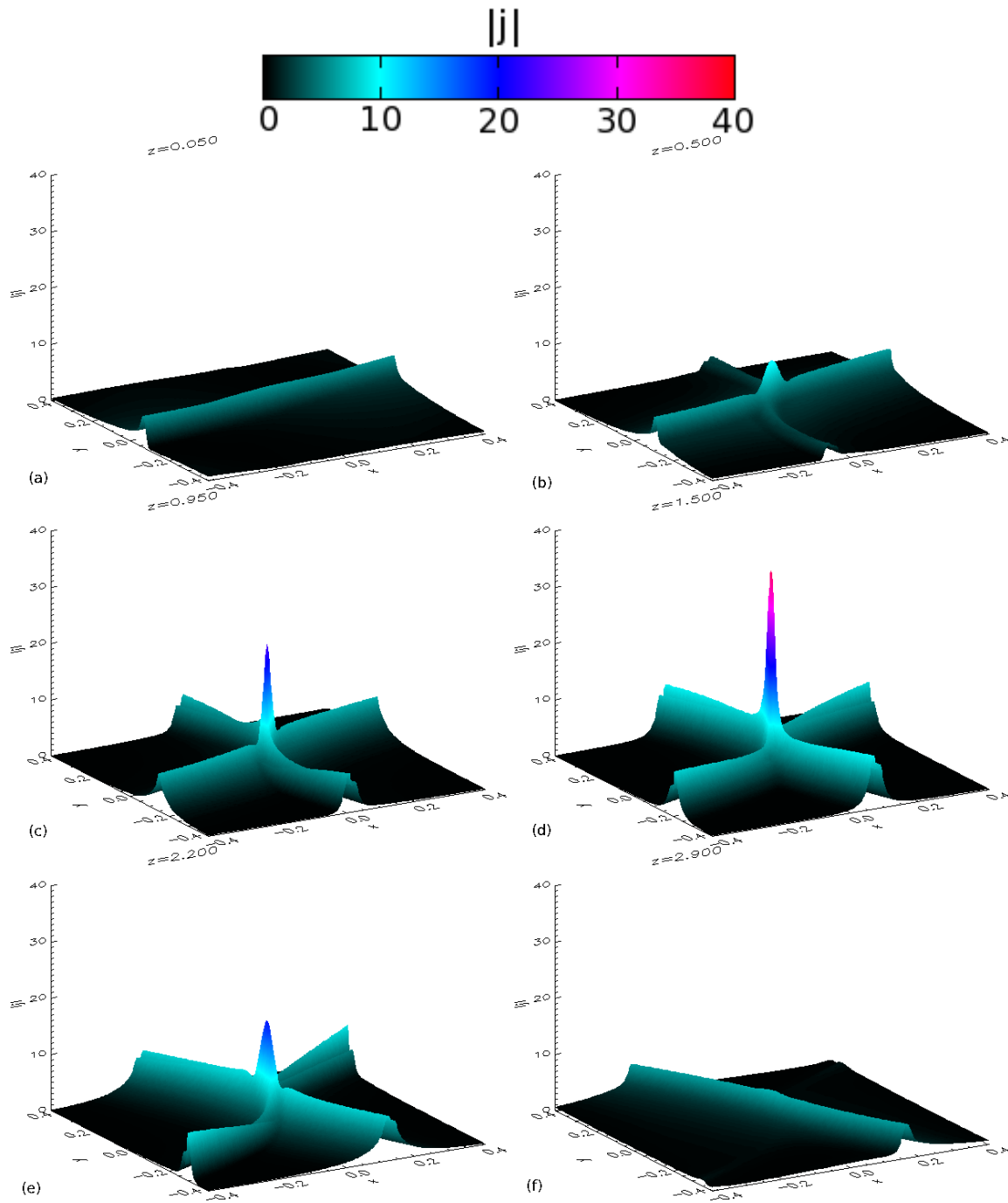


Figure 6.9: Surface plots of $|j|$ in planes perpendicular to the separator at (a) $z = 0.05$, (b) $z = 0.5$, (c) $z = 0.95$, (d) $z = 1.5$, (e) $z = 2.2$ and (f) $z = 2.9$ at $t = 9.34t_f$.

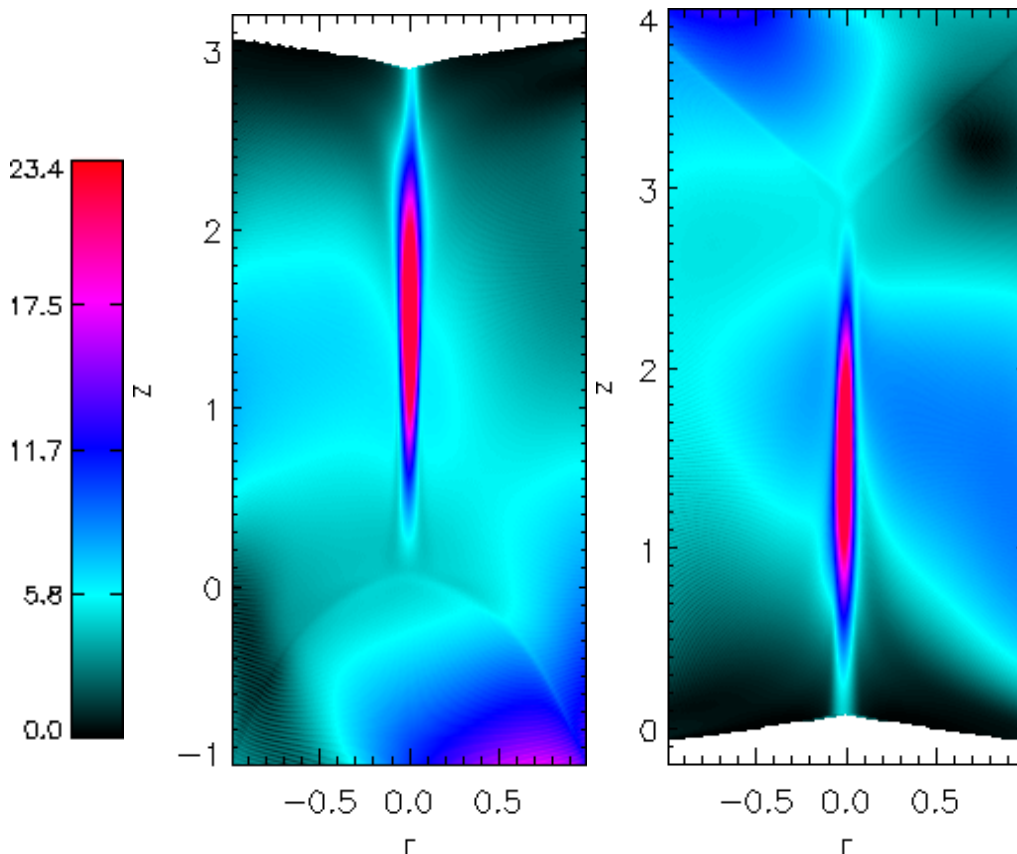


Figure 6.10: Contours of $|\mathbf{j}|$ drawn on the separatrix surfaces of the (a) lower and (b) upper nulls at $t = 9.34t_f$.

experiments discussed in Chapt. 3 and 4 where j_{\parallel} smoothly increased from the lower null to a point around $z^* = 0.4L$ (where $L = 1$) and then smoothly decreased towards the upper null. Here, the peak value of j_{\parallel} occurs at $z^* = 0.51L$, which is just greater than half way along the separator, and the value of the peak ($j_{\parallel} = 35.04$) is roughly six times greater than the value of j_{\parallel} at the nulls ($j_{\parallel} = 5.5$ at the lower null and $j_{\parallel} = 6.7$ at the upper null). The peak magnitude of the current along the separator is greater here than in the high plasma-beta experiments and the value of j_{\parallel} is slightly greater at the upper null than at the lower null.

The value of j_{\parallel} is plotted in a 1D-slice through the depth (solid line) and across the width (dashed line) of the current layer, at $z = 1.5$, in Fig. 6.11b. This plot shows that the current peaks at the current layer and falls off away from it, as was observed in the high plasma-beta relaxation experiments. However, the value of j_{\parallel} plotted through the depth becomes very small on the edge of the current layer, then increases slightly before decreasing away from the separator current layer. This behaviour was not observed in the high plasma-beta experiments.

We calculate the width and depth of the current layer using the contour method, which is first detailed in Chapt. 3. This method involves using the last contour of $|\mathbf{j}|$, in planes perpendicular to the separator, that is elliptic in shape and not X-shaped, i.e., so that the

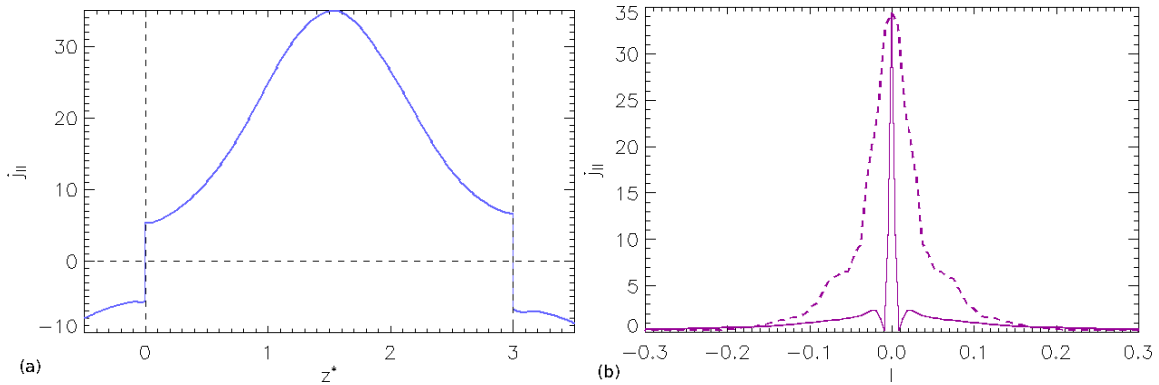


Figure 6.11: j_{\parallel} plotted (a) along the z^* -axis and (b) through the depth (solid line) and across the width (dashed line) of the current layer in a plane perpendicular to the separator at $z = 1.5$ in the equilibrium state at $t = 9.34t_f$.

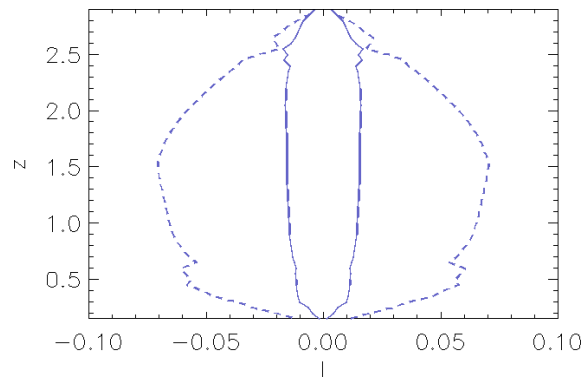


Figure 6.12: The width (dashed lines) and depth (solid lines) of the equilibrium current layer found using the contour method.

area within the contour only picks up the current in the separator current layer. Fig. 6.12 shows the width (dashed lines) and depth (solid lines) of the low plasma-beta current layer found using the contour method. The width of the current layer decreases close to the nulls and bulges in the middle. This was expected from Figs. 6.8 and 6.11a in which the value of j_{\parallel} appeared stronger along the separator away from the null points. The depth of the low plasma-beta current layer also decreases at the null points and is fairly constant along the length of the separator.

As in all non-resistive relaxation experiments discussed in this thesis, the current layer formed along the separator is twisted. The angle, through which the current layer twists from the lower to the upper null, is $\theta = 0.6$ rads. This is an average value compared to the angle through which the current layers of all the high plasma-beta experiments twist in Chaps. 3 and 4.

Next, we examine the plasma and magnetic pressure in the MHS equilibrium state and check to see if the system is in pressure balance.

6.6 Pressure along the length, through the depth and across the width of the current layer

In the high plasma-beta relaxation experiments, discussed in Chapt. 3 and 4, the non-resistive relaxation of the single-separator model led to the initially uniform pressure being changed throughout the domain, with regions of enhanced pressure forming within the cusps formed by the separatrix surfaces of the nulls, and diminished pressure lying outwith these cusps. In the low plasma-beta experiment discussed in this chapter, the pressure is not initially uniform but peaks at the null points and falls off away from them. Fig. 6.13 shows contours of the pressure difference (the equilibrium pressure minus the initial pressure) in planes perpendicular to the separator. Near the null points (Figs. 6.13a, 6.13b and 6.13f), the pressure has been diminished during the relaxation experiment. This is not surprising since there is nothing to maintain the high pressure around the nulls.

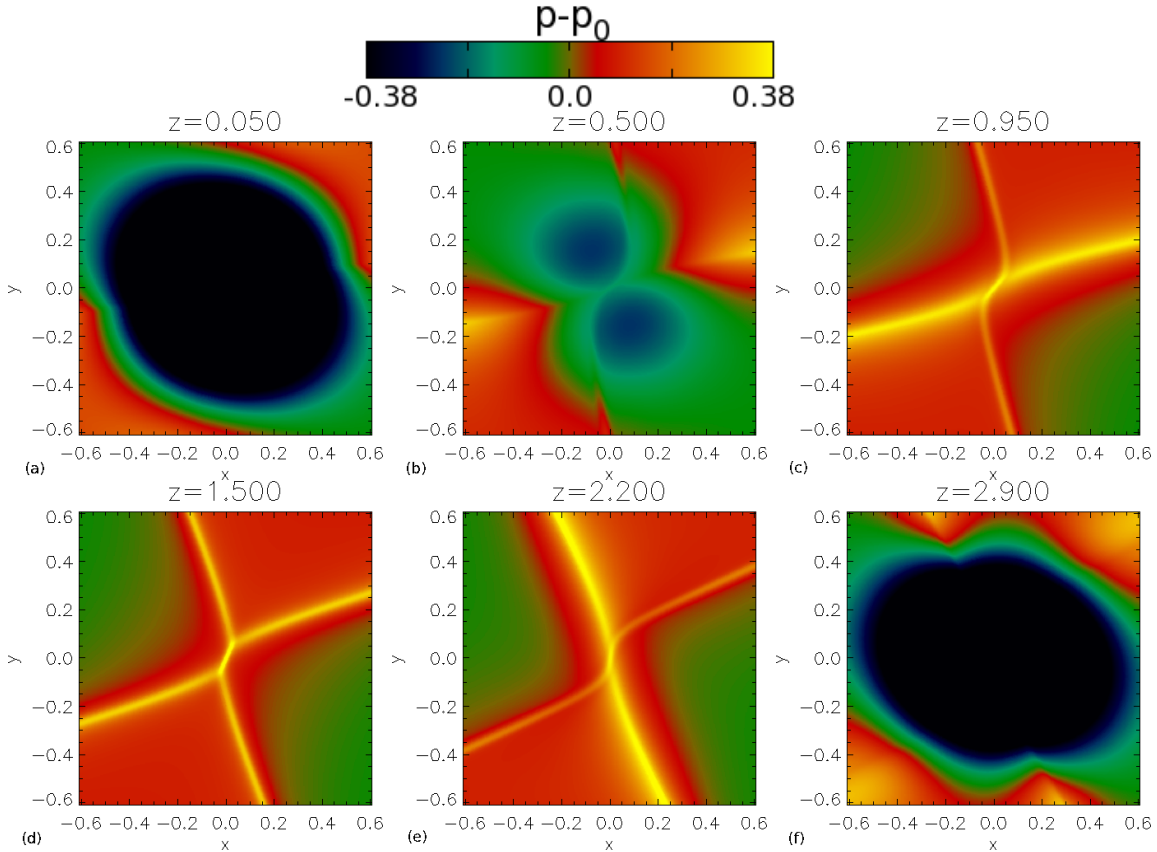


Figure 6.13: Contours of the plasma pressure difference, $p - p_0$, in planes perpendicular to the separator at (a) $z = 0.05$, (b) $z = 0.5$, (c) $z = 0.95$, (d) $z = 1.5$, (e) $z = 2.2$ and (f) $z = 2.9$ at $t = 9.34t_f$.

Along the length of the separator, away from the null points, (Figs. 6.13c, 6.13d and 6.13e), the pressure has been enhanced in the cusp regions, formed by the separatrix surfaces of the nulls, and the pressure even though initially small, is still slightly diminished, outwith these regions. The pressure has become most enhanced on the separatrix sur-

faces and across the current layer. This is slightly different to the results from the high plasma-beta experiments in which there was a gradual drop off outwith the cusp regions, from enhanced pressure to diminished pressure with no peak at the separator or separatrix surfaces.

Through the depth of the current layer, in the plane at $z = 1.5$, the plasma sharply peaks at the separator and falls off in value asymmetrically either side of the separator (Fig. 6.14a). In the high plasma-beta relaxation experiments, the plasma pressure was also found to peak at the separator but the gradient towards and away from the peak was gentler than that found here. Across the width of the current layer (dashed line in Fig. 6.14a) the plasma pressure also peaks at the separator and falls off asymmetrically either side away from the separator current layer. This is different to the results from the high plasma-beta relaxation experiments where the plasma pressure, plotted across the width of the current layer, was fairly constant. We expected to see this behaviour here from having analysed the contour plots of the plasma pressure in planes perpendicular to the separator (Fig. 6.13). These results highlight again that the plasma pressure has built up significantly at the separator current layer and, although enhanced within the cusps, the value of the plasma pressure falls off quickly away from this region.

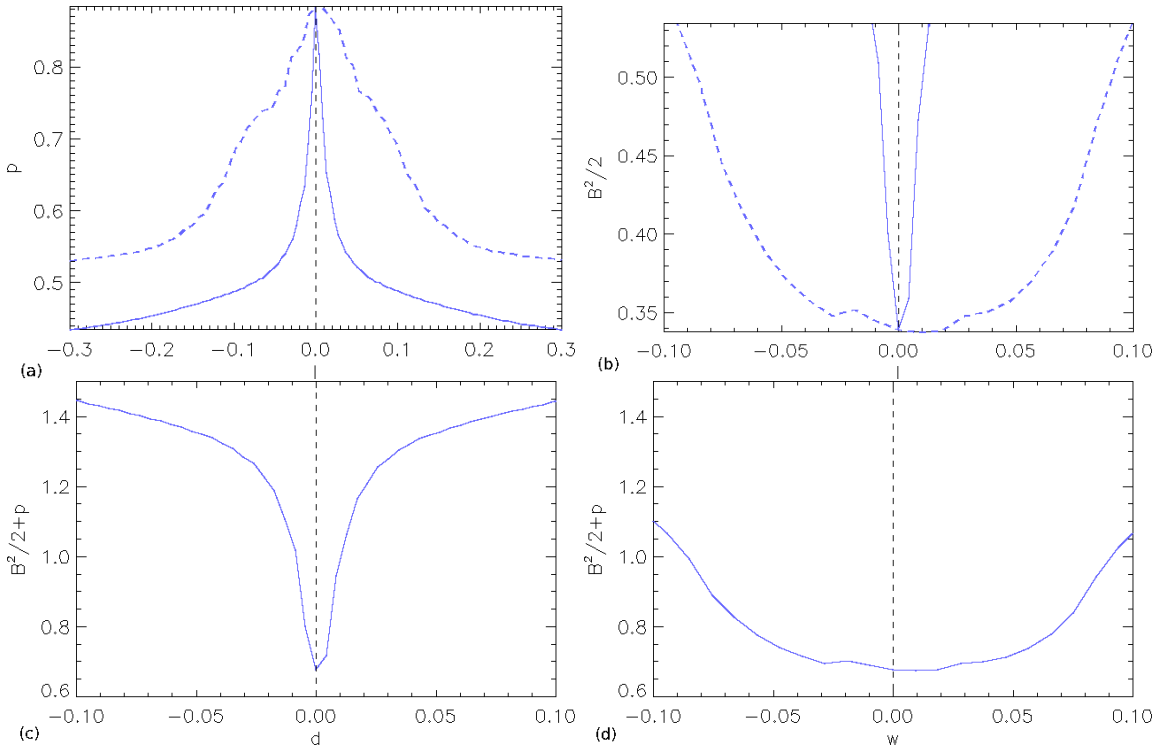


Figure 6.14: (a) The equilibrium plasma pressure and (b) the magnetic pressure plotted through the depth (solid lines) and across the width (dashed lines) of the current layer and the total pressure plotted (c) through the depth and (d) across the width of the current layer, in a plane perpendicular to the separator at $z = 1.5$.

Fig. 6.14b shows the magnetic pressure plotted through the depth and across the width of the current layer. The magnetic pressure behaves inversely to the plasma pressure here:

it has a sharp dip at the separator and increases away from here both through the depth and across the width of the current layer. The magnetic pressure, plotted through the depth, decreases to small values at the separator faster than the magnetic pressure does across the width of the current layer due to both the dimensions of the current layer ($d < w$) and the gradient between magnetic pressure at the separator current layer and the magnetic pressure away from here in the domain. The magnetic pressure increases asymmetrically away from the separator current layer.

The total pressure is shown through the depth and across the width of the separator current layer in Figs. 6.14c and 6.14d, respectively. The total pressure is shown to be fairly constant very close to the separator (around $d = 0$) but increases in value away from this point either side of the separator. The total pressure is fairly constant across the width of the current layer (Fig. 6.14d) but again increases moving away from this region. We note here that it would take an infinite time to gain true pressure balance across the width and through the depth of the separator current layer since it would take such a time to form a true MHS equilibrium.

Fig. 6.15 shows the plasma pressure, the magnetic pressure and the total pressure plotted along the normalised z -axis. The plasma pressure (Fig. 6.15a) is smaller at the

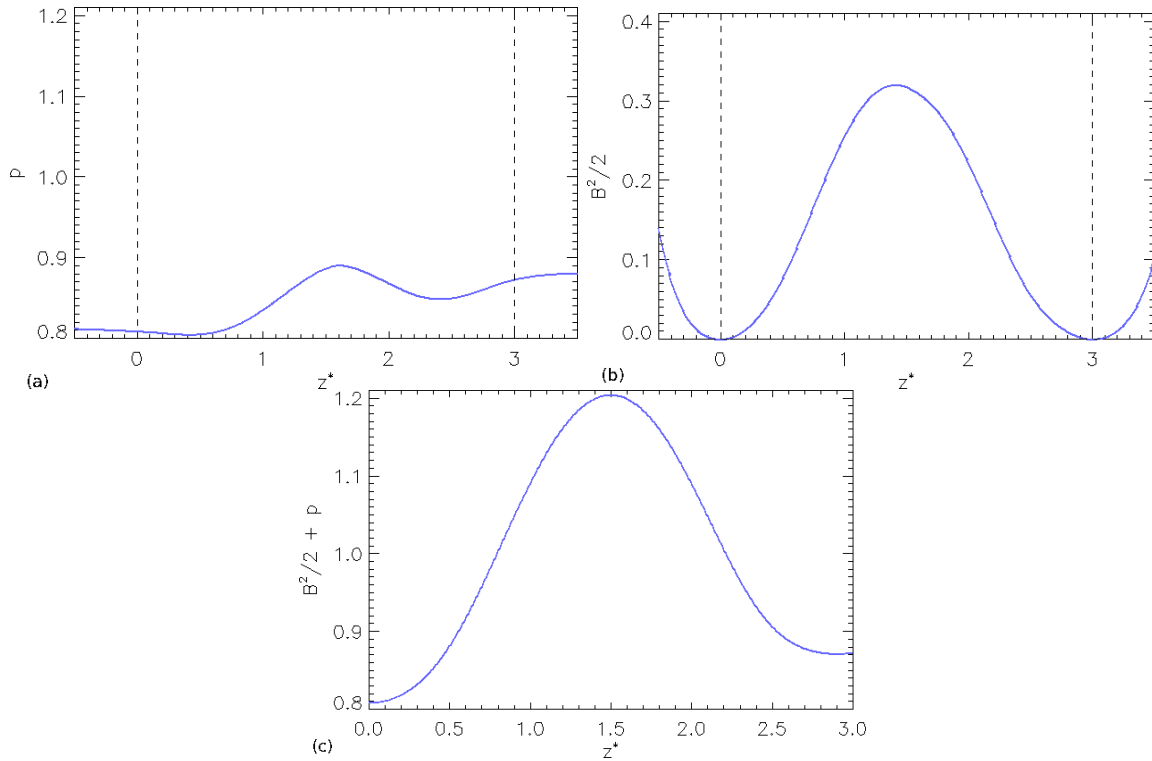


Figure 6.15: The (a) plasma pressure, (b) magnetic pressure and (c) total pressure plotted along the normalised z -axis in the equilibrium state. Note, although the values over which the y -axes span differ, the range in the same in each plot.

lower null than at the upper null in the equilibrium state, even though initially the plasma pressure was identical at the two null points. This was also found in the high plasma-beta relaxation experiments where the initial pressure was constant and uniform throughout

the domain.

The plasma pressure increases along the separator, moving away from the lower null, and peaks at $z^* = 0.54L$, which is just over half way along the separator, with a value of $p = 0.89$. Moving further towards the upper null, along the separator, the plasma pressure decreases slightly before again increasing close to the upper null and almost has the same value here as the maximum found at $z^* = 0.54L$.

The magnetic pressure vanishes at the null points, where $\mathbf{B} = \mathbf{0}$, and peaks at $z^* = 0.47L$ with a value of $B^2/2 = 0.32$ (Fig. 6.15b). The total pressure varies more along the length of the separator, in this low plasma-beta experiment, than it did for the high plasma-beta experiments (Fig. 6.15c).

The total pressure is constant near to the null points and peaks half way along the separator, at $z^* = 0.5L$. We do not expect to find pressure balance along the length of the separator since a component of magnetic tension exists here.

6.7 Total force along the length, through the depth and across the width of the current layer

We have already seen that the separator decreases in length through this non-resistive low plasma-beta relaxation experiment and appears to be approaching a constant value by $t = 9.34t_f$ (Fig. 6.5b). This occurs due to the nature of the total force (which we define as the sum of the Lorentz force and the plasma-pressure force) along the separator. Fig. 6.16a shows that, at the lower null, the equilibrium total force is acting to push this null upwards along the z -axis and at the upper null, it is acting to push this null downwards along the z -axis. However, along the separator there is a strong positive force which is acting to lengthen the separator. Hence, it is unclear whether the total force would shorten, lengthen or not greatly affect the length of the separator if the experiment could be evolved for longer. This is different to the results of the high plasma-beta relaxation experiments in which the total force acted out towards both nulls from some point along the separator, lengthening it. The behaviour here appears to be due to the initial pressure profile, in which the pressure is stronger at the null points than elsewhere in the domain.

The strength of the total force along the separator near to the null points is of the same order of magnitude as that found in the high plasma-beta experiments, but away from the null points, the total force is about ten times stronger in the low plasma-beta experiment. This could be due to the fact that this experiment has not been relaxed for as long as any of the high plasma-beta experiments.

In the high plasma-beta experiments, the total force acted to squeeze the current layer thinner through its depth, and to widen the current layer across its width. Overall, the total force was trying to make the current layer into a long thin 2D band. Through the depth of the low plasma-beta current layer, we also find that the total force is acting to squeeze the current layer thinner (Fig. 6.16b). However, unlike the high plasma-beta experiments, across the width of the current layer, the total force is acting to make the current layer narrower (Fig. 6.16c). This indicates that, overall, the total force is acting to make the current layer thinner through its depth and across its width.

The strength of the residual total forces through the depth and across the width of the current layer are of the same order of magnitude as the values found in the high

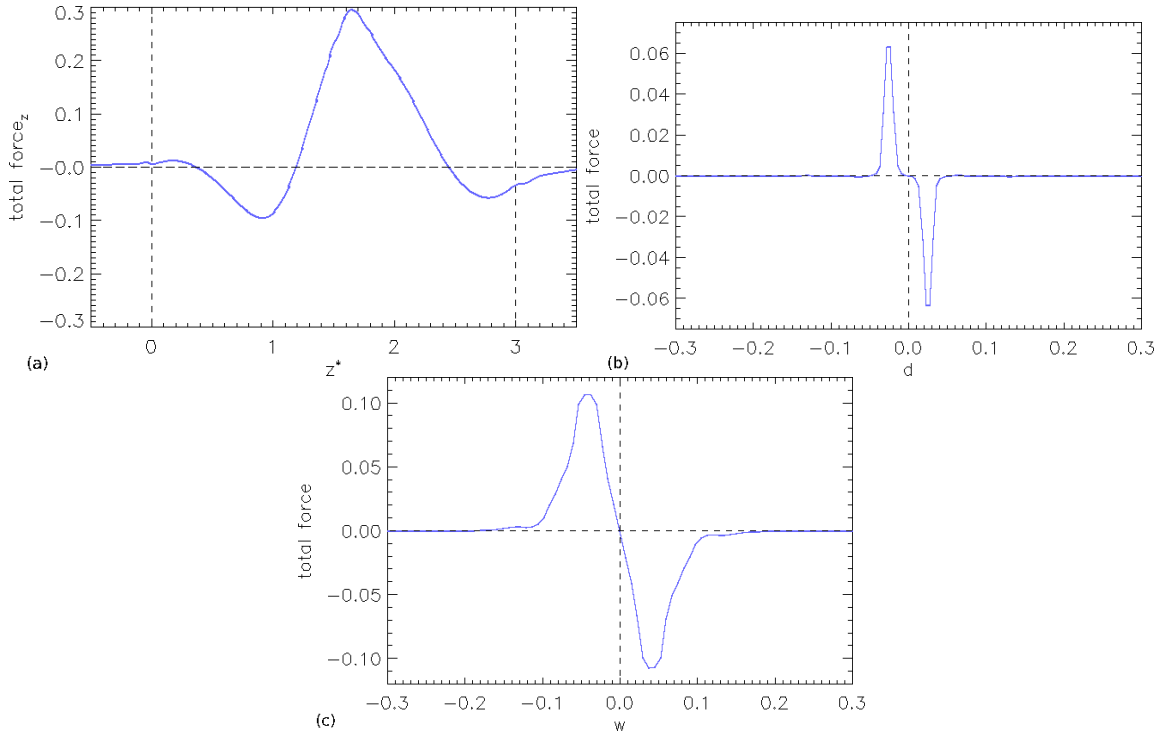


Figure 6.16: The (a) z -component of the total force plotted along the normalised z -axis and the total force plotted (b) through the depth and (c) across the width of the current layer, in a plane perpendicular to the separator at $z = 1.5$, at $t = 9.34t_f$.

plasma-beta experiments.

6.8 Growth rate

Throughout the non-resistive relaxation, the strength of the current in the separator current layer grows. In the high plasma-beta experiments where the value of the initially uniform current, j_{sep} , was varied (Chapt. 3), the maximum value of the current, found along the separator, evolved according to

$$|\mathbf{j}| = j_{sep} \left(1 + a_0 \frac{t}{t_f} \right)^{a_1}, \quad (6.10)$$

where t is time and a_0 and a_1 are scaling parameters. The maximum value of $|\mathbf{j}|$ found along the separator in this low plasma-beta experiment is plotted against time in Fig. 6.17 along with a curve of Eq. 6.10 where $a_0 = 2.6 \times 10^6$ and $a_1 = 0.228$. This figure implies that the current will continue to grow at this rate within the separator current layer.

We also note that the value of a_1 , which was found to be less than 0.5 in all the high plasma-beta experiments, has almost the same value here as the high plasma-beta experiment with $j_{sep} = 0.75$ initially (Chapt. 3). However, the values of the maximum current here are more than five times greater than the values found in the high plasma-beta experiment with $j_{sep} = 0.75$. This seems to imply that changing the separator length,

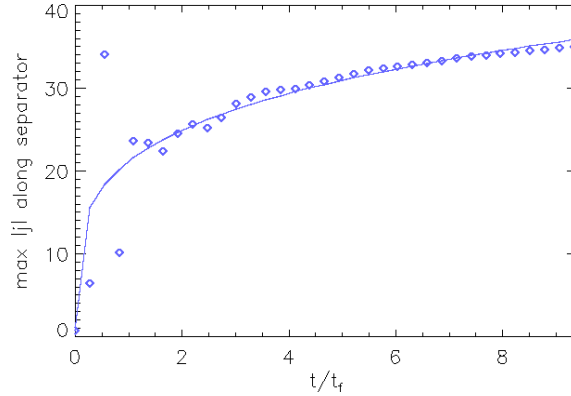


Figure 6.17: The maximum value of $|j|$ along the separator throughout the relaxation experiment. Curve of Eq. 6.10 is over plotted with $a_0 = 2.6 \times 10^6$ and $a_1 = 0.228$.

L , and applying a pressure profile of the form discussed here, does not affect the growth rate of the infinite time singularity, but does increase the strength of the current in the separator current layer.

6.9 Achieving a low plasma beta

The mean plasma beta of our MHS equilibrium discussed above is $\bar{\beta} = 1.22$. This value is not considered a low plasma-beta value since it is greater than one. To gain a low plasma-beta value from this MHS equilibrium, a uniform plasma pressure, p_{sub} , may be subtracted off the plasma in the domain. Once this value has been subtracted, the model is relaxed again to ensure the effects of numerical diffusion do not change the topology within $1t_f$. Decreasing the pressure also affects the internal energy, which decreases by $p_{sub}/(\gamma - 1)$ multiplied by the volume of the domain ($20L_0^3$), at the restart of the experiment.

We restart the experiment discussed above at $t = 7.97t_f$ with nothing changed except that a uniform value of $p_{sub} = 0.2$ is subtracted from the plasma pressure throughout the domain and consequently the internal energy is decreased uniformly throughout the domain by 0.3 per unit volume. This value is large enough such that it reduces the mean value of the plasma beta so that it is less than one, but is small enough that the pressure is still positive everywhere. Therefore, the system is allowed to relax non-resistively from $t = 7.97t_f$ to $t = 9.34t_f$, the time at which the experiment discussed above was ended, with a reduced plasma pressure. For simplicity, we shall call the original experiment discussed in this chapter, Exp. 1, and the experiment which is restarted at $t = 7.97t_f$ with $p_{sub} = 0.2$ subtracted off the plasma pressure, Exp. 2.

Fig. 6.18a shows the plasma pressure plotted through the depth (solid line) and across the width (dashed line) of the current layer and Fig. 6.18b shows the plasma pressure plotted along the z^* -axis at $t = 9.34t_f$ for Exp. 2. This figure highlights that the plasma pressure behaves identically here to as it did in Exp. 1, except the magnitudes have been reduced by 0.2 (c.f. Figs. 6.14a and 6.15a, respectively).

The mean value of the plasma beta, and the value half-way along the MHS equilibrium separator, at $t = 9.34t_f$, is smaller in Exp. 2 than it was in Exp. 1 (Table 6.1). The mean

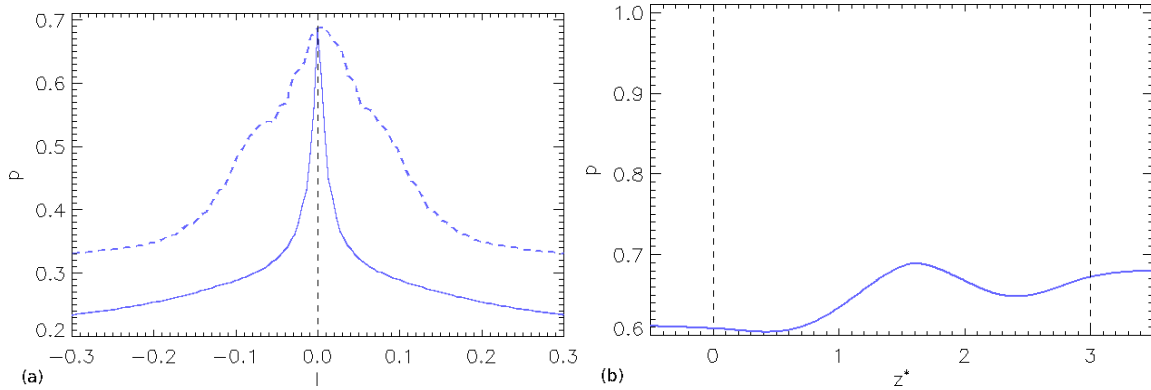


Figure 6.18: The plasma pressure plotted (a) through the depth (solid line) and across the width (dashed line) of the MHS equilibrium current layer, at $z = 1.5$, and plotted (c) along the normalised z -axis at $t = 9.34t_f$ in Exp. 2.

Table 6.1: The mean value of the plasma beta, $\bar{\beta}$, the value of the plasma-beta half-way along the MHS equilibrium separator, $\beta_{l_{sep}/2}$, the MHS equilibrium separator's length, l_{sep} , the width, w , and depth, d , of the equilibrium current layer at $z = 1.5$ and the maximum value of $|\mathbf{j}|$ along the equilibrium separator at $t = 9.34t_f$ for the original experiment discussed here (Exp. 1) and the experiment which was restarted from $t = 7.97t_f$ with 0.2 subtracted from the plasma pressure (Exp. 2).

Experiment	$\bar{\beta}$	$\beta_{l_{sep}/2}$	l_{sep}	w at $z = 1.5$	d at $z = 1.5$	Max $ \mathbf{j} $
Exp. 1	1.22	2.79	2.81722	0.141234	0.0308197	35.037207
Exp. 2	0.88	2.16	2.81728	0.141387	0.0308582	35.059334

value of the plasma beta is now smaller than one and so this experiment could be considered a low plasma-beta relaxation experiment. The topology of the model remains unchanged through Exp. 2, as it did in Exp. 1, with two nulls existing in the domain joined by one separator. The movement of the nulls in Exp. 2 was almost identical to that in Exp. 1, except the separator length is slightly greater at $t = 9.34t_f$ in Exp. 2 (Table 6.1), but these values are very close in magnitude. The energies behave the same in Exp. 2, after the experiment has been restarted, as they did in Exp. 1, except the internal energy has been reduced by $20L_0^3 p_{sub}/(\gamma - 1) = 6$, as discussed previously.

The MHS equilibrium skeleton of the model in Exp. 2, at $t = 9.34t_f$, is shown in Fig. 6.19a. The skeleton of the model is not noticeably different to the skeleton of Exp. 1. The skeleton is also shown in Fig. 6.19b where an isosurface is drawn at $\beta = 1$. This isosurface is smaller than it was in Fig. 6.2a for Exp. 1 since the plasma beta has been reduced.

The current in the system of Exp. 2, continues to slowly grow after p_{sub} has been subtracted at $t = 7.97t_f$ and the experiment has been allowed to relax until $t = 9.34t_f$. Isosurfaces of current, drawn at $j_{||} = 10$, are shown in Fig. 6.19c along with the equilibrium skeleton of Exp. 2. This figure is very similar to that shown in Fig. 6.8, which showed the equilibrium skeleton and isosurfaces drawn at $j_{||} = 10$ for Exp. 1. The maximum current,

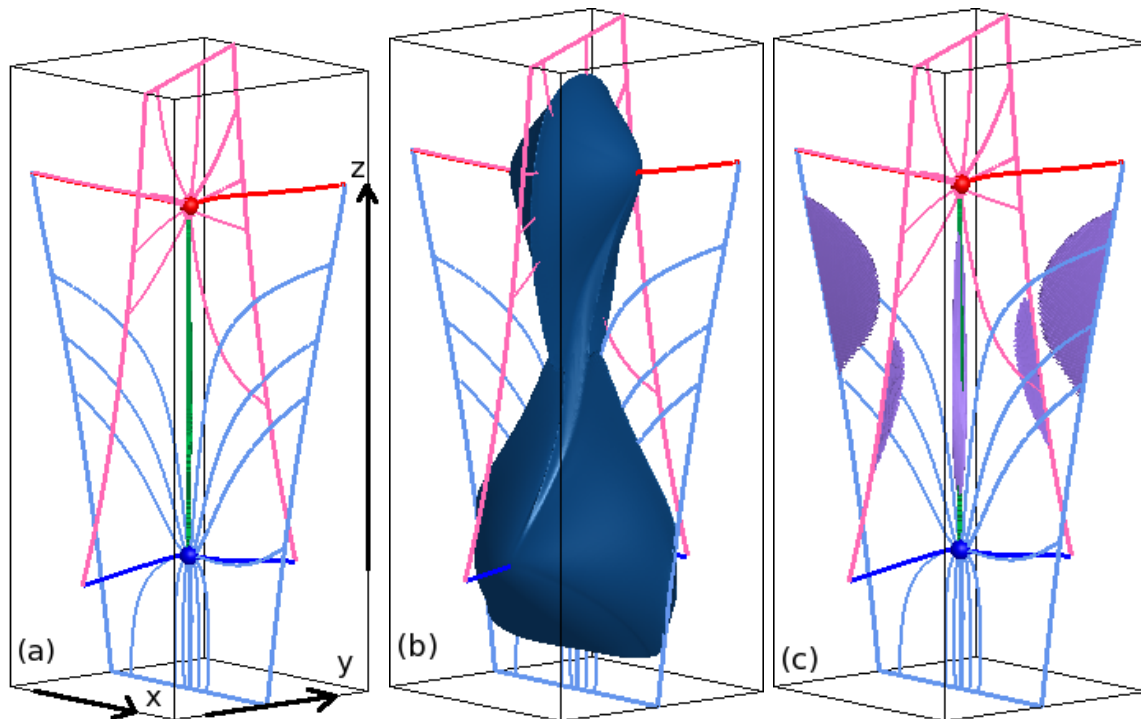


Figure 6.19: (a) The MHS equilibrium skeleton of Exp. 2 containing a positive and a negative null, with blue/red spines and pale-blue/pink separatrix surfaces. The solid pale-blue/pink lines indicate where the separatrix surfaces of the nulls intersect the domain boundaries. The separatrix surfaces of the nulls are intersecting to form the separator (green line) which links the nulls. The same skeleton is shown in (b) with an isosurface drawn at $\beta = 1$ and in (c) with an isosurface drawn at $j_{\parallel} = 10$.

along the separator, grows in the same manner, in Exp. 2 as it did in Exp. 1, but the values are now slightly larger than before (Table 6.1) and the growth rate is also slightly greater.

The widths and depths of the equilibrium current layer, at $z = 1.5$, are given in Table 6.1 for Exps. 1 and 2. These values indicate that the width and depth of the MHS equilibrium current layer in Exp. 2 are slightly greater than in Exp. 1, but these values are very similar. As such, the total force is very similar along the length, through the depth and across the width of the MHS equilibrium current layer in Exp. 2 to the values and behaviour found for Exp. 1.

Therefore, this method appears to cause little change to the MHS equilibrium, but does allow a low value of $\bar{\beta}$ to be achieved without numerical diffusion becoming so great that the topology of the system is changed before it is relaxed. However, it is interesting to note that a low value of beta on the separator itself is much harder to achieve. Indeed, it is not obvious how this can be achieved.

6.10 Summary

In this chapter, we have taken steps towards achieving a low plasma-beta ($\beta < 1$) MHS equilibrium which is formed through non-resistive MHD relaxation using the Lare3d code. The analytical magnetic field model which we have used was first discussed in Chapt. 2 and contains two null points whose separatrix surfaces intersect to form a separator that lies along the z -axis. This model is non-potential and has a component of current, which is uniform and directed parallel to the separator throughout the domain.

We have detailed results from one experiment in which an initial mean plasma beta of $\bar{\beta} = 1.07$ was achieved by increasing the initial separator length, L , from one and applying a plasma pressure profile. This pressure profile allowed us to have high pressure at the two null points, but low pressure elsewhere in the domain such that the mean value of the plasma beta may be kept low. Our motivation for trying to achieve a MHS equilibrium in which the plasma beta is low comes from the fact that the value of the plasma beta in the solar corona is $\beta < 1$. Therefore, to model equilibrium and energy release in the solar corona, we must try to achieve a low plasma beta in our experiments. In the final equilibrium though the mean plasma beta was $\bar{\beta} = 1.22$, and so we have not actually achieved our aim of a low-beta plasma.

Initially, the model has a non-zero Lorentz force and a non-zero plasma pressure force. Through the non-resistive MHD relaxation, a twisted current layer forms along the separator and enhanced current grows on the separatrix surfaces of the nulls. This is the only chapter which deals with non-resistive relaxation to MHS equilibria, in this thesis, in which we do not begin with a uniform plasma pressure and, hence, the relaxation produces slightly different results to the high plasma-beta experiments discussed in Chaps. 3 and 4. This experiment was run for less time than all the high plasma-beta experiments detailed in Chaps. 3 and 4. We stopped this experiment after $t = 9.34t_f$ since numerical diffusion caused multiple separators to exist which linked the two original null points.

Firstly, the energetics of the experiment behave differently in that a rapid expansion occurs in the system near the start of the experiment which leads to a significant amount of adiabatic cooling occurring. This affects the internal energy which is converted into kinetic and magnetic energy near the start of the experiment and appears to be a consequence of the initially high plasma pressure at the null points. After this rapid cooling has occurred, the energetics follow the same trend as observed in the high plasma-beta relaxation experiments: magnetic energy is converted into kinetic energy which, in turn, is converted into internal energy.

We found that the nulls, overall, move towards each other, along the z -axis, during the relaxation. This leads to the length of the separator, and hence the length of the current layer, decreasing during the experiment. This is in contrast to all the high plasma-beta experiments studied in this thesis, where the nulls were found to move apart along the z -axis.

The separator current layer, which forms during the relaxation, has a similar depth and width to those formed in the high plasma-beta relaxation experiments, but the strength of the current here exceeds all experiments discussed previously, that began with j_{sep} equal or greater than the value used here. The current peaks at the separator and is also enhanced on the separatrix surfaces away from the nulls but falls off in value elsewhere.

The pressure, which also changes during the relaxation, is strongly enhanced at the

separator current layer and along the separatrix surfaces of the nulls. Unlike the equilibrium pressure in the high plasma-beta experiments, where the enhanced pressure fell off gradually away from the separator current layer, here, there is a sharp change in pressure (both plasma pressure and magnetic pressure) moving away from the separator.

We have found that, unlike in the high plasma-beta experiments where the equilibrium residual forces act to slowly thin, widen and lengthen the current layer, here the residual forces, which exist in the MHS equilibrium, act to thin and narrow the current layer, forcing it towards a string-like structure. It is unclear whether the total force would shorten, lengthen or not greatly change the length of the separator current layer if the experiment could have been run for longer.

The current builds along the separator following the same form of growth that was discussed in Chapt. 3 (Eq. 6.10). We find that the value a_1 takes for the low plasma-beta experiment, in which $j_{sep} = 0.75$ initially, is almost identical to the value of a_1 found in the high plasma-beta experiment that had $j_{sep} = 0.75$ initially. This may imply that varying the separator length does not affect the overall rate of growth of current along the separator, i.e., while the current grows stronger in the low plasma-beta experiment, once it has achieved high values the rate of growth is similar to that of the high plasma-beta experiments where the strength of the current layer was weaker.

Having relaxed our model non-resistively, we found that $\bar{\beta} = 1.22$ in the MHS equilibrium state at $t = 9.34t_f$. To gain a low value of the plasma beta, we restarted our experiment at $t = 7.97t_f$ with a uniform value of $p_{sub} = 0.2$ subtracted off the plasma pressure throughout the domain, and allowed the system to relax non-resistively until $t = 9.34t_f$. This process did not greatly change the properties of the MHS equilibrium at $t = 9.34t_f$ but did reduce the mean value of the plasma beta throughout the domain to being smaller than one.

We aim to investigate the effects of varying the initial magnetic field parameters (a , b , c and j_{sep}) of this experiment and compare any differences to those found in the high plasma-beta experiments. We also want to analyse the reconnection in such a separator current layer.

Chapter 7

Summary and future work

In this thesis, we have studied MHS equilibria formed through the non-resistive MHD relaxation of analytical magnetic field models which were formulated and discussed in Chapt. 2. These magnetic fields contain two oppositely signed magnetic null points whose separatrix surfaces intersect along the z -axis to form a generic separator, which links the null points together. We discussed four forms of this magnetic field in which the direction of the current was altered.

One form of this analytical magnetic field was then used throughout the rest of the thesis. It contained five parameters, which, if varied, could alter the magnetic configuration of the model. The non-resistive MHD relaxation of this analytical field caused the separatrix surfaces of the nulls to fold towards each other and a current layer to grow along the separator. We discussed the effects of varying one of these parameters (the strength of the current) on the properties of the MHS equilibria formed, which were embedded in a high-beta plasma, in Chapt. 3. In Chapt. 4 we then detailed the results of twelve experiments in which we varied three of the magnetic field parameters, which control the geometry of the magnetic field. Again, the MHS equilibria formed in these experiments were embedded in high-beta plasmas.

Following on from this, we used one of our MHS equilibria as the initial condition in a high plasma-beta reconnection experiment in which the separator current layer was dissipated (Chapt. 5). The details of the reconnection, and the waves and flows it set up in the system, were discussed.

Finally, we discussed different ways of approaching a low plasma beta using our analytical magnetic field model (Chapt. 6). In this chapter, we proceed with one specific method and perform a non-resistive MHD relaxation experiment on the model and analyse the properties of the MHS equilibrium which is formed.

We now summarise the findings of each chapter in turn and discuss future work which could be carried out following on from the work discussed in this thesis.

7.1 Analytical forms for single-separator magnetic fields

We begin, in this thesis, by formulating an analytical potential magnetic field model, which contains two magnetic null points that are linked by a generic separator (Chapt. 2). This field satisfies a series of conditions, which puts constraints on the magnetic field

parameters. The eigenvalues and eigenvectors of the nulls were found and we studied the effects of varying the magnetic field parameters which controlled the geometry of the analytical magnetic field lines.

Next, we examined the effects of adding in a fourth magnetic field parameter which would allow the separator to bend away from the z -axis. It was found that the addition of this parameter would, in most cases, lead to extra nulls being found in the domain.

To make the analytical model more realistic we added a non-zero current. We examined the model with three forms of current; (i) a component of current parallel to the separator, (ii) a component of current perpendicular to the separator and (iii) a component of current parallel to and perpendicular to the separator. In each case, we analysed the nature of the null points by looking at the linear field local to the nulls, found constraints on the magnetic field parameters in order to satisfy our conditions and examined the effects on the magnetic configuration by varying the strength of the current.

Of these four types of analytical magnetic fields we chose the one which had current directed parallel to the separator to use throughout the rest of this thesis since, in this case, current should build most readily along the separator if the model is allowed to relax slowly. This magnetic field may be written as

$$\begin{aligned} B_x &= \frac{B_0}{L_0}(x + cxz + byz - \frac{1}{2}j_{sep}y), \\ B_y &= \frac{B_0}{L_0}((2a - c)yz - (1 + aL)y + bxz + \frac{1}{2}j_{sep}x), \\ B_z &= \frac{B_0}{L_0}(-a(z^2 - zL) + \frac{1}{2}cx^2 + (a - \frac{1}{2}c)y^2 + bxy), \end{aligned}$$

where B_0 and L_0 are the magnetic field and length scaling factors, a , b and c control the magnetic field line geometry, L is the initial length of the separator and the current takes the form $\mathbf{j} = (0, 0, j_{sep})$ where j_{sep} is uniform and directed parallel to the separator throughout the domain.

7.2 Non-resistive MHD relaxation to form a separator current layer: high plasma-beta experiments

To simulate the slow photospheric motions on the Sun which lead to the build up of current layers through the stressing of the magnetic field, we allowed our non-potential magnetic field, with current directed parallel to the separator, to relax non-resistively over time. Having selected values for our magnetic field parameters, we used the MHD code Lare3d to carry out this relaxation.

In this chapter, we firstly detailed the results from one experiment where $j_{sep} = 1.5$. An initial non-zero Lorentz force existed in the domain which, as soon as the experiment began, caused the separatrix surfaces of the nulls to collapse towards each other. During the experiment magnetic energy was converted into kinetic energy and internal energy via viscous heating and adiabatic heating. Oscillations in the energy plots indicated that waves were moving in the system. The relaxation process led to a twisted current layer forming along the separator and an enhanced current was found to lie along the separatrix surfaces of the nulls in the MHS equilibrium.

The collapse of the separatrix surfaces created cusp regions about the separator. These cusp shapes form due to the necessity of having the total pressure balance across the width

and through the depth of the equilibrium current layer. Hence, within the cusp regions, where the magnetic field tends to zero as it approaches the separator, the plasma pressure is enhanced, and outwith the cusp regions, where the magnetic field tends to a finite number as it approaches the separator, the plasma pressure is diminished.

In the MHS equilibrium, which formed due to the non-resistive relaxation, small residual forces were found to exist only along the separatrix surfaces close to the nulls and along the separator. We found that these forces were acting to lengthen the separator current layer, squeeze it thinner and widen it.

Once we had analysed this single experiment, we presented results from four other experiments where the value of the initially uniform current, j_{sep} , was varied.

Through the non-resistive relaxation of each experiment, a twisted current layer formed along the length of the separator. We defined the length of the current layers as the distance between the null points, i.e., the separator length, and found that the length of the equilibrium current layer, and hence the separator, increased with j_{sep} . Defining the width and depth of the current layer was not as straightforward as defining the length and so we discussed two possible methods, namely, the contour method and the full width at half maximum method, and explained why the former was our preferred method.

We found that the width and depth of the current layer increases as j_{sep} increased and that the angle through which the current layer twists, from the lower to the upper null along the length of the separator, increases with j_{sep} .

We checked for pressure balance here through the depth and across the width of the current layer and found that this value was fairly constant.

Finally, we examined how the growth rate of the current in the separator current layer was affected by the value of j_{sep} . We found that increasing j_{sep} leads to stronger current along the separator and that the maximum current here grows according to

$$|\mathbf{j}| = j_{sep} \left(1 + a_0 \frac{t}{t_f} \right)^{a_1}, \quad (7.1)$$

where a_0 and a_1 represent the amplitude and growth rate, respectively. This form of growth of the current has also been found at 2D null point MHS equilibria and is the typical form found in situations that involve an infinite-time collapse.

7.3 The effects of varying the initial separator magnetic field on the MHS equilibrium and its current layer

Having explored the effects of varying the initial current j_{sep} , in Chapt. 4, we detailed the results of three series of experiments in which we in turn varied the magnetic field parameters a then b and then c . In each series we carried out four experiments and compared the properties of the MHS equilibria formed with the other experiments and with that of the main experiment discussed in Chapt. 3.

An initial non-zero Lorentz force acts on the model in all twelve experiments, the maximum and mean values of which depend on the magnetic field parameters. Hence, we expected to see differences in the MHS equilibria formed through the non-resistive MHD relaxation. Each of the twelve experiments underwent non-resistive MHD relaxation, using the Lare3d code, during which magnetic energy was converted into kinetic energy

and internal energy. The amount of magnetic energy remaining in the MHS equilibrium was found to increase as a , b and c increased. In all experiments, a twisted current layer formed along the separator during the relaxation.

The properties of the MHS equilibria formed in the three series of experiments, where either a , b or c was varied, were then discussed in turn. We found that increasing a led to a longer, wider, thinner and more twisted MHS equilibrium current layer. The strength of the current in the current layer, along with the growth rate of current also increased with a . In all cases, in this series, we saw that the pressure was balanced best across the current layer for the experiments with lower values of a , but that in each case high plasma pressure formed in the cusp regions about the separator. The value of the mean plasma beta in domain, as well as the value of β half-way along the equilibrium separator, decreased as a increased, which coincided with the major axis of the lower null aligning more with the $y = x/3$ line, than the $y = 2x/5$ line, and the major axis of the upper null aligning more with the $y = -3x$ line, than the $y = 2.7x$ line. The strength of the residual forces, acting to lengthen, thin and widen the current layer, in the MHS equilibria of each experiment in Series A, increased as a increased.

Next, we varied the magnetic field parameter b . Increasing b led to a shorter, less wide and deeper current layer. Varying b did not greatly affect the angle through which the current layer twisted from the lower to the upper null, but it did change the angle between the lower and upper null's separatrix surfaces since the experiments which began with higher values of b , had a greater angle between the initial separatrix surfaces. The strength of the current along the separator current layer increased for large values of b , as did the growth rate. All experiments in Series B showed good total pressure balance through the depth and across the width of the current layer. The strength of the residual forces acting to thin the current layer through the relaxation, increased as b increased. As b increased, the total force acting across the width of the current layer decreased until $b > 1.5$. The total force acting to widen the equilibrium current layer remained fairly constant until $b > 1.0$ at which point it decreased. We found that as b increased the major axis of the lower null aligned more with the $y = x/3$ line than with the $y = x/2$ line and the major axis became increasingly dominant over the minor axis of this null. This behaviour coincided with the mean plasma beta being reduced as b was increased. At the upper null, the major axis became more dominant until $b > 1.0$ at which point it became less dominant until it was no longer the major axis. This behaviour coincided with the point at which the growth rate of the current changed from being steady to decreasing. The eigenvector associated with the major eigenvalue was fairly unchanged as b was varied.

Finally, we varied the magnetic field parameter c . Increasing c shortened and thinned the separator current layer and reduced the angle through which it twisted, but no clear relationship was found between the value of c and the depth of the equilibrium current layer. The strength of the current in the separator current layer, and its growth rate increased as c increased. The total pressure balanced well through its depth and across the width of the current layer. The strength of the residual forces in the MHS equilibrium increased as c increased for small values of c , but no overall trend could be found. The major axis of the lower null, in this series of experiments, became more dominant as c increased. This dominance was not as strong as in the Series B experiments but coincided with the mean value of the plasma beta decreasing. At the upper null, the eigenvalue which was dominant varied as c increased, with no dominant eigenvalue existing at $c = 0.0$.

Excluding this experiment, the major axis was found to align more with the $y = 2.7x$ line than the $y = 2x$ line as c increased at the equilibrium time.

We note with the experiments discussed in this chapter, that not all were relaxed for the same length of time and hence discrepancies in trends could be due to this.

7.4 Spontaneous reconnection at a high plasma-beta separator current layer

The MHS equilibria, which have been formed through non-resistive MHD relaxation in Chaps. 3 and 4, have separator current layers which contain free energy. In Chapt. 5, we used such a MHS equilibrium as the initial condition for a high plasma-beta reconnection experiment, performed by implementing the Lare3d code with an anomalous resistivity. This resistivity worked such that only the current above a certain value would be dissipated and, hence, only the strong current in the separator current layer would be involved in the reconnection.

As soon as the experiment began, the reconnection dissipated the strong current lying along the separator. We found that most of the magnetic energy was converted into internal energy with only a little being converted into kinetic energy. Most of this energy conversion occurred via Ohmic heating with small contributions from adiabatic cooling and viscous heating, with the latter indicating the movement of waves in the system. From analysing the energetics, and the reconnection rate, we saw that the experiment occurred in two phases; a fast-reconnection phase which was associated with low velocities and high Ohmic heating (phase I), and a slow-steady reconnection phase which had higher velocities and small amounts of Ohmic heating (phase II).

In phase I, during which 88% of the final total reconnected flux was reconnected, we saw that the reconnection was strongest at the separator and occurred asymmetrically along the length of the separator. The strength of the reconnection decreased along its length during phase I and only sporadic short-lived events, which were numerous, existed in phase II. We found that the magnetic field perpendicular to the separator was elliptical local to the strongest areas of reconnection along the separator, and it was X-type elsewhere. This implies the field lines local to the separator twist about it. Also, the flow counter-rotated about the separator around a point close to the point of strongest reconnection.

At the start of phase I, as soon as the reconnection began, waves were launched from the diffusion site about the separator which carried current with them and left behind enhanced pressure within the cusps, and diminished pressure outwith the cusps. These waves set up flows in the system and we saw a quadrupolar vortex scenario formed about the separator with flow bringing flux into the original diffusion site to be reconnected in phase II.

We examined the nature of the energy transport associated with these waves and flows by analysing the transport of magnetic, internal and kinetic energy equations and found that there were five main terms which contributed to the properties of the reconnection. These were the Ohmic heating term, which converted most of the magnetic energy, the enthalpy flux, Poynting flux and work done by the Lorentz and pressure forces which carried this energy away from or towards the original diffusion site. The work done by the Lorentz and pressure forces were similar in size but acted in opposite directions to try to

regain force balance in the system.

Finally we saw that increasing the strength of the reconnection led to a faster first phase with more magnetic energy being converted. If the size of the diffusion region was increased then the first phase was lengthened, since there was more flux to be reconnected, and more magnetic energy was converted. Lastly, varying the value of the background viscosity did not affect the reconnection rate, but did vary the amount of magnetic energy converted and the amount which went into kinetic energy.

7.5 Non-resistive MHD relaxation to form a separator current layer: achieving a low plasma-beta

In Chapt. 6, we detailed several ways in which a low plasma-beta value can be approached with our analytical magnetic field model, which has current parallel to the separator. The best method, which does not lead to high numerical diffusivity, involved increasing the initial length of the separator and applying a pressure profile such that initially the pressure is high around the nulls, but low elsewhere.

We performed a non-resistive MHD relaxation on this low plasma-beta model, using the Lare3d code, and detailed the properties of the MHS equilibrium formed which contained a twisted current layer lying along the separator. This experiment could not be relaxed for as long as the high plasma-beta experiments since numerical diffusion became great enough to affect the topology of the system early on during the relaxation. The energetics were different in this low plasma-beta experiment than they were in all the previous high plasma-beta relaxation experiments; a rapid expansion occurred in the system near the start of the experiment leading to adiabatic cooling. This cooling caused the internal energy to be converted into kinetic and magnetic energy. After this expansion had occurred the energetics behaved as expected, from the high plasma-beta experiments, with magnetic energy being converted into internal energy and kinetic energy.

Unlike in the high plasma-beta experiments, where the nulls moved apart throughout the relaxation, here the null points moved towards each other leading to the separator length, and hence the current layer length, decreasing over time. By the end of the relaxation, the separator length appeared to be approaching a fairly constant value. The strength of the current in the separator current layer was greater than that of all current layers formed through the relaxation of our high plasma-beta models. The width and depth of the current layer did not differ greatly from the high plasma-beta values.

The plasma pressure was found to be enhanced within the current layer and then sharply fall off outwith these regions and we saw that the current layer had pretty good balance through the depth and across the width of the current layer.

Small residual forces existed in the MHS equilibrium which acted to thin and narrow the current layer. It was unclear whether the total force would lengthen, shorten or not affect the separator length if this experiment could have been evolved longer. This was a different result from the high plasma-beta experiments where the residual forces acted to force the current layer into a 2D long wide band. We did find, however, that the growth rate of the maximum current in the current layer followed the same form of equation, and was of similar size, as was found for the high plasma-beta experiments, although the strength of the current in the current layer was greater here.

The mean plasma-beta value of the resulting MHS equilibrium field was greater than one. In order to gain a mean plasma-beta value which was less than one, we subtracted a uniform plasma pressure from the domain a few time steps before the equilibrium time, and restarted the experiment allowing it to relax again to the equilibrium time. The MHS equilibrium formed through this method was compared to the MHS equilibrium of the original experiment. There were no significant differences between the behaviour of the magnetic field or the plasma, but the mean value of the plasma beta was reduced to below one, however, it remained above a value of one everywhere along the separator.

7.6 Future work

The form of current used in Chapt. 3, 4, 5 and 6 is such that the current is parallel to the separator. It would be of interest to explore the non-resistive relaxation of non-potential magnetic fields which have a component of current perpendicular to and/or perpendicular and parallel to the separator (as detailed in Chapt. 2). Studies could be made of where the current grows strongest in such setups and analysis could be undertaken to determine how this affects the pressure and forces in the system and the dimensions of any current layers which may form.

It would be interesting to see how properties of these MHS equilibria were affected by varying the magnetic field parameters which control the geometry of the magnetic configuration, the initial magnitude of the current and the length of the separator. Having formed these MHS equilibria, they could then be used as initial conditions in resistive experiments where the subsequent reconnection could be examined and compared to the experiment where the current was initially directed along the separator.

In Chapt. 6 we discussed one experiment where we formed a MHS equilibrium with a mean plasma-beta value less than one. Although the mean plasma-beta was lower than one, the value half-way along the separator was not. Further analysis and experiments could be carried out to work out if it is possible to achieve a low plasma beta along such a separator.

It would be interesting to vary the magnetic field parameters which control the magnetic configuration, current and separator length, and also vary the initial strength of the plasma pressure profile in a low plasma-beta model and examine how these parameters affect the properties of the MHS equilibrium. Following on from this, reconnection experiments could be carried out with these models where the energetics, strength of the reconnection and the amplitude of the waves could be compared to those we have already studied with the high plasma-beta model.

We have seen that multiple separators readily appear in the low plasma-beta relaxation experiment due to the numerical diffusion becoming great enough such that it makes a significant effect. Investigating a resistive experiment with our low plasma-beta MHS equilibrium may also lead to multiple separators being formed. It would be of interest to study the properties of the reconnection along such separators and again compare this to the high plasma-beta reconnection experiment where only one separator existed.

Appendix A

Values of y for the potential magnetic field

The y -value calculated when solving the potential magnetic field for x , y and z was calculated using Mathematica. A copy of the y -values found is shown in Fig. A.

Potential magnetic field

Solve (Bx,By,Bz) = (0,0,0) for (x,y,z). The solutions for y are as follows (where $s = a^2(2+cL)^2-4b^2(1+a)$)

$$\begin{aligned}
 \text{In[382]= } y1 &= -\frac{1. \sqrt{\frac{a \left(a^2 (8.+cL (16.+cL (10.+2. cL))) + b^2 (-4.-4. cL+2. L \sqrt{s}) + a \left(b^2 L (-8.-6. cL) + (-4.+cL (-6.-2. cL)) \sqrt{s} \right) \right)}{\left(2. b^2+c \left(a (-2.-1. cL) + \sqrt{-4. b^2+a (-4. b^2 L+a (4.+cL (4.+cL))} \right) \right)^2}}{\sqrt{\frac{a^2 c (1.+cL (1.+0.25 cL)) + b^2 (-1. c+0.5 \sqrt{s}) + a c (-1. b^2 L+(-0.5-0.25 cL) \sqrt{s})}{b^2}}} \\
 y2 &= \frac{\sqrt{\frac{a \left(a^2 (8.+cL (16.+cL (10.+2. cL))) + b^2 (-4.-4. cL+2. L \sqrt{s}) + a \left(b^2 L (-8.-6. cL) + (-4.+cL (-6.-2. cL)) \sqrt{s} \right) \right)}{\left(2. b^2+c \left(a (-2.-1. cL) + \sqrt{s} \right) \right)^2}}{\sqrt{\frac{a^2 c (1.+cL (1.+0.25 cL)) + b^2 (-1. c+0.5 \sqrt{s}) + a c (-1. b^2 L+(-0.5-0.25 cL) \sqrt{s})}{b^2}}} \\
 \text{In[380]= } y3 &= -\frac{\sqrt{\frac{a \left(a^2 (8.+cL (16.+cL (10.+2. cL))) + b^2 (-4.-4. cL-2. L \sqrt{s}) + a \left(b^2 L (-8.-6. cL) + (4.+cL (6.+2. cL)) \sqrt{s} \right) \right)}{\left(2. b^2+c \left(a (-2.-1. cL) -1. \sqrt{s} \right) \right)^2}}{\sqrt{\frac{a^2 c (1.+cL (1.+0.25 cL)) + b^2 (-1. c-0.5 \sqrt{s}) + a c (-1. b^2 L+(0.5+0.25 cL) \sqrt{s})}{b^2}}} \\
 y4 &= \frac{\sqrt{\frac{a \left(a^2 (8.+cL (16.+cL (10.+2. cL))) + b^2 (-4.-4. cL-2. L \sqrt{s}) + a \left(b^2 L (-8.-6. cL) + (4.+cL (6.+2. cL)) \sqrt{s} \right) \right)}{\left(2. b^2+c \left(a (-2.-1. cL) -1. \sqrt{s} \right) \right)^2}}{\sqrt{\frac{a^2 c (1.+cL (1.+0.25 cL)) + b^2 (-1. c-0.5 \sqrt{s}) + a c (-1. b^2 L+(0.5+0.25 cL) \sqrt{s})}{b^2}}}
 \end{aligned}$$

Appendix B

Values of y for the magnetic field with current parallel to the separator

The y -value calculated when solving the magnetic field with the component of current parallel to the separator added in for x , y and z was calculated using Mathematica. A copy of the y -values found is shown in Fig. B.

Magnetic field with current parallel to separator (jsep)

Solve $(B_x, B_y, B_z) = (0, 0, 0)$ for (x, y, z) . The solutions for y are as follows
(where $s = 4c^2j^2 + b^2(4j^2 - 16) - a(8cj^2 + 16b^2L) + 16a^2 + a^2cL(16 + 4cL)$ and $j = jsep$)

$$\begin{aligned} y^1 = & -\left(\sqrt{\left(\left(a(c^2j^2(1. + 0.25j^2 + 1.cL) + b^2(-4. - 4.cL + j^2(1. + 2.cL)) + a^2(8. + cL(16. + cL(10. + 2.cL))) + 0.5cj^2\sqrt{s} + 1.b^2L\sqrt{s} + 0.25c^2j^2L\sqrt{s} + \right.\right. \\ & \left.\left. a(-8.b^2L - 2.\sqrt{s} + c(j^2(-4. + cL(-4. - 0.5cL)) + L(-6.b^2L + (-3. - 1.cL)\sqrt{s}))))\right)\right) / \left(2.b^2 + c(-2.a - 1.a cL + 0.5\sqrt{s})^2\right) / \\ & \left(\sqrt{\left(0. + 1 / (2.b - 1.cj)^2 \left(a^2c(4. + cL(4. + 1.cL)) + b(-4.bc + 2.b^2j + 2.c^2j + 1.b\sqrt{s}) + ac(-4.bj - 4.b^2L + (-1. - 0.5cL)\sqrt{s})\right)\right)} \right) \\ y^2 = & \left(\sqrt{\left(\left(a(c^2j^2(1. + 0.25j^2 + 1.cL) + b^2(-4. - 4.cL + j^2(1. + 2.cL)) + a^2(8. + cL(16. + cL(10. + 2.cL))) + 0.5cj^2\sqrt{s} + 1.b^2L\sqrt{s} + 0.25c^2j^2L\sqrt{s} + \right.\right. \\ & \left.\left. a(-8.b^2L - 2.\sqrt{s} + c(j^2(-4. + cL(-4. - 0.5cL)) + L(-6.b^2L + (-3. - 1.cL)\sqrt{s}))))\right)\right) / \left(2.b^2 + c(-2.a - 1.a cL + 0.5\sqrt{s})^2\right) / \\ & \left(\sqrt{\left(0. + 1 / (2.b - 1.cj)^2 \left(a^2c(4. + cL(4. + 1.cL)) + b(-4.bc + 2.b^2j + 2.c^2j + 1.b\sqrt{s}) + ac(-4.bj - 4.b^2L + (-1. - 0.5cL)\sqrt{s})\right)\right)} \right) \\ y^3 = & -\left(\sqrt{\left(\left(a(c^2j^2(1. + 0.25j^2 + 1.cL) + b^2(-4. - 4.cL + j^2(1. + 2.cL)) + a^2(8. + cL(16. + cL(10. + 2.cL))) - 0.5cj^2\sqrt{s} - 1.b^2L\sqrt{s} - 0.25c^2j^2L\sqrt{s} + \right.\right. \\ & \left.\left. a(-8.b^2L + 2.\sqrt{s} + c(j^2(-4. + cL(-4. - 0.5cL)) + L(-6.b^2L + (3. + 1.cL)\sqrt{s}))))\right)\right) / \left(2.b^2 + c(-2.a - 1.a cL - 0.5\sqrt{s})^2\right) / \\ & \left(\sqrt{\left(0. + 1 / (2.b - 1.cj)^2 \left(a^2c(4. + cL(4. + 1.cL)) + b(-4.bc + 2.b^2j + 2.c^2j - 1.b\sqrt{s}) + ac(-4.bj - 4.b^2L + (1. + 0.5cL)\sqrt{s})\right)\right)} \right) \\ y^4 = & \left(\sqrt{\left(\left(a(c^2j^2(1. + 0.25j^2 + 1.cL) + b^2(-4. - 4.cL + j^2(1. + 2.cL)) + a^2(8. + cL(16. + cL(10. + 2.cL))) - 0.5cj^2\sqrt{s} - 1.b^2L\sqrt{s} - 0.25c^2j^2L\sqrt{s} + \right.\right. \\ & \left.\left. a(-8.b^2L + 2.\sqrt{s} + c(j^2(-4. + cL(-4. - 0.5cL)) + L(-6.b^2L + (3. + 1.cL)\sqrt{s}))))\right)\right) / \left(2.b^2 + c(-2.a - 1.a cL - 0.5\sqrt{s})^2\right) / \\ & \left(\sqrt{\left(0. + 1 / (2.b - 1.cj)^2 \left(a^2c(4. + cL(4. + 1.cL)) + b(-4.bc + 2.b^2j + 2.c^2j - 1.b\sqrt{s}) + ac(-4.bj - 4.b^2L + (1. + 0.5cL)\sqrt{s})\right)\right)} \right) \\ & 4 * c * c * j * j + a * (-8 * c * j * j) + a * a * (16 + c * L * (16 + 4 * c * L)) // FullSimplify \\ & -8 a c j^2 - 4 c^2 j^2 + 4 a^2 (2 + c L)^2 \end{aligned}$$

Bibliography

- The Popular Science Monthly*. Number v. 16. D. Appleton, 1880. URL <http://books.google.co.uk/books?id=Z6MVAAAAAYAAJ>.
- The British Association Meeting at Edinburgh. *Nature*, 4:261–278, August 1871. doi: 10.1038/004261a0.
- T. D. Arber, A. W. Longbottom, C. L. Gerrard, and A. M. Milne. A Staggered Grid, Lagrangian-Eulerian Remap Code for 3-D MHD Simulations. *Journal of Computational Physics*, 171:151–181, July 2001. doi: 10.1006/jcph.2001.6780.
- G. Aulanier, E. Pariat, and P. Démoulin. Current-sheet formation in quasi-separatrix layers and hyperbolic flux tubes. *Astron. Astrophys.*, 444:961–976, 2005.
- G. Aulanier, E. Pariat, P. Démoulin, and C. R. DeVore. Slip-Running Reconnection in Quasi-Separatrix Layers. *Solar Physics*, 238:347–376, November 2006. doi: 10.1007/s11207-006-0230-2.
- H. W. Babcock. The Topology of the Sun’s Magnetic Field and the 22-YEAR Cycle. *Astrophys. J.*, 133:572, March 1961. doi: 10.1086/147060.
- M. R. Bareford, A. W. Hood, and P. K. Browning. Coronal heating by the partial relaxation of twisted loops. *Astronomy and Astrophysics*, 550:A40, February 2013. doi: 10.1051/0004-6361/201219725.
- D. Biskamp. Effect of secondary tearing instability on the coalescence of magnetic islands. *Physics Letters A*, 87:357–360, January 1982. doi: 10.1016/0375-9601(82)90844-1.
- D. Biskamp. *Magnetic Reconnection in Plasmas*. September 2000.
- D. Biskamp. Magnetic reconnection via current sheets. *Physics of Fluids*, 29:1520–1531, May 1986. doi: 10.1063/1.865670.
- R. Bowness, A. W. Hood, and C. E. Parnell. Coronal heating and nanoflares: current sheet formation and heating. *Astronomy and Astrophysics*, 560:A89, December 2013. doi: 10.1051/0004-6361/201116652.
- P. K. Browning, C. Gerrard, A. W. Hood, R. Kevis, and R. A. M. van der Linden. Heating the corona by nanoflares: simulations of energy release triggered by a kink instability. *Astronomy and Astrophysics*, 485:837–848, July 2008. doi: 10.1051/0004-6361:20079192.

- T. N. Bungey and E. R. Priest. Current sheet configurations in potential and force-free fields. *Astronomy and Astrophysics*, 293:215–224, January 1995.
- I. J. D. Craig. Current sheet formation and dissipation in general X-point topologies. *Astronomy and Astrophysics*, 283:331–338, March 1994.
- I. J. D. Craig and R. B. Fabling. Exact Solutions for Steady State, Spine, and Fan Magnetic Reconnection. *Astrophysical Journal*, 462:969, May 1996. doi: 10.1086/177210.
- I. J. D. Craig and Y. E. Litvinenko. Current singularities in planar magnetic X points of finite compressibility. *Physics of Plasmas*, 12(3):032301, March 2005. doi: 10.1063/1.1854154.
- I. J. D. Craig, R. B. Fabling, S. M. Henton, and G. J. Rickard. An Exact Solution for Steady State Magnetic Reconnection in Three Dimensions. *Astrophysical Journal*, 455:L197, December 1995. doi: 10.1086/309822.
- I. De Moortel and K. Galsgaard. Numerical modelling of 3D reconnection due to rotational footpoint motions. *Astronomy and Astrophysics*, 451:1101–1115, June 2006a. doi: 10.1051/0004-6361:20054587.
- I. De Moortel and K. Galsgaard. Numerical modelling of 3D reconnection. II. Comparison between rotational and spinning footpoint motions. *Astronomy and Astrophysics*, 459:627–639, November 2006b. doi: 10.1051/0004-6361:20065716.
- P. Demoulin, J. C. Henoux, E. R. Priest, and C. H. Mandrini. Quasi-Separatrix layers in solar flares. I. Method. *Astronomy and Astrophysics*, 308:643–655, April 1996.
- P. Demoulin, L. G. Bagala, C. H. Mandrini, J. C. Henoux, and M. G. Rovira. Quasi-separatrix layers in solar flares. II. Observed magnetic configurations. *Astronomy and Astrophysics*, 325:305–317, September 1997.
- J. C. Dorelli, A. Bhattacharjee, and J. Raeder. Separator reconnection at Earth’s day-side magnetopause under generic northward interplanetary magnetic field conditions. *Journal of Geophysical Research (Space Physics)*, 112:A02202, February 2007. doi: 10.1029/2006JA011877.
- J. W. Dungey. Conditions for the occurrence of electrical discharges in astrophysical systems. *Philosophical Magazine*, 44:725–738, 1953.
- A. S. Eddington. The internal constitution of the stars. *Observatory*, 43:353, 1920.
- B. Edlén. Die deutung der emissionslinien im spektrum der sonnenkorona. mit 6 abbildungen. 1942.
- C. R. Evans and J. F. Hawley. Simulation of magnetohydrodynamic flows - A constrained transport method. *Astrophysical Journal*, 332:659–677, September 1988. doi: 10.1086/166684.
- J. Fuentes-Fernández and C. E. Parnell. Magnetohydrodynamics dynamical relaxation of coronal magnetic fields. III. 3D spiral nulls. *Astronomy and Astrophysics*, 544:A77, August 2012. doi: 10.1051/0004-6361/201219190.

- J. Fuentes-Fernández and C. E. Parnell. Magnetohydrodynamics dynamical relaxation of coronal magnetic fields. IV. 3D tilted nulls. *Astronomy and Astrophysics*, 554:A145, June 2013. doi: 10.1051/0004-6361/201220346.
- J. Fuentes-Fernández, C. E. Parnell, and A. W. Hood. Magnetohydrodynamics dynamical relaxation of coronal magnetic fields. II. 2D magnetic X-points. *Astronomy and Astrophysics*, 536:A32, December 2011. doi: 10.1051/0004-6361/201117156.
- J. Fuentes-Fernández, C. E. Parnell, A. W. Hood, E. R. Priest, and D. W. Longcope. Consequences of spontaneous reconnection at a two-dimensional non-force-free current layer. *Physics of Plasmas*, 19(2):022901, February 2012. doi: 10.1063/1.3683002.
- K. Galsgaard and Å. Nordlund. Heating and activity of the solar corona 1. Boundary shearing of an initially homogeneous magnetic field. *Journal of Geophysical Research*, 101:13445–13460, June 1996. doi: 10.1029/96JA00428.
- K. Galsgaard and C. E. Parnell. Elementary heating events - magnetic interactions between two flux sources. III. Energy considerations. *Astronomy and Astrophysics*, 439:335–349, August 2005. doi: 10.1051/0004-6361:20052775.
- K. Galsgaard, V. S. Titov, and T. Neukirch. Magnetic Pinching of Hyperbolic Flux Tubes. II. Dynamic Numerical Model. *Astrophysical Journal*, 595:506–516, September 2003. doi: 10.1086/377258.
- R. G. Giovanelli. A Theory of Chromospheric Flares. *Nature*, 158:81–82, July 1946. doi: 10.1038/158081a0.
- R. M. Green. Modes of annihilation and reconnection of magnetic fields. In R. Lust, editor, *Stellar and Solar Magnetic Fields*, volume 22 of *IAU Symposium*, page 398, 1965.
- W. Grotrian. Zur frage der deutung der linien im spektrum der sonnenkorona. 27:214–214, 1939.
- A. L. Haynes and C. E. Parnell. A method for finding three-dimensional magnetic skeletons. *Physics of Plasmas*, 17(9):092903, September 2010. doi: 10.1063/1.3467499.
- A. L. Haynes and C. E. Parnell. A trilinear method for finding null points in a three-dimensional vector space. *Physics of Plasmas*, 14(8):082107, August 2007. doi: 10.1063/1.2756751.
- A. L. Haynes, C. E. Parnell, K. Galsgaard, and E. R. Priest. Magnetohydrodynamic evolution of magnetic skeletons. *Royal Society of London Proceedings Series A*, 463:1097–1115, April 2007. doi: 10.1098/rspa.2007.1815.
- M. Hesse and K. Schindler. A theoretical foundation of general magnetic reconnection. *Journal of Geophysical Research*, 93:5559–5567, June 1988. doi: 10.1029/JA093iA06p05559.
- A. W. Hood, P. K. Browning, and R. A. M. van der Linden. Coronal heating by magnetic reconnection in loops with zero net current. *Astronomy and Astrophysics*, 506:913–925, November 2009. doi: 10.1051/0004-6361/200912285.

- F. Hoyle. *Some recent researches in solar physics*. 1949.
- I. Klapper. Constraints on finite-time current sheet formation at null points in two-dimensional ideal incompressible magnetohydrodynamics. *Physics of Plasmas*, 5:910–914, April 1998. doi: 10.1063/1.872659.
- I. Langmuir. *Oscillations in ionized gases*. 1928.
- Y.-T. Lau and J. M. Finn. Three-dimensional kinematic reconnection in the presence of field nulls and closed field lines. *Astrophysical Journal*, 350:672–691, February 1990. doi: 10.1086/168419.
- A. W. Longbottom, G. J. Rickard, I. J. D. Craig, and A. D. Sneyd. Magnetic Flux Braiding: Force-free Equilibria and Current Sheets. *Astrophysical Journal*, 500:471, June 1998. doi: 10.1086/305694.
- D. W. Longcope. Separator current sheets: Generic features in minimum-energy magnetic fields subject to flux constraints. *Physics of Plasmas*, 8:5277–5290, December 2001. doi: 10.1063/1.1418431.
- D. W. Longcope and S. C. Cowley. Current sheet formation along three-dimensional magnetic separators. *Physics of Plasmas*, 3:2885–2897, August 1996. doi: 10.1063/1.871627.
- D. W. Longcope and A. V. R. Silva. A current ribbon model for energy storage and release with application to the flare of 7 January 1992. *Solar Physics*, 179:349–377, May 1998. doi: 10.1023/A:1005071122577.
- S. Masson, E. Parlat, G. Aulanier, and C. J. Schrijver. The Nature of Flare Ribbons in Coronal Null-Point Topology. *Astrophysical Journal*, 700:559–578, July 2009. doi: 10.1088/0004-637X/700/1/559.
- E. N. Parker. Sweet’s Mechanism for Merging Magnetic Fields in Conducting Fluids. *Journal of Geophysical Research*, 62:509–520, December 1957. doi: 10.1029/JZ062i004p00509.
- C. E. Parnell, J. M. Smith, T. Neukirch, and E. R. Priest. The structure of three-dimensional magnetic neutral points. *Physics of Plasmas*, 3:759–770, March 1996. doi: 10.1063/1.871810.
- C. E. Parnell, A. L. Haynes, and K. Galsgaard. Structure of magnetic separators and separator reconnection. *Journal of Geophysical Research (Space Physics)*, 115:A02102, February 2010a. doi: 10.1029/2009JA014557.
- C. E. Parnell, R. C. Maclean, and A. L. Haynes. The Detection of Numerous Magnetic Separators in a Three-Dimensional Magnetohydrodynamic Model of Solar Emerging Flux. *Astrophysical Journal*, 725:L214–L218, December 2010b. doi: 10.1088/2041-8205/725/2/L214.
- C. E. Parnell, R. C. Maclean, A. L. Haynes, and K. Galsgaard. 3D Magnetic Reconnection. In N. H. Brummell, A. S. Brun, M. S. Miesch, and Y. Ponty, editors, *IAU Symposium*, volume 271 of *IAU Symposium*, pages 227–238, August 2011. doi: 10.1017/S1743921311017650.

- D. I. Pontin. Theory of magnetic reconnection in solar and astrophysical plasmas. *Royal Society of London Philosophical Transactions Series A*, 370:3169–3192, July 2012. doi: 10.1098/rsta.2011.0501.
- D. I. Pontin and I. J. D. Craig. Current singularities at finitely compressible three-dimensional magnetic null points. *Physics of Plasmas*, 12(7):072112, July 2005. doi: 10.1063/1.1987379.
- D. I. Pontin and K. Galsgaard. Current amplification and magnetic reconnection at a three-dimensional null point: Physical characteristics. *Journal of Geophysical Research (Space Physics)*, 112:A03103, March 2007. doi: 10.1029/2006JA011848.
- D. I. Pontin, G. Hornig, and E. R. Priest. Kinematic reconnection at a magnetic null point: Spine-aligned current. *Geophys. Astrophys. Fluid Dyn.*, 98:407–428, 2004.
- D. I. Pontin, K. Galsgaard, G. Hornig, and E. R. Priest. A fully magnetohydrodynamic simulation of 3D non-null reconnection. *Phys. Plasmas*, 12:052307, 2005a.
- D. I. Pontin, G. Hornig, and E. R. Priest. Kinematic reconnection at a magnetic null point: Fan-aligned current. *Geophys. Astrophys. Fluid Dyn.*, 99:77–93, 2005b.
- D. I. Pontin, A. K. Al-Hachami, and K. Galsgaard. Generalised models for torsional spine and fan magnetic reconnection. *Astron. Astrophys.*, 533:A78, September 2011.
- D. I. Pontin, E. R. Priest, and K. Galsgaard. On the nature of reconnection at a solar coronal null point above a separatrix dome. *Astrophys. J.*, 774:154, 2013. doi: 10.1088/0004-637X/774/2/154.
- E. Priest and T. Forbes, editors. *Magnetic reconnection : MHD theory and applications*, 2000.
- E. R. Priest and P. Démoulin. Three-dimensional magnetic reconnection without null points. 1. Basic theory of magnetic flipping. *Journal of geophysical research*, 100:23443–23464, December 1995. doi: 10.1029/95JA02740.
- E. R. Priest and T. G. Forbes. New models for fast steady state magnetic reconnection. *Journal of Geophysical Research*, 91:5579–5588, May 1986. doi: 10.1029/JA091iA05p05579.
- E. R. Priest and D. I. Pontin. Three-dimensional null point reconnection regimes. *Physics of Plasmas*, 16(12):122101, December 2009. doi: 10.1063/1.3257901.
- E. R. Priest and V. S. Titov. Magnetic Reconnection at Three-Dimensional Null Points. *Royal Society of London Philosophical Transactions Series A*, 354:2951–2992, December 1996. doi: 10.1098/rsta.1996.0136.
- E. R. Priest, G. Hornig, and D. I. Pontin. On the nature of three-dimensional magnetic reconnection. *Journal of Geophysical Research (Space Physics)*, 108:1285, July 2003. doi: 10.1029/2002JA009812.

- Eric Priest. *Magnetohydrodynamics of the sun*. Cambridge University Press, New York, NY, Jan 2014.
- L. Rastätter, A. Voge, and K. Schindler. On current sheets in two-dimensional ideal magnetohydrodynamics caused by pressure perturbations. *Physics of Plasmas*, 1:3414–3424, October 1994. doi: 10.1063/1.870490.
- R. Schielicke and A. D. Wittmann. On the Berkowski daguerreotype (Königsberg, 1851 July 28): the first correctly-exposed photograph of the solar corona. *Acta Historica Astronomiae*, 25:128–147, 2005.
- K. Schindler, M. Hesse, and J. Birn. General magnetic reconnection, parallel electric fields, and helicity. *Journal of Geophysical Research*, 93:5547–5557, June 1988. doi: 10.1029/JA093iA06p05547.
- B. V. Somov and S. I. Syrovatskii. Hydrodynamic Plasma Flow in a Strong Magnetic Field. In N. G. Basov, editor, *Neutral Current Sheets in Plasmas*, page 13, 1976.
- B. U. Ö. Sonnerup. *Magnetic field reconnection*, pages 45–108. 1979.
- P. A. Sweet. The Neutral Point Theory of Solar Flares. In B. Lehnert, editor, *Electromagnetic Phenomena in Cosmical Physics*, volume 6 of *IAU Symposium*, page 123, 1958.
- S. I. Syrovatskii. Formation of Current Sheets in a Plasma with a Frozen-in Strong Magnetic Field. *Soviet Journal of Experimental and Theoretical Physics*, 33:933, 1971.
- V. S. Titov and E. R. Priest. The collapse of an X-type neutral point to form a reconnecting time-dependent current sheet. *Geophys. Astrophys. Fluid Dyn.*, 72:249–276, 1993.
- V. S. Titov, K. Galsgaard, and T. Neukirch. Magnetic Pinching of Hyperbolic Flux Tubes. I. Basic Estimations. *Astrophysical Journal*, 582:1172–1189, January 2003. doi: 10.1086/344799.
- L. Trenchi, M. F. Marcucci, G. Pallochia, G. Consolini, M. B. Bavassano Cattaneo, A. M. di Lellis, H. Rème, L. Kistler, C. M. Carr, and J. B. Cao. Occurrence of reconnection jets at the dayside magnetopause: Double Star observations. *Journal of Geophysical Research (Space Physics)*, 113:A07S10, July 2008. doi: 10.1029/2007JA012774.
- A. L. Wilmot-Smith and G. Hornig. A Time-dependent Model for Magnetic Reconnection in the Presence of a Separator. *Astrophysical Journal*, 740:89, October 2011. doi: 10.1088/0004-637X/740/2/89.
- A. L. Wilmot-Smith, G. Hornig, and D. I. Pontin. Magnetic Braiding and Quasi-Separatrix Layers. *Astrophysical Journal*, 704:1288–1295, October 2009a. doi: 10.1088/0004-637X/704/2/1288.
- A. L. Wilmot-Smith, G. Hornig, and D. I. Pontin. Magnetic braiding and parallel electric fields. *Astrophys. J.*, 696:1339–1347, May 2009b.
- A. L. Wilmot-Smith, G. Hornig, and D. I. Pontin. Magnetic braiding and quasi-separatrix layers. *Astrophys. J.*, 704:1288–1295, October 2009c.

*“From the moment I picked up your book until I laid it down, I was convulsed with laughter.
Some day I intend reading it.”*
- Groucho Marx